博士論文

Search for third-generation leptoquarks at $\sqrt{s} = 13$ TeV with ATLAS detector

（ATLAS実験における$\sqrt{s} = 13$ TeVでの第3世代レプトクォークの探索）

令和3年3月

神戸大学大学院理学研究科

竹田　康亮

Abstract

The Standard Model (SM) in particle physics is the successful theory to explain most of the experimental results. The last piece of the SM, the Higgs boson, is discovered by the ATLAS and CMS experiments in 2012. However, it is not still perfect and there are still some problems to be solved. Many new scenarios are proposed as the extensions of the SM, which predict some new particles. One of the new particles is known as leptoquarks which couple to a quark and a lepton sector simultaneously.

Recently, B-factory experiments have reported inconsistencies between the SM and the experimental result concerning the B meson leptonic decays. This thesis focuses on one of the inconsistencies, focusing on the $b \to c\tau\nu_\tau$ decay. The ratio of the branching ratio, $R(D^*) = B(\bar{B} \to D^{(*)}\tau\nu_\tau)/B(\bar{B} \to D^{(*)}\ell\nu_\ell)$, is larger than the SM prediction. To describe the discrepancy, we need a mechanism which strongly couples to the third generation matters. One of the possible scenarios is the leptoquarks. The B-anomalies can be explained with existence of the third generation leptoquarks.

This thesis reports an updated result of search for third generation scalar leptoquark ($\mathrm{LQ}_3^{\mathrm{u}}$) via LQ $\to b\tau$ decay mode at ATLAS experiments in LHC. In this search, we focus on LQ pair production events, where one of the τ decaying leptonically and the other τ decaying hadronically. In this channel, the light lepton can be used to select events effectively, and the large branching ratio of the hadronic decaying tau can be used to increase the signal acceptance. Although the previous round analysis was performed in the same channel, the analysis strategy did not work well at the higher energy region. Therefore, we try to tune the selection requirements to realize the high-mass $\mathrm{LQ}_3^{\mathrm{u}}$ specific optimal search. Furthermore, we adopt the Parametric Neural Network model instead of Boosted Decision Tree used in the previous work in order to extend search to higher mass region. In addition, the new approach also makes analysis strategy simpler. The search uses $139\mathrm{fb}^{-1}$ p-p collision data collected by ATLAS detector in LHC at center-of-mass energy of $\sqrt{13}$ TeV. The exclusion limits are set on the pair production of scalar leptoquarks as a function of the mass.

Contents

List of Figures

List of Tables

Chapter 1

Introduction

Thousands of particle physicists have tried to describe the fundamental structure of matter over the past, and our knowledge is encapsulated in an elegant series of theories, referred to as the Standard Model of particle physics. The theories describe how matter particles (lepton and quarks) and three of fundamental forces (gauge bosons) are related to each other.

Although the SM gives the best description which is consistent with current experimental results, it does not give the complete picture of the universe. One of the limitations is that the SM cannot give a reasonable reason why there are two types of fermions, leptons and quarks. The leptons and quarks have several similarities, but the SM treats the fermions independently with each other. This work aims to find the reason by focusing on a theory model, which expects leptoquark (LQ) bosons. As a consequence of the LQ existence, leptons and quarks have a relation [3–9].

Recently, independent B-factory experiments (Babar, Belle and LHCb) have reported results which are not consistent with the SM predictions in the lepton flavor universality [10]. The tension is known as "B-anomalies", which implies a possibility of the LQ model existence. This thesis focuses especially on the LQ mode decaying into a pair of b-quark and τ lepton, because this LQ model coupled to the third generation can solve "B-anomalies".

As discussed above, the LQ are predicted by a lot of theoretical models. Therefore, the detailed properties of the LQ depend on each theoretical model. In this thesis, we don't focus on a specific model, but model independent treatments according to Büchmuller-Rüchl-Wyler (mBRW) model [11] are adopted.

New physics processes including the LQ model can be searched directly using the Large Hadron Collider (LHC), which is the most powerful proton accelerator in the world. The LHC has four collision points, where four types of detectors are located for each physics goal. This thesis used data samples collected by A Troidal LHC Apparatus (ATLAS) experiment [12], which is one of the general purpose detectors.

Previous work by the ATLAS Collaboration have reported a lower limit on the LQ mass by using data of 36 fb^{-1} [13]. The lower mass limit is 1030 GeV. In the context of the B-anomalies, the possible mass range is within $\mathcal{O}(1\mathrm{TeV})$. Therefore, it is important to search higher mass region with respect to the previous work.

This thesis focuses on a search for the heavy LQ model by using 139 fb^{-1} data at $\sqrt{s} = 13$ TeV with the ATLAS detector aiming to conclude what causes the "B-anomalies". The number of heavy signal events is expected to be small, then it is necessary to develop a technique to extract such subtle signature. Therefore, the multi-variate analysis (MVA) technique used in the previous work was replaced by a newer model, Parametric Neural Network (PNN) [14].

Recently, various MVA techniques are used in particle physics. The previous work also used one of the techniques, Boosted Decision Tree (BDT) [15]. The BDT is one of the most commonly techniques, because the method can work with limited statistics. However, there are some disadvantages. In the previous work, the BDT models were trained at each interesting LQ mass region. As a consequence, the BDT models cannot work fine at a mass point, where the BDT wasn't trained. In addition, the BDT is based on the classical Decision Tree technique, then the performance is worse than a neural network based techniques. Therefore, this analysis decided not to use the BDT models, but to use Parametric Neural Network (PNN) [14]. The PNN model can take LQ mass as an input information, then the trained model can be as a function of the LQ mass. The advantage solves the first problem of the BDT. Furthermore, the PNN model is based on a neural network technique. The PNN model can improve the sensitivities, while make the analysis method simplified. This analysis using the 139 fb^{-1} data set and the improved analysis techniques describes a search for LQ in heavier mass region than the previous work.

Structure of the dissertation

The first part discuss the theoretical backgrounds, experimental setup, and simulation toolkit used in the analysis.

- Chapter 2 describes theoretical motivations in the thesis, and presents the current experimental results.
- Chapter 3 describes the experimental overview; the Large Hadron Collider and the ATLAS detectors.
- Chapter 4 describes the configurations of event simulations in the analysis.

The main descriptions of the leptoquark search are given by the following Chapters.

- Chapter 5 describes the reconstruction method of the produced particles by the proton-proton collisions.
- Chapter 6 describes the event selection to define the LQ events enriched region.
- Chapter 7 describes the statistical treatment used in the analysis.
- Chapter 8 describes the background process estimation method.

Result and the discussion are given by the following Chapters.

- Chapter 9 describes the final discriminant variables for this analysis, and summarizes the results with the expected analysis sensitivities.
- Chapter 10 discussed the impact as a consequence of the results.

Chapter 2

Theoretical Backgrounds

The Standard Model of particle physics is a quantum field theory to describe the interactions between elementary particles. Although the theory is outstandingly consistent with the current experimental results, there are still remained problems which it cannot solve. This chapter reviews the Standard Model briefly, and introduces Leptoquark model as a beyond SM.

2.1 The Standard Model

The Standard Model (SM) describes fundamental interactions successfully within our present knowledge. This model consists of gauge theories [16, 17]; strong interaction with $SU(3)_C$, and electro-weak interaction with $SU(2)_L \times U(1)_Y$. The gauge theories are invariance under the local transformations, and this is the guiding principle of the SM. The electro-weak sector is broken down to the subgroup $U(1)_{\text{em}}$ through the Brout-Englert-Higgs (BEH) mechanism.

There are three types of particles in the SM; fermions with the 1/2 spin that compose matters, gauge bosons with the 1 spin that mediate the interactions between the fermions (and gauge bosons), and the Higgs boson with spin 0 that feeds masses through the BEH mechanism. The gauge bosons are three types; photon, weak bosons (W, Z boson) and gluons characterize electromagnetic, weak and strong interactions respectively[1]. The fermions have two families; quarks and leptons, where both of them have up- and down-type. The quarks can interact via all the three fundamental interactions, while the leptons are coupled to weak and electromagnetic gauge bosons. In addition, there exist two more duplicates of fermions with exactly the same properties except the masses, referred to as "2nd/3rd generation". Each fermion furthermore has its charge conjugated partner called the anti-fermion. All of these particles in the SM are shown in Table 2.1 and Table 2.2.

In the quantum field theory, Lagrangian is used to describe the behavior of particles. The simplified SM lagrangian can be described as [18]:

$$\begin{aligned}\mathcal{L} = &-\frac{1}{4}F_{\mu\nu}F^{\mu\nu} \\ &+ i\bar{\psi}\not{D}\psi + h.c. \\ &+ y\bar{\Psi}\Psi + h.c. \\ &+ |D_\mu\phi|^2 - V(\phi),\end{aligned} \tag{2.1}$$

---

[1] The SM cannot describe the gravitational interaction, but the effects can be neglected with respect to amplitudes of the three interactions.

Table 2.1: Summary table of the standard model fermions.

Particle	Symbol	Q	Spin	mass
electron	e	-1	1/2	0.511 MeV
electron neutrino	ν_e	0	1/2	0
muon	μ	-1	1/2	105.658 MeV
muon neutrino	ν_μ	0	1/2	0
tau	τ	-1	1/2	1776.86 MeV
tau neutrino	ν_τ	0	1/2	0
up	u	2/3	1/2	2.16 MeV
down	d	-1/3	1/2	4.67 MeV
charm	c	2/3	1/2	1.27 GeV
strange	s	-1/3	1/2	93 MeV
top	t	2/3	1/2	172.67 GeV
bottom	b	-1/3	1/2	4.18 GeV

Table 2.2: Summary table of the standard model boson.

Particle	Symbol	Q	Spin	mass
photon	γ	0	1	0
W boson	W	-1	1	80.37 GeV
Z boson	Z	0	1	91.18 GeV
gluon	g	0	1	0
Higgs	h	0	0	125.10 GeV

where the first term is the scalar product of the field strength $F_{\mu\nu}$ which is the kinetic term of the gauge bosons, the second term describes the kinetic term of fermions and coupling between fermions and gauge bosons ($\psi, \bar{\psi}$ means quarks, leptons, anti-quarks, or anti-leptons), the third term describes how fermions couple to the BEH field ϕ and obtain their masses, and the fourth term describes the kinetic and potential terms of BEH field and the coupling to gauge bosons which can give the mass to gauge bosons. Here, the *h.c.* is the hermitian conjugate of each term.

2.2 Looking beyond the Standard Model

In the SM, the lepton number L and baryon number B are formally independent of each other. On the other hand, they are rather similar with respect to the generation and multiple structure of the electroweak interactions, left-handed $SU(2)$ doublets and right-handed $SU(2)$ singlets. There is indeed a close relation between these quantum numbers in the SM, and the symmetry between quarks and leptons leads to the cancellation of triangle anomalies which make the SM renormalizable [19]. This is one of the important relation for the SM to be a consistent quantum field theory [20]. The triangle anomalies are cancelled by the requirement [21, 22]:

$$\sum_{\text{repr.}} \mathrm{tr}[T^a\{T^b, T^c\}] = 0, \tag{2.2}$$

where $T^{a,b,c}$ is generators of $SU(3)$, $SU(2)$ or $U(1)$ in the SM. This condition is true under the sum taken by all of fermions (leptons and quarks).

The relation may imply the more fundamental theory of quarks and leptons, which is then expected to contain bosonic fields mediating these particles simultaneously. Examples for such theories are Grand Unified Theory (GUT) [23], the Pati-Salam $SU(4)$ mode [3], and models of quark and lepton substructure [4]. Although the new fields can give a reason to the lepton-quark independence, these also give rise to lepton and baryon number non-conservation and flavour changing neutral current at a tree-level. There are strong experimental bounds from proton lifetime measurements. However, bosons which exclusively induce lepton-quark interaction, referred to as "leptoquark", are relatively weak constrained by current experimental results. Furthermore, they can be light enough to be produced by the LHC experiment. This is because this analysis focused on the "leptoquark" model to give the reason why the lepton and quark sectors exist in the SM.

2.3 Leptoquark models

As discussed in 2.2, there are weak constraints for the leptoquark models. However, any current experiments have not found any evidence of the leptoquark yet. Therefore, many theoretical models can be taken into account for properties of the leptoquark. On the contrary, this analysis adopts a strategy where leptoquark interactions are given independent on each theoretical model as much as possible. This section describes the adopted leptoquark models, and the current experiment limitations on the production cross-section.

2.3.1 Buchmuller-Ruchl-Wyler model

This paper focuses on a model-independent LQ framework, Büchmuller-Rüchl-Wyler (BRW) framework [11]. In the model, $F = 3B + L$ quantum number is introduced, and the model still have the $SU(3)_C \otimes SU(2)_L \otimes U(1)_Y$ gauge invariant interactions with the SM fermions and bosons. The LQs can be scalar or vector particles, and each lepton-LQ or quark-LQ Yukawa coupling is denoted by a dimensionless parameter, λ. The general Lagrangian of the BRW model can be written as the sum of seven scalar and seven vector couplings [24, 25]. For scalar LQs, the interaction lagrangian is given by:

$$\begin{aligned} L_S = \{ & \left(\lambda_L^{S_1} \bar{q}_L^c i\tau_2 \ell_L + \lambda_R^{S_1} \bar{u}_R^c e_R\right) S_1^\dagger + \lambda_R^{\tilde{S}_1} \bar{d}_R^c e_R \tilde{S}_1{}^\dagger + \\ & \left(\lambda_L^{S_2} \bar{u}_R \ell_L + \lambda_R^{S_2} \bar{q}_L i\tau_2 e_R\right) S_2^\dagger + \lambda_L^{\tilde{S}_2} \bar{d}_R \ell_L \tilde{S}_2{}^\dagger + \\ & \lambda_L^{S_3} \bar{q}_L^c i\tau_2 \vec{\tau} \ell_L \vec{S_3}{}^\dagger \} \\ & + h.c. \ , \end{aligned} \tag{2.3}$$

and for vector LQs, the interaction lagrangian is given by:

$$\begin{aligned} L_V = &\left(\lambda_V^{V_1}\bar{q}_L\gamma_\mu\ell_L + \lambda_R^{V_1}\bar{d}_R\gamma_\mu e_R\right)V_1^{\mu\dagger} + \lambda_R^{\tilde{V}_1}\bar{u}_R\gamma_\mu e_R\tilde{V}_1^{\mu\dagger}+ \\ &\left(\lambda_V^{V_2}\bar{d}_R^c\gamma_\mu\ell_L + \lambda_R^{V_2}\bar{q}_L^c\gamma_\mu e_R\right)V_2^{\mu\dagger} + \lambda_R^{\tilde{V}_2}\bar{u}_R^c\gamma_\mu e_L\tilde{V}_2^{\mu\dagger}+ \\ &\lambda_R^{\tilde{V}_3}\bar{q}_L^c i\tau_2\vec{\tau}\ell_L\vec{V}_3^{\mu\dagger} \\ &+ h.c. \;. \end{aligned} \tag{2.4}$$

The S and V denote the scalar and vector LQs, respectively. The Yukawa couplings λ_L and λ_R represent the chirality of the corresponding LQ as given in the superscripts ($\lambda^{LQ}, LQ = S_1, S_2, S_3, V_2, V_2, V_3$). The Dirac gamma matrices are denoted by γ_μ ($\mu = 0, 1, 2, 3$), Pauli matrices are denoted by τ_i ($i = 1, 2, 3$), and $i\tau_2$ provides the antisymmetric $SU(2)_L$ contraction. Fermion spinors are taken to be in the chiral basis such that $\bar{f}_{R,L} = (P_{R,L}f)^\dagger\gamma^0$ and $f_L^c = (P_L f)^c$ where $P_{R,L} = (1 \pm \gamma^5)/2$ are the chiral projection operators and charge conjugation is defined as $f^c = Cf^* = -i\gamma^2 f^*$. $SU(3)_C$ and $SU(2)_L$ indices are suppressed for clarity and a sum over all fermion generations is implied for each term. In the most general form, the Yukawa couplings carry two generation indices, λ^{ij}, such that an i^{th} generation quark is coupled to an j^{th} lepton via the LQ vertex.

This analysis adopts additional assumptions as the "minimal" BRW model (mBRW) [11]. The mBRW model imposes some constraints on the properties of the LQs, and can make the analysis strategy very clear.

These constrains are related to the Yukawa coupling parameters λ in the BRW model, where λ is free parameter. The mBRW model takes the current experimental results into account. One of the experimental results is the very long proton lifetime, which implies that there is no mechanism to promote the rapid proton decay. If the LQs can couple to the first generation particles easily, the proton (uud) cannot keep the stability. Therefore, the amplitude of the Yukawa couplings including the first generation is very small. Similarly, in order to avoid large contributions to the helicity suppressed $\pi^+ \to e\nu_e$ decays, the LQs doesn't couple to L and R particles simultaneously. Thus, in the BRW effective model, LQs are assumed to have chiral couplings with a single generation of SM fermions at a time. The LQ states and the associated quantum numbers in the mBRW are summarized in Table 2.3 [26, 27]. The above assumptions and constraints imply the existence of the LQs which couple strongly to third generation quarks and leptons.

2.3.2 B-anomalies constraint from other experiments

The LQs are searched by both various directly and indirectly experiments. The direct searches (including this analysis) are performed recently at hadron colliders experiments, and many results have been reported. In addition, the indirect searches are performed, ex. B-factory experiments.

Recently, an excess has been observed in the $R(D^{(*)})$ ratios by B-physics experiments (BaBar, Belle, and LHCb) [28–30] in the semi-leptonic B decays, known as "B-anomalies". The ratio is explained as :

$$R_{D^{(*)}} = \frac{B(B \to D^{(*)}\tau\nu_\tau)}{B(B \to D^{(*)}\ell\nu_\ell)} = 0.41 \pm 0.05, \tag{2.5}$$

Table 2.3: Summary table of the Scalar and Vector LQs, where couple to third generation quarks and leptons.

Leptoquark	Spin	F	$SU(3)_C \otimes SU(2)_L \otimes U(1)_Y$	Q_{EM}	Decay mode
S_1	0	-2	$(\mathbf{3}, \mathbf{1}, -2/3)$	-1/3	$t\tau$, $b\nu$
$\tilde{S}_1$	0	-2	$(\mathbf{3}, \mathbf{1}, -8/3)$	-4/3	$b\tau$
S_2	0	0	$(\bar{\mathbf{3}}, \mathbf{2}, -7/3)$	(-2/3, -5/3)	$t\nu$, $b\tau$, $t\tau$
$\tilde{S}_2$	0	0	$(\bar{\mathbf{3}}, \mathbf{2}, -1/3)$	(+1/3, -2/3)	$b\nu$, $b\tau$
S_3	0	-2	$(\mathbf{3}, \mathbf{3}, -2/3)$	(+2/3, -1/3, -4/3)	$t\nu$, $t\tau$, $b\nu$, $b\tau$
V_1	1	0	$(\bar{\mathbf{3}}, \mathbf{1}, -4/3)$	-2/3	$b\tau$,$t\nu$
$\tilde{V}_1$	1	0	$(\bar{\mathbf{3}}, \mathbf{1}, -10/3)$	-5/3	$t\tau$
V_2	1	-2	$(\mathbf{3}, \mathbf{2}, -5/3)$	(-1/3, -4/3)	$b\nu$, $t\tau$, $b\tau$
$\tilde{V}_2$	1	-2	$(\mathbf{3}, \mathbf{2}, -1/3)$	(+2/3, -1/3)	$t\nu$, $t\tau$
V_3	1	0	$(\bar{\mathbf{3}}, \mathbf{3}, -4/3)$	(+1/3, -2/3, -5/3)	$b\nu$, $b\tau$, $t\nu$, $t\tau$

where the numerator is the branching ratio to the third generation particles, while the denominator is the branching ratio to the first or second generation particles ($\ell = e$ or μ). This value is a combined one from the three B-factory experiments, and this value appears to be about 3σ above the SM prediction, $R_D^{SM} = 0.286 \pm 0.012$. These results are shown in Fig 2.1. This anomalies can be explained in models with TeV scale leptoquarks, and this result especially implies a LQs with large couplings to the third generation particles.

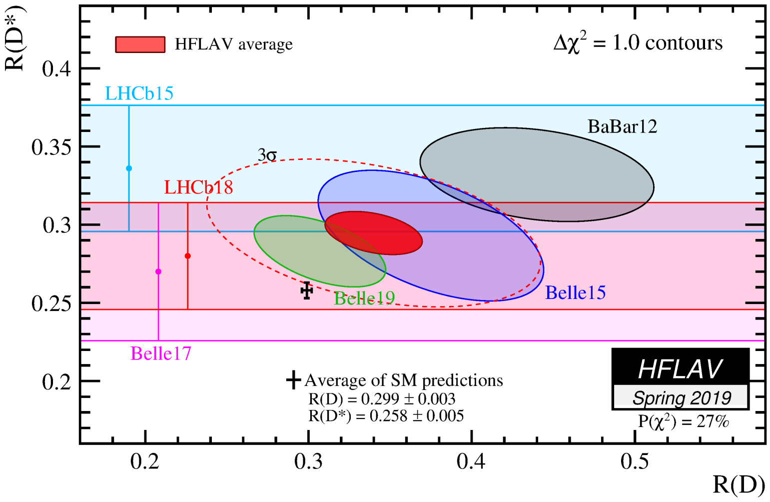

Figure 2.1: The $R(D)$ and $R(D^*)$ combined result [1].

From the point of view of the B-anomalies, two possible LQ models are favored, LQ → $b+\tau$ or LQ → $c+\nu_\tau$. These process contribute the semi-leptonic B-hadron decay as shown in Fig 2.2. This analysis especially focuses on the former model because of the following two reasons. One is that there is no strong limits on the third generation leptoquarks. The other is that it is difficult to treat the final state including the neutrinos, which cannot be measured directly in the hadron collider experiment. Therefore, this analysis searched the LQ → $b + \tau$ model.

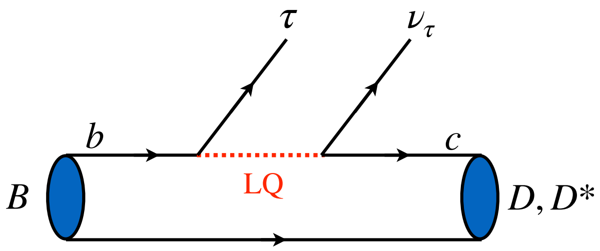

Figure 2.2: Semi-leptonic B-hadron decay mode via a leptoquark. This process includes two couplings of the leptoquark, LQ → $b + \tau$ or LQ → $c + \nu_\tau$.

2.3.3 Production and Decay of Leptoquarks

In the hadron collider experiments, the LQs can be produced as single production or pair production via the Yukawa couplings λ. The overview of each production mode is shown in Fig 2.3. In the single production mode, the production cross section depends on the Yukawa coupling λ, which is one of the free parameters in the BRW model. On the contrary, the pair production cross section can be described by the well-known strong coupling constant, α_s. Therefore, this analysis focuses on the pair production mode to remove the theoretical dependencies as much as possible. Although the vector LQs can be produced via the pair production mode, this analysis also decided not to focus on the vector LQs. The vector LQs cross section depends on not only the α_s but also other theoretical free parameters. The corresponding leading order Feynman diagrams for the pair production processes are given in Fig 2.4.

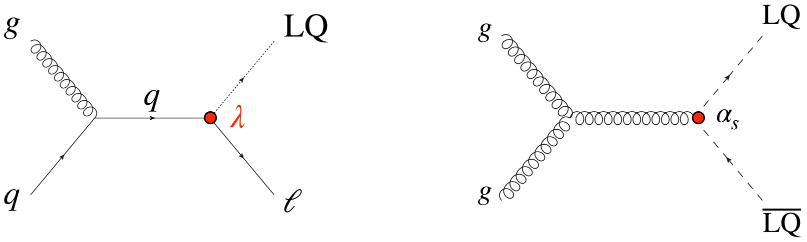

Figure 2.3: The tree-level Feynman diagrams of the single production (left) and pair production (right) of the LQ(s). The single production depends on the free parameter λ in the BRW mode, therefore the single production search needs a lot of assumptions to analyze the experimental data.

The leading order pair-production cross sections are given by [31, 32]:

$$\hat{\sigma}^{gg}_{\text{LO}_\text{s}\overline{\text{LQ}}_\text{s}} = \frac{\alpha_s^2 \pi}{96\hat{s}} \times \left[\hat{\beta}(41 - 31\hat{\beta}^2) + (18\hat{\beta}^2 - \hat{\beta}^4 - 17) \ \log \left| \frac{1+\hat{\beta}}{1-\hat{\beta}} \right| \right], \tag{2.6}$$

$$\hat{\sigma}^{q\bar{q}}_{\text{LO}_\text{s}\overline{\text{LQ}}_\text{s}} = \frac{2\pi \alpha_s^2 \hat{\beta}^3}{27\hat{s}}, \tag{2.7}$$

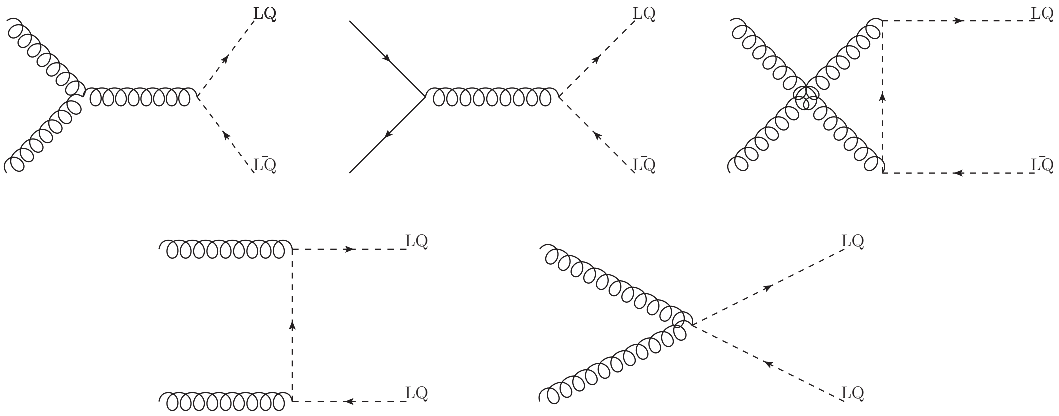

Figure 2.4: The possible tree-level Feynman diagrams of the pair production of the LQs.

where the gg or $q\bar{q}$ is the initial state of the pair production process, the $\sqrt{\hat{s}}$ is the subprocess center-of-mass system energy, and the $\hat{\beta} = \sqrt{1 - 4m_{\mathrm{LQ}}^2/\hat{s}}$. As shown in Eq (2.6) and Eq (2.7), the pair-production cross section depends on only the LQ mass.

Finally, the decay width of the interesting LQ model is discussed. The third-generation scalar leptoquark of the interesting has two decay modes, $b\tau$ or $t\nu_\tau$. Therefore, the branching fraction B into $q\ell = b\tau$ is given by :

$$B = \frac{\Gamma_{b\tau}}{\Gamma_{b\tau} + \Gamma_{t\nu_\tau}}. \tag{2.8}$$

For a scalar leptoquark decay to pair of charged lepton and quark ($q\ell$), the tree-level decay width is given as [27]:

$$\Gamma_{q\ell} = \frac{\lambda^2 M_{\mathrm{LQ}}}{16\pi}\left(1 - \frac{m_q^2}{M_{\mathrm{LQ}}^2}\right) \simeq \frac{\lambda^2 M_{\mathrm{LQ}}}{16\pi} \quad (\because m_q = m_b \ll M_{\mathrm{LQ}}), \tag{2.9}$$

where the quark mass dependency is shown (m_b is the bottom quark mass) in the first equality. A similar relation holds for the LQ decays to a neutral lepton and a quark ($q'\nu$). The corresponding decay length is given by:

$$d = \gamma c\tau = \frac{1}{\Gamma}\frac{|\vec{p}|}{M_{\mathrm{LQ}}}, \tag{2.10}$$

where the Γ is the decay width, $\vec{p}$ is the vector of the LQ momentum. If the $\lambda > 10^{-5}$, the decay length can be computed as $d < 10\mu$m. Therefore, the LQ decays rapidly before reaching at the ATLAS detectors volume.

2.3.4 Current Experimental limits

Previous ATLAS limit with 36.1 fb^{-1} for the leptoquark pair production [13] is shown in Fig 2.5. These results are used to set lower limit on the leptoquark mass as a function of the branching ratio B. This analysis focuses on the $b\tau b\tau$ final state, then the analysis sensitivity is the best in the case of $B = 1$, where both of the LQ decay into $b + \tau$. From the data, masses below 1030 GeV are excluded, at 95% CL for the case of $B = 1$.

In addition, the upper limit of the cross section as a function of B is shown in Fig 2.6. The $b\tau b\tau$ analysis (green colored) was optimized for the LQ pair-production with LQLQ $\rightarrow b\tau b\tau$.

Therefore, the green line has the best sensitivity at the $B(\mathrm{LQ}_3^{\mathrm{u}} \to \mathrm{b}\tau) = 1$. As discussed above, the LQ can decay into $t\nu_\tau$, and the other analyses were performed to search the decay modes including the neutrinos, where E_T^{miss} represents the neutrinos as discussed in Chapter 5. The decay mode including the neutrinos were excluded by the re-interpretations of other analysis channels with the same final state. As a consequence, it is necessary for the $b\tau b\tau$ mode to develop an optimized analysis.

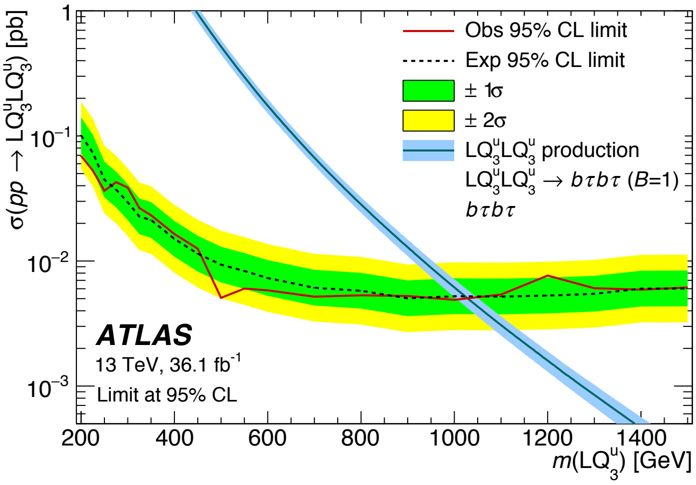

Figure 2.5: Expected and observed 95% CL upper limits on the cross-section for the scalar leptoquark pair production with $B = 1$ as a function of leptoquark mass for the combined decay channels [13]. The observed limit is shown as the solid line. The thickness of the theory curve represents the theoretical uncertainty from PDFs, renormalization and factorization scales, and the strong coupling constant α_s.

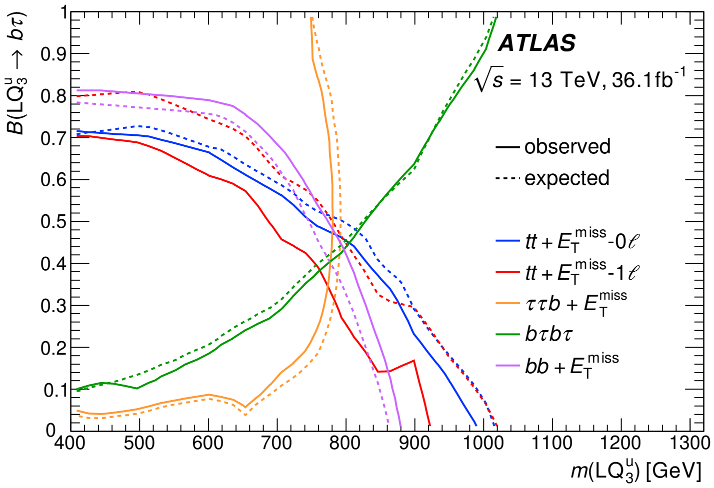

Figure 2.6: Limits on the branching ratio into charged leptons for scalar third-generation up-type leptoquark pair production ($\mathrm{LQ} \rightarrow b\tau/t\nu$) as a function of the leptoquark mass [13]. The limits are based on a dedicated LQ search for two b-jets and two τ-leptons ($b\tau b\tau$), and reinterpretations of the search for bottom-squark pair production ($bb + E_T^{\mathrm{miss}}$) [33], for top-squark pair production with one ($tt + E_T^{\mathrm{miss}}$-1ℓ) [34] or zero leptons ($tt + E_T^{\mathrm{miss}}$-0ℓ) [35] in the final state, and for top squarks decaying via τ-sleptons ($\tau\tau b + E_T^{\mathrm{miss}}$) [36]. The region to the left of the contour lines is excluded at 95% confidence level.

Chapter 3

The ATLAS experiment

3.1 The Large Hadron Collider

The Large Hadron Collider (LHC) is a large proton accelerator at CERN facility, which is a 27 km long circular embedded underground of the Geneva area. Four collision points and prepared for corresponding experiments (ATLAS [37], CMS [38], ALICE [39] and LHCb [40]). The ATLAS and CMS are general purpose detectors to measure and search varying benchmark physics models, while the ALICE and LHCb are dedicated detectors to study heavy-ion and b-hadrons physics respectively. The CERN LHC experiments started in 2010 with $\sqrt{s} = 7$ or 8 TeV and stored 20.3fb^{-1} until 2012 (Run-1). After repairing and upgrading the accelerators and detectors, these experiments re-started in 2015 with $\sqrt{s} = 13$ TeV and stored 139 fb^{-1} until 2018 (Run-2).

To accelerate proton beams in the LHC ring at such high energy, there are multiple accelerators, as shown in Fig 3.1. These brief descriptions are summarized below :

LINAC2

Linear accelerator 2 (LINAC2) is the starting point for the protons used in the LHC experiments. The proton source is a bottle of hydrogen gas at one end of LINAC2, where the hydrogen gas is ionized and protons enter the accelerator. An 800 m long transfer line carries the proton beam at 50 MeV to the entrance to the next apparatus.

PS Booster

Proton Synchrotron Booster (PS Booster) receives protons from the LINAC2, and increase the energy to 1.4 GeV. PS Booster allows the next stage, i.e. Proton Synchrotron, to accept over 100 times more protons with its four rings.

PS

Proton Synchrotron (PS) with a circumference of 628 metres accelerates the beam to 25 GeV.

SPS

The Super Proton Synchrotron (SPS) with a circumference of nearly 7 kilometres is the second-largest machined in CERN accelerators. The SPS receives protons from the PS and accelerate them to provide beam for the LHC. The SPS operates at up to 450 GeV.

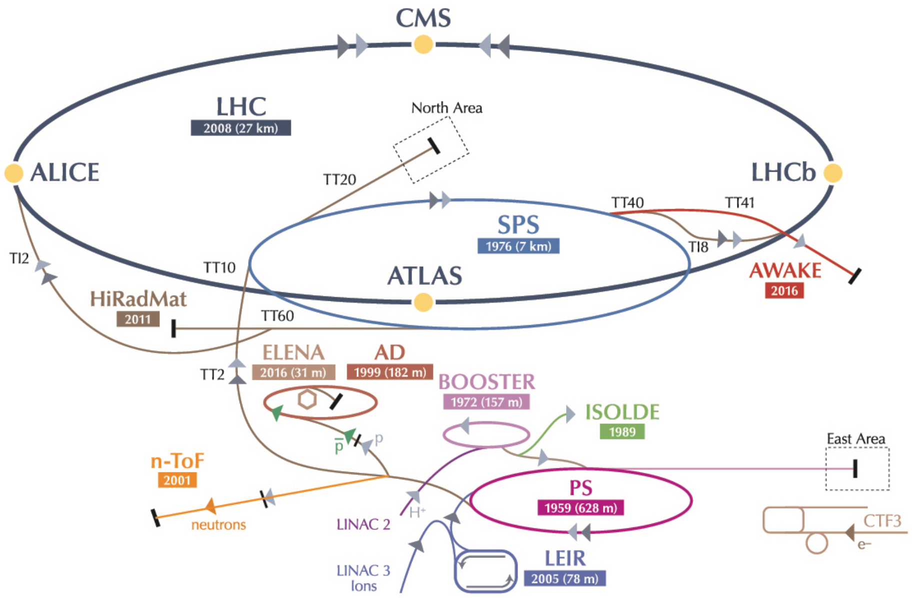

Figure 3.1: Accelerator system at CERN [41].

The LHC accelerator receives proton beams from the SPS, and furthermore accelerate the beams to achieve up to 6.5 TeV. The proton beam is not like continuous string of particles, but is divided into chunks which is referred to as "bunch". The LHC was operated with the peak instantaneous luminosity $2.1 \times 10^{34}\text{cm}^{-2}\text{s}^{-1}$, and collides bunches at 40 MHz. The number of events per second from the collisions is described as [42]:

$$\frac{dR}{dt} = \mathcal{L} \times \sigma, \tag{3.1}$$

where $\mathcal{L}$ is the number of interactions called as the instantaneous luminosity and σ is the production cross section. The unit of the luminosity is $\text{cm}^{-2}\text{s}^{-1}$. The instantaneous luminosity is expressed as [43]:

$$L = \frac{N_B^2 f_{\text{rev}} k_B}{4\beta^* \epsilon_{xy}} \times F, \tag{3.2}$$

where f_{rev} is the revolution frequency, the k_B is the number of bunches per beam, $\epsilon_{xy} = \epsilon_n/(\gamma_{\text{rel}}\beta_{\text{rel}})$ is the geometric emittance and F is a geometric reduction factor. The F can be given by:

$$F = \frac{1}{\sqrt{1 + \frac{(\sigma_s \tan\phi)^2}{\epsilon_{xy}\beta^*}}}, \tag{3.3}$$

here σ_s is the bunch length and ϕ is the half crossing angle.

3.2 The ATLAS detector

As introduced in Section 3.1, A Troidal LHC ApparatuS (ATLAS) experiment uses one of two general-purpose detectors at the LHC. The detector can cover a wide range of physics, from measurements of well-established theories to new physics. Although the ATLAS experiment has the same goals as the CMS experiment, there are big differences of the detector designs. In this section, the overviews of the ATLAS detectors and the sub-systems, where the descriptions are mainly referred from [44].

3.2.1 The coordinate system

The ATLAS experiment uses a right-handed Cartesian coordinate system with its origin at the interaction point [45]. The beam direction defines the z-axis, the positive x-axis points from the interaction point towards the center of the LHC ring and the positive y-axis points upwards. Polar angle θ and azimuthal angle ϕ are defined by the cylindrical representation (θ, ϕ, z), where θ ranges from 0 to π with respect to the z-axis, and ϕ ranges from $-\pi$ to π from the x-axis. These overview is shown in Fig 3.12. The ATLAS detector is made up of a barrel region and two endcaps, with each region consisting of several detector sub-systems. The two end-caps in the ATLAS detector are referred to as "A-side" $(z > 0)$ and "C-side" $(z < 0)$.

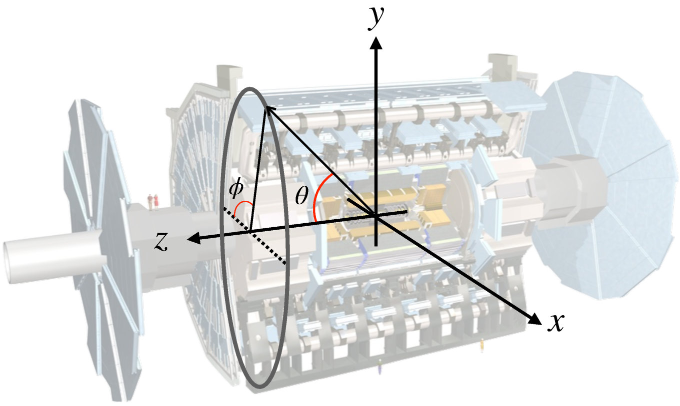

Figure 3.2: Overview of the ATLAS detector and the coordinate system [37]. The details of the coordinate system is described in Section 3.2.1

Hard collisions, which are most intersting processes for ATLAS, occur between partons in protons, thus the energy of the initial state is not symmetry. Therefore, particles generated are usually highly boosted along z-axis. From this point of view, pseudo-rapidity η is useful to describe hadron collider properties, which is defined below:

$$\eta = -\ln\tan\frac{\theta}{2} \tag{3.4}$$

Angular distance between two particles are commonly expressed by ΔR, defined as:

$$\Delta R = \sqrt{(\Delta\eta)^2 + (\Delta\phi)^2}. \tag{3.5}$$

3.2.2 Magnet system

The ATLAS magnet system consists of one solenoid and three troidal magnets (one barrel and two end-caps), which are shown in Fig 3.3a. The central solenoid magnet is aligned on the z-axis and provides a 2 T axial magnetic field for the inner detector. The materials are suppressed to minimize the radiative materials in front of the barrel calorimeters. The troid magnets produce a troidal magnetic field of approximately 0.5 T and 1 T for the muon detectors in the barrel and end-cap regions, respectively. Due to the very complicated structure of these magnetic fields, the bending power is lower in the two magnet overlap region ($1.4 < \eta < 1.6$), referred to as transition region as shown in Fig 3.3b.

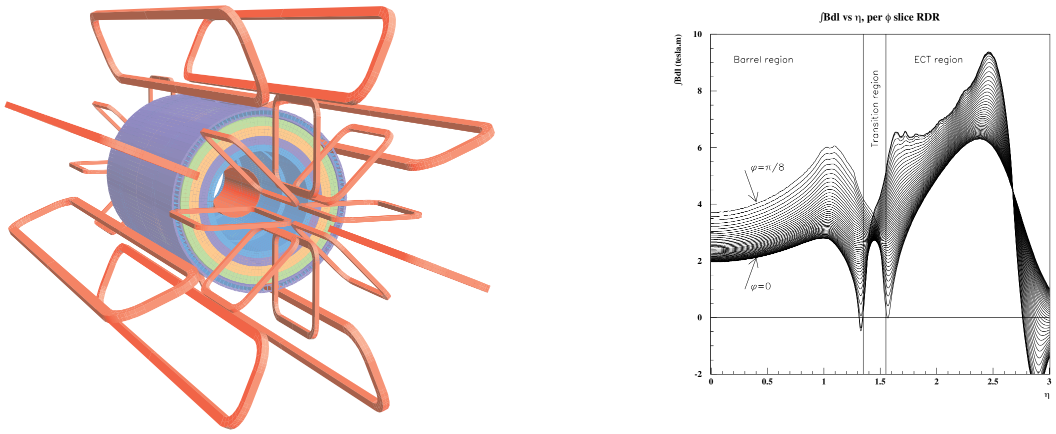

(a) Magnet system

(b) $\int Bdl$ vs η

Figure 3.3: (a) Geometry of magnet systems. The eight barrel troid coils, with the end-cap coils interleaved are visible [37]. (b) The bending power distribution in the η plane [37].

3.2.3 Inner detector

The inelastic cross-section of proton-proton collision is about 20 mb and the peak luminosity reaches $2 \times 10^{34}\text{cm}^{-2}s^{-1}$, thus a lot of charged tracks are created. These momenta and vertices should be measured very precisely to achieve the benchmark physics processes. At a very large track density environment, these are three types of detectors with high-precision granularity located at the inner most of the ATLAS detector; Silicon Pixel detector (Pixel) and Semiconductor Tracker (SCT) and Transition Radiation Tracker (TRT). The layout of the Inner Detector (ID) is shown in Fig 3.4.

Silicon Pixel detector

The Silicon Pixel detector (Pixel) is the inner detector covering $|\eta| < 2.5$. The Pixel detector is composed of modules as shown in Fig 3.5. The 1744 modules are prepared in the pixel detector, and these modules are arranged in four barrel layers and two end-caps each with three disk layers segmented in R-ϕ and z. All pixel sensors are identical and have a minimum pixel size in R-$\phi \times z$ of $50 \times 400\mu\text{m}^2$. The intrinsic accuracy in the barrel are 10 μm (R-ϕ) and 115 μm (z) and in the disks are 10 μm (R-ϕ) and 115 μm (z). The inner most Pixel layer is called as "B-layer" [46] (IBL) to focus on reconstructions of B-hadrons. The IBL is one of new detectors which was installed at the beginning of Run-2, where the sensor size is $50 \times 250\mu\text{m}^2$.

Semiconductor Tracker

The Semiconductor Tracker (SCT) is a silicon strip detector. In the barrel region, there are four cylindrical layers, and in the end-cap region there are nine disks. The SCT barrel module is shown in Fig 3.6, which uses small-angle (40 mrad) stereo strips to measure both coordinates,

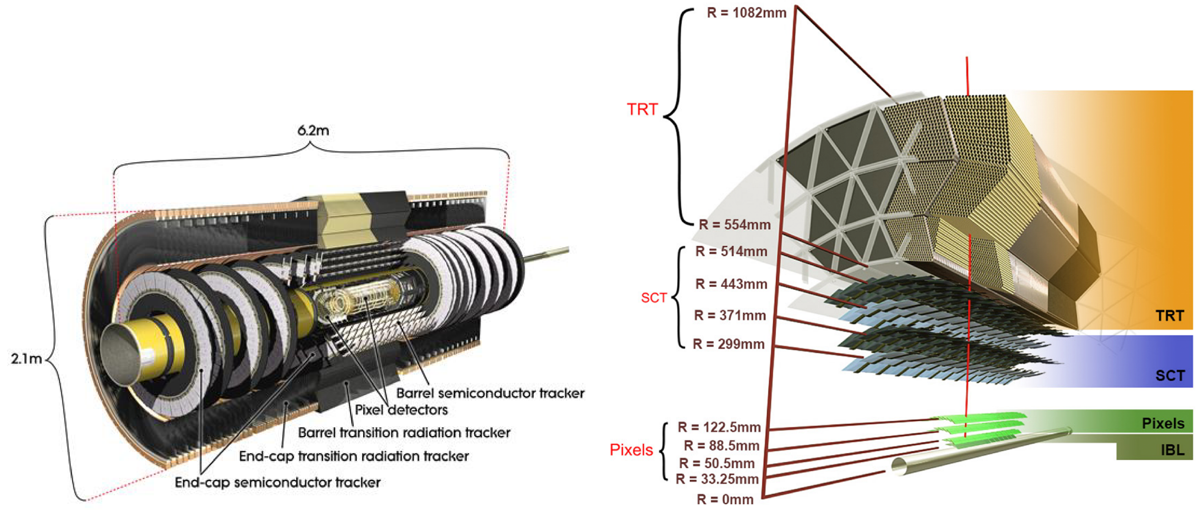

(a) (b)

Figure 3.4: (a) The structure of the ATLAS Inner Tracking Detector made of highly granular silicon pixels, silicon strips and straw tubes [37]. (b) The cover region of each inner detector [37].

R-ϕ. The mean pitch of the strips is also approximately 80 μm. The intrinsic accuracy per module in the barrel are 17 μm (R-ϕ) and 580 μm (z) and in the disks are 17 μm (R-ϕ) and 580 μm (z-ϕ, R). The total number of readout channels in the SCT is approximately 6.3 million.

Transition Radiation Tracker

The Transition Radiation Tracker (TRT) comprises many layers of gaseous straw tube elements interleaved with transition radiation material, as shown in Fig 3.7. A large number of hits (typically 36 per track) are provided by the 4 mm diameter straw tubes up to $|\eta| = 2.0$. The TRT only provides z-ϕ information, for which it has an intrinsic accuracy of 130 μm per straw. In the barrel region, the straws are parallel to the beam axis and are 144 cm long, with their wires divided into two halves, approximately at $\eta = 0$. In the end-cap region, the 37 cm long straws are arranged radially in wheels. The total number of TRT readout channels is approximately 351,000.

3.2.4 Calorimeters

ATLAS experiment uses sampling calorimeters to measure particle energies, which covers the range $|\eta| < 4.9$. The calorimeter system is composed of the electromagnetic (EM) calorimeters and the hadronic calorimeters to suit to the widely varying requirements of the benchmark physics processes, as shown in Fig 3.8. It is usually designed to stop entire or absorb most of the particles coming from a collision, forcing them to deposit all of their energy within the detector.

LAr electromagnetic Calorimeter

The ATLAS electromagnetic (EM) calorimeter is a sampling calorimeter with a Pb as an absorber and a liquid Ar as a active material, which is divided into a barrel part ($|\eta| < 1.475$) and two end-cap components ($1.375 < |\eta| < 3.2$) [47]. The EM calorimeter uses accordion-shaped kapton electrodes and lead absorber plates, where the accordion

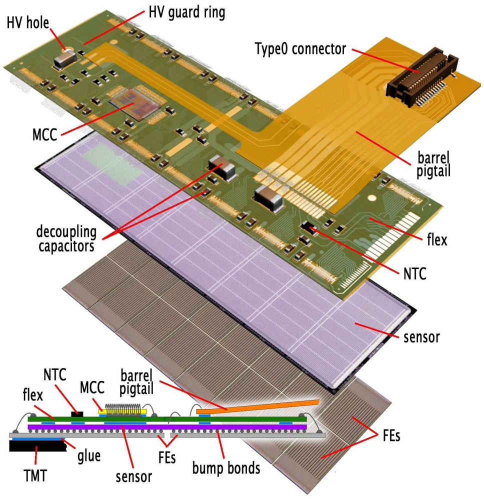

Figure 3.5: Schematic view of a barrel pixel module [37].

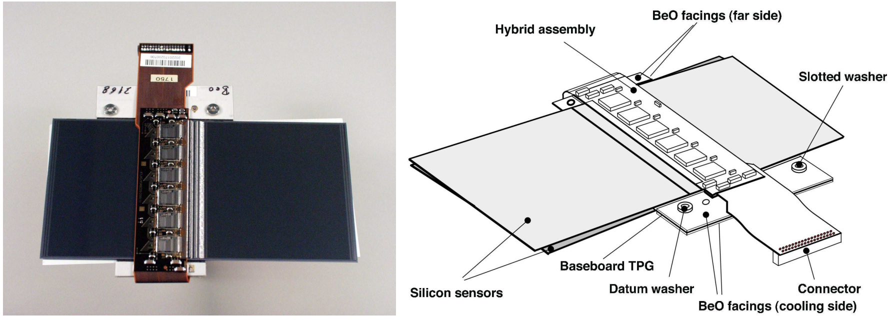

Figure 3.6: Schematic view of SCT module [37].

geometry provides full coverage in ϕ without any cracks. The LAr EM calorimeter has three layers as shown in Fig 3.9a. The designed energy resolution is [48]:

$$\frac{\sigma_E}{E} = \frac{10\%}{\sqrt{E}} \oplus \frac{17\%}{E} \oplus 0.7\%, \tag{3.6}$$

for the measured energy of E (GeV).

Hadronic Calorimeters

The ATLAS hadronic calorimeters consist of the barrel Tile calorimeter ($|\eta| < 1.7$), LAr hadronic end-cap calorimeter (HEC), and LAr forward calorimeter (FCal). The intrinsic resolution of barrel Tile HC and end-cap LAr HC is [49]:

$$\frac{\sigma_E}{E} = \frac{50\%}{\sqrt{E}} \oplus 3\%, \quad \text{(Tile HC)} \tag{3.7}$$

$$\frac{\sigma_E}{E} = \frac{100\%}{\sqrt{E}} \oplus 10\% \quad \text{(End-cap LAr HC)}. \tag{3.8}$$

The tile calorimeter is a sampling calorimeter using steel as the absorber and scintillating tiles as the active material, which is placed outside the EM calorimeter. The calorimeter

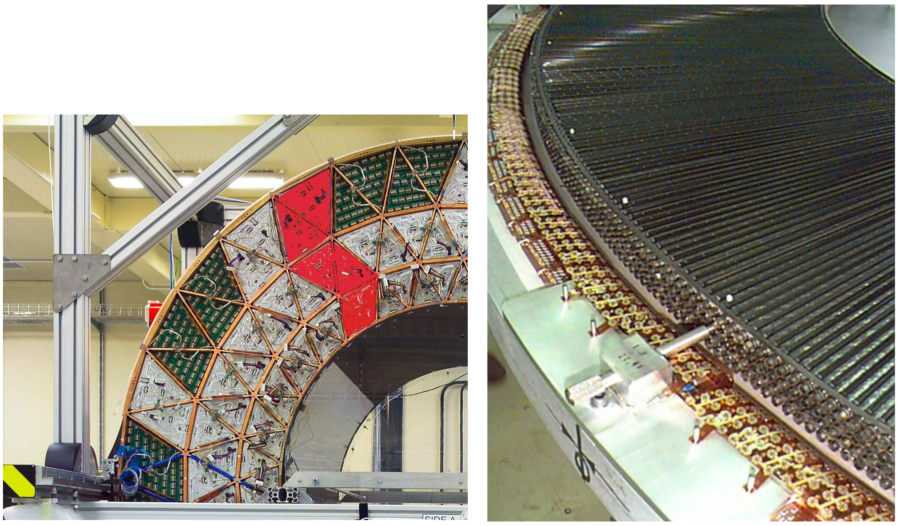

(a) (b)

Figure 3.7: Photograph of (a) one quarter of the barrel TRT and (b) a four-plane TRT end-cap wheel during assembly.

consists of one barrel tile calorimeter ($|\eta| < 1.0$) and two extended barrels calorimeter ($0.8 < |\eta| < 1.7$). The HEC and FCal are sampling calorimeters using liquid Ar as the active material. As the absorber, copper and copper-tungsten plates are used in HEC and FCal respectively.

3.2.5 Muon spectrometers

There are four types of muon spectrometers, which are located outermost in the ATLAS systems as shown in Fig 3.10; Resistive Plate Chambers (RPC), Thin Gap Chambers (TGC), Monitored Drift Tubes (MDT), and Cathode Strip Chambers (CSC). These chambers can be categorized into trigger chambers (RPC, TGC) and high-precision tracking chambers (MDT and CSC).

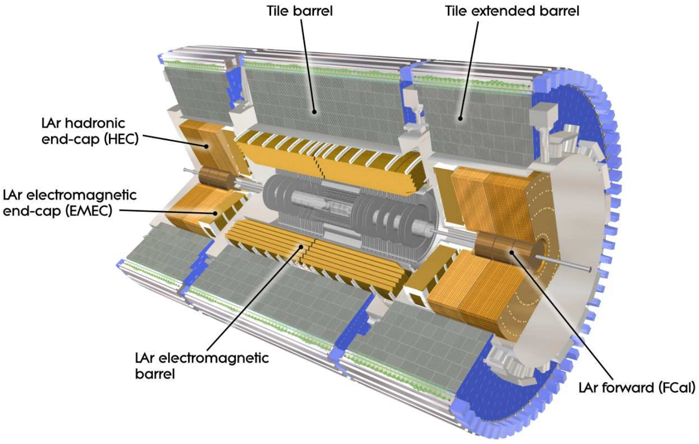

Figure 3.8: Cut-away view of the ATLAS calorimeter system [37].

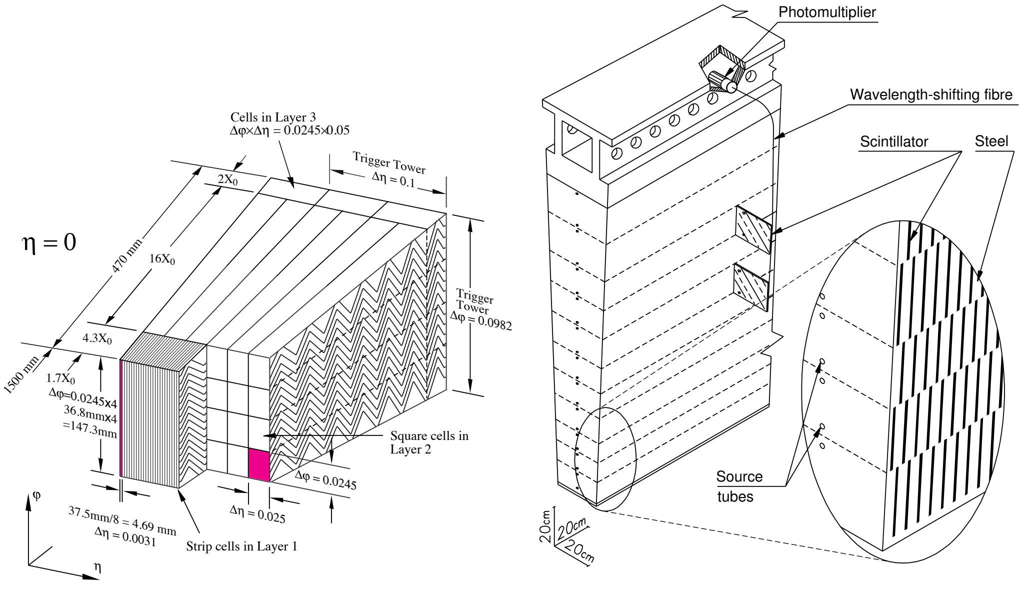

(a) (b)

Figure 3.9: Geometry of the barrel LAr EM calorimeter sampling layers and Tile calorimeters [37].

All of these chambers are outside of the central solenoid magnet, thus troidal magnetic field is important to measure the muon tracks precisely.

Monitored Drift Tubes (MDT)

The basic element of the monitored drift tube chambers is a pressurised drift tube with a diameter of 29.970 mm that are covered by a 400 μm-thick wall, operation with Ar/CO$_2$ (0.93:0.07) gas at 3 bar. The electrons resulting from ionisation are collected at the central tungsten-rhenium wire with a diameter of 50 μm, at a potential 3080 V. The average resolution is 60-80 μm per tube. The limit for safe operation of the MDT's is at counting rates of about 150 Hz/cm^2, which will be exceeded in the region $|\eta| > 2$ in the first layer of the end-cap. In this η region of the first layer, the MDT's are replaced by cathode-strip chambers, which combine high spatial, time and double track resolution with high-rate capability and low neutron sensitivity.

Cathode Strop Chambers (CSC)

The CSC are multi-wire proportional chambers with the wires oriented in the radial direction ($|\eta| > 2.0$). The gas gap is filled a gas mixture (80% Ar, 20% CO$_2$) and with a bias voltage of 1900 V applied. The cells are symmetric in terms of the pitch of read-out cathodes and the anode-cathode spacing, which is equally set to 2.54 mm. Since the spatial resolution of the CSCs is sensitive to the inclination of tracks and the Lorentz angle, the chamber is fixed at tilted posture so that tracks originating from the IP become approximately orthogonal to the chamber surface.

Resistive Plate Chambers (RPC)

The RPC is a gaseous parallel electrode-plate detector ($|\eta| < 1.05$), where two resistive

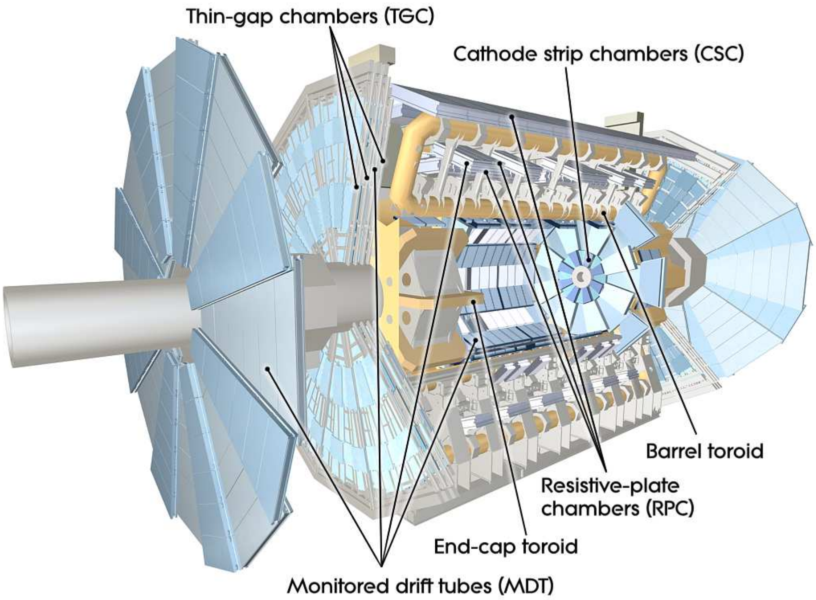

Figure 3.10: Overview of the ATLAS muon detectors [37].

plates are kept parallel to each other at a distance of 2 mm by insulating spacers. The electric field between the plates of about 4.9 kV/mm allows avalanches to form along the ionising tracks towards the anode. The gas gap is filled with gas mixture (94.7% $C_2H_2F_4$, 5% Iso-C_4H_{10}, 0.3 % SF_6). The average spatial and timing resolution are 1 cm and 2 ns respectively.

Thin Gap Chambers (TGC)

The TGC is a multi-wire proportional chambers with a small distance between the anode wire and the cathode strips (1.4mm). The gas gap is filled with a gas mixture (55% CO_2, 45% n-pentan).

3.3 Trigger and data acquisition system

Due to high bunch crossing rate 40 MHz, all of these collision data cannot be recorded. However, most of these collision events are not interesting physics process, because there are a lot of soft QCD interactions shown in Fig 3.11. For example, the higgs production cross section is about 10^{-2} nb, while the total cross section is about 10^8 nb. Thus some systems are needed to reject unnecessary events while keeping actual interesting events. To achieve this goal, the ATLAS experiment adopted two-level trigger and robust readout system, called as ”Trigger and Data Acquisition systems (TDAQ system)”. Triggers of the TDAQ system consists of two distinct triggers, Level-1 Trigger (L1) and High-Level Trigger (HLT). The L1 trigger is the hardware based trigger systems to be fired quickly, while the HLT is implemented in the software system.

The L1 trigger searches for signatures from high-p_{T} muons, electrons/photons, jets and τ leptons decaying into hadrons. Large missing transverse energy (E_T^{miss}) is also selected. The high-p_{T} muons are searched by RPC and TGC, while other all objects are searched by the calorimeters. The maximum L1 publishing rate is 100 kHz in Run-2, and the HLT system receives the L1 results and calculates more precise trigger decisions. After passing HLTs, the corresponding collision events are stored at disk via network and distributed the data over the world data centers.

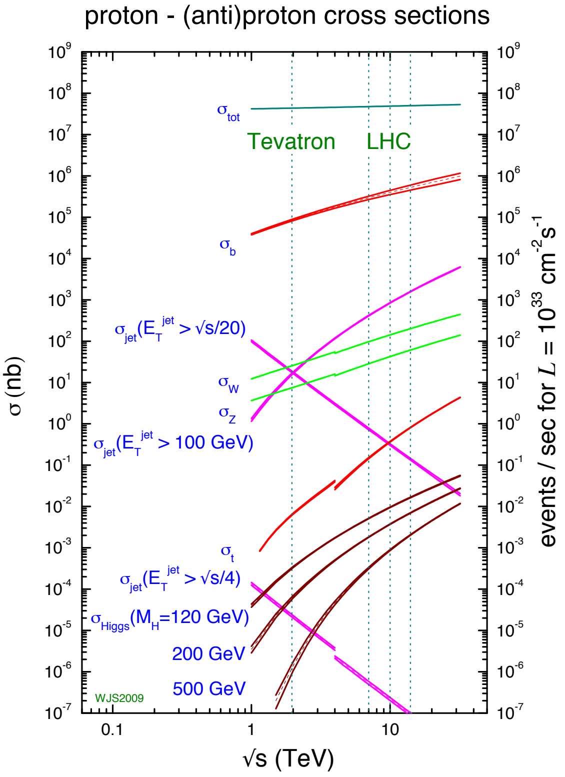

Figure 3.11: Proton-proton cross section as a function of center-of-mass energy $\sqrt{s}$ [50].

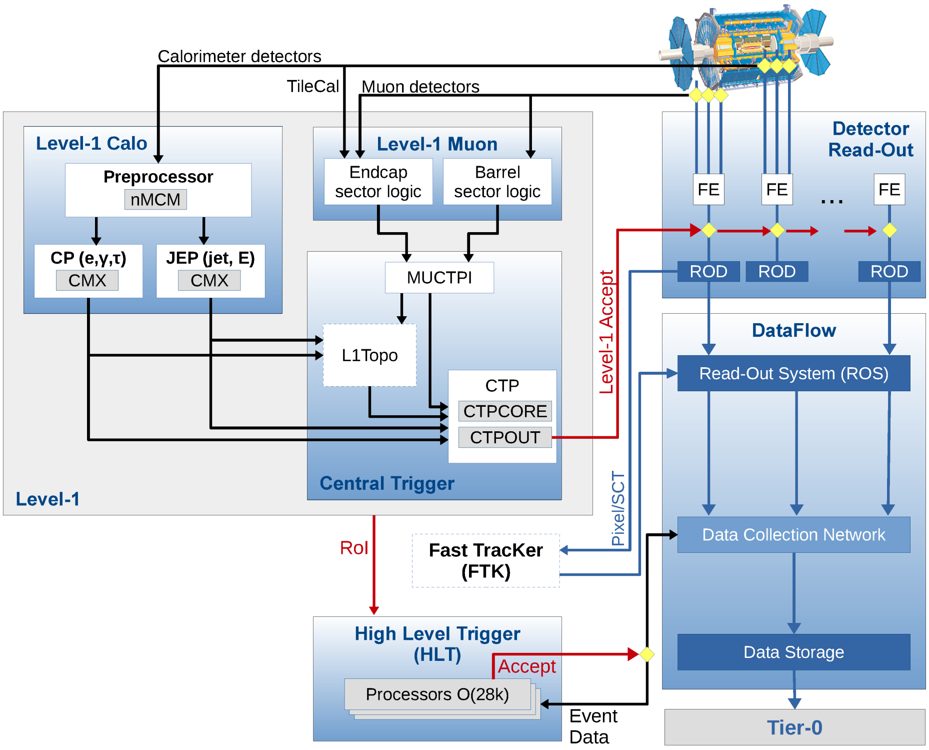

Figure 3.12: The ATLAS trigger and data acquisition system [51].

Chapter 4

Dataset and Simulated samples

The LHC provided the proton-proton collisions for physics analysis during 2015-2018, called as Run-2 data taking period. In this thesis, the leptoquark pair production in the $LQ \to b\tau$ decay channel is analyzed using the full Run-2 data set at $\sqrt{s} = 13$ TeV. This chapter explains the experimental data, and Monte Carlo (MC) samples which are used to model the signal and background productions.

The MC simulation [52] is an essential component of experimental particle physics. The technique can simulate pp collision events and detector responses at high level of accuracy. Various MC samples are produced for signal and background processes, and the samples are compared with the collision data in order to search the signal processes contributions. Furthermore, alternative configuration MC samples are used to estimate systematics uncertainties, as discussed in Section 9.3. All of these simulation samples are computed in the common framework [53].

4.1 ATLAS Run-2 Collision Data

The LHC provided data corresponding to an integrated luminosity of 156 fb^{-1} at $\sqrt{s} = 13$ TeV for the ATLAS experiment. The ATLAS detectors worked very fine and recorded 147 fb^{-1} in the end. To use these data for physics analysis, selected events are required to have detector in good working condition [54]. The recorded data are filtered by XML based database, so-called Good Runs List (GRL), which are fully integrated into the analysis tools used by the Collaboration [55]. After passing the GRL selections, the data set are called as "good for physics" data, and the resulting integrated luminosity is 139 fb^{-1}. These correlations are shown in Fig 4.1 as a function of recorded year.

4.2 Event Generation

The event generation of a hadron-hadron collision is split into several steps as shown in Fig 4.2. The big red blob in the center of the figure shows a scattering of partons (blue lines) from each hadron. The scattering is characterized by the momentum transfer Q^2. The large Q^2 scattering is referred to as "hard" scattering, while the low Q^2 scattering is "soft" scattering. The color-charged partons from the hard scattering emit QCD radiation (red colored tree-like structures), referred to as "parton shower". Partons from the radiations form colourless hadrons (green lines), referred to as "hadronization" (light green blobs). After hadronization, hadron

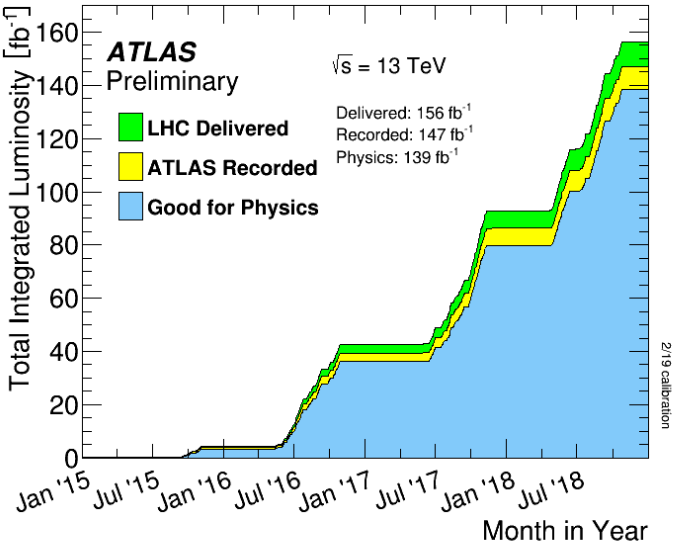

Figure 4.1: Cumulative luminosity delivered to ATLAS (green), recorded by ATLAS (yellow), and certified to be good quality data (blue) during stable beams for pp collisions at $\sqrt{s}$ = 13 TeV in 2015-2018 [56].

may decay (dark green blobs) and resulting hadrons (small dark green blobs in the end) are measured by the detectors, while small Q^2 electron/photon radiation are emitted (yellow lines). In addition to the main scattering, the hadron-hadron collision also contains a secondary hard scattering event (purple blob).

4.2.1 Hard Scattering Processes

The cross sections of pp interaction (two protons, p_1 and p_2) to produce final-state particles, n, is given by [58]:

$$\sigma_{p_1 p_2 \to n} = \sum_{a,b} \iint_0^1 dx_a dx_b \int \{ f_a^{p_1}(x_a; \mu_F) f_b^{p_2}(x_b; \mu_F) \} d\hat{\sigma}_{ab\to n}(\mu_F, \mu_R), \tag{4.1}$$

where $f_a^{p_1}(x_a; \mu_F)$ and $f_b^{p_2}(x_b; \mu_F)$ are the Parton Distribution Functions (PDF) of p_1 and p_2 respectively. The PDF depends on the momentum fraction x of parton a and b, and also depends on the factorization scale μ_F. The PDF describes the momentum distribution functions of the partons within the proton at the energy scale Q^2. Considering the process of $a + b \to c$ and $a+b \to c+d$ mode, typically one hard scale Q^2 is identified such that $\mu_F = \mu_R = Q^2$. The PDFs has been computed by a simultaneously global fit on the experimental data from deep inelastic scattering experiments or collider experiments [59]. Fig 4.3 shows a PDF of various partons for $\mu^2 = 10$ and 10^4 GeV^2. The analysis uses PDF4LHC sets [60] which is one of the most used sets in the ATLAS experiments. The uncertainties coming from the differences of those PDF sets are taken into.

In addition to the PDFs, Eq (4.1) is also factorized into a parton-level cross section, which describes a process from the initial state a and b to the n final-state particles, $\hat{\sigma}_{ab\to n}(\mu_F, \mu_R)$. Parton-level cross section for the production of the final state n through the initial partons a

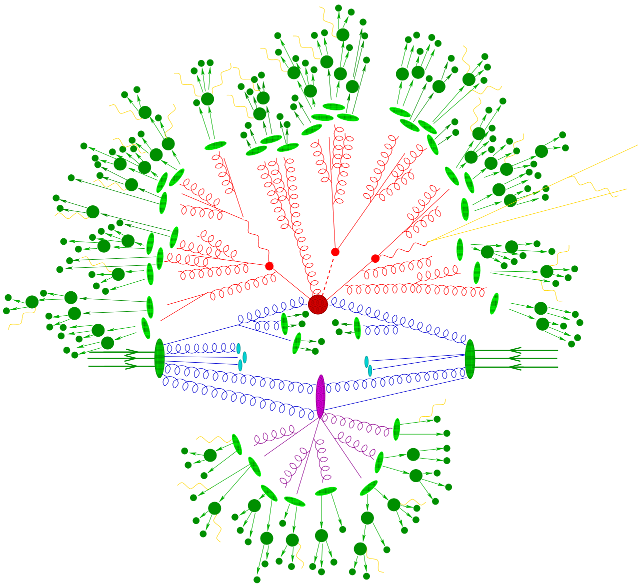

Figure 4.2: Sketch of a hadron-hadron collisions simulated by Monte Carlo simulation [57].

and b can be obtained by the differential phase space element over the final-state particles:

$$d\hat{\sigma}_{ab\to n} = \left[\prod_{i=1}^{n} \frac{d^3 p_i}{(2\pi)^3 2E_i}\right] \delta^4\left(p_a + p_b - \sum_i^n p_i\right) |\mathcal{M}_{ab\to n}|^2, \tag{4.2}$$

where $p_{a,b}$ and p_i are the momenta of initial and final state particles, respectively. The parton-level cross section can be computed with perturbative expansion in powers of the strong coupling constant α_s.

The matrix element $\mathcal{M}_{ab\to n}$ represents a sum over all of the Feynman diagrams from ab initial-state particles to n final-state particles, described as:

$$\mathcal{M}_{ab\to n} = \sum_i \mathcal{F}^{(i)}_{ab\to n}. \tag{4.3}$$

For two-body scattering to produce two particles, it is straightforward to draw all tree-level Feynman diagrams and apply the Feynman rules [61]. There are highly automated tools to calculate the tree-level matrix elements, CompHep [62], CalcHep [63], MadGraph [64] and others [65–69].

4.2.2 Parton Showering Process

Color-charged partons from the hard scattering processes discussed in Section 4.2.1 would emit gluons. The gluons can cause further gluons or quarks emissions because they are color charged. This phenomenon is referred to as "parton showering", as shown in Fig 4.2 (red lines).

For any hard processes associated with partons of any flavour i, the cross section of a process σ_0 accompanied by a parton j with momentum fraction z is given by:

$$d\sigma \simeq \sigma_0 \sum_{\text{partons},i} \frac{\alpha_s}{2\pi} \frac{d\theta^2}{\theta^2} dz\ P_{ji}(z,\phi) d\phi, \tag{4.4}$$

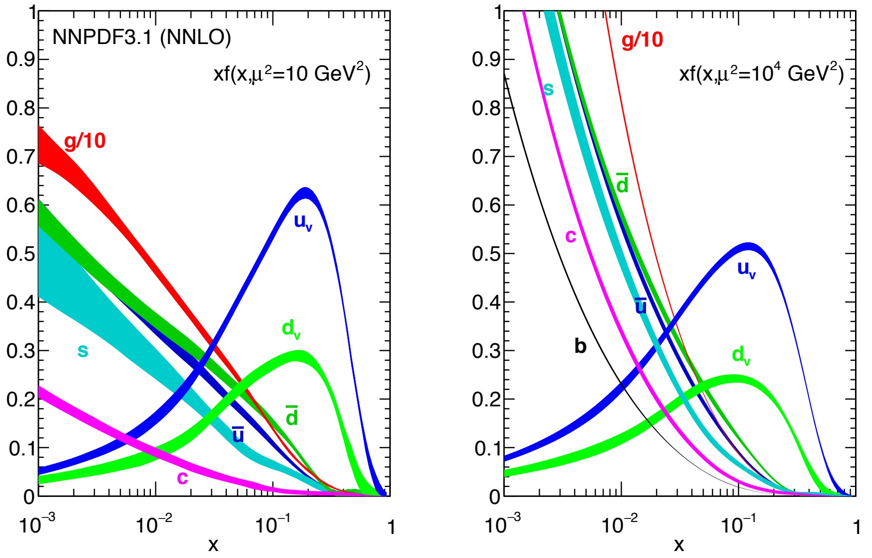

Figure 4.3: The NNPDF3.1 NNLO PDFs evaluated at $\mu^2 = 10$ GeV^2 (left) and $\mu^2 = 10^4$ GeV^2 (right) [59].

where α_s is the strong coupling constant, θ is the opening angle between parent partons and emitted partons, ϕ is an azimuthal angle of a parton j around an axis defined by the parent parton i. $P_{ji}(z, \phi)$ is spin-averaged functions defined by:

$$P_{g\to qg}(z) = \frac{4}{3}\frac{1+z^2}{1-z}, \tag{4.5}$$

$$P_{q\to gq}(z) = \frac{4}{3}\frac{1+(1-z)^2}{z}, \tag{4.6}$$

$$P_{g\to gg}(z) = 3\frac{z^4+1+(1-z)^4}{z(1-z)}, \tag{4.7}$$

$$P_{g\to q\bar{q}}(z) = \frac{1}{2}\left(z^2+(1-z)^2\right). \tag{4.8}$$

The $P_{ji}(z)$ is DGLAP evolution equations [70–72]. Algorithms to model the parton showering use the DGLAP equations to construct the probability distribution for one parton emission from a hard process. The algorithm will continue to emit partons until the momentum transfer of the parent parton q or g is below the terminate scale $\simeq 1$ GeV.

4.2.3 Hardonization

Resulting partons from the hard scattering and following parton showers form the colour-neutral bound states because of quark confinement, which is referred to as "hadronization" process. There are two types of models to reproduce the process, cluster and string model [73]. The basic concepts are shown in Fig 4.4.

Cluster model

This method is based on a property of the parton showering process, preconfinement of colour [74]. The preconfinement implies the pairs of colour-connected neighbouring parton have an asymptotic mass distribution that falls rapidly at high masses. The model starts by splitting gluons from the parton shower to form colour-single $q\bar{q}$ combinations. The pairs are assumed to form clusters, which mostly undergo simple isotropic decay into pairs of hadrons.

String model

The model is based on the dynamics of a relativistic string, representing the colour flux stretched between the initial $q\bar{q}$ pairs. The string produces a linear confinement potential [73]. After constructing the string, the hadronization occurs according to the string area.

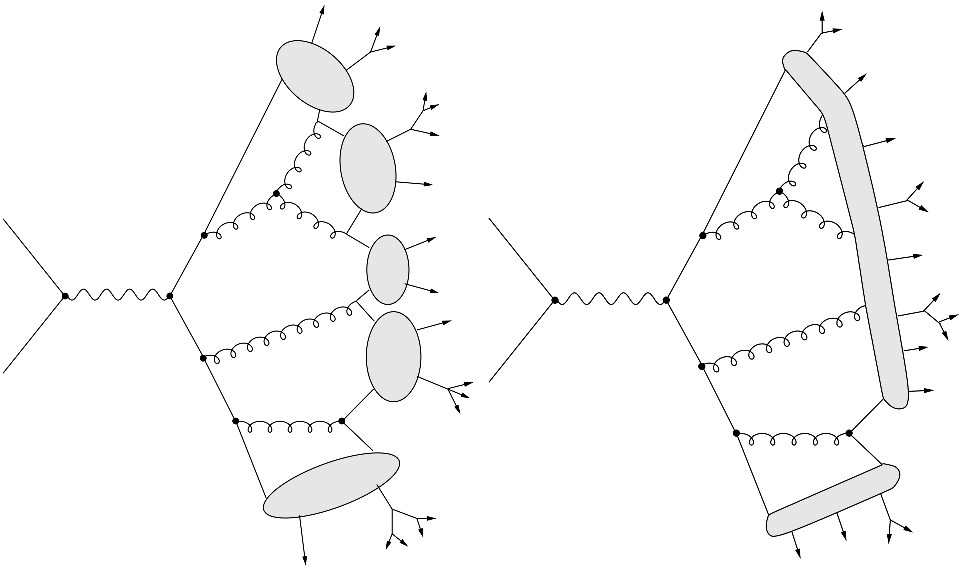

Figure 4.4: Sketches of the cluster (left) and string (right) model [73].

4.3 Detector Response simulation

It is also important to describe the detector responses to check how the generated events are measured. The GEANT4 (GEometry And Tracking) [75, 76] simulation toolkit is used within the common computing framework. The full precise simulation takes a lot of CPU times. A large fraction of simulation time is spent by the calculation of interaction with the electromagnetic calorimeter, thus fast simulation has been developed [77,78]. These fast simulation parameterize the response of the calorimeters to reduce the process time, and are used to estimate systematics uncertainties in this analysis.

4.3.1 Pile-up Simulation

There are multiple proton proton collisions in a single pp-crossing, which is referred to as "pile-up" effect. The effect is caused by proton-proton inelastic scattering ($\sigma \simeq 10^8$ nb), while the order of the interesting process is $\sigma \simeq 10^2$-10^{-3} nb. The mean number of the average pile-up $\langle\mu\rangle$, defined as the mean number of interactions per bunch crossing, has been evolved according to the peak luminosity. The μ profile in Run-2 is shown in Fig 4.5, where the peak μ is typically

20-40. All simulated events are generated with a varying number of proton-proton collisions to account for the pile-up effects. Minimum-bias interactions (generic proton-proton inelastic scattering) are simulated with by Pythia 8.186 using the A3 tune [79] and the MSTW2008LO PDF set [80].

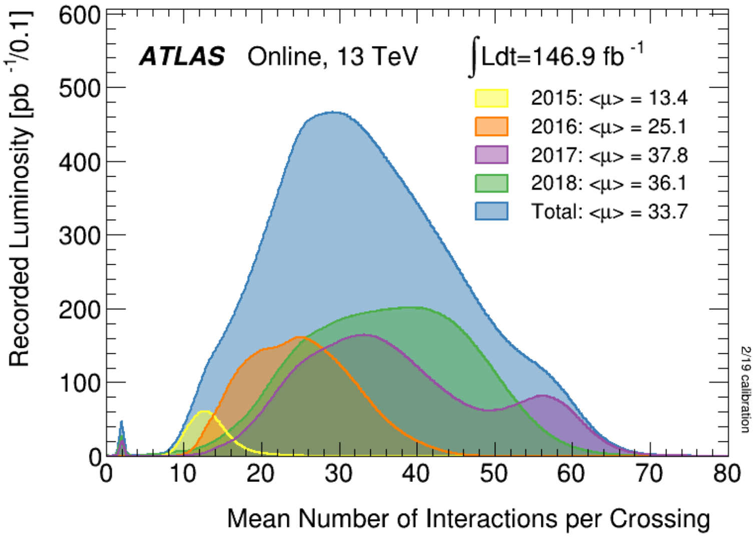

Figure 4.5: The mean number of interactions per bunch crossing, $\langle\mu\rangle$, in 2015-2018, where each colored distributions correspond to each recorded year [56].

4.4 Setup of Simulated Events

Events of the LQ signal and Standard Model background processes are simulated by each dedicated MC simulation. The setup configuration is summarized in Table 4.1.

4.4.1 Signal Processes

Reproduction of the mBRW

The mBRW LQ processes are parameterized by its mass, the Yukawa coupling λ, and the branching ratio β. As discussed in Section 2.3, there are two types of decay modes, $LQ \to b\tau$ or $LQ \to t\nu_\tau$. The decay mode is controlled by the β. The λ is set to 0.3 for all samples [32] as a conservative choice, because the value is equal to the electromagnetic coupling, $e = \sqrt{4\pi\alpha} \simeq 0.312$ for $\alpha = 1/128$. The overview of the reproduction is shown in Fig 4.6.

Samples are produced for each leptoquark mass points ranging from 300 GeV to 2000 GeV. In addition, the β is set to 0.5 so that a Leptoquark decays either into $b\tau$ or $t\nu_\tau$. This makes it possible to investigate the effect of branching ratio as well as to share signal samples with other analysis channels and enables efficient sample production. After producing the samples, the samples need to be reweighed to obtain the target β value. The exact relation between the neutral and charged lepton decay widths for third generation leptoquarks are given by

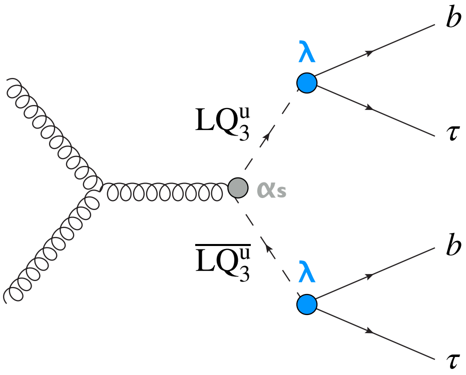

Figure 4.6: In the context of the mBRW, after producing the pair of the LQ, each of them decays into a pair of b and τ via Yukawa coupling λ.

$$\begin{aligned}\Gamma(\mathrm{LQ_3}^u \to b\tau) = & \frac{(m_{LQ}^2 - m_b^2 - m_\tau^2)}{48\pi m_{LQ}^3} \\ & \times \sqrt{m_{LQ}^4 + m_b^4 + m_\tau^4 - 2(m_{LQ}^2 m_b^2 + m_{LQ}^2 m_\tau^2 + m_b^2 m_\tau^2)}3\lambda^2\beta,\end{aligned} \tag{4.9}$$

where m_{LQ}, m_b and m_τ is the LQ, bottom quark and τ lepton mass, respectively.

Setup

The LQ pair production are generated with MadGraph5_aMC@NLO version 2.6.0 at NLO in QCD interfaced to Pythia 8 version 8.230 for the parton showering and hadronization, and EvtGen version 1.6.0 program is used for the bottom and charm hadron decays. The PDF set used is NNPDF3.0 NLO with the A14 set of tuned underlying-event and parton shower parameters. Matching of the matrix element with parton showering was performed, with a matching scale set to one quarter of the mass of the leptoquark. All signal cross sections are calculated to approximate NNLO in the strong coupling constant, adding the re-summation of soft gluon emission at next-to-next-to-leading-logarithm accuracy (approximate NNLO+NNLL), as shown in Fig 4.7.

4.4.2 Background Processes

The $t\bar{t}$ and single top-quarks production are simulated using the PowhegBox v2 generator [81–83] with NNPDF 3.0 NLO [84]. After generating the events, Pythia 8 version 8.230 cause the parton shower, and hadronization with the A14 set of tuned parameters with the NNPDF23LO PDF set. The EvtGen v1.6.0 program is used to model the properties of the bottom and charm hadron decays [85]. For all these top processes, top-quark spin correlations are preserved (for t-channel production, top quarks are decayed using MadSpin), where the top-quark mass is set to 172.5 GeV. The NLO $t\bar{t}$ production cross section is corrected to the theory prediction calculated at NNLO+NNLL. Only for single top-quark processes, the cross sections were corrected to the theory predictions calculated at NLO.

Events containing W or Z bosons produced in association with jets are simulated using the Sherpa version 2.2.1 generator. The NNPDF30NNLO PDF set is used in conjunction with

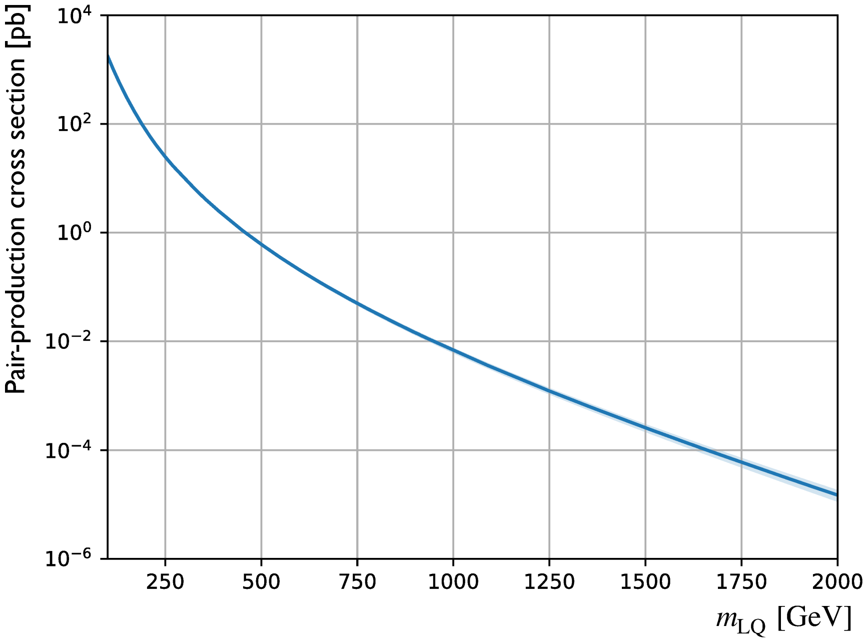

Figure 4.7: Cross section of LQ pair production as a function of leptoquark mass, at the NNLO+NNLL accuracy. The blue band corresponds to the calculation error.

dedicated parton shower tuning developed by the SHERPA authors. These W/Z + jets events are normalised to the predicted cross sections using NNLO calculations.

Diboson processes (WW,WZ,ZZ) with one of the bosons decaying hadronically and the other leptonically are simulated using the SHERPA version 2.2.1 generator. The NNPDF30NNLO PDF set is used in conjunction with dedicated parton shower tuning developed by the SHERPA authors. The generator NLO cross sections are used.

Table 4.1: Setup of simulated leptoquark signal and the Standard Model background samples.

Physics process	Matrix Element	Parton Shower	PDF set
LQ processe	MADGRAPH5_aMC@NLO 2.6.0	PYTHIA 8 v8.230	NNPDF30NNLO
$t\bar{t}$	POWHEGBOX v2	PYTHIA 8 v8.230	NNPDF30NNLO
Single-top (Wt-channel)	POWHEGBOX v2	PYTHIA 8 v8.230	NNPDF30NNLO
Single-top (s-channel)	POWHEGBOX v2	PYTHIA 8 v8.230	NNPDF30NNLO
Single-top (t-channel)	POWHEGBOX v2	PYTHIA 8 v8.230	NNPDF30NNLO
$Z+$ jets	SHERPA	dedicated SHERPA	NNPDF30NNLO
$W+$ jets	SHERPA	dedicated SHERPA	NNPDF30NNLO
WW, WZ, ZZ	SHERPA	dedicated SHERPA	NNPDF30NNLO

Chapter 5

Object reconstruction

Particles from pp collisions pass through the detectors and leave hit position and energy information. To detect and measure the properties of these particles, the detector information is used as "objects" to reconstruct particles. This reconstruction algorithm is prepared for each object type and is performed at off-line level in the ATLAS experiment. This chapter focuses on the off-line reconstruction algorithm for each particle type; photons, electrons, muons, τ_{had}, jets and missing transverse energy.

5.1 Tracks

Charged particles pass through detectors and leave hits along their trajectories. Hit positions are grouped into a trajectory called as "track" for each charged particle. A track curves in the magnetic field and its radius is used to reconstruct the momentum and electric charge of the particle. Furthermore, the tracks can be used to determine the primary vertex of an event (discussed in Section 5.2), jet-flavor tagging (discussed in Section 5.5), and other object reconstruction techniques. Therefore, the tracks are the most basic reconstructed information for the physics analysis. The detailed discussions are found in [86]. The reconstruction procedures are summarized briefly in the following section.

5.1.1 Clusterizations

The track reconstruction begins with a connected component analysis (CCA) [87] algorithm, which groups hits of Pixel and SCT strips into several clusters. Based on these clusters, three-dimensional points along a trajectory, referred to as "space-points", are created. Each cluster in the Pixel equates to one space-point, while in the SCT, the space point is obtained by combining both sides of the layer.

5.1.2 Seeding and Track finding

A seed for track reconstruction is formed with a set of three space-points. This approach maximizes the number of possible combinations, while still allowing a crude estimate of the track momentum. The reconstruction precision can be further improved by using remaining space-points in the other layers. A choice of space-points is carefully determined by a combinatorial Kalman filter [88]. Resultant space-points including the seed forms track candidates, while multiple track candidates are created if plural space-points consistent with the extension of the seed exists on the same layer. As all combinations of space-points have been made, there are a number of track candidates where space-points overlap or have been incorrectly assigned.

The reconstructed trajectory of the particle can be described by five helix parameters [89]:

$$P = (d_0, z_0, \phi_0, \cot\theta, Q/p), \tag{5.1}$$

where d_0 is the transverse impact parameter, z_0 is the longitudinal impact parameter, ϕ_0 is the azimuthal angle, θ is the polar angle of the track, and Q/p is the charge over the momentum. The overview is shown in Fig 5.1. These parameters will be determined by a high-resolution fit at the next stage (Section 5.1.3), then at this stage, a crude estimation is performed by assuming a perfect helical trajectory in a uniform magnetic field.

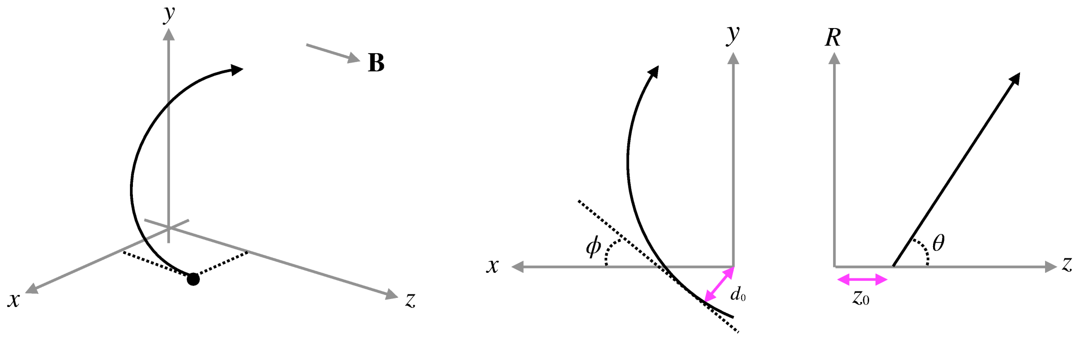

Figure 5.1: Overview of a trajectory by a single charged particle, the three-dimensional overview (left), xy-plane projected trajectory (center), and Rz-plane projected trajectory (right).

5.1.3 Ambiguity solving

The loose track candidate finding algorithm (discussed in Section 5.1.2) is followed by a stringent ambiguity-solver, which evaluates the individual tracks by assigning a track score [90]. The score is increased by clusters which is assigned to a track, and decreased by holes or the poor χ^2 of the track fit result. After calculating the track score, track candidates are ranked by the scores from highest to lowest, and track candidates with low score are rejected at this stage.

Next, the ambiguity-solver treats clusters which is assigned to multiple track candidates. Clusters are divided into two types, merged clusters or shared clusters. The merged cluster is created by multiple charged particles in dense environments. The shared cluster is created by a single charged particle, but the cluster is assigned to multiple tracks due to incorrect assignments. The ambiguity-solver classifies the clusters according to above type by using a neural network [91]. The ambiguity-solver has a shared cluster criterion, where clusters cannot be shared by more than three tracks, or a track cannot have more than three shared clusters. If the criterion isn't satisfied by adding the cluster to the track, the track score is calculated again without adding the cluster, and the track is returned to the list of remaining candidates to be processed. The track candidate is rejected if it fails to satisfy basic quality criteria [86].

5.1.4 Track fit

After passing the requirements and ambiguity-solver process, the track candidates are fitted by a high-resolution fit with all available information. For the fit, the cluster position and uncertainty are determined by another neural network [91].

After the reconstruction of tracks in the Pixel and SCT region, the candidates are extended to the TRT region if there is a valid set of matching drift circles [92]. Increased track length improves momentum measurement.

5.2 Primary Vertices

The position where a proton-proton collision occurred, referred to as ”primary vertices” (PV), is determined by using reconstructed tracks [93]. The reconstruction procedure is divided into two stages; vertex finding and vertex fitting [94].

The vertex finding algorithm takes a set of tracks that pass the selection criteria summarized in Table 5.1. First of all, the algorithm selects a seed position, which is based on the peak of z-coordinates of the tracks. After the seed position is selected, an adaptive vertex finding algorithm begins [95] to find the optimal vertex position. The algorithm computes a weight for each input track, which reflects on the compatibility with the vertex estimate. Then the vertex position is re-calculated using the weighted tracks, and the finding algorithm is repeated. Tracks inconsistent with the vertex are removed and may be used in the determination of another vertex.

The above procedures are repeated with the remaining tracks in the event. The typical number of the reconstructed PV is 10-30 in one bunch-collision, while a hard scattering occurs in the only one PV among them. The ’PV of interesting’ is defined as a PV with the highest sum of associated track momentum.

Table 5.1: Requirements for tracks as inputs to reconstruct primary vertices [94]. The $\sigma(d_0, z_0)$ is the uncertainties of d_0 and z_0 discussed in [96]. The criteria on the impact parameters can reduce contamination from tracks originating from secondary interactions.

Item	Criteria
Transverse momentum p_T	$>$ 400 MeV
$\lvert d_0 \rvert$	$<$ 4mm
$\sigma(d_0), \sigma(z_0)$	$<$ 5mm, $<$ 10mm
$\lvert\eta\rvert$	$<$ 2.5
Hits in the first two Pixel layers	≥ 1
A maximum shared modules	1
Pixel holes	0
SCT holes	≤ 1

5.3 Topological Clustering

Particles leave its energy in the calorimeter cells, and the energy deposit of each cell are merged as clusters. In this analysis, the clusters of three-dimensional connected calorimeter cells are employed to suppress electric noise and other background sources. This cluster of cell is referred to as "Topo-cluster" (TC), as a basic unit of calorimeter information [97]. The basic observable controlling the cluster formation is the $\zeta_{\text{cell}}^{\text{EM}}$ defined as :

$$\zeta_{\text{cell}}^{\text{EM}} = \frac{E_{\text{cell}}^{\text{EM}}}{\sigma_{\text{noise,cell}}^{\text{EM}}}, \tag{5.2}$$

where the $E_{\text{cell}}^{\text{EM}}$ is the cell deposit energy and $\sigma_{\text{noise,cell}}^{\text{EM}}$ is the R.M.S. of noise variation in the cell. Thus the $\zeta_{\text{cell}}^{\text{EM}}$ means the cell signal significance against the noise. The superscript EM means the energy is measured according to the electromagnetic energy scale. This scale reconstructs the energy deposited by electrons and photons correctly but does not include any corrections for the loss of signal for hadrons due to the non-compensating character of calorimeters. After creating the TCs, the enregy calibration, referred to as "local hadronic cell weighting", is applied for jets or τ-leptons [98].

The clustering starts from finding a seed cell with energy deposit larger than $\zeta_{\text{cell}}^{\text{EM}} > 4$ significance. The neighboring cells with $\zeta_{\text{cell}}^{\text{EM}} > 2$ significance are added into the cluster. This process is repeated until there are no more cells to be added to the cluster.

5.4 Jets

Hadrons are measured as jets, which are the experimental signatures of quarks and gluons produced in high-energy processes. Due to the color-confinement, a lot of color-neutral hadrons are produced and leave its energy in the calorimeters. This process formed a kind of particle spray, referred to as "jet".

The unit of the calorimeter signals are TCs as discussed in Section 5.3, and the clusters are used to reconstruct the jets. This analysis uses Particle flow algorithm to reconstruct it to achieve better performance of jets reconstruction.

5.4.1 Concept of Particle Flow Algorithm

This particle flow algorithm combined tracks (discussed in Section 5.1) and Topo-clusters (Section 5.3) for the reconstruction of hadronic jets. With this algorithm, the following advantages are achieved:

Better resolution

The calorimeter energy resolution is parameterized by :

$$\frac{\sigma(E)}{E} = \frac{50\%}{\sqrt{E}} \oplus 3.4\% \oplus \frac{1\%}{E}, \tag{5.3}$$

while the tracking detector resolution for the transverse momenta is parameterized by :

$$\sigma\left(\frac{1}{p_T}\right) p_T = 0.036\% \cdot p_T \oplus 1.3\%, \tag{5.4}$$

where the energies and transverse momenta are measured in GeV, and the $\oplus$ means the quadratic sum. For lower energy particles, the tracker resolution is better than the calorimeter. In addition, to the energy resolution, the angular resolution of the trackers is also better than the calorimeter. The Particle flow algorithm uses the tracker resolution for the jet reconstruction, thus this is because the use of the tracker and calorimeter information at one step becomes the big advantage.

Low-p_{T} particles swept out

Due to the strong magnetic field, the low-p_{T} particles are swept out from the calorimeter clusters. The algorithm can recover such low-p_{T} particles into the cluster, because the tracker angular information can be used. Furthermore, much lower energy particles, i.e. $p_T < 400$ MeV, cannot pass the noise threshold of the Topo-Clusters.

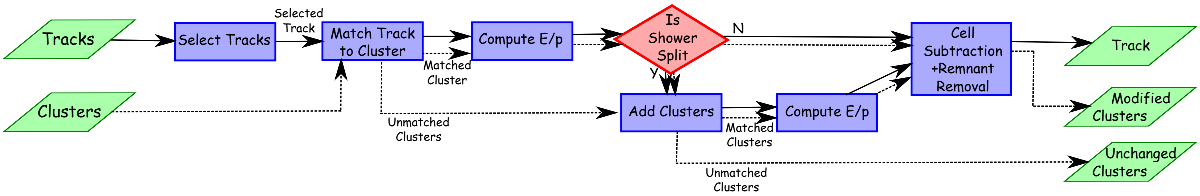

Figure 5.2: The schematic overview of the particle flow jet reconstruction [2].

5.4.2 Subtraction of cell energy due to tracks

The algorithm aims to complement the calorimeter's ability using the tracking systems. When a track which matches to the cluster is found in the input list, energy subtraction procedure are performed to avoid double counting. After subtraction, a set of new topo-clusters are obtained. There are five main steps to correct the input list of the tracks and topo-clusters. The brief descriptions are discussed in the following paragraphs, and the overview is shown in Fig 5.2. More details of the subtraction procedures are discussed in [2].

Track selection

Input tracks are selected according to the following requirements; at least nine hits in the silicon detectors, no missing Pixel hits, $|\eta| < 2.5$ and $p_{\mathrm{T}} > 0.5$ GeV. This step aims to select tracks which reach the calorimeter region and deposit the energies. Tracks with $p_{\mathrm{T}} > 40$ GeV, however, are not used for the algorithm, because such high-energy particles are not isolated well from nearby activities in calorimeters.

Matching tracks to topo-clusters

At this step, the algorithm attempts to match each selected track to one topo-cluster. Topo-clusters are ranked by a distance metric R' defined as :

$$\Delta R' = \sqrt{\left(\frac{\Delta\phi}{\sigma_\phi}\right)^2 + \left(\frac{\Delta\eta}{\sigma_\eta}\right)^2} \tag{5.5}$$

where the $\Delta\phi$ and $\Delta\eta$ is the distance between the center of the topo-cluster and the tracks, and the σ_η and σ_ϕ represent the topo-cluster widths. The closest preselected topo-cluster in $\Delta R'$ is taken to be the matched topo-cluster.

Evaluation of the expected deposited particle energy

It is necessary to know the correlation between the measured momentum of the track, p_{track}, and the actual energy deposit in the topo-cluster, E_{deposit}. The expected energy deposit $\langle E_{\text{deposit}} \rangle$ is evaluated as:

$$\langle E_{\text{deposit}} \rangle = p_{\text{track}} \times \left\langle E^{\text{ref}}_{\text{cluster}} / p^{\text{ref}}_{\text{track}} \right\rangle , \tag{5.6}$$

where the $\left\langle E^{\text{ref}}_{\text{cluster}} / p^{\text{ref}}_{\text{track}} \right\rangle$ is the expectation value of the energy deposit. The value is determined by single pion MC simulation samples beforehand. The superscription "ref" means the reference measurement values by the MC samples.

Recovering split showers

Particles in a jet do not always deposit all their energy in a single topo-cluster, therefore it is necessary to handle the multiple topo-clusters in some cases. The variable to distinguish the single and multiple topo-cluster events is the significance:

$$S(E_{\text{cluster}}) = \frac{E_{\text{cluster}} - \langle E_{\text{deposit}} \rangle}{\sigma_{\text{deposit}}}, \tag{5.7}$$

where the E_{cluster} is the measured energy of the cluster, the $\langle E_{\text{deposit}} \rangle$ is from Eq (5.6), and the σ_{deposit} is the standard deviation of the E_{deposit}. If a hadronic shower is split, the topo-cluster energy E_{cluster} will be smaller than the expected energy deposit energy. Thus shower split shower tends to have negative $S(E^{\text{cluster}})$, and the recovery procedure is performed.

Cell-by-cell Subtraction

When a set of topo-clusters corresponding to the track has been selected, the energy subtraction algorithm is performed. The algorithm starts from the extrapolated track position into the layer of the highest energy deposit. Rings are formed in η-ϕ space around the extrapolated track, and the algorithm runs from the inner most rings to the outer side. If the energy in the cells in the current rings is less than the $\langle E_{\text{deposit}} \rangle$, these cells are removed. If, instead, the energy withing the rings region has more energy, the process halts.

Remnant removal

If the energy remaining in the set of cells and/or topo-clusters that survive the energy subtraction is consistent with the width of the $E^{\text{cluster}}_{\text{ref}} / p^{\text{cluster}}_{\text{ref}}$ distribution, specifically if this energy is less than $1.5\sigma(E_{\text{deposit}})$, it is assumed that the topo-cluster system was produced by a single particle. The remnant energy therefore originates purely from shower fluctuations and so the energy in the remaining cells is removed. Conversely, if the remaining energy is above this threshold, the remnant topo-cluster(s) are retained.

5.4.3 Reconstruction

After the original topo-clusters are corrected by the particle flow algorithm, jets are reconstructed by anti-k_T algorithm [99]. As usural jet clustering, there are two distance parameters, $d_{i,j}$ between any particle, i.e. calorimeter cluster, i and j and $d_{i,B}$ a distance between any cluster

i and the beam (B). In the anti-k_T algorithm, these distances are extended to the following quantities:

$$
\begin{aligned}
d_{i,j} &= \min\left(p_{T,i}^{-2}, p_{T,j}^{-2}\right)\frac{\Delta_{i,j}^2}{R^2}, && (5.8)\\
d_{i,B} &= p_{T,i}^{-2}, && (5.9)
\end{aligned}
$$

where $\Delta_{i,j}^2 = (y_i - y_j)^2 + (\phi_i - \phi_j)^2$ and p_T, y and ϕ are the transverse momentum, rapidity and the asimuthal angle of cluster i. The R is the anti-k_T parameters, where the R value is fixed to 4 in this analysis. The anti-k_T algorithm calculates these quantities for all input topo-clusters and finds the minimum among these quantities. If $d_{i,j}$ is the smallest, the i and j topo-clusters are grouped, and the algorithm proceedes next step. If $d_{i,B}$ is the smallest, the topo-clusters are removed from the processing, and the cluster i is called as a jet.

5.4.4 Energy Calibration

As discussed in Section 5.3, the energy of the topo-clusters are calculated at the electromagnetic (EM) energy scale. This section discusses the details of the energy calibration flow for the reconstructed jets.

The overview of the calibration stages is shown in Fig 5.3. First of all, the four-momentum of the jet is corrected to point to the hard-scatter primary vertex, because the original direction point to the center of the detector. The correction keeps the jet energy constant, and it can improve the η resolution. Next, the pile-up correction removes the effect of the pile-up, which causes the excess energies. The MC-based calibration corrects the jet four-momentum to the particle-level absolute energy scale by using truth jets information derived from di-jet MC samples. Further improvements to the reconstructed energy and related uncertainties are achieved through the use of calorimeter, muon spectrometers, and track-based variables in the global sequential calibration. Finally, a residual in-situ calibration is applied only to data to account for the actual detector response and the MC simulation. The details are discussed in [100].

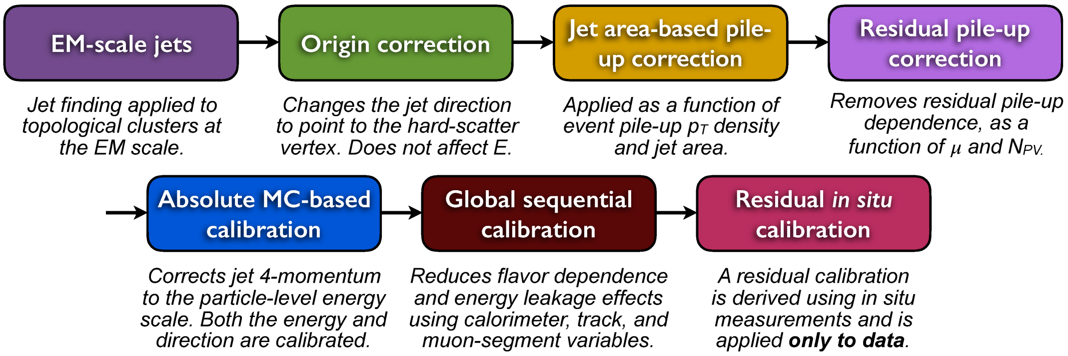

Figure 5.3: Calibration stages from the original EM-scale jets to the full-calibrated jets [100].

5.5 B-tagged jets

The identification of the b-quark initiated jets [101] plays an important role in this analysis. The algorithm is referred to as b-tagging algorithm, and the identified jets are called as "b-tagged" jets. The b-tagging algorithm uses a property of heavy hadrons. The heavy hadrons have some vertices which are displaced from the primary interaction points, because the cascade decay occurs in the chain. Especially, b-hadrons have life time, $c\tau \simeq 500\ \mu$m, thus the displaced vertices can be measured with the ATLAS detectors resolution. Therefore, the goal of the b-tagging algorithm is to reconstruct a secondary (or possibly tertiary) vertex along the b-hadrons decay cascade. In addition, large branching ratio to semi-leptonic decays of b-hadrons ($\simeq 21\%$) implies the presence of muons within jets can be used as a discriminating feature for flavor tagging.

The b-tagging algorithm is a set of low-level and high-level tagger. The low-level tagger focuses on the basic kinematics information of jets, and output a score. There are five low-level taggers (IP3D, RNNIP, SMT, SV1 and JetFitter), where each tagger has different advantages. Furthermore, the high-level tagger uses these scores as inputs, and compute a score corresponding to the b-jet probability. In this analysis, DL1r is used as the high-level tagger for the final identification discriminant.

5.5.1 Low-level taggers

Impact Parameter based Algorithm: IP3D

The IP3D algorithm is a track-based impact parameter tagger, which utilizes a log-likelihood ratio discriminant separating tracks associated to jets according to whether or not they are compatible to the primary vertex hypothesis [102] . The IP3D uses the transverse and longitudinal impact parameters taking into account their correlations. Fig 5.4 shows the transverse and longitudinal impact parameter distributions for tracks from b-, c- and light-flavour jets. The final discriminant for the IP3D algorithms is shown in Fig 5.5.

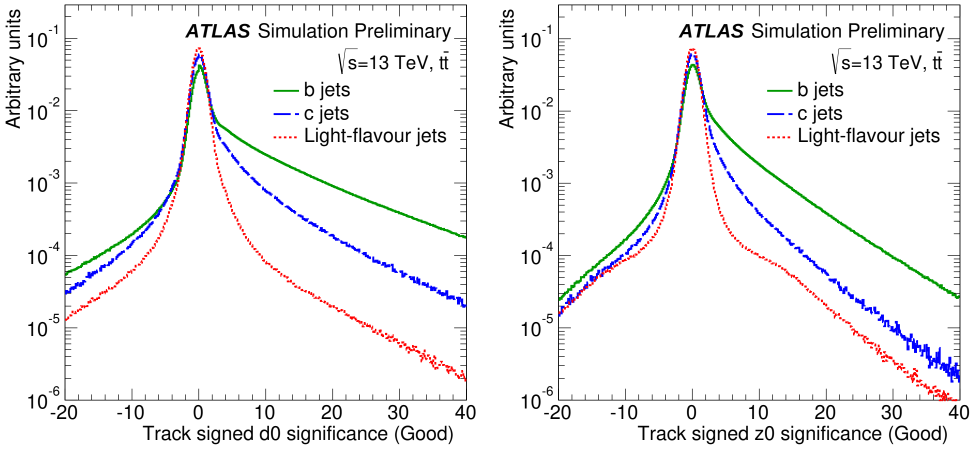

Figure 5.4: The transverse (left) and longitudinal (right) impact parameters of tracks in $t\bar{t}$ events. The "Good" is a quality of the jets defined in [102].

Impact Parameter based Algorithm: RNNIP tagger

Although the IP3D calculates the correlations of impact parameters, the track-to-track correlations aren't taken into account. To complement the disadvantages, an approach is prepared with a recurrent neural network (RNN). The method is called as RNNIP tagger [103], and the

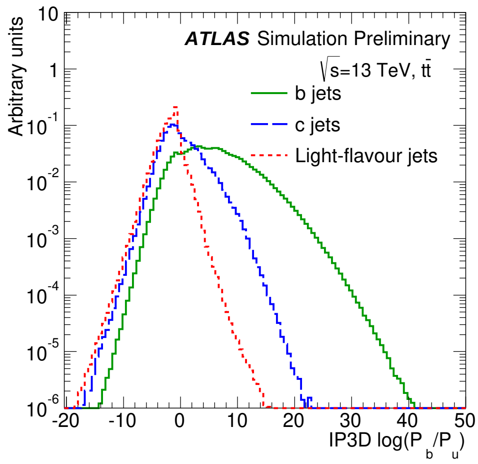

Figure 5.5: The log-likelihood ratio of the IP3D algorithm output [102].

schematic is shown in Fig 5.6. The outputs are probabilities, p_{light} for light-quarks, p_c for c-quarks, p_b for b-quarks and p_τ for tau leptons. The input variables used in the IP3D and RNNIP are compared in Table 5.2.

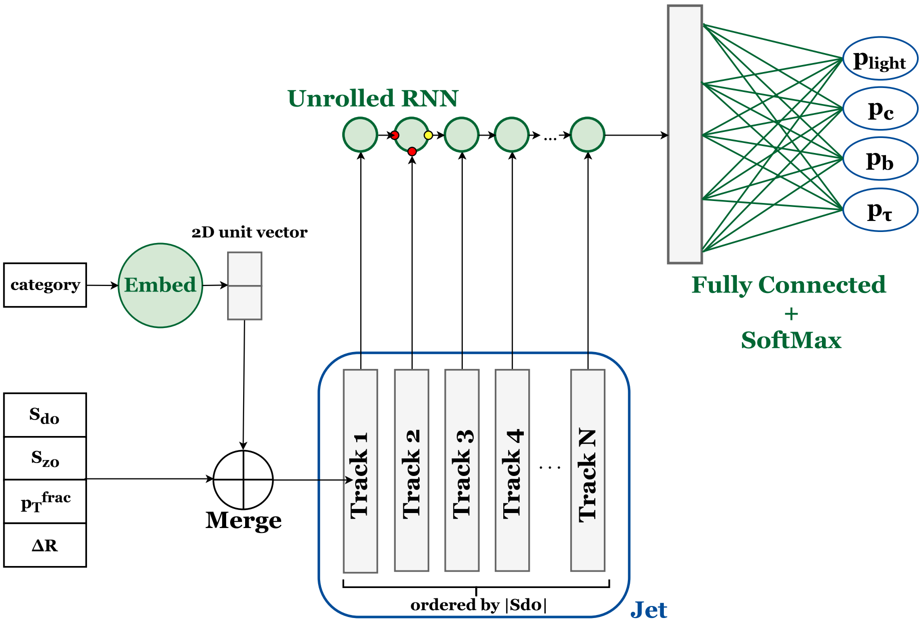

Figure 5.6: Schematic diagram of the RNN based tagger [103].

Secondary Vertex Finding Algorithm: SV

The secondary vertex based algorithm (SV) [102] aims to explicitly reconstruct an inclusive displaced secondary vertex within the jet. Fig 5.7 shows the distribution of some of the properties of the reconstructed secondary vertex comparing vertices from b, c and light-flavour jets.

Table 5.2: Track input variables used in IP3D and RNNIP.

Variable	Description	IP3D	RNNIP
S_{d_0}	Transverse impact parameter divided by its error	✓	✓
S_{z_0}	Longitudinal impact parameter devised by its error	✓	✓
p_T^{frac}	The fraction of transverse momentum carried by the track relative to the jet		✓
$\Delta R(\text{track, jet})$	The angular distance between the track and the jet axis		✓

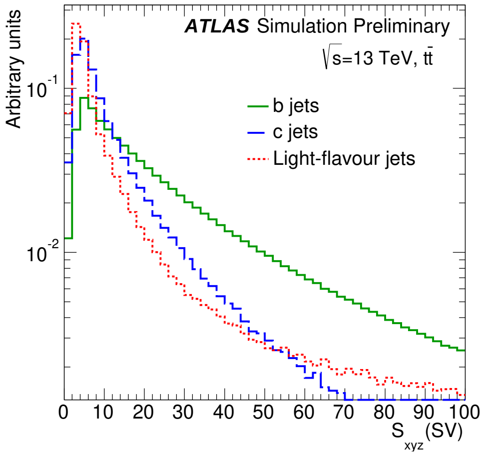

Figure 5.7: Three-dimensional decay length significance of the secondary vertex reconstructed by the SV algorithm [102].

Decay Chain Multi-Vertex Algorithm: JetFitter

The decay chain multi-vertex reconstruction algorithm, JetFitter, exploits the topological structure of weak b- and c-hadron decays inside the jet and tries to reconstruct the full PV → b → c-hadron decay chain. A Kalman filter is used to find a common line on which the primary vertex and the bottom and charm vertices lie, approximating the b-hadron flight path, as well as their positions. With this approach, the b- and c-hadron vertices, whenever resolution allows, can be resolved, even when only a single track is attached to each of them.

5.5.2 High-level identification; DL1r

The high-level tagger is referred to as DL1r, which is a kind of deep neural network schema. The DL1r architecture is a mixture of fully-connected, maxout, and batch normalization layers with rectified linear units as activation functions. Dropout is used as a stochastic regularization technique. The network is trained to minimize the cross-entropy loss using the Adam optimizer. A thorough grid search is performed to select the network structure and hyper-parameters such as the number of hidden layers, number of nodes per layer, and the learning rate. The three output nodes calculate the probabilities associated with each jet flavor (p_b, p_c, p_u) as highly non-linear functions of the input features. These probabilities are shown in Fig 5.8. A final discriminant is obtained as a function of the fraction of c-jets, f_c, in the background:

$$\mathrm{DL1}(f_c) = \ln\left(\frac{p_b}{f_c p_c + (1 - f_c)p_u}\right). \tag{5.10}$$

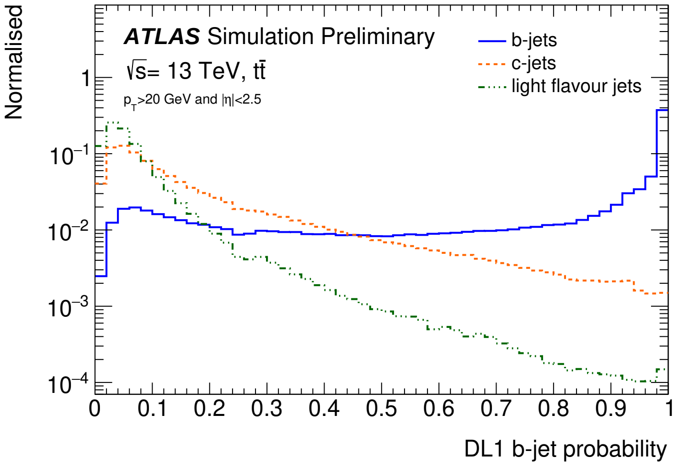

Figure 5.8: Neural network b-jet probability output distribution for jets with $p_{\mathrm{T}} > 20$ GeV and $|\eta| < 2.5$ in $t\bar{t}$ events with at least one leptonically-decaying W boson [104]. b-jets are shown in blue, c-jets in orange, and light flavour jets in green. Each histogram is normalized to unity.

5.6 Electrons

Electrons can leave a significant amount of its energies in the electromagnetic calorimeters as the collimated clusters. In addition, the cascade shower can occur in the inner detector volume, thus it is necessary to match multiple tracks to the same electromagnetic cluster. Therefore, the electron reconstruction algorithm is based on not only the calorimeters but also the inner detectors. Fig 5.9 shows the electron path and the schematic overview of the reconstruction combination procedure.

5.6.1 Reconstruction

Electrons are selected and defined as objects consisting of clusters build from energy deposit in the calorimeter and matched track(s) [105]. First of all, the reconstruction algorithm prepares the tracks and clusters. The seed clusters are reconstructed by a sliding window with a size of 3×5 (units is 0.025×0.025) in $\eta \times \phi$ of the electromagnetic calorimeter. In addition, a pattern recognition and track fit are performed for electron track seeds. Track candidates are fit, according to the hypothesis used in the pattern recognition, using the ATLAS Global χ^2 Track Fitter [106].

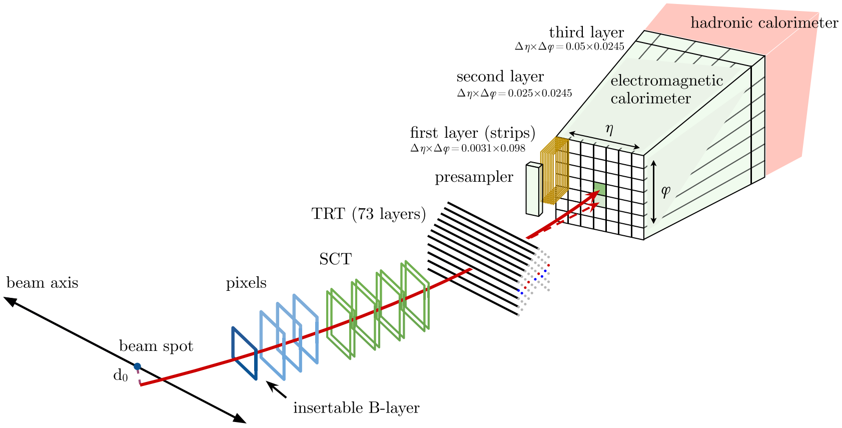

Figure 5.9: A schematic illustration of the path of an electron through the detector [105]. The red trajectory shows the hypothetical path of an electron, which first traverses the tracking system (Pixel, SCT and lastly TRT detectors) and then enters the electromagnetic calorimeter. The dashed red trajectory indicates the path of a photon produced by the interaction of the electron with the material in the tracking system.

5.6.2 Identification

The electron identification algorithm [105] is based on a likelihood (LH) technique with the signal and background probability density function (PDF) given by :

$$\mathcal{L}_{S(B)}(\vec{x}) = \prod_{i=1}^{n} P_{S(B),i}(x_i), \tag{5.11}$$

where $\vec{x}$ is the vector of discriminating variables, and $P_{S(B),i}(x_i)$ is the value of the signal or background PDF of the variable x_i. The typical input variables are listed below:

- Hadronic leakage (R_{had}) :
  Ratio of E_T in the first layer of the hadronic calorimeter to E_T of the EM cluster
- Track conditions (d_0, $|d_0/\sigma(d_0)|$, $\Delta p/p$) :
  Transverse impact parameter, significance of transverse impact parameter and momentum lost by the track respectively

The PDFs for the signal and background are obtained from simulated samples of $Z \rightarrow ee$ and di-jet respectively. Four electron identification working points are prepared, Very Loose, Loose, Medium and Tight. Fig 5.10 shows the basic three points working point identification efficiencies.

5.6.3 Isolation

In addition to the identification, identified electrons are required to be isolated from other track or clusters to further distinguish the signal and background. The isolation variable quantify the energy of the particles produced around the electron candidate. The efficiencies of the isolation working points for the electrons are shown in Fig 5.11.

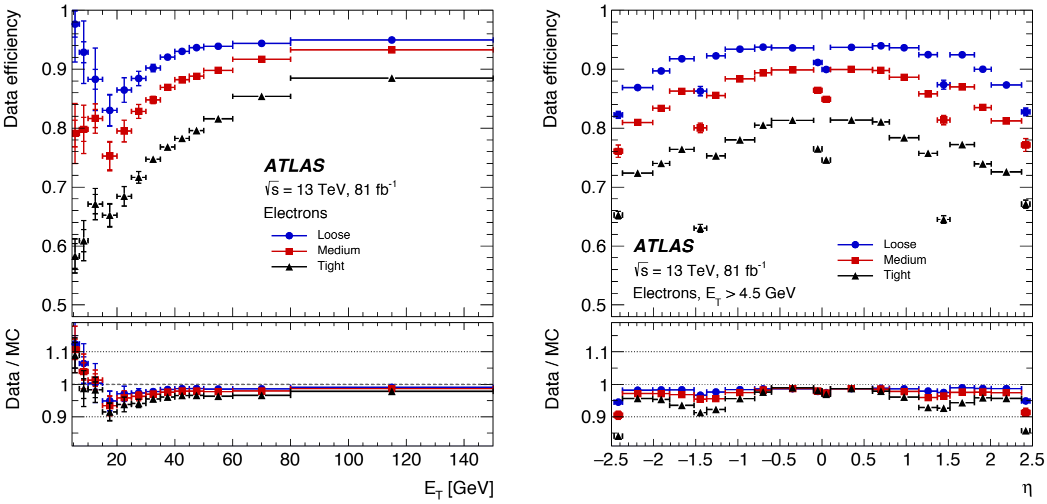

Figure 5.10: Electron identification efficiency [107].

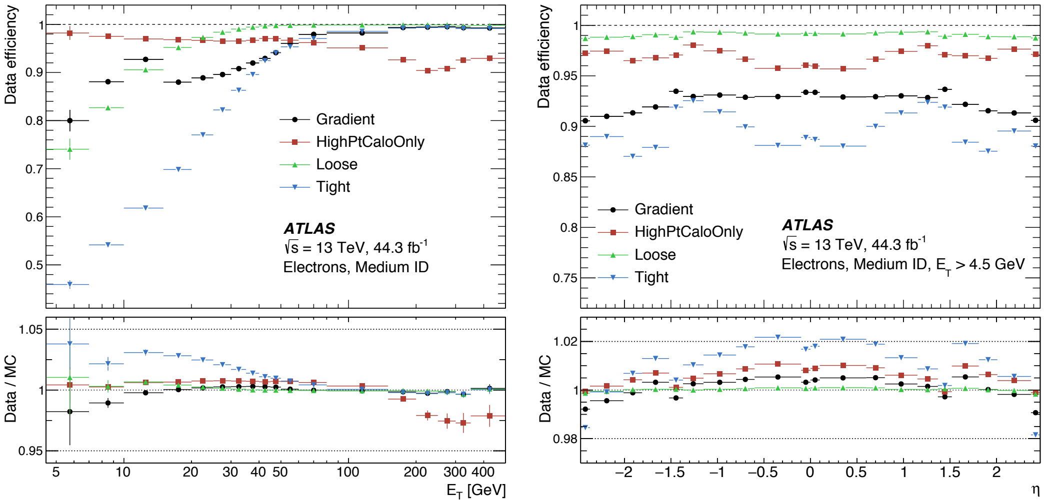

Figure 5.11: Electron isolation efficiency [107].

5.6.4 Energy resolution

The electron energy resolution is defined by [108]:

$$\frac{\sigma_E}{E} = \frac{a}{\sqrt{E}} \oplus \frac{b}{E} \oplus c, \tag{5.12}$$

where a, b and c are the sampling term, the noise term and c is constant term respectively. The typical a term is assumed as 10% (in the barrel) or 15% (in the end-cap) for $E = 1$ GeV, the typical b term is assumed as 45 MeV, and the typical c is assumed as 0.7 % from test-beam studies [109].

In addition to three terms above, systematic uncertainties of a material in calorimeter is taken into account obtained by other specific measurements. Fig 5.12 shows the energy resolution as a function of $|\eta|$ [110]. The quantity E_{gen} is the true energy of the generated particle and E_{calib} is the reconstructed energy after applying the regression algorithm.

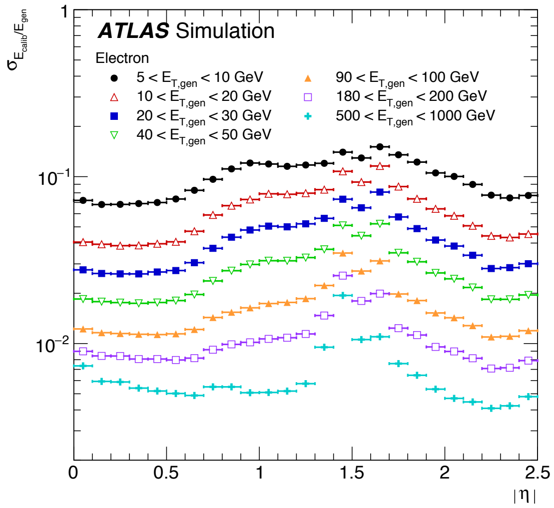

Figure 5.12: Energy resolution, $\sigma_{\mathrm{Ecalib}}/E_{\mathrm{gen}}$, estimated from the interquartile range of $E_{\mathrm{calib}}/E_{\mathrm{gen}}$ as a function of $|\eta|$ for electrons [108].

5.7 Muons

Muons behave as minimum ionization particles (MIP) in the ATLAS experiment energy scale, therefore its energy deposits in the calorimeters are very small with respect to other reconstructed objects. Most of other particles loss its energy in the calorimeters, while the muons can reach at the muon spectrometers region easily. To take into the properties, the muon detectors are located in the outer most of the ATLAS detectors as discussed in Chapter 3. The muon reconstruction and identification algorithm use not only the muon spectrometers but also the inner detectors and calorimeters. The brief descriptions are summarized below.

5.7.1 Reconstruction

There are four muon reconstruction algorithms, which is based on the inner detectors, calorimeters and muon spectrometers. One of the big differences between the muons and other objects is that the muons traverse the troidal magnetic field. The outermost detectors, or muon spectrometers, can use the longest lever arm to measure the momenta. The brief descriptions of four algorithms are summarized below, and the details are discussed in [111].

Combined muon

Track reconstructions are performed in the inner detectors and muon detectors independently, and a combined track is reconstructed with a global refit using these hits information.

Segment-tagged muon

If a track in the inner detector is extrapolated to the muon spectrometer and associated with at least one local track in the MDT or CSC, the track is classified as segment-tagged muon. The segment-tagged muon is used when a muon passes only one layer of the muon spectrometers, due to the low-p_{T} or limitation of the acceptance.

Calorimeter-tagged muons

If a track in the inner detector is matched to an energy deposit in the calorimeters compatible with a MIP scale, the track is classified as calorimeter-tagged muon. The calorimeter-tagged muon is the lowest purity, but it can recover the acceptance of the muon spectrometers. For the calorimeter-tagged muon, $15 < p_T < 100$ GeV and $|\eta| < 0.1$ are applied as the identification criteria.

Standalone muons

The standalone muons are reconstructed by only the segments in the muon spectrometers. This standalone muons can recover the acceptance in the forward region ($2.5 < \eta < 2.7$), which is not covered by the inner detectors.

Overlaps between different muon types are resolved before moving to the physics analysis stage. When two muon types share the same track in the inner detector, preference is given to combined muons, then to standalone muons, and finally to calorimeter-tagged muons. The overlap with standalone muons in the muon system is resolved by analyzing the track hit content and selecting the track with better fit quality and larger number of hits.

5.7.2 Identification

In addition to the reconstruction criteria, the reconstructed need to pass a set of quality cuts to suppress backgrounds, mainly from pion and kaon decays. The muon candidates originating from decays of such charged hadrons are characterized by the presence of a distinctive "kink" topology in the reconstructed track. Therefore, the fit quality of the tracks results can be used as the discriminate variable. As a consequence, three variables are used as identification criteria:

- $\boldsymbol{q/p}$ significance : The ratio of the charge to its momentum in the inner detector and muon spectrometers.
- $\boldsymbol{\rho'}$: The absolute value of the difference between the transverse momentum in the inner detectors and muon spectrometers divided by the p_{T} of the combined track.
- $\boldsymbol{\chi^2}$: Normalized χ^2 of the combined track fit.

Four muon identification working points are defined : `Loose`, `Medium`, `Tight`, and `HighPt`. This analysis use `Medium` as the default muons. The reconstruction efficiency for the `Medium` working point is shown in Fig 5.13.

5.7.3 Isolation

Muons from heavy interesting particles, W, Z, or other new bosons, are often produced isolated from other particles. However, muons from semi-leptonic decays of charged hadrons are measured in the jets. Therefore, the "isolation" can be useful information to discriminate the muons of interesting and suppress backgrounds.

The muon isolation criteria are defined in a similar way as for the electrons. Scalar sum of the E_T of the topo-clusters or the p_{T} of the tracks around the muon are used to define the isolation working points. The efficiencies for `LooseTrackOnly`, `Loose`, `GradientLoose` and `FixedCutLoose` are shown in Fig 5.14. This analysis uses `Loose` working point as the default muon isolation criteria.

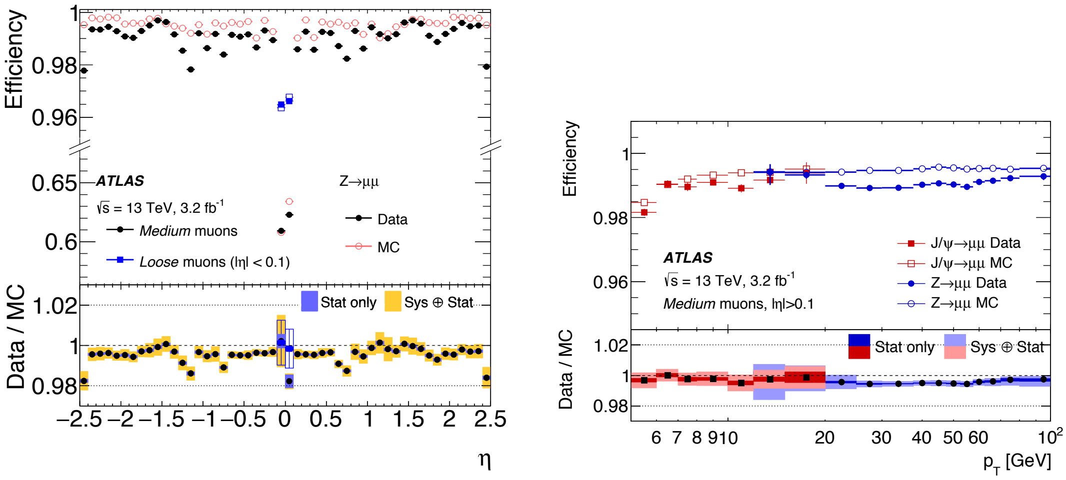

Figure 5.13: Muon reconstruction efficiency for `Medium` working point [111].

5.7.4 Calibration

The calibration is defined as momentum corrections to the simulated muon transverse momenta reconstructed in the inner and muon detectors to reproduce the experimental data. The corrected transverse momentum $p_T^{\mathrm{Cor,Det}}$ (det = inner detector, muon chambers) is defined by following :

$$p_T^{\mathrm{Cor,Det}} = \frac{p_T^{\mathrm{MC,Det}} \sum_{n=0}^{1} s_n^{\mathrm{Det}}(\eta, phi) \left(p_T^{\mathrm{MC,Det}}\right)^n}{1 + \sum_{m=0}^{2} \Delta r_m^{\mathrm{Det}}(\eta, \phi)(p_T^{\mathrm{MC,Det}})^{m-1} g_m} \tag{5.13}$$

The correction factors are obtained from the observed $Z \to \mu\mu$ and $J/\psi \to \mu\mu$ line shape with fitting the momentum scale and smearing.

5.8 Taus

Tau lepton is the heaviest lepton with a mass of $m_\tau = 1776.86 \pm 0.12$ MeV. The tau lepton decays into hadrons or light leptons (e or μ) with a mean lifetime 290×10^{-5} sec via weak charged current interactions. The leptonic decay, $\tau \to \ell\nu_\ell\nu_\tau$ ($\ell = e, \mu$), is labelled as τ_{lep}, and the hadronic decay, $\tau \to qq' + \nu_\tau$, is labelled as τ_{had}. For τ_{had} mode, the decay product contains an odd number of charged hadrons. The main decay mode is associated with 1 or 3 charged particles, which are referred to as "1-prong" or "3-prong" mode respectively. There are other decay modes, ex. 5-prong mode, but the branching ratio is very small with respect to 1- or 3-prong decay mode, thus these minor events are not taken into account for the reconstruction and identification algorithms in this analysis. Each main decay mode and branching ratio is summarized in Table 5.3.

The decay length $c\tau$ is 87.03 μm, then almost all τs decay are happened before reaching active regions of the detector. Therefore the τ_{lep} cannot be distinguished from light lepton process, ex. $W^- \to e^-\bar{\nu}_e$. The τ_{lep} is treated as same as light leptons, as discussed in Section 5.6, Section 5.7. This section focuses on the τ_{had} reconstruction and identification algorithm.

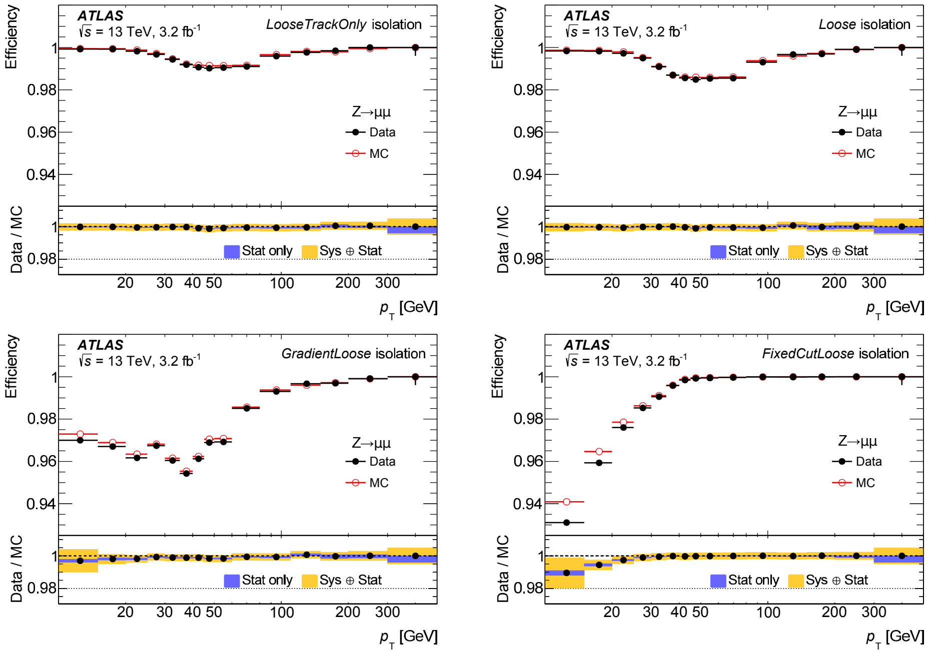

Figure 5.14: Muon isolation efficiency `LooseTrackOnly` (top left), `Loose` (top right), `GradientLoose` (bottom left), and `FixedCutLoose` (bottom right) muon isolation working point [111].

5.8.1 Overview of Reconstruction and Identification

The τ_{had} deposits its energy in the calorimeters as same as hadronic jets, then the reconstructions of τ_{had} starts by treating the energy depositions. Therefore, first of all, as an input for the reconstruction, hadronic jets reconstructed by the anti-k_T algorithm with a distance parameter $R = 0.4$. The reconstruction algorithm create τ_{had} "candidates" from the hadronic jets, but a lot of hadronic jets are also reconstructed as the τ_{had} object candidates. These mis-identified candidates are referred to as "fake τ_{had} " in this analysis. Therefore, it is necessary to apply a rejection algorithm to discriminate the origin of the candidates and reject the contamination of the hadronic jets to the τ_{had} objects (fake τ_{had}). These procedures are achieved by dedicated two-level algorithms, reconstruction and identification stage. Each final discriminant variable is the multi-variable analysis results distributions, Boosted Decision Tree (BDT) and Recurrent Neural Network (RNN) respectively. The overview of the sequence is summarized in Fig 5.15.

5.8.2 Reconstruction of Taus

Jets formed by anti-k_T algorithm with a distance parameter of $R = 0.4$ [112] are used as seeds for τ_{had} reconstruction algorithm. The seed jets are required to have $p_T > 10$ GeV and $|\eta| < 2.5$. To increase the τ_{had} reconstruction efficiency, the τ_{had} production vertex (TV) is defined at this stage. The TV association algorithm uses as input all tracks in the region $\Delta R < 0.2$ around the jet seed direction. The p_{T} of these tracks is summed and a primary vertex is chosen if the largest fraction of the p_{T} sum is matched to the vertex candidate. The efficiency of the TV assignment is shown in Fig 5.16.

After reconstructing the TV, track selection algorithm defines $\Delta R < 0.2$ region around the

Table 5.3: Tau decay mode breakdown.

decay mode	Main final state	Branching ratio	Total
τ_{lep}	$e^- + \nu_\tau + \bar{\nu_e}$	$17.82 \pm 0.04\%$	35.21 ± 0.06
	$\mu^- + \nu_\tau + \bar{\nu_\mu}$	$17.39 \pm 0.04\%$	
τ_{had} (1-prong)	$\pi^- + \nu_\tau$	$10.82 \pm 0.05\%$	49.37 ± 0.08
	$\pi^- + \pi^0 + \nu_\tau$	$25.49 \pm 0.09\%$	
	$\pi^- + \pi^0\pi^0 + \nu_\tau$	$9.26 \pm 0.10\%$	
τ_{had} (3-prong)	$\pi^-\pi^-\pi^+ + \nu_\tau$	$9.80 \pm 0.05\%$	$15.20 \pm 0.06\%$
	$\pi^-\pi^-\pi^+ + \pi^0 + \nu_\tau$	$5.29 \pm 0.05\%$	

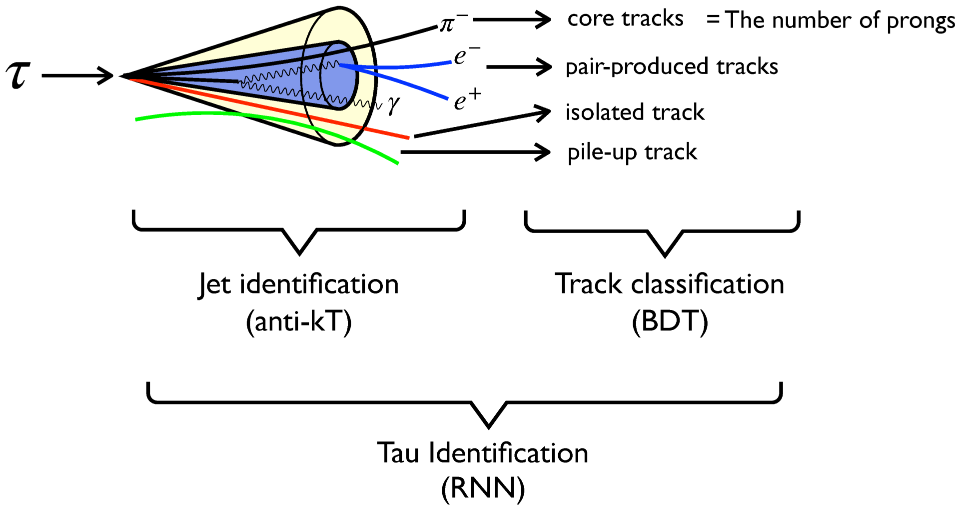

Figure 5.15: Overview of tau lepton identification algorithms.

seed jet as the core region, and classify the origin of tracks. The tracks are classified as core tracks (tracks directly from τ_{had}), pair-produced track (tracks from conversion process), isolated track (tracks not in the core region) or pile-up track (tracks from un-related process). The track classification algorithm is based on Boosted Decision Tree (BDT), and the efficiency is shown in Fig 5.17.

5.8.3 Identification of Taus

The τ_{had} identification algorithm is based on a RNN technique in 2015-2018 period [113]. The main purpose of the RNN identification algorithm is to separate true τ_{had} events and mis-identified τ_{had} events originating from quark and gluon-initiated hadronic jets. The τ_{had} and hadronic jet events are measured by the calorimeters, thus the algorithm focuses on the differences of the shape and properties of the calorimeter clusters. Due to the distinct signatures of 1- and 3-prong τ_{had} decays, dedicated RNN algorithms are prepared for 1- and 3-track τ_{had} respectively.

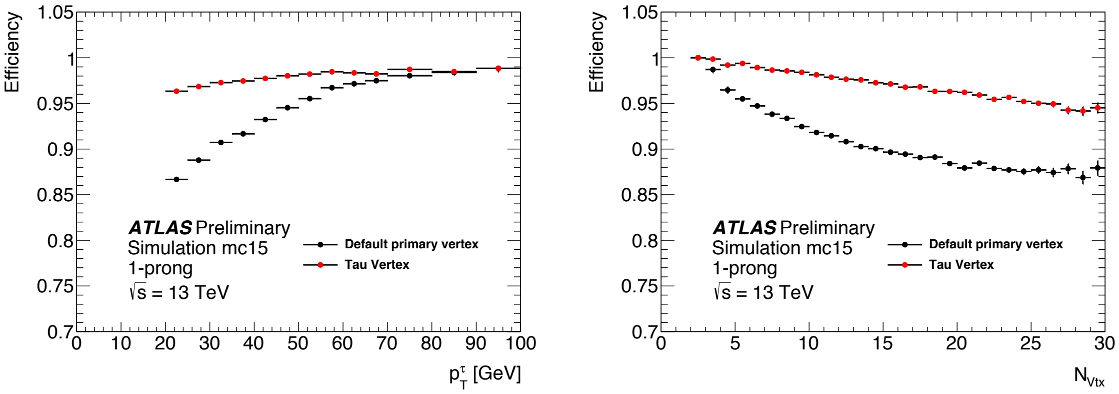

Figure 5.16: Efficiency for correct production vertex assignment in 1-prong tau decays for the tau reconstruction algorithm and the default choice of the vertex with the highest $\sum p_T^2$, as a function of τ_{had} p_{T} (Left) and of the number of reconstructed vertices in the event (Right) [113].

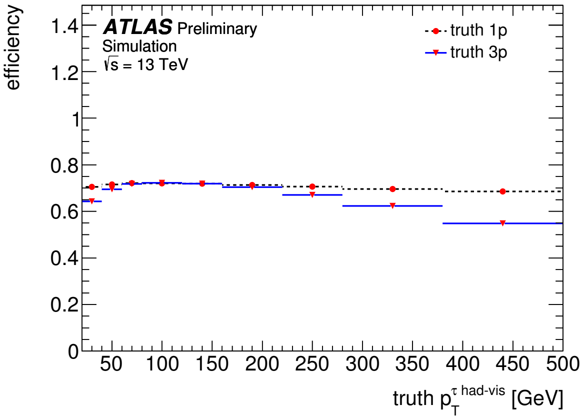

Figure 5.17: Efficiency for reconstructing the same number of tracks as the number of charged decay products of the tau lepton as a function of τ_{had} pT [113].

Input variables

As input variables to the RNN identifications algorithm, two-types of the input variables are prepared; a low-level input variables (individual tracks and calorimeter clusters), and combinations of each variable. The brief descriptions of each variable are summarized in Table 5.4.

Network architecture

The RNN ID network architecture is shown in Fig 5.18. The network is split into three dedicated branches for each type of input, tracks, clusters and other high-level variables. The sequences of track and cluster representations are then passed into recurrent layers employing the long-short-term memory (LSTM).

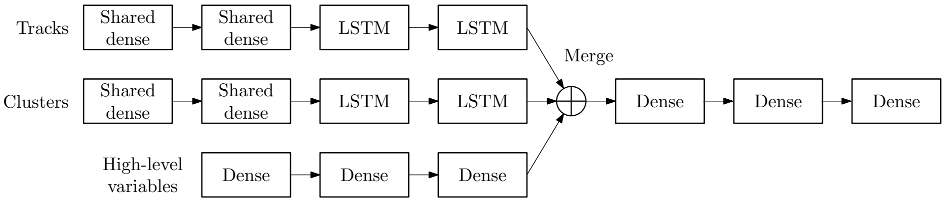

Figure 5.18: Schematic overview of the network for the tau identification. The dense layers are fully connected to adjacent layers [113].

Training and evaluation

Two simulation samples were prepared to train and evaluate the RNN algorithm. The signal sample consists of $\gamma^* \to \tau\tau$ events, while background samples consist of di-jet event. The signal sample $\gamma^* \to \tau\tau$ events were forced to decay hadronically to maximize the available training sample. The available sample consists of approximately 20 million signal candidates and 46 million background candidates. The sample is split into dedicated samples for training of the network (40%), monitoring of training progress (10%) and performance evaluation (50%).

Identification performance

The performance of RNN ID algorithm is evaluated on statistically independent test samples of $\gamma^* \to \tau\tau$ and di-jet events. The RNN performance is also compared to that of the previous BDT-based τ_{had} identification algorithm (used in early Run-2), as shown in Fig 5.19. The rejection power in the y-axis is defined as the inverse of the background selection efficiency, thus the smaller rejection power means a good rejection of many backgrounds. Four working points with increasing background rejection (`Very Loose`, `Loose`, `Medium` and `Tight`) are defined. The corresponding signal selection efficiencies and rejection powers are shown in Table 5.5. The selection efficiencies as function of some important properties are shown in Fig 5.20.

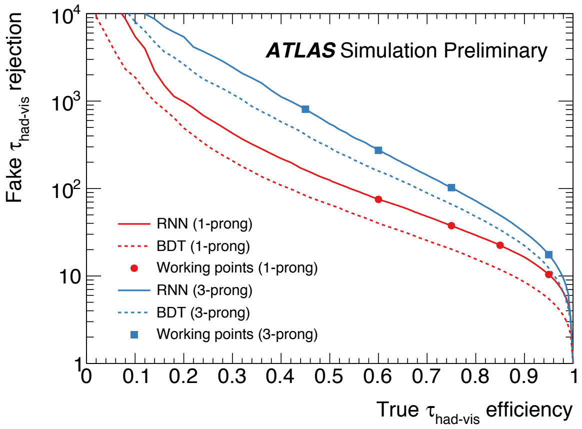

Figure 5.19: Rejection power for quark and gluon jets misidentified as $\tau_{\text{had-vis}}$ (referred as to Fake $\tau_{\text{had-vis}}$) depending on the true $\tau_{\text{had-vis}}$ efficiency [113].

5.8.4 Fake-τ_{had}

As discussed in Section 5.8.1, the jet-to-τ_{had} fakes are referred to as "fake-τ_{had} " backgrounds in this analysis. It is hard to estimate the probability of the fake rate using fully MC predictions, because the fake-τ_{had} events are caused by the limited detector responses. Furthermore, to calculate the probability with MC predictions, it is needed to create a lot of MC predictions with QCD jets. In this analysis, the fake-τ_{had} estimation used not only the MC predictions but also the data information. The main concept is that the fake-τ_{had} from the MC predictions are corrected by some scale factors. Therefore, the corrected MC-based fake-τ_{had} backgrounds are used as the fake-τ_{had} backgrounds to this analysis. The method of the scale factor calculations are discussed in Chapter 8.

5.9 Missing Transverse Energy

Some interesting physic process have multiple neutrinos in the final state, but the ATLAS detectors cannot measure the signature. To "measure" the neutrino energies, this analysis uses the energy conservation law in the transverse plane (xy-plane).

The physics process in the LHC environment are caused by the partons in the initial proton beams, and the initial parton momentum always changes. The initial energy of the partons is unknown, thus the total energy conservation law cannot be used. However, in the transverse plane (xy-plan) the initial momentum is always zero, thus the neutrinos can be measured as missing transverse momentum (E_T^{miss}) which is measured as an imbalance in the sum of visible transverse momentum [114]. The vector $\vec{E}_T^{\text{miss}}$ is calculated using the components along x and y axes :

$$E_{x(y)}^{\text{miss}} = E_{x(y)}^{\text{miss},\mu} + E_{x(y)}^{\text{miss},e} + E_{x(y)}^{\text{miss},\gamma} + E_{x(y)}^{\text{miss},\tau} + E_{x(y)}^{\text{miss,jets}} + E_{x(y)}^{\text{miss,soft}}, \tag{5.14}$$

where e, μ, γ, τ, jets represent each reconstructed object, and the soft term is electric signals not associated with reconstructed objects.

5.10 Overlap removal between the reconstructed objects

The object reconstruction algorithms run on the same particle, then a particle is reconstructed as two or more "objects" simultaneously. To distinguish the the issue, ambiguities between the objects are resolved by a dedicated procedure, referred to as "overlap removal" procedure.

The algorithm begins with the electron-electron overlap removal. If two electron share the tracks, the lower-p_{T} electron is rejected. Next, the τ_{had}-lepton (e or μ) overlap removal is performed. The τ_{had} is rejected if $\Delta R < 0.2$ between the τ_{had} and the lepton. Furthermore, the electron and muon overlap removal is performed, and the muon is rejected if both lepton share the track and the muon is calorimeter-based muon. Finally, the jet-lepton (e or μ) overlap removal is performed. For the electron, the jet is rejected if $\Delta R < 0.2$ (for non b-tagged jet) or if the electron $p_{\text{T}} > 100$ GeV (for b-tagged jet). For the muon, the jet is rejected if the number of tracks is less than 3, and $\Delta R < 0.2$ (for non b-tagged jet). For both of leptons, the leptons are rejected if the ΔR <0.4.

Table 5.4: List of input variables for 1- and 3-prong dedicated RNN algorithm. The ✓shows that the variable is used by each 1-prong or 3-prong dedicated algorithm.

Observable	Description	1-prong	3-prong
$p_T^{\text{seed jet}}$	The seed jet p_{T}	✓	✓
p_T^{track}	Each associated track p_{T}	✓	✓
$\Delta\eta^{\text{track}}$	η distance between each track and the τ_{had} axis	✓	✓
$\Delta\phi^{\text{track}}$	ϕ distance between each track and the τ_{had} axis	✓	✓
$\lvert d_0^{\text{track}}\rvert$	Transverse impact parameter	✓	✓
$\lvert z_0^{\text{track}} \sin\theta\rvert$	Longitudinal impact parameter	✓	✓
$N_{\text{IBL hits}}$	The number of hits in IBL	✓	✓
$N_{\text{Pixel hits}}$	The number of hits in Pixel	✓	✓
$N_{\text{SCT hits}}$	The number of hits in SCT	✓	✓
E_T^{cluster}	Each topo-cluster transverse energy	✓	✓
$\Delta\eta^{\text{cluster}}$	η distance between the cluster moment [97] and the τ_{had} axis	✓	✓
$\Delta\phi^{\text{cluster}}$	ϕ distance between the cluster moment [97] and the τ_{had} axis	✓	✓
λ_{cluster}	Longitudinal distance between the topo-cluster center and the calorimeter face	✓	✓
$\langle\lambda^2_{\text{cluster}}\rangle$	Second moment of the longitudinal distance between topo-cluster center and each cell	✓	✓
$\langle r^2_{\text{cluster}}\rangle$	Second moment of the radial distance between topo-cluster axis and each cell	✓	✓
$p_T^{\text{uncalibed}}$	p_{T} of the τ_{had} candidate before the calibration	✓	✓
f_{cent}	Fraction of transverse energy in $\Delta R < 0.1$ to $\Delta R < 0.2$ around the τ_{had} axis	✓	✓
$f^{-1}_{\text{leadtrack}}$	Fraction of transverse energy sum to the highest-p_{T} core track	✓	✓
ΔR_{max}	The maximum ΔR between a track in the core region and the τ_{had} axis	✓	✓
$\lvert S_{\text{leadtrack}}\rvert$	Transverse impact parameter of the highest-p_{T} core track divided by its uncertainty	✓	
$\lvert S_T^{\text{flight}}\rvert$	The decay length of the secondary vertex divided by its uncertainty		✓
$f_{\text{iso}}^{\text{track}}$	Scalar sum of the isolation tracks p_{T} divided by the sum of all core and isolated tracks p_{T}	✓	✓
$f_{\text{track}}^{\text{EM}}$	Ratio of the sum of cluster energy to the sum of the momentum of core tracks	✓	✓
$p_T^{\text{EM+track}}/p_T$	Ratio of the τ_{had} p_{T} to the calorimeter-only measurement of the τ_{had} p_{T}	✓	✓
$m^{\text{EM+track}}$	Invariant mass of core tracks and up to two most energetic EM clusters in the core region	✓	✓
m^{track}	Invariant mass calculated from the sum of all core and isolation tracks		✓

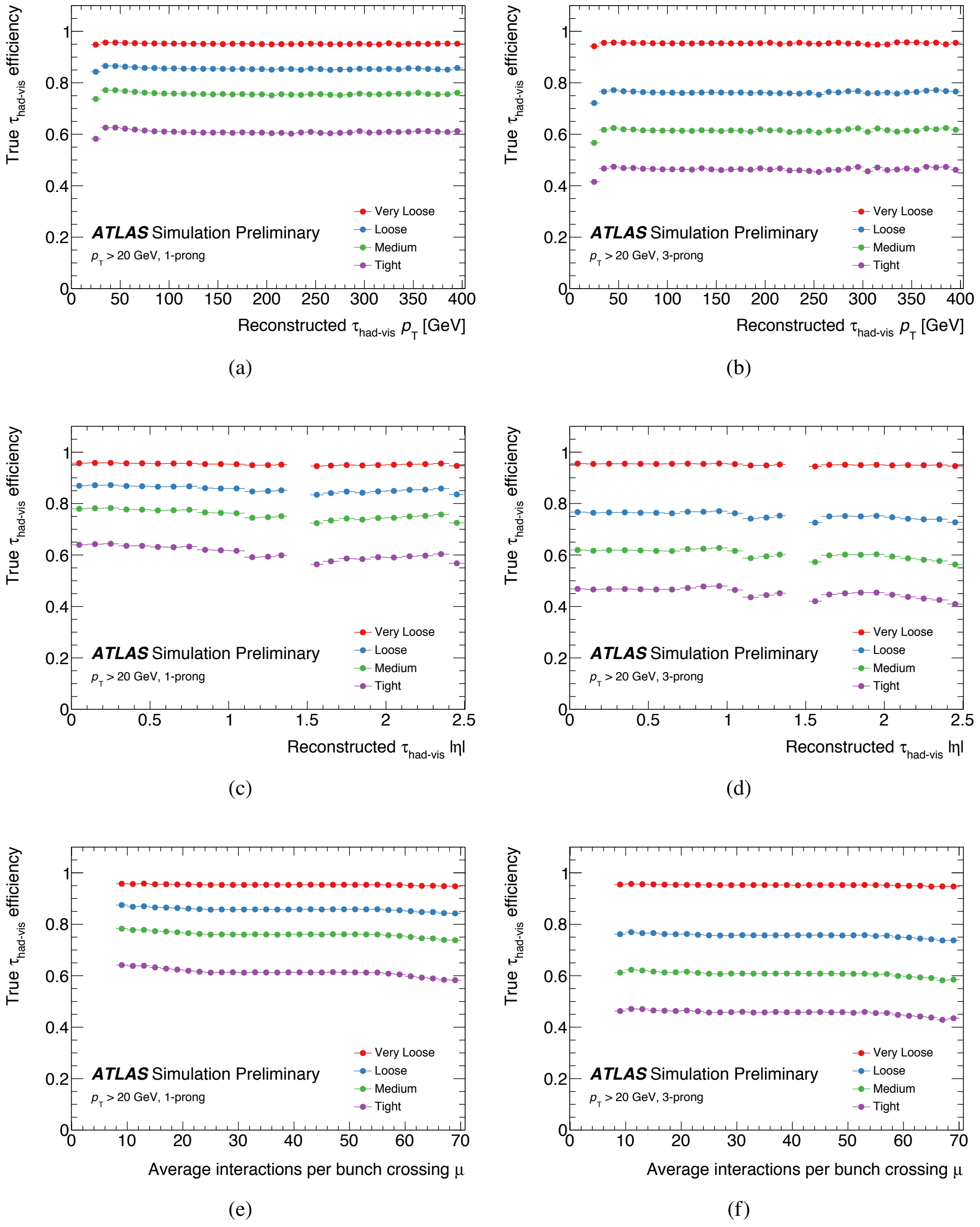

Figure 5.20: Selection efficiency for true 1- and 3-prong $\tau_{\text{had-vis}}$ candidates depending on the transverse momentum, pseudo-rapidity an the average number of interactions per bunch crossing [113]. Each color represents the defined working point of the tau RNN.

Table 5.5: Defined working points with fixed true $\tau_{\text{had-vis}}$ selection efficiencies and the corresponding background rejection factors for misidentified $\tau_{\text{had-vis}}$ in di-jet events.

	Signal efficiency		Background rejection RNN	
Working point	1-prong	3-prong	1-prong	3-prong
Tight	60%	45%	70	700
Medium	75%	60%	35	240
Loose	85%	75%	21	90
Very Loose	95%	95%	9.9	16

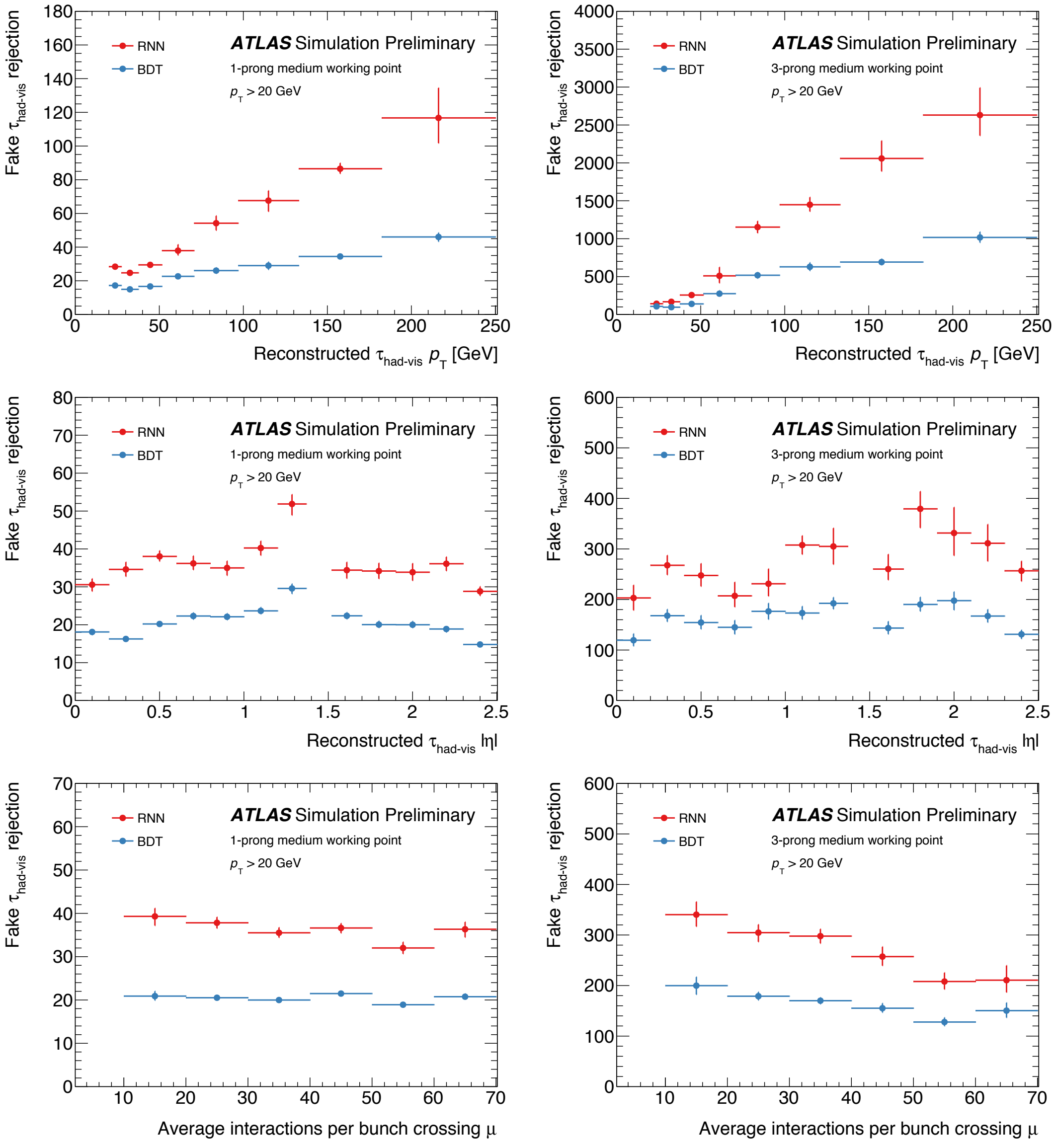

Figure 5.21: Rejection power for quark and gluon jets misidentified as $\tau_{\text{had-vis}}$ for 1- and 3-prong $\tau_{\text{had-vis}}$ candidates using the Medium working point [113].

Chapter 6

Event Selections

In this chapter, the details of this analysis strategy are explained. The goal of this analysis is to construct the optimal strategy to search LQ production. In general, the signal events cannot be detected easily because the cross section is expected to be much smaller than the Standard Model processes, which are referred to as "background" events. It is necessary to introduce some requirements to suppress the backgrounds. One of the requirements is based on differences final state features, referred to as "topologies". The signal events can be categorized according to the topologies. Other requirement is based on the difference of the energy scale between the signal and background events. Therefore, thresholds for reconstructed objects are useful to enhance signal events. The requirement is referred to as "cut-based selection".

6.1 Signal topologies

As discussed in Section 2.3, this analysis focuses on the LQ pair-production process, where each third-generation leptoquark decays into a b-quark and a tau lepton. The final state ($2b$ + 2τ), however, is not unique to the LQ event. There are some ordinary processes in the Standard Model (SM), which seems to have the almost same final state. The number of signal events is expected to be smaller than the backgrounds. Therefore, it is very important to understand the features of the signal and background events and to suppress the contamination of the background events.

Considering the final state ($2b+2\tau$), the main background is top-pair production, $t\bar{t}$ process. A top quark decays into a b-quark and a W boson with almost 100% branching ratio. When each W boson decays into a pair of τ and ν_τ, the $t\bar{t}$ process has two b-quarks, two tau leptons and two tau neutrinos. A schematic of the final states of the leptoquark and the $t\bar{t}$ are shown in Fig 6.1. Neutrinos cannot be measured directly as discussed in Section 5.9. Therefore, the top-pair production is recognized to have the same final state as the LQ events.

Therefore, some requirements other than objects in the final state are indispensable for this analysis. One of the simple ideas is that an invariant mass of the b-quark and tau lepton system may reproduce the parent particle mass. The invariant mass resolution may be worse because of missing ν_τ and resolution of jet energies. However, the reconstructed energy of the LQ system is expected to be much larger than the top-quark system because of the mass difference, $m_{\mathrm{LQ}} \geq 1000$ GeV vs $m_t \simeq 173$ GeV.

In order to get better mass resolution for the LQ, it is important to consider how the b-

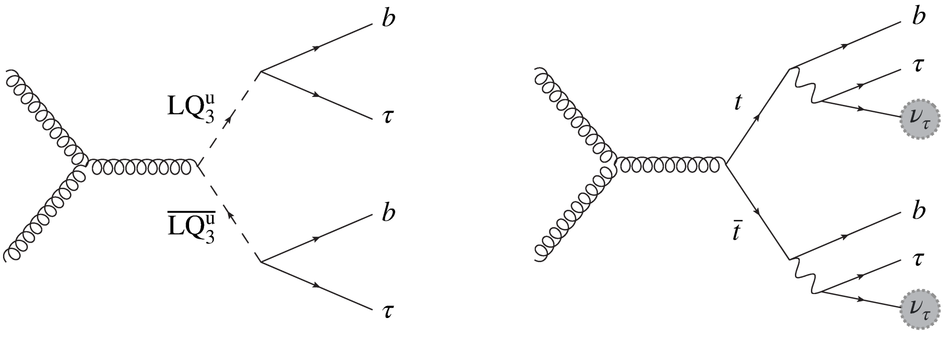

Figure 6.1: Left: Leptoquark pair production. Right : Top-quark pair production, where the W boson decays into a τ lepton and a ν_τ. The neutrino (gray colored) in the final state cannot be measured as a particle object in the ATLAS experiment, then the final state are the almost same as the LQ.

quark and the tau lepton are measured in the experiment. The b-quark is reconstructed as a B-tagged jet. On the other hand, the tau lepton has two decay modes, and both of them include at least one neutrino. Therefore, the tau lepton decay modes affects categorization of events in this analysis. One is leptonic decay mode, $\tau \to \ell\nu_\ell\nu_\tau$ denoted as τ_{lep}. Another is hadronic decay mode, $\tau \to qq'\nu_\tau$ denoted as τ_{had}. The LQ process can be divided into three categories according to the tau decay modes. These are $\tau_\ell\tau_\ell$ channel, $\tau_\ell\tau_{\mathrm{had}}$ channel and $\tau_{\mathrm{had}}\tau_{\mathrm{had}}$ channel. The number of neutrinos in the LQ final state is 4, 3 and 2 respectively, as shown in Fig 6.2.

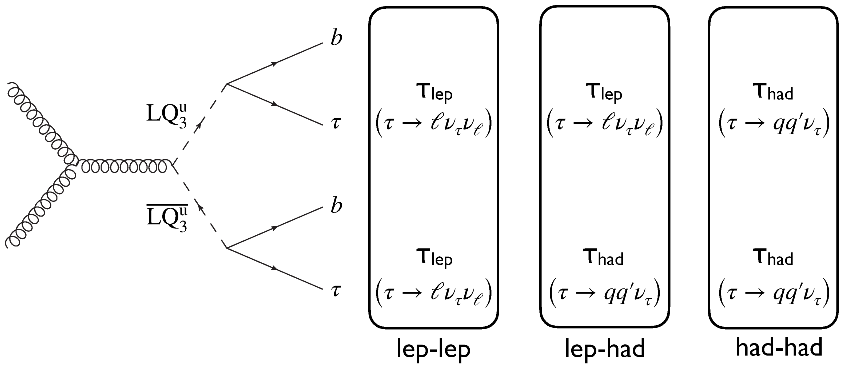

Figure 6.2: Categorization of the LQ decay mode. There are three categories according to the tau lepton decay modes. Both tau decay leptonically ($\tau_\ell\tau_\ell$), one of the tau decays leptonically ($\tau_\ell\tau_{\mathrm{had}}$) and both tau decay hadronically ($\tau_{\mathrm{had}}\tau_{\mathrm{had}}$).

In the $\tau_\ell\tau_\ell$ channel, the light lepton (e or μ) is a powerful signature to reject huge amount of QCD multi-jets backgrounds. Light leptons (e, μ) with high-p_{T} more than 20 GeV are rare in hadron colliders, because the leptons come from electro-weak processes as W, Z production and heavy quark decays. Although $\tau_\ell\tau_\ell$ channel realize clean environments, the invariant mass resolution of the b-and-tau system is the worst. The $\tau_\ell\tau_\ell$ channel has 4 neutrinos in the LQ final state (6 neutrinos in top-pair production final state). This is a disadvantage for the $\tau_\ell\tau_\ell$ channel.

In the $\tau_{\mathrm{had}}\tau_{\mathrm{had}}$ channel, the large branching ratio of the tau lepton to hadrons is an advantage in addition to better LQ mass resolution. This channel, however, is highly contaminated by the fake τ backgrounds as discussed in Sec 5.8.4. It is very hard to estimate the contamination of fake backgrounds using the background Monte Carlo samples, because the fake τ_{had} can be caused by QCD multi-jets backgrounds.

By contrast, the $\tau_\ell\tau_{\text{had}}$ channel can use both of them advantages. Namely, the τ_{lep} provides a light lepton to reject QCD multi-jet backgrounds, and the τ_{had} provides a large branching ratio. The $\tau_\ell\tau_{\text{had}}$ channel is adopted in this analysis to obtain better signal to background ratio. Two more requirements are applied to events with the $\tau_\ell\tau_{\text{had}}$ channel. One is the number of B-tagged jets, n_B. The number of b-jets in the LQ events is exactly two, but b-jets are not always labeled as B-tagged jets. Therefore, it is necessary to use events with $n_B = 1$ and $n_B = 2$. The other requirement is that the light lepton from τ_{lep} and τ_{had} should have the opposite sign (OS). This requirement of the OS can also suppress the QCD multi-jet backgrounds. The following sections treat the $\tau_\ell\tau_{\text{had}}$ events, where the the n_B and OS requirements have been already applied.

6.2 Pairing method

In the $\tau_\ell\tau_{\text{had}}$ channel, there are two b-jets, a light lepton (e, μ) and a τ_{had}. To reconstruct the parent mass, it is necessary to identify which pair of a b-jet and a τ would originate from the same leptoquark. Several approaches explained in the following have been tested. The distribution of used variables are shown in Fig 6.3.

- **max $\sum \Delta\phi$** :
  Choose the combination that maximize the sum of the opening angle $\Delta\phi$ between a b-jet and a lepton(τ_{had}, τ_{lep}), where the $\Delta\phi$ is defined as:
  $$\Delta\phi = \phi_i - \phi_j \tag{6.1}$$
  where i, j represents the kind of the particles (leading b-jet, sub leading b-jet, ℓ, τ). The leptoquark is very heavy particle, therefore the opening angle $\Delta\phi$ tends to be the largest if the b-τ pair is correct.

- **min $|\pi - \Delta R|$** :
  Choose the pairs that minimize the sum of absolute values of $\pi - \Delta R(b, \tau)$ of two pairs. The ΔR is defined as :
  $$\Delta R = \sqrt{\Delta\eta^2 + \Delta\phi^2}, \tag{6.2}$$
  where the $\Delta\eta$, $\Delta\phi$ is the difference in η and ϕ coordinate between b-jet and τ.

- **min $|\Delta m|$** :
  Choose the combination that minimizes the mass difference between two pairs, where the energy of tau is corrected by collinear approximation [115]. For the correct combination, mass of each pair represents the leptoquark mass, so the mass difference, $\Delta m = |m_1 - m_2|$ should be zero. However, the final state has multiple neutrinos and the resolution of mass is not so small.

The efficiencies for these different approaches are shown in Fig 6.4. The efficiencies of the min $|\Delta m|$ method is the best, therefore this analysis decided to use the method.

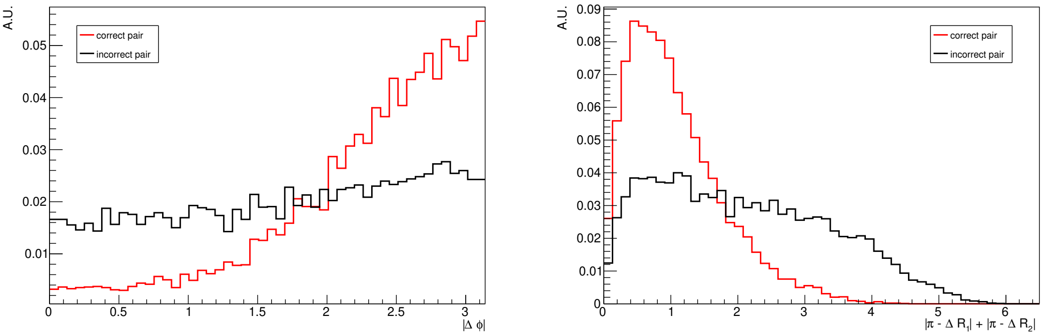

(a) max $\sum \phi$

(b) min $|\pi - \Delta R|$

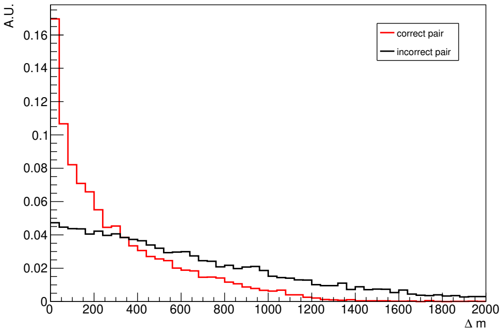

(c) min $|\Delta m|$

Figure 6.3: Distributions of variables used in pairing methods.

6.3 Trigger Selections

The analysis used a light lepton (e or μ) from a τ decay to select interesting events. Therefore, the trigger for single high-p_{T} electron/muon is used to collect events. The final state with e is called electron channel, while the state with μ is called as muon channel. Several different thresholds are used to maximize the signal acceptance. These are un-prescaled primary triggers [116]. It means that very high trigger efficiencies have been kept during Run-2 period. The list of relevant triggers are shown in Table 6.1.

6.3.1 Electron trigger

In the electron channel, events are required to have exact one electron with $p_{\mathrm{T}} > 24$ GeV that satisfies the "medium" identification criteria and "loose" isolation requirements, as discussed in Section 5.6.2. In later data-taking periods, the p_{T} threshold is raised to 26 GeV and identification requirement is changed to "tight". In addition, events are accepted if they have exact one electron with $p_{\mathrm{T}} > 60$ GeV that satisfies the "tight" identification criteria but not require isolation. Furthermore, events are also accepted if they have exact one electron with $p_{\mathrm{T}} >$ 120-140 GeV that satisfies the "loose" identification criteria but not require isolation.

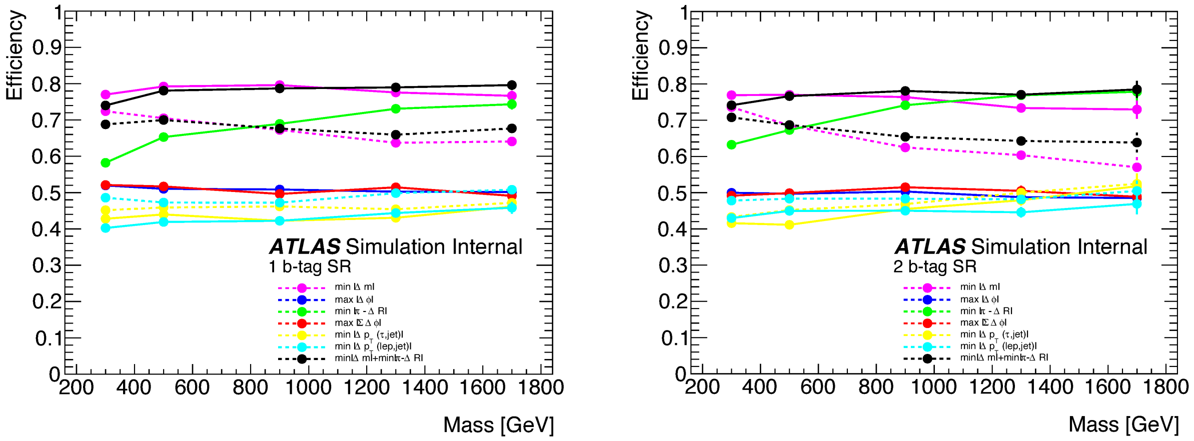

Figure 6.4: Efficiency of pairing the final state b-quarks and τ .

6.3.2 Muon trigger

In the muon channel, events are required to have exact one muon with $p_{\mathrm{T}} > 24$-26 GeV, where the threshold depends on the data-taking period. The muon needs to satisfy a ”loose” isolation criteria, as discussed in Section 5.7.2. Additionally, events are accepted if the have exact one muon with $p_{\mathrm{T}} > 50$ GeV but no other requirements.

Table 6.1: Single lepton triggers used for data taking in the $\tau_{\ell}\tau_{\mathrm{had}}$ channel.

Period	Single Electron Triggers (SET)	Single Muon Triggers (SMT)
2015	HLT_e24_lhmedium_L1EM20VH()	HLT_mu20_iloose_L1MU15
	HLT_e60_lhmedium	HLT_mu50
	HLT_e120_lhloose	HLT_mu60_0eta105_msonly
2016	HLT_e26_lhtight_nod0_ivarloose	HLT_mu26_ivarmedium
	HLT_e60_lhmedium_nod0	HLT_mu50
	HLT_e60_medium	
	HLT_e140_lhloose_nod0	
	HLT_e300_etcut	
2017 & 2018	HLT_e26_lhtight_nod0_ivarloose	HLT_mu26_ivarmedium
	HLT_e60_lhmedium_nod0	HLT_mu50
	HLT_e140_lhloose_nod0	HLT_mu60_0eta105_msonly
	HLT_e300_etcut	

6.4 Signal Region Definition

It is necessary to take into account data quality conditions before proceeding the physics analysis, which is referred to as "event cleanings". The procedure select data samples for the physics analysis. After the physics data preparation, this analysis categorized the events for the LQ search. The categorization considers the kind of particles in the final state, and the main purpose is to reject QCD multi-jet events. Therefore, the top-pair production still remains significantly in the categorized events. It is necessary to reduce the contamination of the top-pair productions. In addition to the categorization, some thresholds of each particle are proposed to realize the reduction. The cut-based selections create a signal-enriched data set which realizes the large signal acceptance and small contamination of the backgrounds. The set is referred to as "signal region" (SR).

6.4.1 Event Cleaning

The data taking efficiency of the ATLAS experiment is almost 100%, but there are some data taking period in bad conditions. Event cleaning procedure is to get rid of such data samples. All events are subjected to the standard event cleaning procedure. Data sample must be included in the Good Run Lists (GRLs) as described in Chapter 3. In addition, events with the following bad conditions are rejected; LAr noise burst and data corruption [117], Tile data corruption events [118], events affected by the SCT recovery procedure from single event upsets and incomplete events [119].

6.4.2 Cut-based selections

This analysis uses two types of cut-based selection. One is to focus on the number of reconstructed objects in the final state. This selection aims to choose events with the same topologies as the $b\tau_{\text{lep}}\ b\tau_{\text{had}}$. However, the selection doesn't have power to reduce the main backgrounds, $t\bar{t}$ processes. Therefore, as another selection, kinematic thresholds are investigated. The selections focused on the energies and the detector acceptances.

Selections based on the number of reconstructed objects

To choose $b\tau_{\text{lep}}\ b\tau_{\text{had}}$ topologies, this analysis used the following selections for leptons:

- The number of light lepton ($\ell = e$ or μ) is exactly 1,
- The number of τ_{had} is exactly 1.

In addition, the electric charge between the ℓ and τ_{had} must be opposite.

For (B-tagged) jets, this analysis also used several requirements. There are many hadronic jets in events bescause of several radiation effects, and the B-tagging efficiency is not 100%. Therefore, the requirements for those jets are defined as:

- The number of jets is more than 2,
- The number of B-tagged jets is 1 or 2.

After applying these requirements, kinematic thresholds are considered for each object.

Selections based on Kinematic properties

Although the backgrounds can be highly suppressed by tight requirements, it is important to keep the signal acceptance. Therefore, optimal thresholds were chosen for this analysis. The kinematic thresholds were applied to the light lepton, τ_{had}, (B-tagged) jets. In addition, several combination variables were used as the thresholds.

For the light lepton, the corresponding trigger threshold is used as the transverse momentum requirements. Therefore, the minimum value is 25 GeV. For the τ_{had}, $p_{\mathrm{T}} > 100$ GeV is applied, because the τ_{had} p_{T} distribution of the signal events has much entries in the higher energy region. Fig 6.5b shows the comparison, where the black colored histogram represent all of the backgrounds, and the red point represent LQ signals with m_{LQ} =1000GeV. In addition, the τ_{had} is required to exist in $|\eta| < 2.3$.

All jet candidates are required to have $p_{\mathrm{T}} > 20$ GeV within $|\eta| < 2.4$. Jets caused by detector effects, beam backgrounds and cosmic rays are eliminated. In addition to the basic requirements, this analysis requires the transverse momentum threshold to the leading jet. To define the cut value, the jet p_{T} distribution is checked as shown in Fig 6.5a. There is few signal events below the $p_{\mathrm{T}} = 60$ GeV. Therefore, it is required that the p_{T} of the leading jet is larger than 60 GeV to keep high signal acceptance.

As the other kinematic threshold, scalar sum of energies was used, which is defined as:

$$s_T \coloneqq |E_T^{\mathrm{miss}}| + |p_T^{\text{leading jet}}| + |p_T^{\text{sub-leading jet}}| + |p_T^{\tau}| + |p_T^{\ell}| \tag{6.3}$$

The leptoquarks have higher energy particles in the final state, thus the s_T tends to be distributed in higher energy region shown in Fig 6.5c. To reject the backgrounds, the s_T is above > 400 GeV. These selections are summarized in Table 6.2.

6.4.3 Validation of the SR

Here, the defined SR are evaluated how much the thresholds are effective. The number of B-tagged jets distribution with those cut-based selections is shown in Fig 6.6. This plot is normalized to an arbitrary unit to look at the shape difference, where the fake τ_{had} background is not included. The black line represents the SM backgrounds (top-pair production + other backgrounds), and the red and blue points are the leptoquark signals, m_{LQ} =1000 GeV and m_{LQ} =1500 GeV respectively. The signal-to-noise ratio ($S/\sqrt{B}$) is shown in Table 6.3. After applying the cut-based selections, the $S/\sqrt{B}$ is found to be improved.

The signal events have two b-jets, and the n_B is almost in $n_B = 1$ or $n_B = 2$ bin. When the red and blue points are compared, the peak of the n_B is depending on LQ mass. To keep high signal acceptance at the larger leptoquark mass, it is better to use both $n_B = 1$ and $n_B = 2$. The $n_B = 0$ bin also contains as many signal events as for n_B=1 and n_B=2. However, the bin contains a lot of backgrounds, thus the $S/\sqrt{B}$ becomes worse if the $n_B = 0$ is included to this analysis. On the contrary, the number of signal events in the $n_B = 3$ bin is greater than the backgrounds. Although the $S/\sqrt{B}$ is a bit good, the compositions of the backgrounds in the bin is complexed. In addition, the number of signal events too small not to affect the analysis sensitivities. Thus, events with $n_B = 3$ are decided to be excluded.

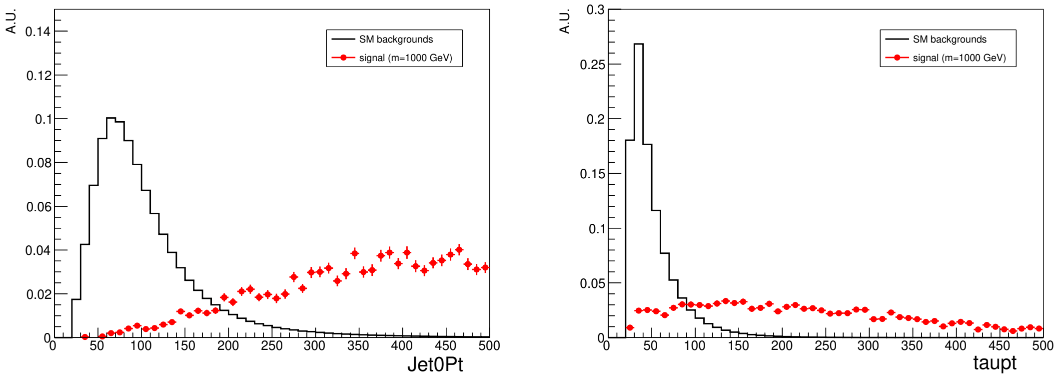

(a) Leading Jet p_T (b) Hadronic tau p_T

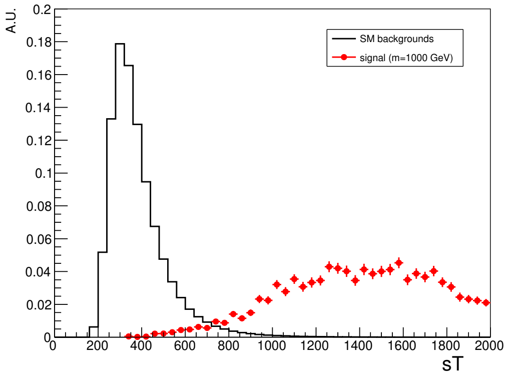

(c) Scalar sum of energies: s_T

Figure 6.5: The basic kinematics variables to decide the object-base threshold. The black line is the SM background and the red point is the LQ signal events.

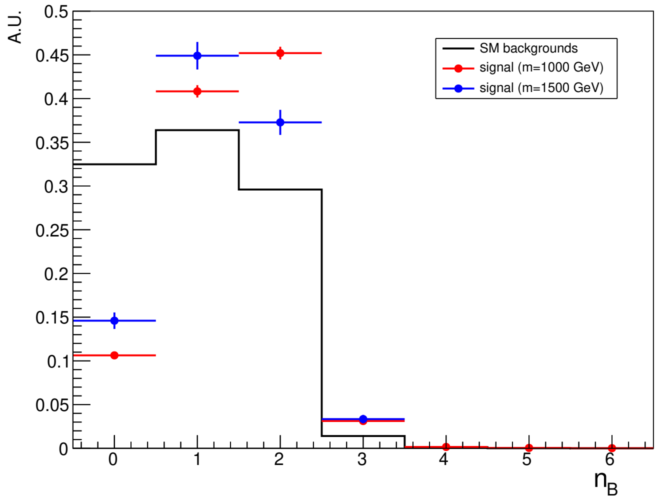

Figure 6.6: The number of B-tagged jets distribution for the standard model backgrounds (black histogram) and the reference signal (m_{LQ} =1000 GeV, red line, m_{LQ} =1500 GeV, blue line). The events with the cut-based selections are filled in the histogram.

Table 6.2: Preselection

Object	Requirement
e, μ	exact one lepton
	$p_T > 1$GeV + the trigger threshold[†,‡]
	† : $e = 24$, 26, 120-140 GeV
	‡ : $\mu = 24$, 26, 50 GeV
	e must pass the 'tight' identification
	μ must pass the 'medium' identification
τ	exact one
	$p_T > 100$ GeV
	$\lvert\eta\rvert < 2.3$
Jets	the leading jet $p_T > 60$ GeV
	the sub-leading jet $p_T > 20$ GeV
	the number of B-tagged jets = 1 or 2
Others	$s_T > 400$ GeV
	Opposite charge sign between ℓ and τ_{had}

Table 6.3: Signal-to-noise ratio in the number of B-tagged jets with m_{LQ} =1000 GeV. The "before" and "after" represent the events with/without the cut-based selections. After applying the selections, the signal-to-noise ratio is improved.

n_B	$S/\sqrt{B}$ (Before)	$S/\sqrt{B}$ (After)
0	0.016	0.093
1	0.081	0.336
2	0.099	0.413
3	0.039	0.131
4	0.009	0.023
5	0.006	0.026
6	0.021	-

Chapter 7

Statistical Treatment

In this chapter, the statistical treatment are described, which are used in the background estimation and the result computations. This chapter is widely referenced from [120].

7.1 Parameter Estimation with Profile Likelihood Function

This analysis uses a maximum-likelihood method to estimate a parameters of interest, or a signal strength factor (μ) [121]. The signal strength factor acts as a scaling to the total rate of signal events, defined as :

$$\mu := \frac{\sigma_{\text{experiment}}}{\sigma_{\text{theory}}}, \tag{7.1}$$

where the σ_{eq} is the experimental cross section of the leptoquark pair production, and the σ_{th} is the theoretical expectation cross section values. The $\mu = 0$ corresponds to the background only result, and $\mu = 1$ is the background + signal result.

For purpose of using the maximum-likelihood fit, this analysis builds a profile likelihood function by histograms. The number of entries in the ith bin from signal and background, s_i and b_i, are:

$$s_i(\boldsymbol{\theta}_s) = s_{\text{tot}} \int_{i\text{-th bin}} f_s(x;\boldsymbol{\theta}_s)dx, \tag{7.2}$$

$$b_i(\boldsymbol{\theta}_b) = b_{\text{tot}} \int_{i\text{-th bin}} f_b(x;\boldsymbol{\theta}_b)dx, \tag{7.3}$$

where the s_{tot} (b_{tot}) are the total number of signal (background) events, the $f_s(x;\boldsymbol{\theta}_s)$ ($f_b(x;\boldsymbol{\theta}_b)$) are the probability density function (PDF) of the variable x, and $\boldsymbol{\theta}_s$ ($\boldsymbol{\theta}_b$) represent parameters that characterize the shape of PDFs. The set of parameter $\boldsymbol{\theta}$ is referred to as ”nuisance parameters” (NPs) in this analysis. The NPs correspond to systematics uncertainties in this analysis, but the value is not the goal of this analysis. Therefore, the expected number of events in the i-th bin, n_i, can be written in:

$$E[n_i] = \mu s_i(\boldsymbol{\theta}_s) + b_i(\boldsymbol{\theta}_b), \tag{7.4}$$

where the parameter μ determines the number of signal events in the i-th bin. Below, the parameter set $\boldsymbol{\theta} \equiv (\boldsymbol{\theta}_s, \boldsymbol{\theta}_b, b_{\text{tot}})$ is used to denote all of the nuisance parameter. which will often be constrained by using the auxiliary measurements.

This analysis assumes that each event distributes according to Poisson probability:

$$f(x) = \frac{\lambda^x}{x!}e^{-\lambda}, \tag{7.5}$$

where λ is the expected number of events and the x is the observed number of events. Then the expected number of events in an i-th bin, λ_i, is:

$$\lambda_i = \mu s_i(\boldsymbol{\theta}) + b_i(\boldsymbol{\theta}). \tag{7.6}$$

The likelihood function is the product of Poisson probabilities for all bins:

$$L(n|\mu, \boldsymbol{\theta}) = \prod_{j=0}^{N} \frac{(\mu s_j(\boldsymbol{\theta}) + b_j(\boldsymbol{\theta}))^{n_j}}{n_j!} e^{-(\mu s_j(\boldsymbol{\theta}) + b_j(\boldsymbol{\theta}))} \times \prod_{k=0}^{M} \frac{u_k(\boldsymbol{\theta})^{m_k}}{m_k!} e^{-u_k(\boldsymbol{\theta})} \tag{7.7}$$

where the second term represents the auxiliary measurements with the expected number of events in k-th bin, m_k. In the auxiliary measurements, the signal contamination is usually removed by some kinematical cuts. Then the $u_k(\boldsymbol{\theta})$ represents the only background distributions in the measurements.

It is useful to find the minimum of the negative logarithm of the likelihood, $-\ln L(n|\mu, \boldsymbol{\theta})$, instead of the maximum of the likelihood. The most common tool for finding the minimum-likelihood estimator is `MINUIT` [122], and this analysis uses a tool wrapped it, `HistFactory` [123]. The estimators are denoted as $(\hat{\boldsymbol{\mu}}, \hat{\boldsymbol{\theta}})$, which is referred to as "best fit value".

7.1.1 Concrete Likelihood Template for Systematics

The profile likelihood is a way to include systematics uncertainties in the likelihood expression. The idea behind is that systematic uncertainties come from imperfect knowledge of parameters of the model. The systematics are included as the nuisance parameters, then the number of expected events is parameterized as :

$$\nu_{p,i}(\boldsymbol{\theta}) = n_{p,i} \times \eta_{cs}(\boldsymbol{\alpha}) \times \sigma_{csi}(\boldsymbol{\alpha}), \tag{7.8}$$

where the $\boldsymbol{\theta} = (\eta_{cs}(\boldsymbol{\alpha}), \sigma_{csi}(\boldsymbol{\alpha}))$, the $n_{c,p,i}$ is the number of events of process p in the i-th bin, and $\eta(\boldsymbol{\alpha})$ or $\sigma(\boldsymbol{\alpha})$ correspond an acceptance or a shape systematics uncertainties, respectively. The acceptance uncertainty is referred to as "`OverallSys`", which affects only the total number of events of the histogram, while the shape uncertainty is referred to as "`HistoSys`", which affects the total events and the shape of the histogram. The $\boldsymbol{\alpha}$ is a set of all of the variance of the systematics uncertainties, which is constrained by a Gaussian form:

$$\prod \mathcal{G}(\alpha_p|0,1), \tag{7.9}$$

where the α_p is the variance of the p-th systematics sources. Therefore, the profile likelihood including the systematics as the nuisance parameters in the function form is given by:

$$L(\mu, \boldsymbol{\theta}) = \prod_{i=0}^{N} \mathcal{P}(\nu_{p,i}|\mu, \boldsymbol{\theta}) \times \prod_{j \in syst} \mathcal{G}(\alpha_p|0,1). \tag{7.10}$$

7.2 Hypothesis Test

In addition to the parameter estimation in the Section 7.1, testing one or multiple hypotheses are also important in this analysis [124]. For discovering or excluding new physics hypothesis, the hypothesis test is often performed to check if a dataset is consistent with the hypothesis. The test uses two hypothesis, null hypothesis, H_0, and the alternative hypothesis, H_1. The null hypothesis describes only known processes, or the Standard Model, which is referred to as background only hypothesis in this context. The alternative hypothesis describes both background and signal process.

7.2.1 Profile Likelihood Ratio as Test Statistics

The hypothesis test needs a good test statistic to separate the H_0 and H_1. As an optimal best choice of the test statistic, the likelihood ratio is defined by the Neyman-Pearson lemma:

$$\lambda(\mu) := \frac{L(\mu, \hat{\hat{\boldsymbol{\theta}}})}{L(\hat{\mu}, \hat{\boldsymbol{\theta}})}, \tag{7.11}$$

where $\hat{\hat{\boldsymbol{\theta}}}$ is the value of $\boldsymbol{\theta}$ that maximizes L for the specified μ. The likelihood ratio is converted to a convenient test statistic form:

$$q_\mu = -2 \ln \lambda(\mu). \tag{7.12}$$

Higher value of q_μ correspond to increasing inconsistency between data and the hypothesis. The disagreement can be quantified by:

$$p_\mu = \int_{q_\mu,\mathrm{obs}}^{\infty} f(q_\mu|\mu) dq_\mu, \tag{7.13}$$

where $q_{\mu,\mathrm{obs}}$ is the value of the test statistic q_μ observed from the data and $f(q_\mu|\mu)$ denotes the PDF of q_μ under the assumption of the signal strength μ.

7.2.2 Upper limits

After observing a result which is consistent with the background hypothesis, an upper limit test is performed to compute the limit on the strength parameter μ. For the purpose, two test statistics are defined:

$$q_\mu = \begin{cases} -2 \ln \lambda(\mu) & (\hat{\mu} \leq \mu), \\ 0 & (\hat{\mu} \geq \mu). \end{cases} \tag{7.14}$$

In the upper limit test, the signal strength μ is scanned from $\hat{\mu}$ to find a threshold where the model can be excluded with 95% confidence level (CL). The confidence level is computed as a ratio of the Eq (7.14) [125]:

$$CLs := \frac{p_\mu}{p_0}. \tag{7.15}$$

When the value of the CLs is 0.05, the μ is interpreted as the upper limit. As discussed in Section 7.1, the signal strength correspond to the signal cross section. Therefore, the upper limit on the cross section can be extracted via the limit of the μ.

7.3 Asymptotic Regime

In order to use the test statistics Eq (7.13), it is necessary to know the sampling distribution of the test statistics. Therefore, in this analysis, the test statistics is performed using the asymptotic formulas based on [120]. In large statistics data samples, the distribution of the test statistic can be approximated according to Wald's theorem [126]:

$$-2\ln\lambda(\mu) = \left(\frac{\mu-\hat{\mu}}{\sigma}\right)^2 + \mathcal{O}(1/\sqrt{N}), \tag{7.16}$$

where N is the data sample size. The $\hat{\mu}$ follows a Gaussian distribution with a standard deviation σ and mean μ'. The standard deviation σ of $\hat{\mu}$ is obtained from the covariance matrix of the estimators for all the parameters, $V_{ij} = \mathrm{cov}[\hat{\theta}_i, \hat{\theta}_j]$, where the θ_i represent both μ and the nuisance parameters ($\theta_0 = \mu$). In the large sample limit, the bias of maximum-likelihood estimators is zero in general, then the inverse of the covariance matrix can be written as:

$$V_{ij}^{-1} = -E\left[\frac{\partial^2 \ln L}{\partial\theta_i \partial_j}\right], \tag{7.17}$$

where the expectation value assumes a strength parameter μ'. The asymptotic formulae needs this σ, thus the "Asimov" dataset is constructed. The approximation presented here are valid to the extent that the $\mathcal{O}(1/\sqrt{N})$ term can be neglected. A mean value of μ' gives $\hat{\mu} = \mu'$ and the test statistic is approximated as:

$$-2\ln\lambda_A(\mu) \simeq \frac{(\mu-\mu')^2}{\sigma^2}, \quad \text{with } \sigma_A^2 = \frac{(\mu-\mu')^2}{q_{\mu,A}}, \tag{7.18}$$

where the test statistic under the Asimov dataset is $q_{\mu,A} = \lambda_A(\mu)$.

7.3.1 Upper limit

Assuming the validity of the Wald's theorem [126], the test statistics can be written as:

$$q_\mu = \begin{cases} \frac{(\mu-\hat{\mu})^2}{\sigma^2} & (\hat{\mu} \le \mu), \\ 0 & (\hat{\mu} \ge \mu). \end{cases} \tag{7.19}$$

In addition, the PDF $f(q_\mu|\mu')$ is given by:

$$f(q_\mu|\mu') = \Phi\left(\frac{\mu'-\mu}{\sigma}\right)\delta(q_\mu) + \frac{1}{2}\frac{1}{\sqrt{2\pi}}\frac{1}{\sqrt{q_\mu}}\exp\left[-\frac{1}{2}\left(\sqrt{q_\mu} - \frac{\mu-\mu'}{\sigma}\right)^2\right]. \tag{7.20}$$

The cumulative distribution is

$$F(q_\mu|\mu') = \Phi(\sqrt{q_\mu} - \frac{\mu-\mu'}{\sigma}). \tag{7.21}$$

The p-value of the hypothesized μ is

$$p_\mu = 1 - F(q_\mu|\mu') = 1 - \Phi(\sqrt{q_\mu}). \tag{7.22}$$

Therefore, the upper limit on μ can be explained as :

$$\mu_{\mathrm{up}} = \hat{\mu} + \sigma\Phi^{-1}(1-\alpha). \tag{7.23}$$

Chapter 8

Background Estimation

In this chapter, the background estimation methods for this analysis are described. As discussed in Chapter 5 and Chapter 6, the final data for the leptoquark production are contaminated by the Standard Model processes, referred to as "background" processes. Although the backgrounds are modelled well by the Monte Carlo (MC) simulations, there are still room to understand the modeling.

8.1 Overview of background composition

As discussed in Section 5.8.4, due to limitation of rejection power, hadronic jets are mis-identified as tau leptons decaying into hadron, τ_{had}. This is referred to as jet-to-τ_{had} fakes, in short fake τ_{had}, here. Therefore, background processes can be divided into two categories; backgrounds with true τ_{had} or with fake τ_{had}. This section is also divided into two parts corresponding to each τ_{had} component.

8.1.1 Backgrounds with True τ_{had}

As discussed in Section 6.1, $t\bar{t}$ process is the main component of the background with true τ_{had}. However, the $t\bar{t}$ process have been already discussed in Section 6.1, the description is presented again to complement the background descriptions. In addition, other background sources are also described here.

Top-quark pair production

The $t\bar{t}$ process is the dominant background as shown in Fig 8.1, because the final state has two real b-jets and two real τ leptons.

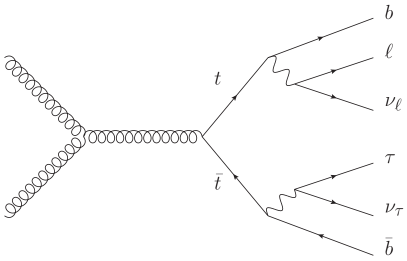

Figure 8.1: Feynman diagram of $t\bar{t}$ production.

Z+jets

Z boson with some heavy-flavor jets processes (Z+ HF) are also considered as background processes, if the Z boson decays into tau lepton pair with τ_{lep} + τ_{had} as shown in Fig 8.2. However, the cross-section of such Z+ HF process cannot be predicted well by the MC simulations, because there are some uncertainties coming from the Parton Distribution Function (PDF) and the initial state radiations. In addition, this is known problem related to the SHERPA. In this analysis, the Z+ HF MC samples are scaled by the fit, which is described in Chapter 9.

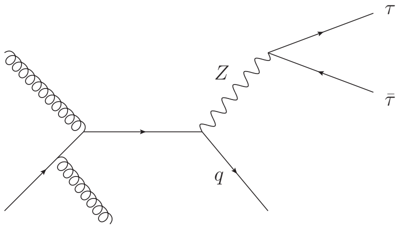

Figure 8.2: Feynman diagram of Z+ jets production.

Single-top process

These are three types of single top process, t-channel, s-channel and Wt associated production, as shown in Fig 8.3. The true τ_{had} appears via the t-quark decay mode, $t \to b + W(\to \tau_{\text{had}}\nu_\tau)$. This analysis requires exact one light lepton (e or μ), then the final data are contaminated by t- and s- channel if radiated jets fake to the lepton. On the contrary, in the Wt-channel, the primary W can decay into leptonic mode. Therefore the Wt-channel is the main backgrounds in this single-top process.

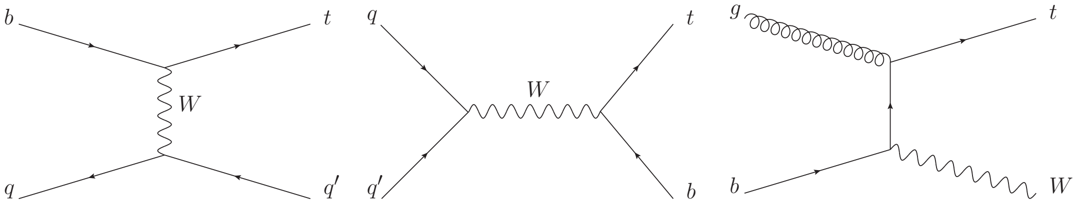

(a) t-channel (b) s-channel (c) Wt-channel

Figure 8.3: Feynman diagram of single-top productions.

W+jets

Events of W boson productions with jets is shown in Fig 8.4. The τ_{had} appears via the W boson decay, $W \to \tau_{\text{had}}\nu_\tau$. Thus, if the quark or gluon initiated jets are mis-identified as light lepton, the W+jets events remain in the signal region.

Other minor backgrounds

There are two minor backgrounds, di-boson productions (WW,ZZ and WZ) and Standard Model higgs productions.

The true τ_{had} backgrounds are well modelled by the MC simulations, except for the $t\bar{t}$ and Z+ HF backgrounds. Although the W+jets are not also well modelled, the contamination is

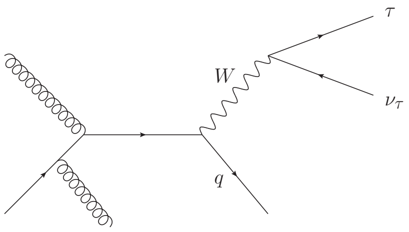

Figure 8.4: Feynman diagram of $W+$ jets production.

much smaller than the two processes. Therefore, only for the two backgrounds ($t\bar{t}$ and $Z+$ HF), each normalization factor is treated as freely floating parameter in the final fit. This meant that the normalization of $t\bar{t}$ and Z+jets backgrounds are determined by using the experimental data. For the other backgrounds, the MC simulated events are scaled by the corresponding luminosity factors.

8.1.2 Backgrounds with Fake τ_{had}

It is also necessary to estimate background events with mis-identified τ_{had} objects, which are referred to as fake τ_{had} backgrounds. As discussed in Section 5.8.4, the fake τ_{had} originate from hadronic jets. In this analysis, the dominant fake τ_{had} backgrounds also comes from $t\bar{t}$ processes, where one of the W boson decays into the leptonic mode and the other W boson decay hadronically. In addition, other backgrounds can be sources of the fake τ_{had} backgrounds. The Z + jets remains in the final data as fake τ_{had} backgrounds, if the Z decays into $\ell\ell$ and associated jets are mis-identified as τ_{had}. The single-top process remains if t decays into $bW(\ell\nu_\ell)$ and and associated jets are mis-identified as τ_{had}. Finally, the W + jets process remains if the Z decays into $\ell\nu_\ell$ and associated jets are mis-identified as τ_{had}.

These fake τ_{had} backgrounds are estimated by so-called scale factor method, which aims to correct the MC simulation by using the data samples. The method is based on the statistical treatment as discussed in Chapter 7, where the fits are performed in several control regions. The detailed descriptions are provided in Section 8.3.

8.2 $Z \to \tau\tau$ background estimation

The cross section of $Z \to \tau\tau$ production in association with heavy flavour (b, c) jets is known to be not well modelled by the SHERPA, thus this backgrounds are required to be normalised by using real data. In this analysis, the normalization factor is included as freely floating parameter in the final fit which is constrained by a control region ($Z+$ HF CR). The production probability of heavy-flavor jets is independent of the decay mode of the Z boson, thus the control region uses $Z \to \mu\mu/ee$ + heavy flavour jets. The definition of the $Z+$ HF CR are shown in Table 9.3. Since the data set with the event selections is orthogonal to the leptoquark signal enriched region, the region is fitted simultaneously with the signal region.

The composition of the control region is shown in Table 9.3, and the di-lepton invariant mass, $m_{\ell\ell}$, distribution is shown in Fig 8.5. As shown the figure, the $m_{\ell\ell}$ distribution shape is determined by the $Z \to \ell\ell$ ($\ell = e,\ \text{or}\mu$) events. Then, the shape is useful information for the likelihood fit.

Table 8.1: Definition of a control region for Z + heavy flavor jets.

Requirement	Value
Number of leptons	exactly 2 μ or 2 e
Number of b-jets	exactly 2 b-jets (DL1r 77%)
Di-lepton mass ($m_{\ell\ell}$)	75 GeV $< m_{\ell\ell} <$ 110 GeV
Di-bjets mass (m_{bb})	$m_{bb} <$ 40 GeV or $m_{bb} >$ 210 GeV

Table 8.2: Pre-fit event yields in the Z+jets CR.

Background	Yields
$Z \to ee$	20201.852 ± 160.928
$Z \to \mu\mu$	27545.478 ± 197.638
$t\bar{t}$	34985.695 ± 83.160
Total backgrounds	85001.866 ± 261.72
Data	95730

The $Z+$ HF CR is included in the final fit as the $m_{\ell\ell}$ distribution. The normalization factors are found to be :

$$F_{m_{\ell\ell}} = 1.29 \pm 0.019, \tag{8.1}$$

In addition to the binning optimization, the event selections are optimized. The $Z \to \ell\ell$ enriched region can be defined by the E_T^{miss} significance, which is defined as:

$$\mathcal{S} = \frac{|E_T^{\text{miss}}|}{\sqrt{\sum E_T}}, \tag{8.2}$$

where the $|E_T^{\text{miss}}|$ is the reconstructed magnitude of the missing transverse momentum, and the $\sqrt{\sum E_T}$ event-based approximations to the total E_T^{miss} resolution [127]. The Fig 8.6 shows this variable for ee and $\mu\mu$ channels respectively. As a test point, $m_{\ell\ell}$ distributions with $\mathcal{S} < 2.5$ are shown in Fig 8.7. The $\mathcal{S}$ can obviously reduce the $t\bar{t}$ contributions, and the $Z+$ HF CR is dominated by $Z \to \ell\ell$ events. When the $Z+$ HF CR with E_T^{miss} significance requirement is fitted, the normalisation factor is found to be :

$$F_{m_{\ell\ell},\mathcal{S}<2.5} = 1.29 \pm 0.019. \tag{8.3}$$

These normalization factor and their uncertainties are compatible between the $Z+$ HF CR with and without E_T^{miss} significance requirement. In addition, the side band region of the $Z+$ HF CR without the E_T^{miss} significance can be used as a kind of $t\bar{t}$ CR to constrain the modeling uncertainties. Thus, the E_T^{miss} significance cut is not applied to select the control region events and the definition is kept as the one described in Table 8.1.

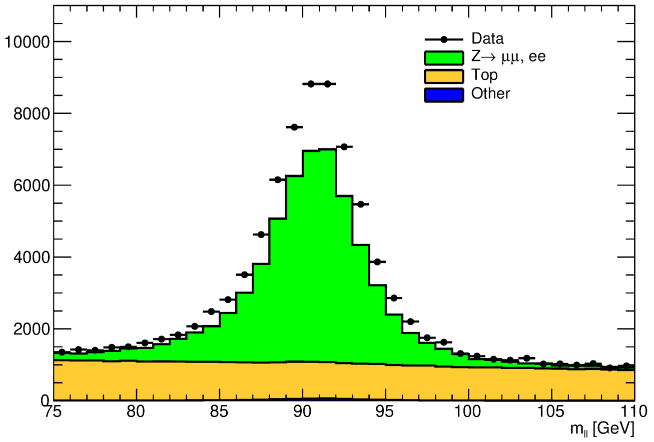

Figure 8.5: Pre-fit $m_{\ell\ell}$ distribution.

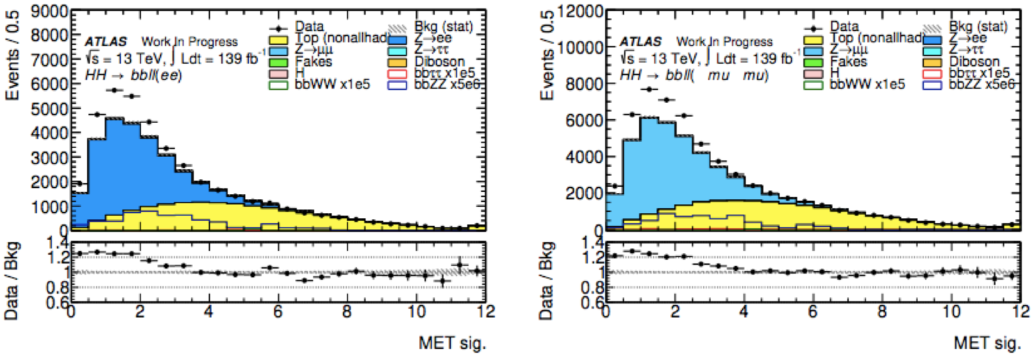

Figure 8.6: Pre-fit E_T^{miss} significance distribution in the $Z+$ HF control region.

8.3 Fake τ_{had} Background estimation

It is difficult to estimate contribution of fake τ_{had} by only using the MC simulations, because it is hard to compute enough QCD multi-jets MC samples due to the CPU limitations. This analysis used a method to provide a scale factor (SF) to estimate the fake τ_{had} background by comparing the data and MC simulation results. As discussed in Section 8.1.2, the main components of the fake backgrounds is also $t\bar{t}$ process. Although the other minor backgrounds can be the fake background sources, these contribution is very small. Therefore, this analysis aimed to evaluate the scale factors for the $t\bar{t}$ fake backgrounds. In this analysis, the dedicated regions are prepared, and are used to estimate the fake τ_{had} SF. The following sections describes the definition of regions, likelihood fit configurations and the results of the fake SF.

8.3.1 Definition of the Fit Region

For the fake τ_{had} SF calculations, this analysis prepared a region for the fit (Fit Region; FR). The fake-τ_{had} FR is prepared so that the region is not affected by LQ signal but selected the same criteria as much as possible. In addition, to avoid the QCD multi-jet fakes contaminations, only 2-tagged regions are defined as the FR. There are only two differences between the SR and

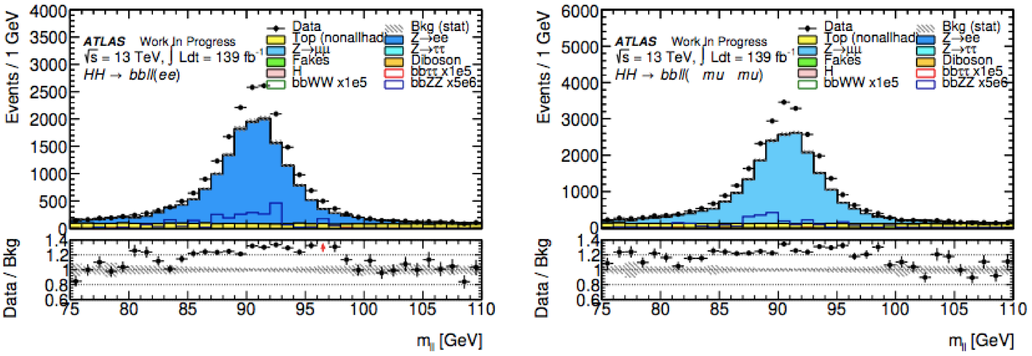

Figure 8.7: Pre-fit m_{ll} distribution in the Z+HF control region after applying E_T^{miss} significance < 2.5 cut.

the FR, which are the s_T and the E_T^{miss} criterias to divide the regions.

However, the SF is expected to be depend on the s_T and b-tagged regions. Therefore, this analysis also prepared three types of control regions (CRs) for the test of the s_T and b-tagged dependencies. The three types of regions are subset of the FR parameterized by the s_T and b-tagged requirements, as shown in Fig 8.8. The CR1 is the lower s_T region, the CR2 is the higher s_T region and the CR3s are used to evaluate the difference between b-tagged regions. The fit is performed at each CRs to calculate the corresponding SFs, and the differences are evaluated as the uncertainties on the SFs. These definitions of the regions are summarized in the Table 8.3.

These dependencies are evaluated as differences of each SF central values. This analysis defines the SFs with conservative errors to cover the s_T and b-tag dependencies explained as:

$$\text{SF} = \text{SF}_0 \pm \sqrt{\sigma_0^2 + \sigma_{s_T}^2 + \sigma_{\text{btag}}^2}, \tag{8.4}$$

where $\text{SF}_0 \pm \sigma_0$ is computed in FR, the σ_{s_T} is computed by comparisons between CR1 and CR2, and the σ_{btag} is computed by comparisons between 1-tag CR3 and 2-tag CR3.

Table 8.3: Definition of scale factor regions. The SR uses scale factors computed in the FR, which have conservative errors estimated by each CRs.

Variable	SR	FR	CR1	CR2	CR3	
B-tagged jets	1 or 2	2	2	2	1	2
p_{T} (e, μ)	p_{T} >1 GeV + trigger threshold					
$\lvert\eta\rvert$ (τ_{had})	< 2.3					
p_{T} (jets)	> 60 (40) GeV					
Charge	Opposite-sign (ℓ, τ_{had})					
p_{T} (τ_{had})	> 100 GeV	> 25 GeV				
E_T^{miss}	> 100 GeV	–	–	–	–	–
s_T	> 600 GeV	< 600 GeV	$[0, 400]$ GeV	$[400, 600]$ GeV	$[300, 600]$ GeV	$[300, 600]$ GeV

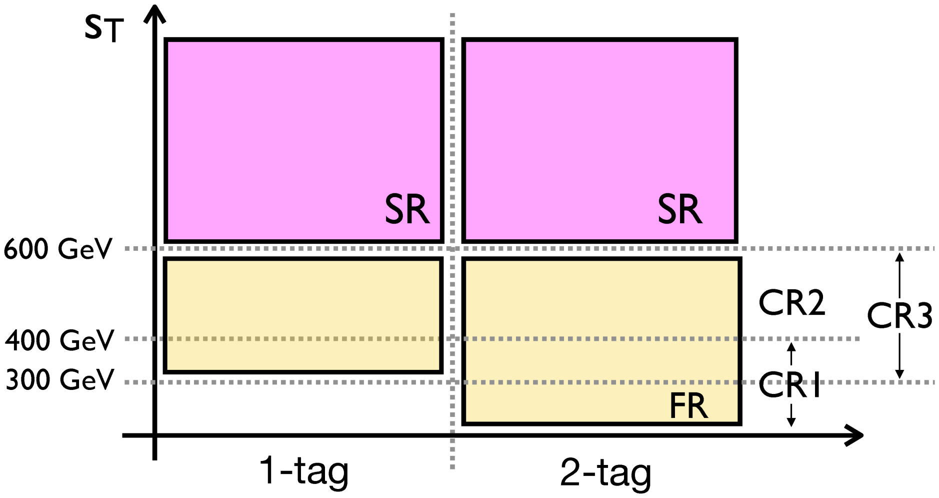

Figure 8.8: Fake scale factors are calculated in each region, FR, CR1, CR2 and CR3. The only CR3 has two types, 1-tag region and 2-tag region.

8.3.2 Fit Strategy

The fake SF aims to measure data-driven corrections by the fit at a dedicated region. At the fit stage, the modeling uncertainties of the $t\bar{t}$ true τ_{had} are also considered to compute the precise SFs. Therefore, the fit used a kinematics variable, m_T^W defined as :

$$m_T^W = \sqrt{2p_T^{\ell}E_T^{\text{miss}}(1-\cos\Delta\phi)}, \tag{8.5}$$

where the p_T^{ℓ} is the transverse momentum of the light lepton ($\ell = e$ or μ), the missing transverse energy E_T^{miss}, and the difference of each ϕ. The $t\bar{t}$ background tends to have a peak at $m_T^W \approx 80$ GeV. This variable can have a pure $t\bar{t}$ true τ_{had} background region at the higher mass, while the other regions are admixture of the fake and true τ_{had} backgrounds.

The fit strategy is based on the profile-likelihood method, as discussed in Chapter 7. The estimators are the fake τ_{had} SFs, and the $t\bar{t}$ normalization factor. In addition, the $t\bar{t}$ modeling uncertainties are also considered. All of the parameters are included as nuisance parameters of the profile-likelihood function. The fake SF is parameterized as a function of the τ_{had} transverse momentum and the number of prongs. The parametrization is summarized in Table 8.4.

Table 8.4: The fake SF is parameterized by the transverse momentum and the number of prongs (prongness). The bin width is determined by the available statistics in each bin. Especially, the last bin of the 3-prong τ_{had} begins from p_{T} =70 GeV, due to the statistics.

Prongness	p_{T} range
1-prong	[25, 35], [35, 40], [40, 45], [45, 50], [50, 55], [55, 70], [70, 100], [100, ∞]
3-prong	[25, 35], [35, 40], [40, 45], [45, 50], [50, 55], [55, 70], [70, ∞]

8.3.3 s_T Dependencies Test

The s_T dependencies of the SF are estimated by using the two regions, CR1 and CR2. To test the dependencies, each SF is computed in the corresponding regions. The differences between the central values in each bin are included as the uncertainties on the FR SFs. The SFs are shown in Fig 8.10. For the $p_{\mathrm{T}} > 100$ GeV bin of the 1-prong τ_{had}, the corresponding systematics is the differences between CR1 and CR2, $\sigma s_T = \pm 0.332$. For the $p_{\mathrm{T}} > 100$ GeV bin of the 3-prong τ_{had}, the corresponding systematics is the differences between CR1 and CR2, $\sigma s_T = \pm 0.192$.

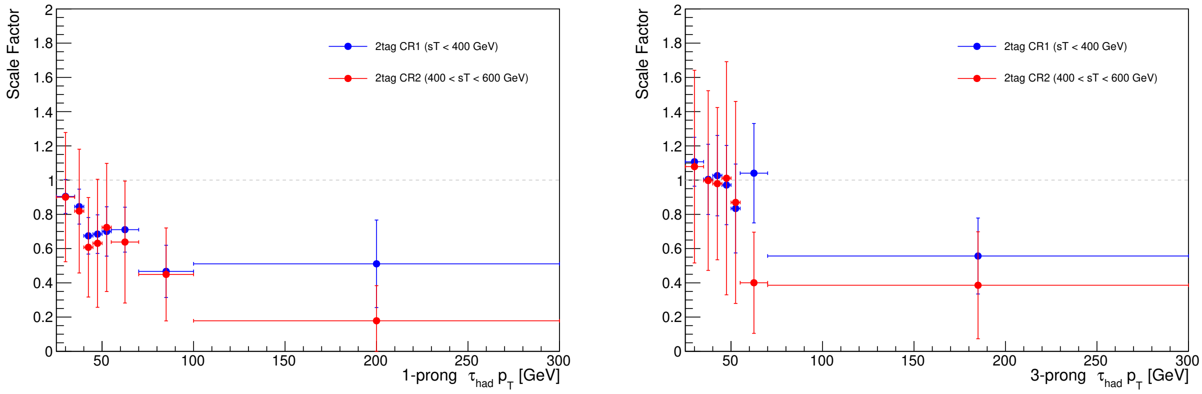

(a) Fake SF for 1 prong τ_{had}

(b) Fake SF for 3 prong τ_{had}

Figure 8.9: Fake scale factors in CR1 and CR2. The 8.10a is for the 1-prong τ_{had}, and the 8.10b is for the 3-prong τ_{had}.

8.3.4 B-tag Dependencies Test

The number of b-tagged jets dependencies of the SF are estimated by comparing of two regions, 1-tag CR3 and 2-tag CR3. To test the dependencies, each SF is computed in the corresponding regions. The differences between the central values in each bin are included as the uncertainties on the SFs. The SFs in each region are shown in Fig 8.10. For the $p_{\mathrm{T}} > 100$ GeV bin of the 1-prong τ_{had}, the corresponding systematics is the differences between 1-tag CR1 and 2-tag CR1, $\sigma_{\mathrm{btag}} = \pm 0.171$. For the $p_{\mathrm{T}} > 100$ GeV bin of the 3-prong τ_{had}, the corresponding systematics is the differences between 1-tag CR1 and 2-tag CR1, $\sigma_{\mathrm{btag}} = \pm 0.017$.

8.3.5 Fit Results

The fit was performed at the FR, and the pre-fit/post-fit results are shown in Fig 8.11-Fig 8.14. The data yields are less than the background stacked histogram in the pre-fit distributions, because the modeling of the $t\bar{t}$ true τ_{had} backgrounds are not completely [128]. After performing the fit, the backgrounds are corrected by the fake SF and the $t\bar{t}$ normalization. Therefore, the data yields matched with the corrected backgrounds in the post-fit distributions.

The SFs are shown in Fig 8.15, where the gray error band represent the conservative errors. In addition, the Fig 8.16 shows how the conservative error covers the dependencies. Each SF are within the error bands, therefore the Eq (8.4) can cover the concrete form to represent the fake scale factors for the SR. The SF is applied to the SR at the final fit stage as discussed in

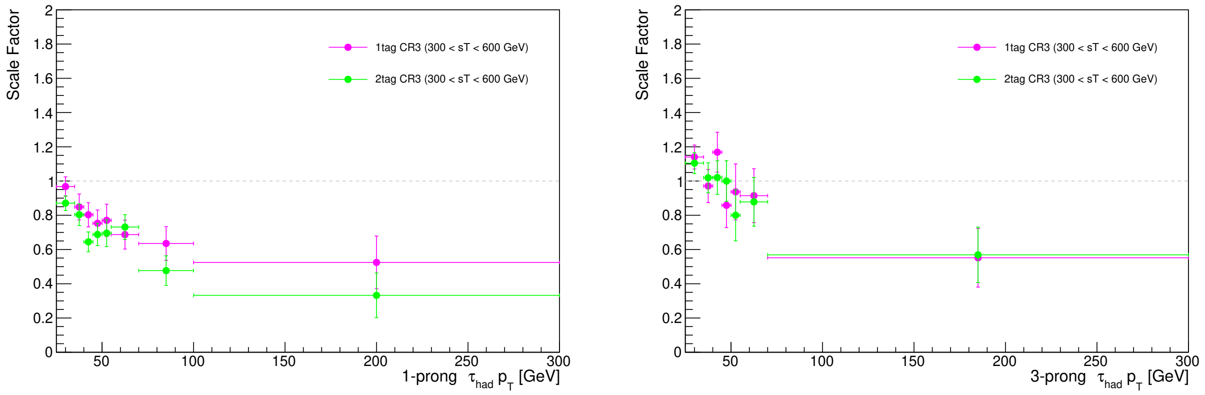

(a) Fake SF for 1 prong τ_{had}

(b) Fake SF for 3 prong τ_{had}

Figure 8.10: Fake scale factors in each region, CR^1_{sub}, CR^2_{sub}, and CR^3_{sub}. The 8.10a is for the 1-prong τ_{had}, and the 8.10b is for the 3-prong τ_{had}. The black line represents CR^1_{sub}, the red line represents CR^2_{sub} and the green represents CR^3_{sub}.

Chapter 9. In addition, the systematics uncertainties related to the s_T and b-tag dependencies are also included as the final fit.

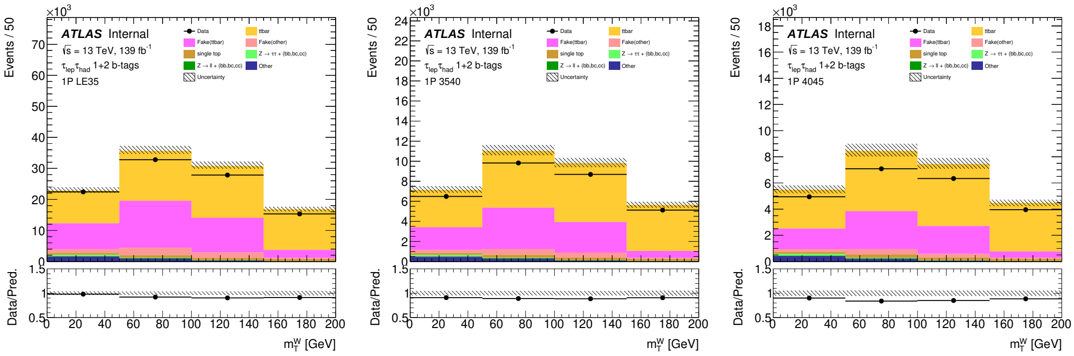

(a) 1 prong ($p_T < 35$) (b) 1 prong ($35 < p_T < 40$) (c) 1 prong ($40 < p_T < 45$)

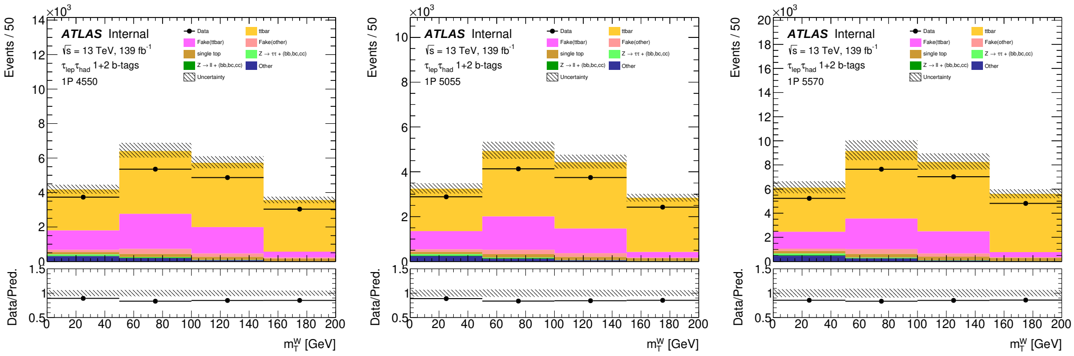

(d) 1 prong ($45 < p_T < 50$) (e) 1 prong ($50 < p_T < 55$) (f) 1 prong ($55 < p_T < 70$)

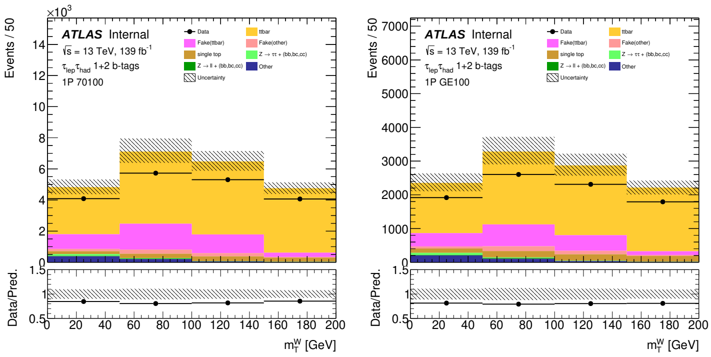

(g) 1 prong ($75 < p_T < 100$) (h) 1 prong ($100 < p_T$)

Figure 8.11: Post-fit distribution in the CR for 1-prong τ_{had}. The m_T^W distributions are parameterized as a function of τ_{had} transverse momentum, and the number of prongs. The background sources in each bin are categorized by the corresponding colors. The black point is the experimental data, and the yellow colored histogram is the $t\bar{t}$ true τ_{had} background, and the magenta colored source is $t\bar{t}$ fake τ_{had} background. Other sources are also categorized as shown in the legend of each histogram.

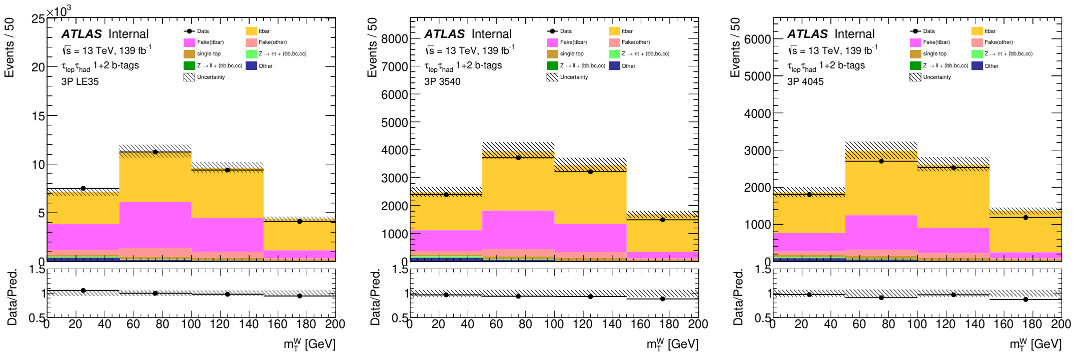

(a) 3 prong ($p_T < 35$) (b) 3 prong ($35 < p_T < 40$) (c) 3 prong ($40 < p_T < 45$)

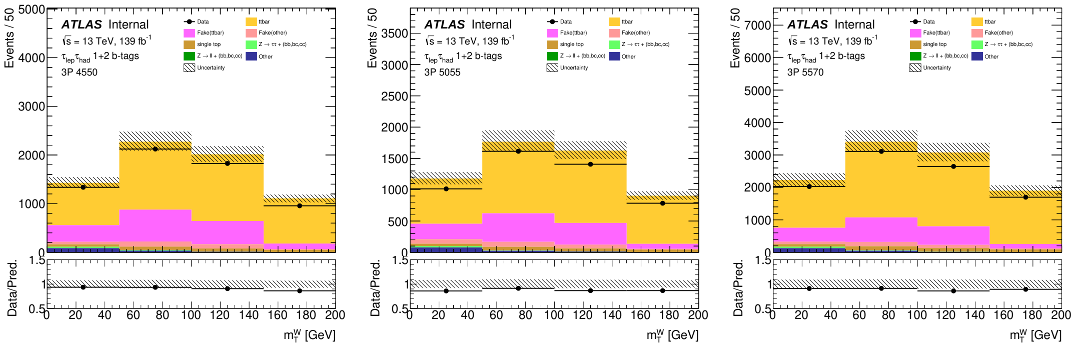

(d) 3 prong ($45 < p_T < 50$) (e) 3 prong ($50 < p_T < 55$) (f) 3 prong ($55 < p_T < 70$)

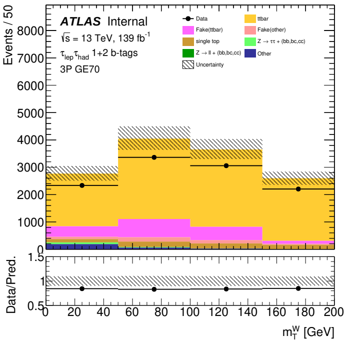

(g) 3 prong ($70 < p_T$)

Figure 8.12: Post-fit distribution in the CR for 3-prong τ_{had}. The m_T^W distributions are parameterized as a function of τ_{had} transverse momentum, and the number of prongs. The background sources in each bin are categorized by the corresponding colors. The black point is the experimental data, and the yellow colored histogram is the $t\bar{t}$ true τ_{had} background, and the magenta colored source is $t\bar{t}$ fake τ_{had} background. Other sources are also categorized as shown in the legend of each histogram.

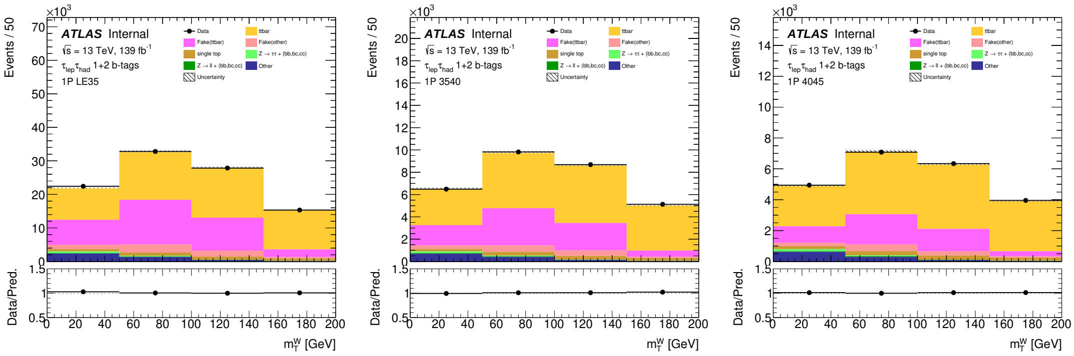

(a) 1 prong ($p_T < 35$) (b) 1 prong ($35 < p_T < 40$) (c) 1 prong ($40 < p_T < 45$)

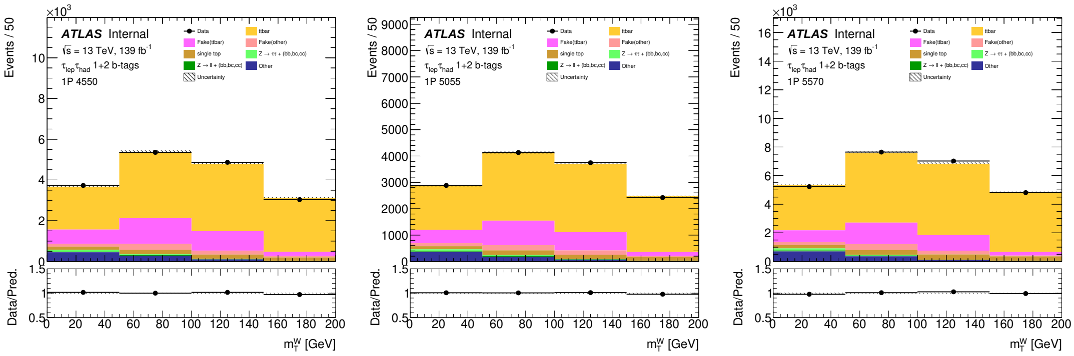

(d) 1 prong ($45 < p_T < 50$) (e) 1 prong ($50 < p_T < 55$) (f) 1 prong ($55 < p_T < 70$)

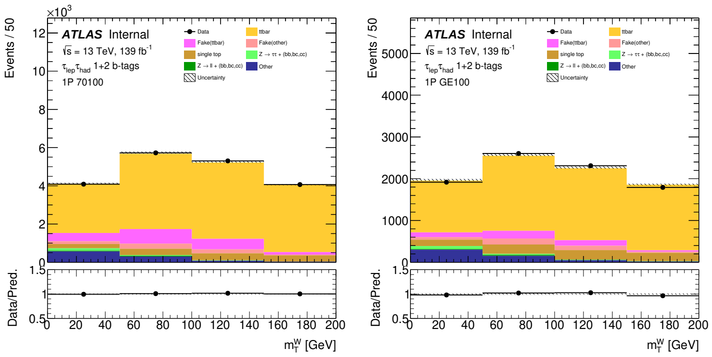

(g) 1 prong ($75 < p_T < 100$) (h) 1 prong ($100 < p_T$)

Figure 8.13: Post-fit distribution in the CR for 1-prong τ_{had}. The m_T^W distributions are parameterized as a function of τ_{had} transverse momentum, and the number of prongs. The background sources in each bin are categorized by the corresponding colors. The black point is the experimental data, and the yellow colored histogram is the $t\bar{t}$ true τ_{had} background, and the magenta colored source is $t\bar{t}$ fake τ_{had} background. Other sources are also categorized as shown in the legend of each histogram.

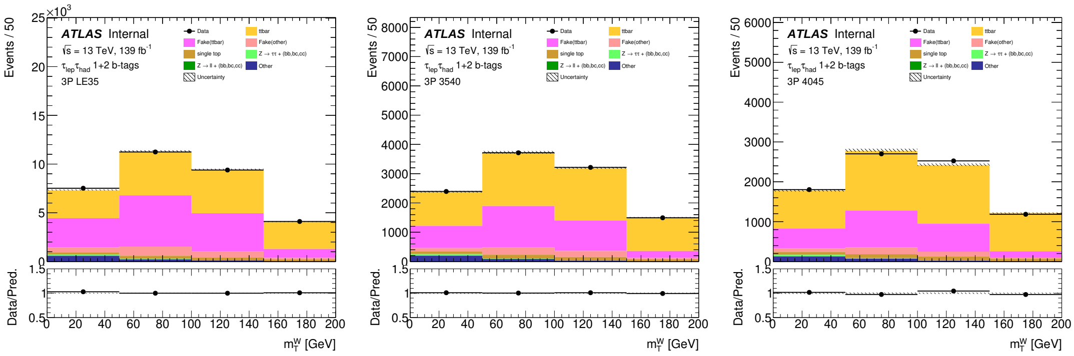

(a) 3 prong ($p_T < 35$) (b) 3 prong ($35 < p_T < 40$) (c) 3 prong ($40 < p_T < 45$)

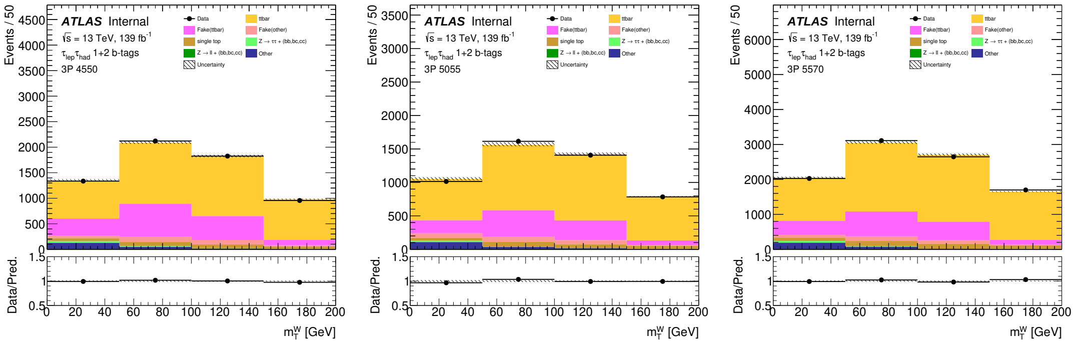

(d) 3 prong ($45 < p_T < 50$) (e) 3 prong ($50 < p_T < 55$) (f) 3 prong ($55 < p_T < 70$)

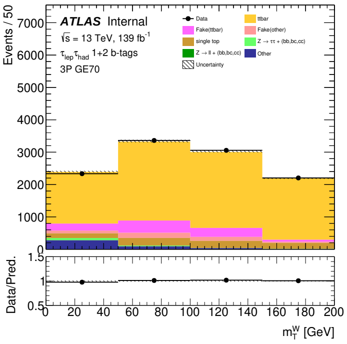

(g) 3 prong ($70 < p_T$)

Figure 8.14: Post-fit distribution in the CR for 3-prong τ_{had}. The m_T^W distributions are parameterized as a function of τ_{had} transverse momentum, and the number of prongs. The background sources in each bin are categorized by the corresponding colors. The black point is the experimental data, and the yellow colored histogram is the $t\bar{t}$ true τ_{had} background, and the magenta colored source is $t\bar{t}$ fake τ_{had} background. Other sources are also categorized as shown in the legend of each histogram.

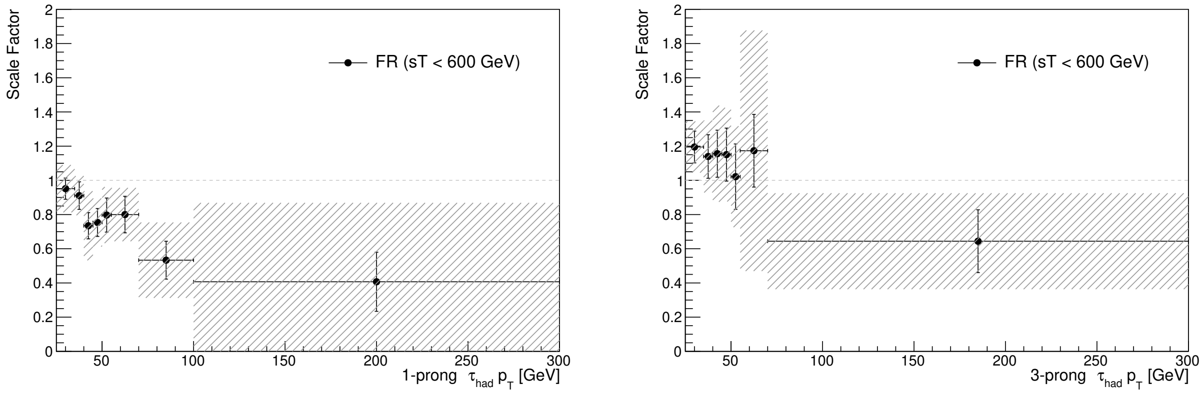

(a) Fake SF for 1 prong τ_{had} (b) Fake SF for 3 prong τ_{had}

Figure 8.15: Fake scale factors in the FR. The 8.16a is for the 1-prong τ_{had}, and the 8.16b is for the 3-prong τ_{had}. The gray error bands represent the parametrized error defined as Eq (8.4).

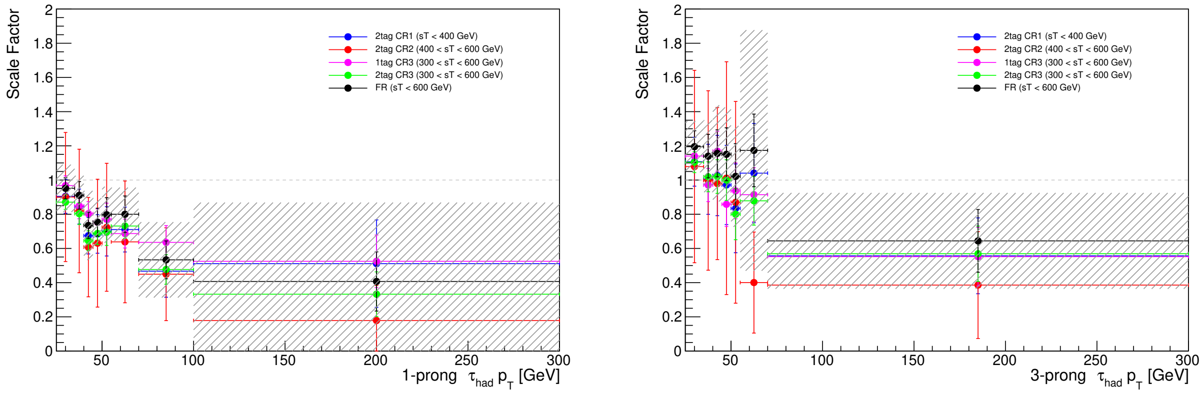

(a) Fake SF for 1 prong τ_{had} (b) Fake SF for 3 prong τ_{had}

Figure 8.16: Fake scale factors in all regions. The 8.16a is for the 1-prong τ_{had}, and the 8.16b is for the 3-prong τ_{had}. The gray error bands can cover the all dependencies, then the Eq (8.4) parametrization is conservative form.

Chapter 9

Cross-section measurements

The background estimation strategy has been already fixed as discussed in Chapter 8, the number of backgrounds are estimated with statistical treatments. The statistical results correspond to the cross section of the leptoquark production cross section. This analysis doesn't use the experimental data to obtain the upper limit on the cross section. But, expected upper limit from the obtained luminosity is estimated.

This chapter begins with the introduction of Parametric Neural Network (PNN) [14] technique to construct final discriminant variables. After calculating the PNN distribution, its binning strategy to rebin are described. The rebinned PNN scores are used to extract the upper limit according to the statistical treatment Chapter 7, and finally the interpretation are presented.

9.1 Parametric Neural Network

In particle physics, machine learning (ML) techniques are very powerful tool. One of the main usages is to reconstruct particle objects, as discussed in Chapter 5. In addition, these techniques can be used to classify the events into signals and backgrounds. This analysis decided to use the ML technique as same as the previous work [13]. The previous work used Boosted Decision Tree (BDT) [15] technique, which is one of the most commonly used techniques. The BDT method can work fine with limited statistics, therefore the high energy experiments use the technique for a long time.

The previous and current work prepared the signal MC samples for several leptoquark masses. However, there is a problem to use the BDT models with these samples. One BDT model is necessary to be trained for one mass value, therefore it is necessary to train many BDT models. In other words, it is necessary to prepare many BDT models in order to scan all of the interesting mass parameters. It may make the analysis procedure complicated, then this is one of the disadvantages for the BDT model. Furthermore, the BDT models cannot work fine at a mass value, where the BDT isn't trained for. To prepare the complete set of the BDT model for all of the interested mass values, a lot of signal MC samples are needed. However, the MC sample preparation takes a lot of CPU time, thus the only limited mass values can be used in the analysis. Therefore, the analysis decided not to use the BDT models, but to use Parametric Neural Network (PNN) [14] model. The PNN can solve the problems.

The PNN for this analysis is based on a neural networks architecture, which is also widely used in high-energy physics. The PNN is expected to work fine for any mass values in interested region even if no signal MC sample is prepared for a specific mass value. This is an important reason why the PNN is adopted in this analysis.

9.1.1 PNN architecture

The PNN can tackle a full set of related tasks with a single network, while the BDT need to tackle it with many trained models. This is done by including not only the traditional set of event-level features as input variables, but also parameters that describe the theoretical expectations such as a new particle's mass. The approach can be applied to any classification algorithm. Therefore, a single parameteric network can replace a set of the BDT models, as well as smoothly interpolate to cases where it has not been trained.

The PNN has one input layer, some hidden layers and one output layer as same as traditional neural networks. Input variables are taken as a vector of signal features, $\boldsymbol{x} = (x_1, x_2, ..., x_n)$, which is based on event-level quantities, e.g. momentum p, energy E, position information ϕ, η and so on. Furthermore, as discussed above, the PNN takes one or more theoretical parameters, $\boldsymbol{\theta}$. This is a critical difference between traditional neural networks and the PNN. The PNN use both sets of inputs, $\boldsymbol{x}$ and $\boldsymbol{\theta}$.

After training, the resulting network is then a function of these features in terms of $\boldsymbol{\theta}$, i.e. $f(\boldsymbol{x}, \boldsymbol{\theta})$. This is yielding different output values for different choices of the parameters $\boldsymbol{\theta}$ shown in Fig 9.1. The PNN last layer has one neuron which computes the output value by using sigmoid function. The output value distributes from 0 (background-like events) to 1 (signal-like events), where the value is called as the PNN score. Training and test sample give a certain PNN score, $f(\boldsymbol{x}, \boldsymbol{\theta})_{train}$ and $f(\boldsymbol{x}, \boldsymbol{\theta})_{test}$. These scores are compared to validate the training. In this analysis, the leptoquark mass is chosen as the $\boldsymbol{\theta}$.

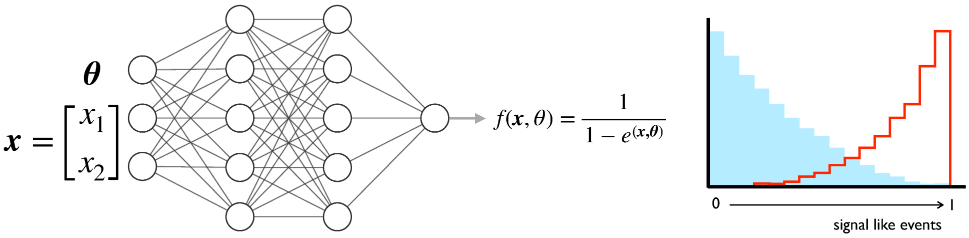

Figure 9.1: The concept overview of the PNN. The last layer outputs a certain value using sigmoid function. The PNN distributes the signal events (red colored line) around 1, while it distributes the background events (blue colored histogram) around 0. If a event distributes around 1, we found that the event could be from the signal process.

9.1.2 Input variables

Events are required to pass the selection criteria described in Sec. 6.4.2, and the MC samples are weighted by their predicted cross sections. The input variables are computed from the events, where the bτ pairs are decided by the min$|\Delta m|$ method described in Section 6.2. Here, the experimental objects are summarized in Fig 9.2. There are two b-jets, one light lepton, one hadronic jet (τ_{had}) and the E_T^{miss}. These variables distribution are shown in Fig 9.3. Each colored stuck histograms show the components of the background. On the other hand, the colored dots show the signal distribution.

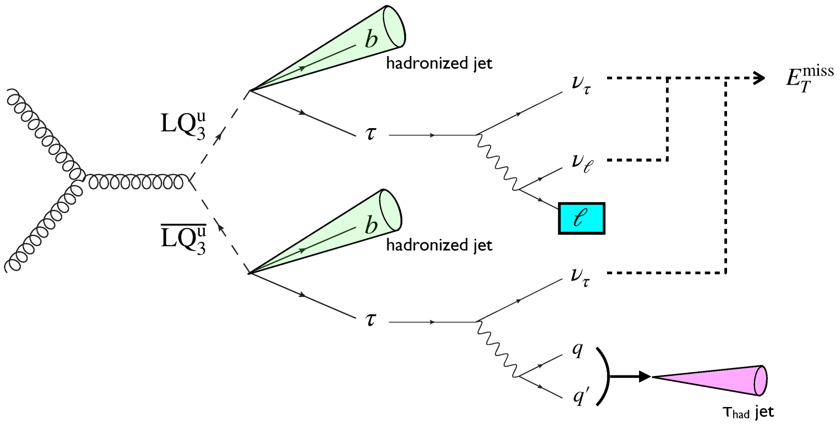

Figure 9.2: The objects used for the input variables of the PNN. In the final state, there are two jets from b-quarks, one jet from hadronic tau, one light lepton and the E_T^{miss} from neutrinos.

- **$\Delta R(\ell, \mathrm{jet})$**
  The ΔR between the light lepton and its paired jet. The LQ is very heavy particle, thus the LQ rest frame has no velocity with respect to the ATLAS laboratory frame. The b-jet and the tau lepton from a LQ could pass away back-to-back. Therefore signal events could have a peak around $\Delta R \sim 3$.

- **$\Delta\phi(\ell, E_T^{\mathrm{miss}})$**
  The opening angle between the light-lepton and the missing energy. As shown in Fig 9.3, the E_T^{miss} comes from τ_{lep} mainly. Furthermore, each object from a leptoquark is highly boosted. Therefore the opening angle of the signal events tend to be smaller than backgrounds'.

- **s_T**
  Scalar sum of the energies defined as Eq (6.3). The leptoquark events are very hard process, thus the distribution tends to the higher energy region than the backgrounds distribution.

- **E_T^{miss} centrality**
  This variable quantifies the position in ϕ of the E_T^{miss} with respect to the visible decay products of the two taus.

$$E_T^{\mathrm{miss}} \text{ Centrality} = \frac{A+B}{\sqrt{A^2+B^2}} \tag{9.1}$$

where A and B are given by:

$$A = \frac{\sin(\phi_{E_T^{\mathrm{miss}}} - \phi_\tau)}{\sin(\phi_\tau - \phi_\tau)} \tag{9.2}$$

$$B = \frac{\sin(\phi_\tau - \phi_{E_T^{\mathrm{miss}}})}{\sin(\phi_\tau - \phi_\tau)} \tag{9.3}$$

The centrality is :

  - $\sqrt{2}$ when the E_T^{miss} lies exactly between the two taus
  - 1 if the E_T^{miss} is perfectly aligned with either of taus
  - < 1 if the E_T^{miss} lies outside of the ϕ angular region defined by the two taus

  Signal events tend to have larger values of the E_T^{miss} centrality as in these cases the two taus are produced from the decay of a leptoquark and the reconstructed E_T^{miss} ϕ angle generally falls in between the two visible tau decay products.

- **$m_{\tau,\text{jet}}$, $m_{\ell,\text{jet}}$**
  The invariant mass between hadronic tau and its paired jet, and between the light lepton and its paired jet, respectively. Although the invariant mass doesn't have a good resolution, the variables can still characterize the signal events.

- **Hadronic tau p_T**
  Transverse momentum of the τ_{had}. Since the leptoquark is heavier than other SM particles, then the p_{T} tends to be larger.

9.1.3 Training of the PNN

The only $t\bar{t}$ process is used for the training as the background, because it is dominant background. The PNN has several parameters, referred to as ”hyperparameters”, to specify the network architecture. Here, the hyperparameter set is summarized in Table 9.1. The number of events per each signal sample is shown in Table 9.2. This analysis used 26 mass points, where the interesting region around 1000 GeV is divided per 50 GeV. For the backgrounds, the mass parameter is given at random within [300, 2000] GeV. In addition, the training validations are shown as the overtraining checks Appendix A.

Table 9.1: PNN hyperparameter values are used in this analysis.

Items	Optimized value
Epochs	64
Batch size	32
The number of hidden layers	3
The number of neurons per each hidden layer	32
Learning rate	0.1
Decay rate	10^{-5}

9.2 Binning Strategy

To calculate the expected cross-section of the LQ pair-production, the PNN distributions are used for a binned-likelihood fit. The raw PNN scores, however, are continuous value from 0 to 1, then it is necessary to construct histograms from the distributions, while keeping the fit stability. The binned-likelihood fit could be affected by the number of bins and the statistical

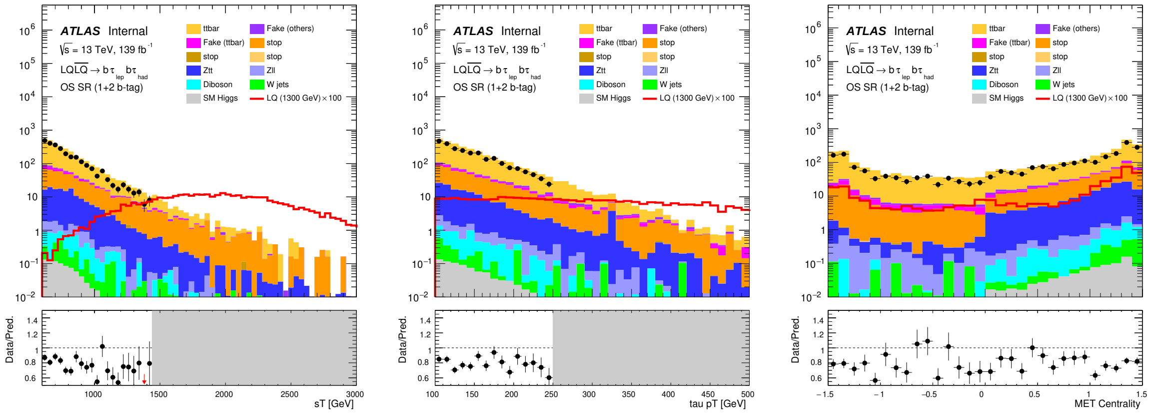

(a) s_T (b) τ_{had} pT (c) E_T^{miss} Centrality

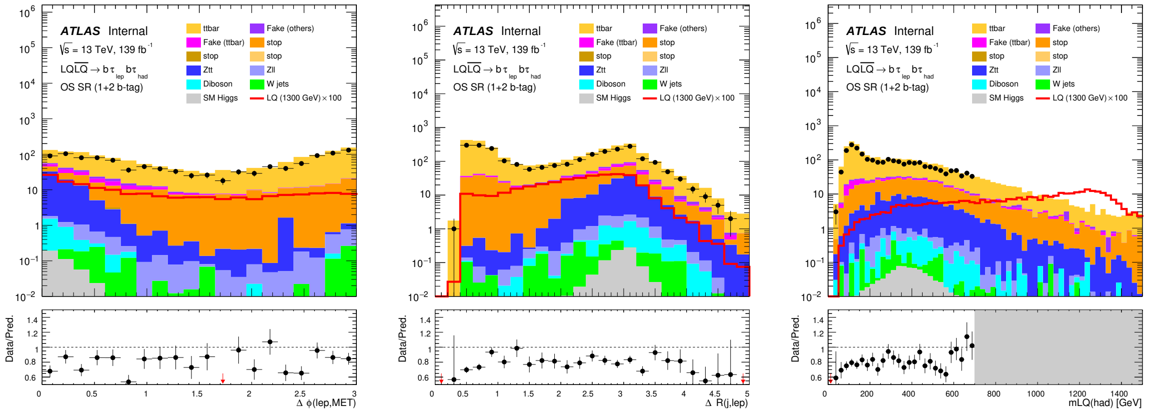

(d) $\Delta\phi$ (e) ΔR (f) m_{lep}

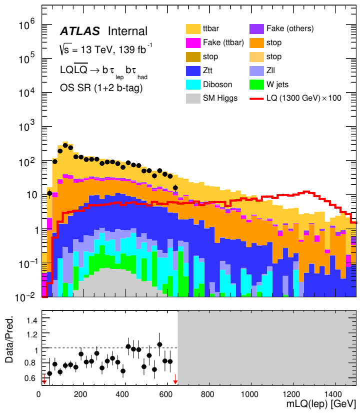

(g) m_{had}

Figure 9.3: Distribution of PNN input variables at the pre-selection level. Some variables are blined, because such higher energy regions have some discriminating power to find the signals. As conservative strategy, such signal sensitive regions are blinded.

Table 9.2: LQ τ_{lep} τ_{had} yield table as the PNN input sample.

mass(GeV)	MC raw events	sum of weight ($B = 1$)
300	7574	4.49e+04
400	8914	1.84e+04
500	32918	7.73e+03
600	12064	3.06e+03
700	12830	1.24e+03
800	12988	578
900	32709	270
950	9456	177
1000	9706	131
1050	9598	87.7
1100	9491	61.8
1150	9523	43.5
1200	9373	30.2
1250	4453	22.7
1350	2106	10.8
1400	2077	7.98
1450	2067	5.99
1500	2025	4.08
1550	1182	3.1
1600	1173	2.28
1700	8365	1.23
1800	1057	0.635
1900	1104	0.382
2000	993	0.196

flacutuations. Therefore, this analysis adopted a binning strategy which has been studied [129] to optimize the search sinsitivity.

In the binning strategy, a function Z_D is defined as :

$$Z_D(k,l) = \frac{z_s \cdot n_s(k,l)}{N_s} + \frac{z_b \cdot n_b(k,l)}{N_b}, \tag{9.4}$$

where $z_{s,b}$ are free prameters, $N_{s,b}$ are the total number of signal (background) events of the input histogram, and $n_{s,b}(k,l)$ are the number of signal (background) events from k-th bin to l-th bin of the input histogram.

Here, the number of bins of the input histogram is $N_{\text{bin}}^{\text{input}}$. The transfromation starts with a rightmost bin, $k = l = N_{\text{bin}}^{\text{input}}$. The range of the $[k,l]$ is increased by adding a bin one by one from the rightmost to the leftmost, i.e. the k is decreasing by each step. The value of $Z_D(k,l)$ is calculated at each step. When the condition $Z_D(k,l) > 1$ is fulfilled with $k = k_1$, the position is deined as the second bin boundary. All bins in the interval $[k_1, k_0]$ are merged into a single bin for the output histogram. Next, the transformation re-starts with the bin boundary, $k = l = k_1 - 1$, and repeats the sampe stems to search a next bounday, k_2. This is continued until all input bins are remapped and kN_{bin} is found, where N_{bin} is the number of bins in the output histogram.

9.2.1 Background Breakdown in the Signal Regions

The breakdown of these backgrounds are shown in Fig 9.4 as a function of the PNN score, where the fake-τ_{had} backgrounds are estimated by the MC simulation. Other mass points breakdown are also shown in Appendix B. Although the number of top-quark processes is larger than single-top process, the single-top backgrounds dominate in the higher PNN score region. The particles from the single-top processes have larger energy than the $t\bar{t}$ process, thus the single-top backgrounds tend to have PNN higher scores thant the $t\bar{t}$ processes. The number of each background source in signal region of PNN score > 0.9 is also shown in Table 9.3.

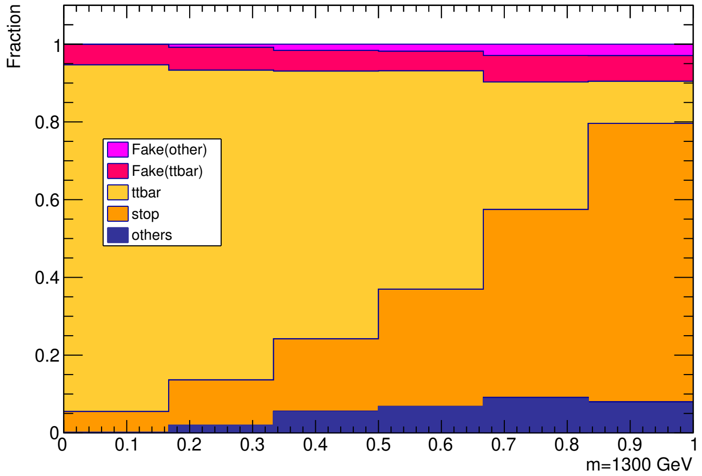

Figure 9.4: Background composition in terms of the PNN score for m_{LQ} =1300 GeV signal.

Table 9.3: The number of backgrounds in the signal region.

Background	Yields
VH	5.96
diboson(WW, WZ, ZZ)	30.30
W+Jets	28.98
Z+Jets	469.62
single top	1446.50
$t\bar{t}$	13943.66
Fakes	3722.49

9.3 Systematics Uncertainties

Systematics uncertainties in measurements other than statistical fluctuation. As discussed in Chapter 4, physics processes are simulated by the MC generators, but the modelling are not perfect. Furthermore, there are limits of the detector resolutions, thus there are also imperfect understanding of the experimental setup. In this analysis, these uncertainties are categorized as either "theoretical" or "experimental" uncetainties.

9.3.1 Theoretical Uncertainties

MC generators use some assumptions to model the perturbation QCD calculations, thus theoretical uncertainties arise from them. As discussed in Chapter 8, the dominant background is $t\bar{t}$, Z+jets and single-top process, then the theoretical uncertainties are estimated for only these three background components. For other minor backgrounds, this type of systematics are not considered.

This analysis prepared MC samples to estimate the theoretical uncertainties. The differences between nominal configuration samples and such alternative samples are included as the theoretical uncertainties in the final fit. The PNN score distributions are used to compare the samples. This analysis devided the uncertainties into two parts, normalization and shape effect. The normalization effect represents the difference of the expected number of events between nominal and alternative samples, and the shape effect represetnts the difference of the shape of the distributions. These studies are summarized in the Appendix A.

Partonic cross-section uncertainty

As discussed in Chapter 4.2.1, the total pp scattering cross section can be computed according to Eq (4.1). The third term on the right side is expanded by the strong coupling constant α_s as:

$$\hat{\sigma}^{(n)} = \alpha_s \hat{\sigma}^{(0)} + \alpha_s^2 \hat{\sigma}^{(1)} + ... + \mathcal{O}(\alpha_s^{n+1}). \tag{9.5}$$

The typical MC samples drops the higher-order tems in the Eq (9.5), such as terms beyond NNLO (α_s^3) for the NLO (α_s^2) calculation. To estimate the uncertainty, nominal MC samples are compared with alternative configuration (with respect to μ_R and μ_F) MC samples.

PDF + α_s uncertainty

There are several sources that affect the determination of PDF, and the effects are considered as uncertainty on the PDF. This analysis used `PDF4LHC15_30 PDF` set with 30 error sets [60], which is the Hessian representation [130]. The each of error setcorresponds to an eigenvector of the covariance matrix in parameter space. The PDF uncertainties are estimated by the following equation:

$$\delta^{\mathrm{PDF}}\sigma = \sqrt{\sum_{k=1}^{30} \left(\sigma^{(k)} - \sigma^{(0)}\right)^2}, \tag{9.6}$$

where $\sigma^{(k)}$ is cross-section. This value represents the contribution of each eigenvector k to the total Hessian PDF uncertainty. In addition, the α_s uncertainty is computed as

$$\delta^{\alpha_s}\sigma = \frac{\sigma(\alpha_s = 0.1195) - \sigma(\alpha_s = 0.1165)}{2}. \tag{9.7}$$

The uncertainties from PDF and α_s are combined for this analysis as follows:

$$\delta^{\mathrm{PDF}+\alpha_s}\sigma = \sqrt{(\delta^{\mathrm{PDF}}\sigma)^2 + (\delta^{\alpha_s}\sigma)^2}. \tag{9.8}$$

Modeling Uncertainties from MC generators

In addition to the caluculation of perturbation QCD, uncertainties on the modeling of the matrix element, parton showering and radiations are considered in this analysis. Alternative MC samples are prepared to be compared with the nominal configuration samples. For the matrix element, difference between POWHEG + PYTHIA 8 and MC@NLO+PYTHIA 8 are tested. For the parton showering, difference between POWHEG + PYTHIA 8 and POWHEG + HERWIG 7 are tested. For the initial- or final-state radiation, the μ_R and μ_F parameter are also tuned. The up variation estimation used μ_R and μ_F scaled by 0.5 from the default value, and the down variation estimation used μ_R and μ_F are scaled by 2 from the default value.

9.3.2 Experimental uncertainties

Experimental uncertainties are related to the detector response and the object reconstruction and identification of the various physics objects, electron, muons, τ_{had} and jets. Common tools are provided by the ATLAS combined performance groups are used to estimate these systematic uncertainties.

Luminosity

The total recorded luminosity for the physics analysis is 139 fb^{-1} during 2015-2018 data taking period. The luminosity is interpreted as the number of events, thus the uncertainty in the measurement of the total integrated luminosity affects the expected signal and background yields. So to measure the accuracy, there is a dedicated detector, LUCID-2 detector [131]. In 2015-2018, the combineded uncertainty on the integrated luminosity is 1.7%. It was applied to all of the backgrounds and signal samples.

Electrons

Uncertainties from the differences between data and simulation are considered. This systematics are related to the identification and resonstruction efficiencies measured by other dedicated analysis [107] . This analysis consider four types of uncertainties on the reconstructed electron objects about the efficiencies of trigger, reconstruction, identification and isolation. All these uncertainties are summarized in Table B.7. The four types of uncertainties are measured using the $Z \to \ell\ell$ and $J/\Psi \to \ell\ell$ events for the tag and probe method.

Muons

Uncertainties from the differences between data and simulation are considered. This systematics are related to the identification and resonstruction efficiencies measured by other dedicated analysis [132]. All these uncertainties are summarized in Table B.4. Same types of uncertainties as electrons' are measured using the $Z \to \ell\ell$ and $J/\Psi \to \ell\ell$ events for the tag and probe method.

Taus

There are five types of uncertainties on the reconstructed τ_{had} objects about the efficiencies of the trigger, reconstruction, identification, energy scale (TES), and electron veto. This analysis used single lepton (e or μ) triggers, thus the uncertainties on the triggers are not taken into account. All these uncertainties are summarized in Table B.5. The uncertainties have been evaluated using each dedicated MC simulation samples with defferent configurations.

The uncertainties on the reconstruction efficiency are summarized in Fig 9.5. The variations is found to be uniform along η and the sum of all contributions is in the range between 2% and 4.5%. The main sources come from pile-up effect and the inner detector material. The former affects the TV association algorithm (Section 5.8.2), because the probability of incorrectly identifications depends on the amount of interactions reconstructed in the event as shown in Fig 5.16. The latter affects directly the track classification stage, as the number of reconstructed conversion tracks and the efficiency to reconstruct pion tracks can both be affected by the amount of detector material.

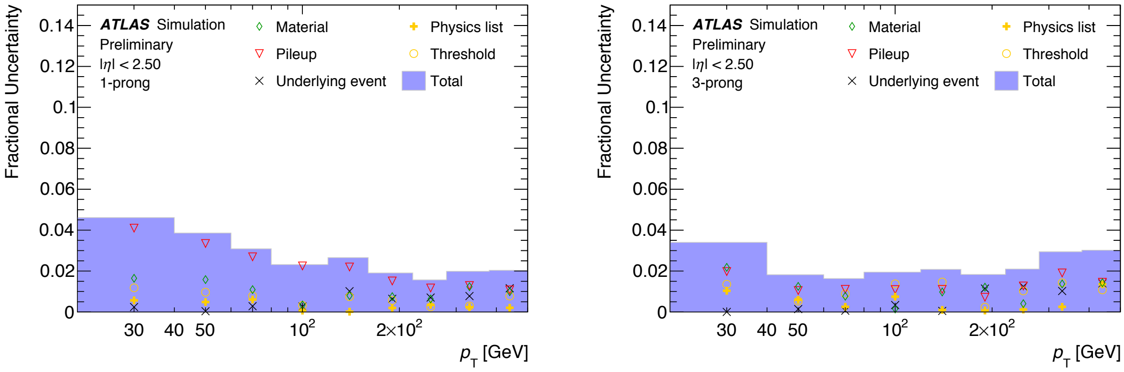

Figure 9.5: Relative systematic uncertainties on the efficiency for reconstructing the same number of tracks as the number of charged decay products of the tau lepton as a function of τ_{had} p_{T} [133].

The uncertainties on the tau identification efficiency are summarized in Fig 9.6 for the $|\eta| < 1.37$ region as an example. At large p_{T} range ($>$ 100 GeV), the pile-up uncertainty dominates. Especially for 1-prong decays, the detector material affects the identification efficiency. This is mainly due the effect of the additional material on the impact parameter resolution.

The uncertainties on the tau energy scale are summarized in Fig 9.7. For $p_{\mathrm{T}} > 100$ GeV region, the detector responce mainly affect the uncertainties.

The uncertainties on the discrimination against electrons are summarized in Fig 9.8. For p_{T} $>$ 100 GeV, the uncertainties are below 1% in different η regions.

Jets

As explained in Section 5.4.4, the measured energy of jets are scaled to restore the energy of quark/gluon level. Jets are calibrated according to the steps described in [2]. Uncertainty on this calibration is referred to as the jet energy scale (JES) uncertainty, or JES. Fig 9.9 shows the total JES uncertainty as a function of the p_{T} of the jet. The uncertainty is largest at low

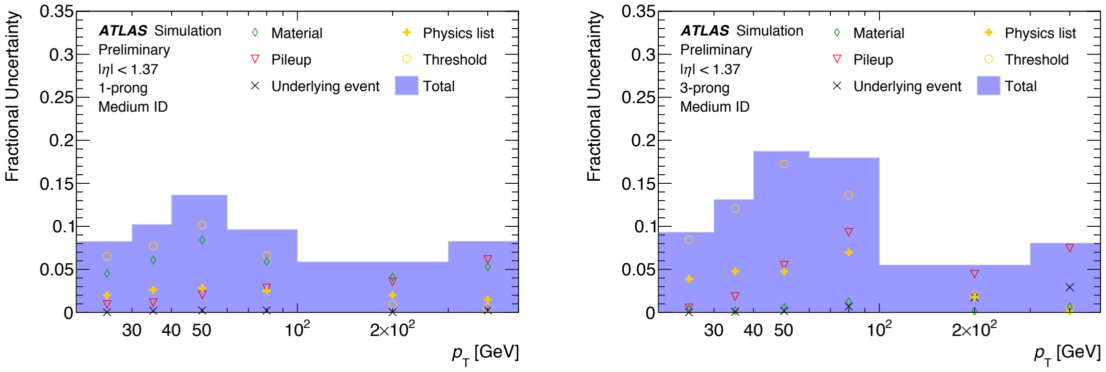

Figure 9.6: Relative systematic uncertainty on the efficiency for the Medium working point of τ_{had} identification as a function of the τ_{had} p_{T}, for 1-track (Left) and 3-track (Right) τ_{had} candidates in the central $|\eta| < 1.37$ region [133]. The different sources of systematics uncertainties are listed in the legend, the grey area is the square sum of the individual contribution.

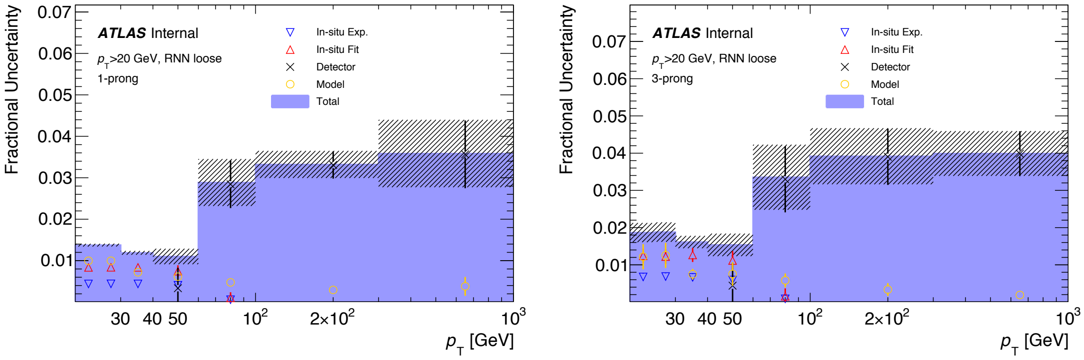

Figure 9.7: Tau energy scale uncertainties [133].

p_{T}: 4.5% at 20 GeV, and decreasing to 1% at 200 GeV. In higher p_{T} region, the uncertainty ries again due to the statistical unceratintins related to the calibration at the final step.

The uncertainty is constant as a function of η and reaches a maximum of 2.5% for the most high-η jets. A sharp feature can be seen in the region $2.0 < |\eta| < 2.6$ due to the nonclosure uncertainty of the η-intercalibration, which corrects the average response of high-η jets to that of well-measured low-η jets responces.

Jet Energy Resolution

Precise konwledge of the jet energy resolution (JER) is important in the measurements of the jets, which is measured in the dijet system [134]. The jet energy resolution can be parametrized by a functional form analogy of calorimeter resolutions as:

$$\frac{\sigma(p_T)}{p_T} = \frac{N}{p_T} \oplus \frac{S}{\sqrt{p_T}} \oplus C, \tag{9.9}$$

where N, S and C is the noise, stochastic, and constant term. The N term represents the contribution of the detector noise to the measruement or pile-up effect. The S term represents the limiting term in the resolution up to several hudred GeV in jet p_{T}. The C term represents

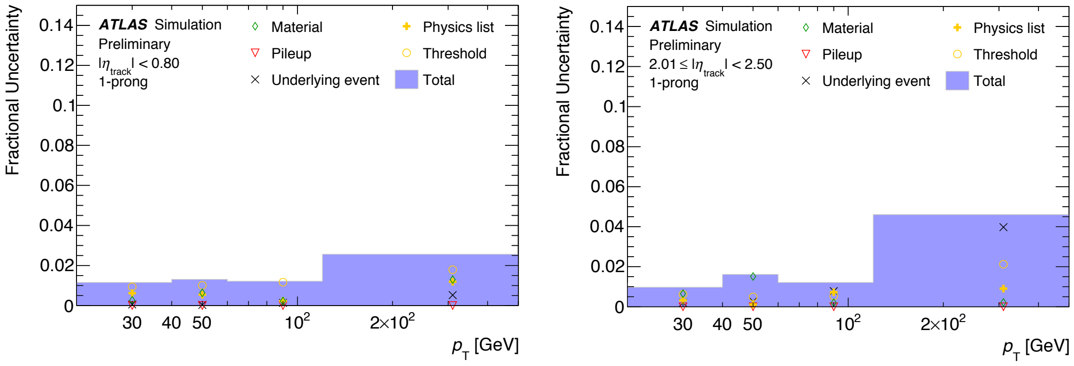

Figure 9.8: Relative systematic uncertainties on the effiency of the $\tau_{\text{had}} - e$ discrimination for 1-track τ_{had} candidate as a function of the p_{T} for difeerent η ranges of the track direction [133].

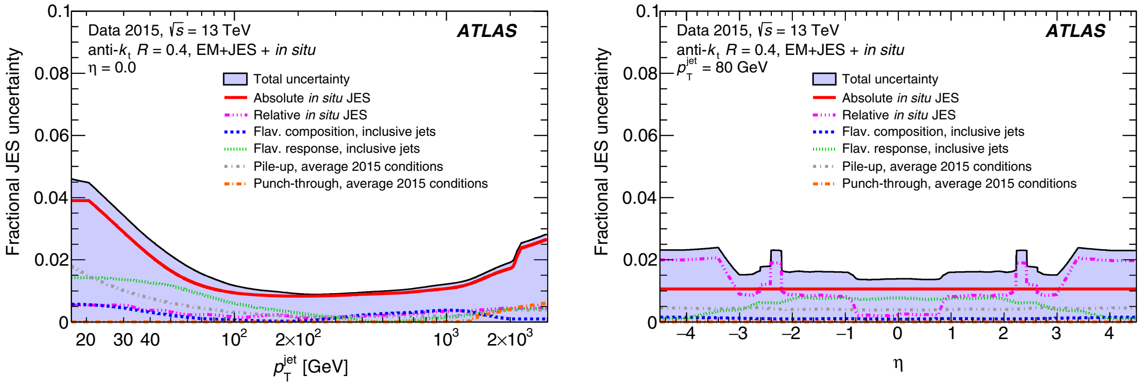

Figure 9.9: Combined uncertainty in the JES of fully calibrated jets as a function of jet p_{T} at $\eta = 0$ (left), and η at $p_{\text{T}} = 80$ GeV (right) [100].

fluctuations of the jet energy depositios. Fig 9.10 shows the absolute uncertainty on the JER as a function of jet p_{T}. For the low p_{T} jet, the N term is largest uncertainty source, while for the high p_{T} jet the largest uncertainty comes from the in-situ measurements.

Uncertainties on the flavor tagging efficiency are also important, because this analysis used the number of b-jets for the event selection. This analysis considered the uncertainties on the tagging efficiency and mis-tag (incorrect tagging) efficiency. MC-to-data scale factors and corresponding systematic uncertainties are divided into several components based on several measurements [135]. The typical size of uncertainty is order of 2 to 10 % and 20 to 50 % for b-jets and light-flavour jets, respectively.

9.3.3 Systematics Effects

All the theoretical and experimantal uncertainties are summarized in Appendix B. This analysis uses the PNN score shapes for the final fit, where the lower region can constraint the background distribution and the higher score region can have the sensitivitiy for the leptoquark signal. Then, the analysis sensitivity is affected by the last bin uncertainties. The follwing discussion summarizes the systematis effect for the last bin. In the theoretical unertainties of the $t\bar{t}$ process, the ISR shape difference has the biggest effect, $+1\sigma = 70\%$. In the theoretical unertainties

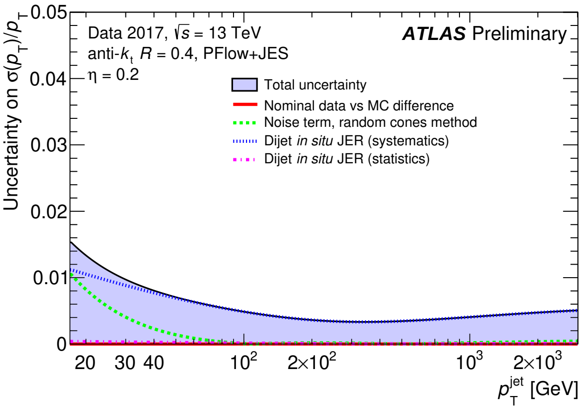

Figure 9.10: Absolute uncertainty on the relative JER as a function of jet p_T [134].

of the single-top process, the Wt interference shape difference has the biggest effect, $+1\sigma = 98.1\%$. In the experimental uncertainties, the almost source have less than 1% effect, but the `TAUS_TRUEHADTAU_EFF_RNNID_HIGHPT` has $1\sigma = 2\%$ effect.

9.4 Event yields and PNN score distributions

The PNN score distributions are shown in Fig 9.11-Fig 9.12 especially for several mass points, which is transformed according to the strategy discussed in Section 9.2. This analysis sensitivitiy depends on the around ightmost bins, therefore a blind analysis technique was adopted to hide such regions to avoid a bias [136]. In this analysis, the higher PNN score region with 85% signal events are blinded from right to left side as a conservative strategy. In addition to the distributions, this analysis also checked the fit validation plots as shown in Appendix D.

9.5 Expected Cross Section Upper Limit

The expected exclusion limits are calculated using the simulation normalized to the integrated luminosity of $L = 139\text{fb}^{-1}$. The expected limit for the $B = 1$ is shown in Fig 9.13. The blue colored line is the theoretical expecation cross section values, while the black solid line is the result. The intersection of two lines is $m_{\text{LQ}} = 1360$ GeV, which is the expected lower mass limit with 139 fb^{-1} data.

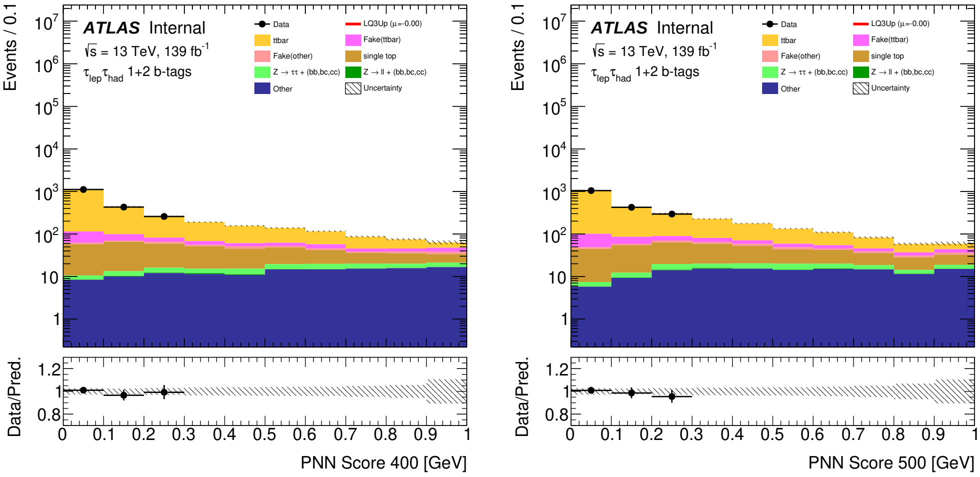

(a) m_{LQ} =400 GeV (b) m_{LQ} =500 GeV

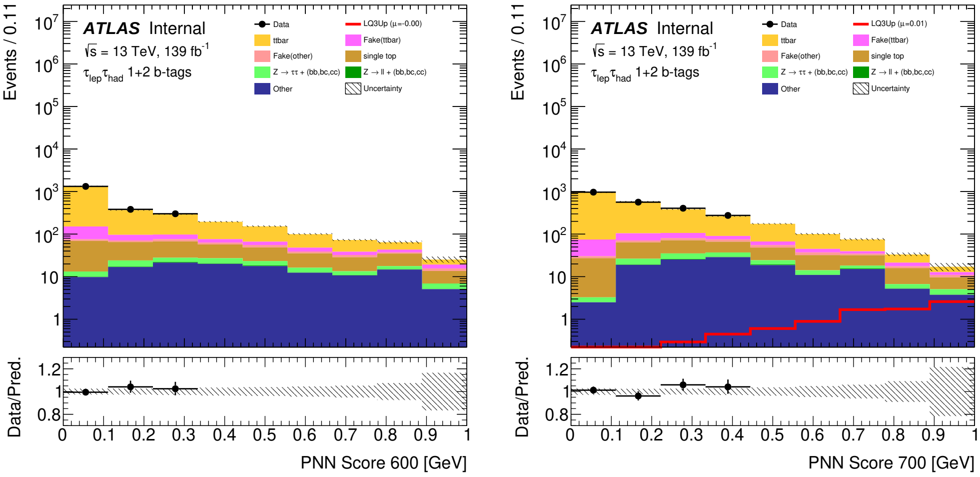

(c) m_{LQ} =600 GeV (d) m_{LQ} =700 GeV

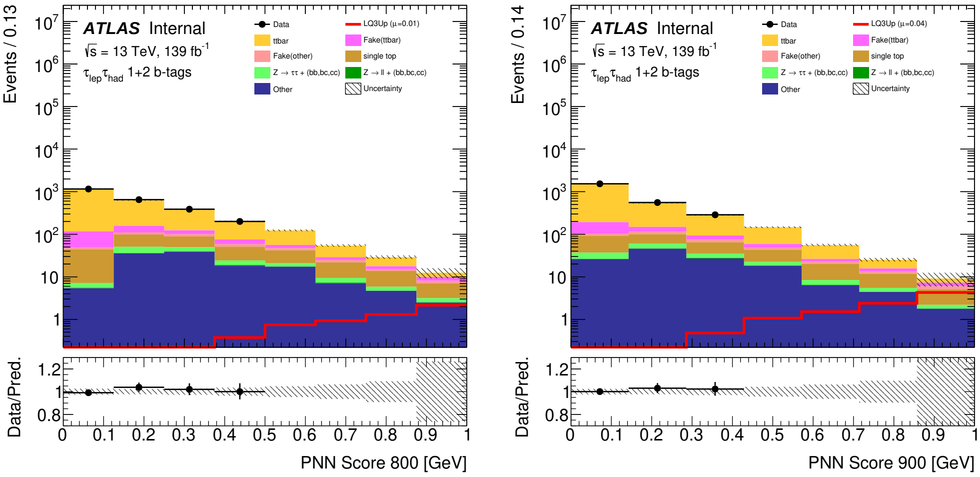

(e) m_{LQ} =800 GeV (f) m_{LQ} =900 GeV

Figure 9.11: PNN score diretributions for 400, 500, 600, 700, 800 and 900 GeV leptoquark masses. The blind strategy was performed to hide the data points from the right side.

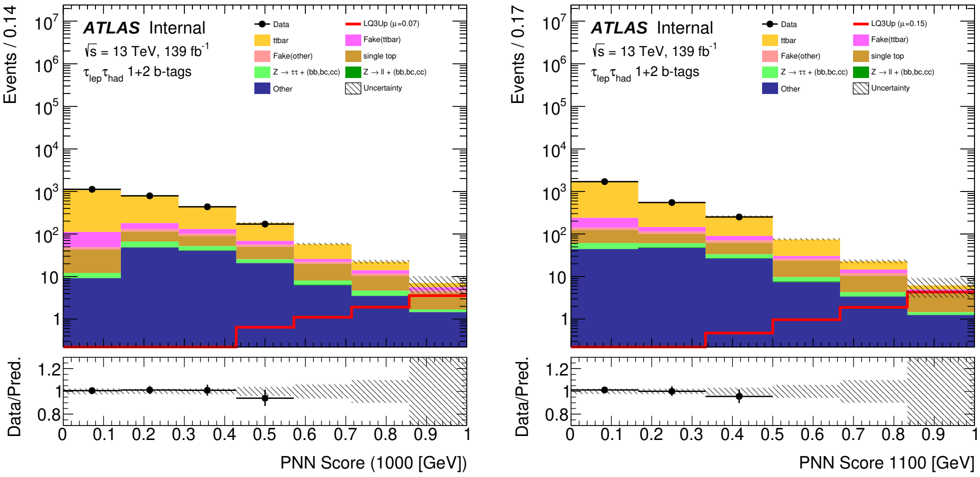

(a) m_{LQ} =1000 GeV (b) m_{LQ} =1100 GeV

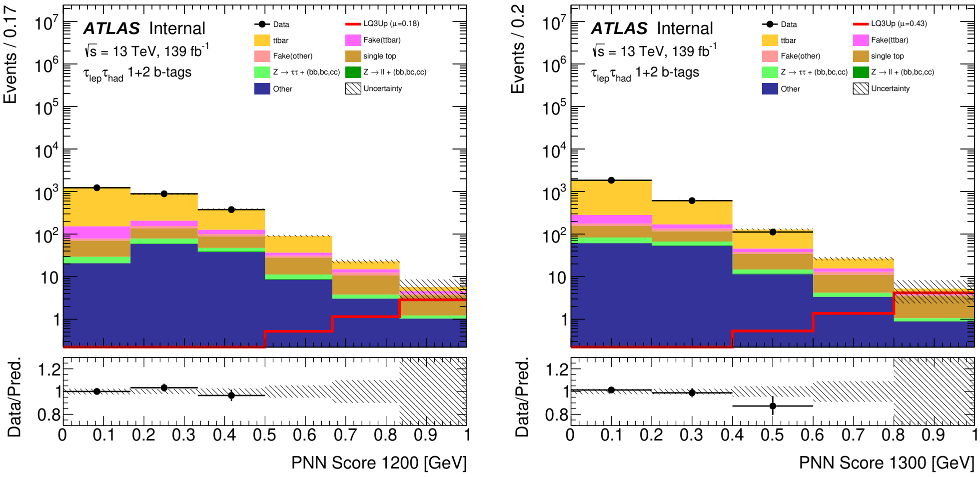

(c) m_{LQ} =1200 GeV (d) m_{LQ} =1300 GeV

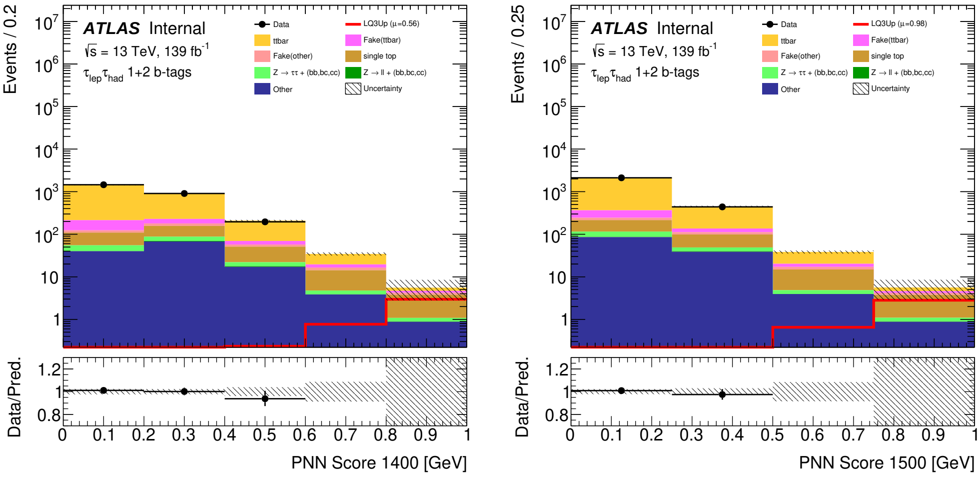

(e) m_{LQ} =1400 GeV (f) m_{LQ} =1500 GeV

Figure 9.12: PNN score diretributions for 1000, 1100, 1200, 1300, 1400 and 1500 GeV. The blind strategy was performed to hide the data points from the right side.

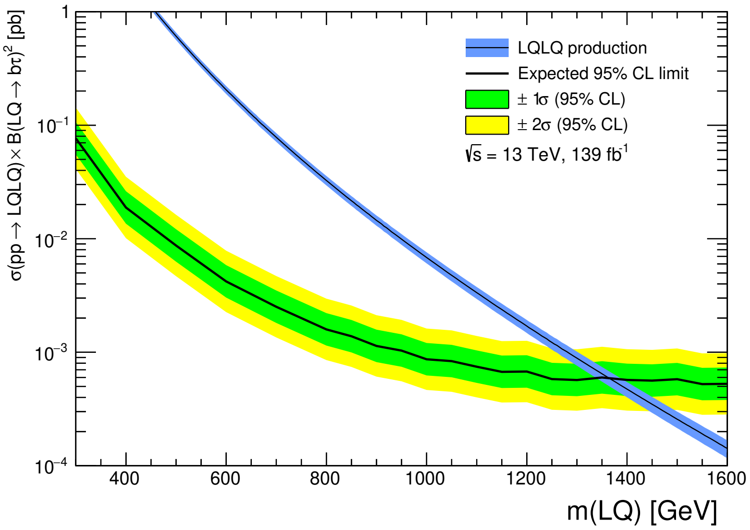

Figure 9.13: Expected exclusion (95% CL) for the $B = 1$ leptoquark. The blue line is the theroretical expectation, while the black line is the expected limit.

Chapter 10

Conclusion

This thesis presents the third generation scalar leptoquark search using *pp* collision at $\sqrt{s} = 13$ TeV with the ATLAS detector. The data samples are the integrated luminosity 139 fb^{-1} collected in 2015-2018 (Run-2) period. Although the leptoquark is expected to exist in the higher energy region with respect to the Standard Model processes, there are a lot of irreducible processes, referred to as backgrounds. Therefore, to reduce the contamination and extract the signal events, a machine learning technique, Parameterized Neural Network (PNN), is introduced. The improvement is one of the big improvements with respect to the previous work. The PNN technique can improve the analysis sensitivities, while making the analysis procedure simple.

This thesis reported the improved candidate of the analysis strategy by using the Run-2 data set. When the reported strategy is performed, the exclusion limit for the target leptoquark model at 95% confidence level can be calculated, and exclude up to 1.36 TeV by this analysis strategy. This expected analysis sensitivity for the leptoquark is the best in the world.

Acknowledgements

I had a very productive five years of master and doctoral course in Kobe University. I learned and experienced a lot of foundations and applications about the high-energy frontier in the particle physics. I would not have completed this thesis without supports from many colleagues.

I would like to express my gratitude to the staffs of Kobe University for helping my research activities. I am deeply grateful to Prof. Hisaya Kurashige for all the comments and suggestions for putting together the work into the thesis. He taught me a lot of things from the basics of particle physics, and his ideas and advice led me to the right direction to complete the work throughout my undergraduates. I am also grateful to Prof. Yuji Yamazaki for the supervision and discussion, and his sharp opinion always moved forward my work. I also learned various programming knowledge and computing techniques from Dr. Junpei Maeda, and these advice proceeded the physics analysis. I am also appreciate to Prof. Atsuhiko Ochi for giving me advice from the several points of view. They helped me to accelerate my work, and I finished to write the thesis with their supports.

I would appreciate to the member of ATLAS HH and LQ group and the AJ WG1 Tau team. Prof. Allison Mccarn Deiana and Prof. Tatjana Lenz gave a lot of suggestions for the leptoquark analysis to establish the strategy. Prof. Yasuyuki Okumura is a wonderful expert of the analysis, and gave me a lot of useful comments. I have greatly benefited from his advice. Dr. Soshi Tsuno gave insightful comments and suggestions about the tau physics, and my presentation of JPS conference was very successful with his supports. I also learned a lot of thins how to proceed the research from Dr. Tatsuya Masubuchi and Dr. Yuji Enari. I learned a lot of things about not only the tau particles but also analysis techniques from their comments and advice. In addition, I received generous support from Dr. Tomoya Iizawa, who is a main analyzer of the leptoquark analysis. He helped me many times by not only Skype but also face-to-face discussions. I believe the analysis would not have been completed without his supports.

I would like to extend my appreciations to all the members of ATLAS Japan group and TGC trigger group, because I learned a lot of things how to analyze the data and simulations. Their supports were essential for my research activities.

I would also like to thank to all friends in CERN. My research life is also supported by them; Yuta Okazaki, Tomimi Kawaguchi, Rena Wakasa, Naoki Yamaguchi and Nobuo Matsuzawa. They started working at the same time, and I believe I could survive on a long stay at CERN with their existence. In addition to them, Hiroaki Hibi, who is my junior coworker in Kobe University, lectured me how to enjoy alcohol at CERN. His advice made me grow a lot, and I acquired new skills for the drinking party. I had interesting experiences, thanks to them and other senior colleagues.

Finally, I would like to express me deepest thanks to my parents for allowing me to challenge anything I wished to do. Their supports have always encouraged me to overcome difficult items. I could not spend my research life without their supports.

Appendix A

PNN Score Validations

A Overtraining Checks

The PNN classifiers are trained by using the hyperparameter set as shown in Section 9.1. To check the training status, this section compares the PNN score distributions of test and training samples. The test and training sample distributions are the same shape, thus this check indicates there is no overtraining effects.

B Breakdown

This section shows the background breakdown for all of the mass point. The PNN scores are rebinned according to the Section 9.2. Each color represents the types of the background sources.

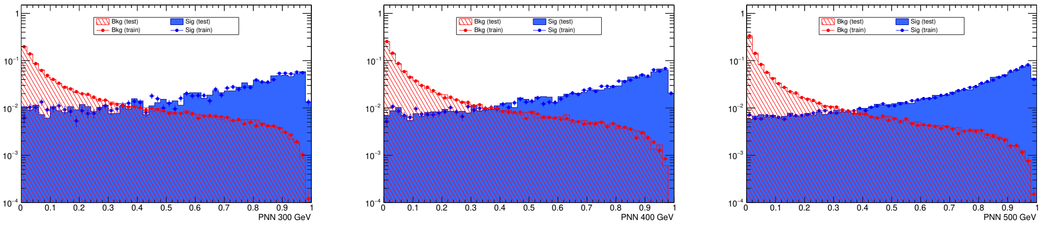

(a) m = 300 GeV (b) m = 400 GeV (c) m = 500 GeV

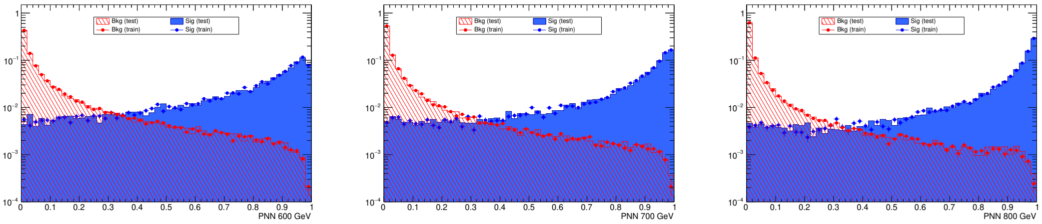

(d) m = 600 GeV (e) m = 700 GeV (f) m = 800 GeV

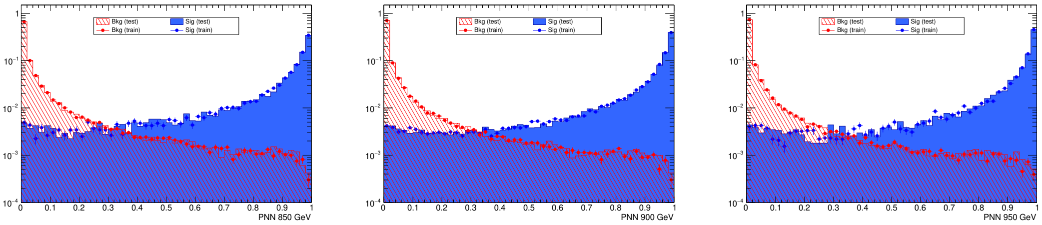

(g) m = 850 GeV (h) m = 900 GeV (i) m = 950 GeV

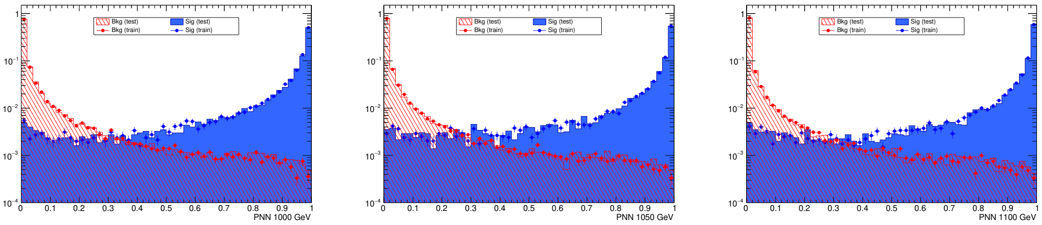

(j) m = 1000 GeV (k) m = 1050 GeV (l) m = 1100 GeV

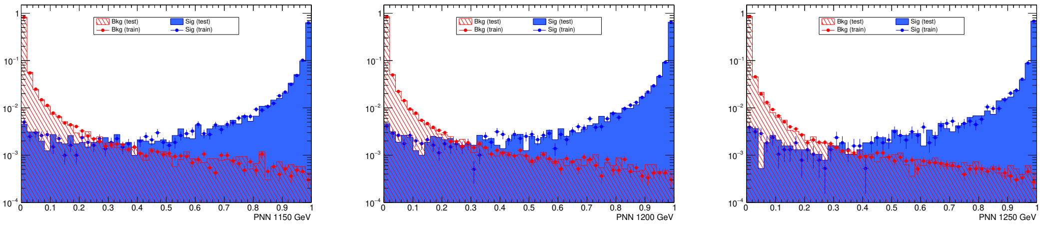

(m) m = 1150 GeV (n) m = 1200 GeV (o) m = 1250 GeV

Figure A.1: Overtraining checks as a function of the PNN score. The histograms are for the test samples, and the points are for the training samples.

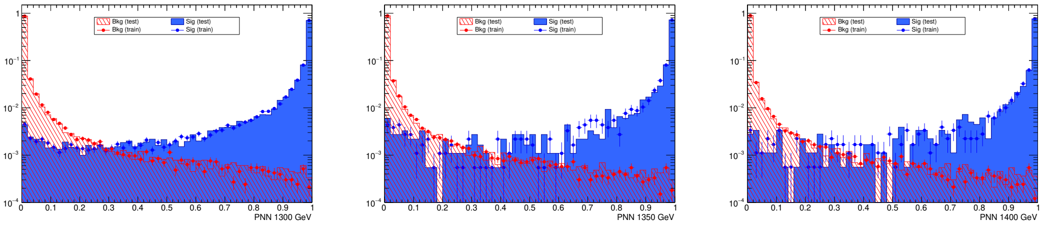

(a) m = 1300 GeV

(b) m = 1350 GeV

(c) m = 1400 GeV

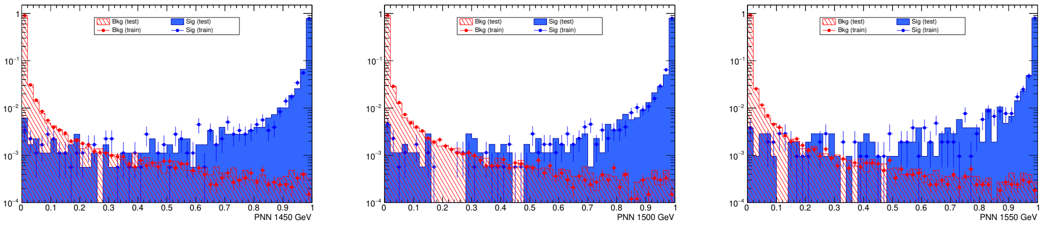

(d) m = 1450 GeV

(e) m = 1500 GeV

(f) m = 1550 GeV

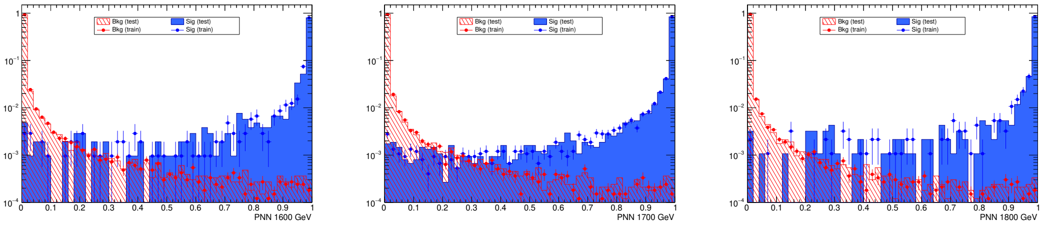

(g) m = 1600 GeV

(h) m = 1700 GeV

(i) m = 1800 GeV

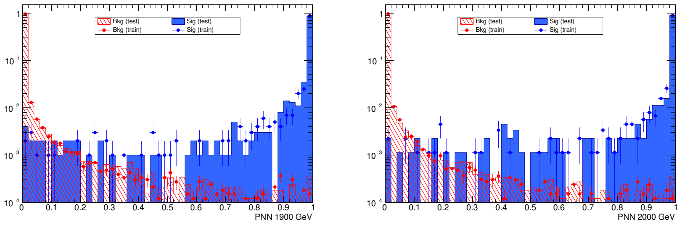

(j) m = 1900 GeV

(k) m = 2000 GeV

Figure A.2: Overtraining checks as a function of the PNN score. The histograms are for the test samples, and the points are for the training samples.

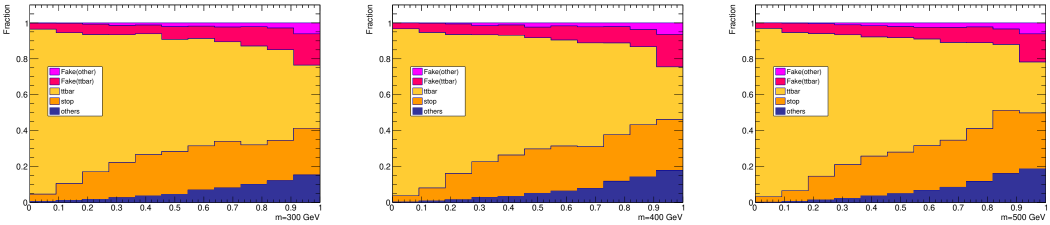

(a) m = 300 GeV (b) m = 400 GeV (c) m = 500 GeV

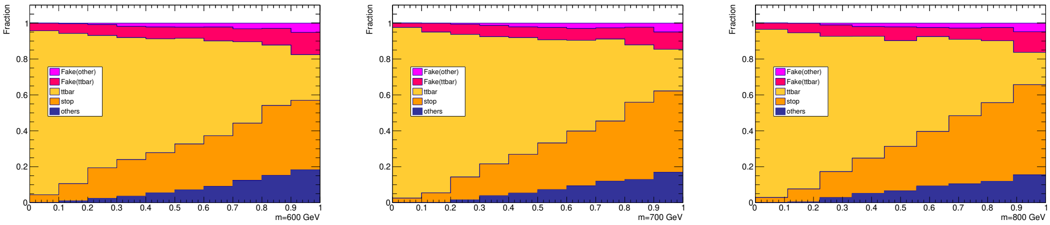

(d) m = 600 GeV (e) m = 700 GeV (f) m = 800 GeV

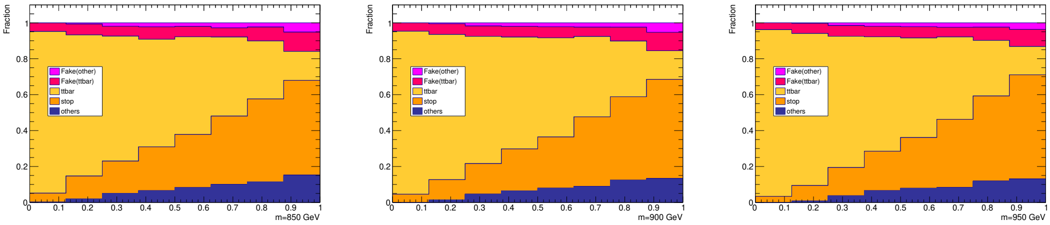

(g) m = 850 GeV (h) m = 900 GeV (i) m = 950 GeV

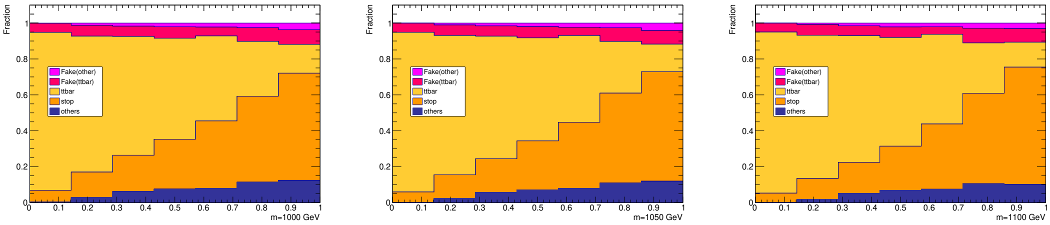

(j) m = 1000 GeV (k) m = 1050 GeV (l) m = 1100 GeV

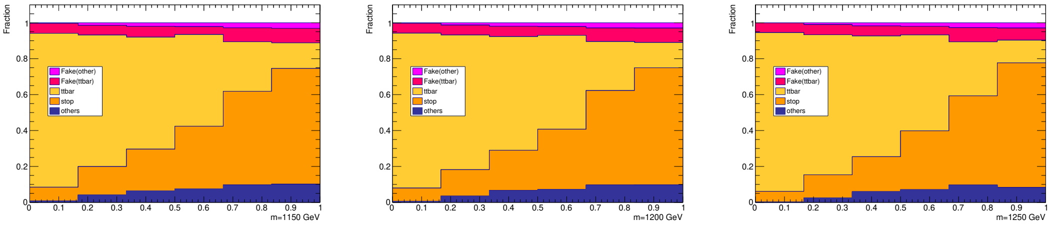

(m) m = 1150 GeV (n) m = 1200 GeV (o) m = 1250 GeV

Figure A.3: Fraction of each background components in the PNN score distributions.

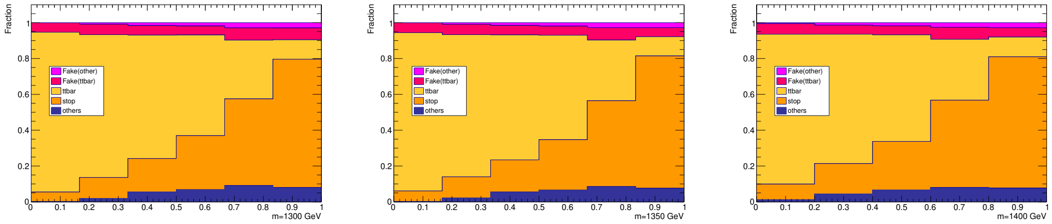

(a) m = 1300 GeV (b) m = 1350 GeV (c) m = 1400 GeV

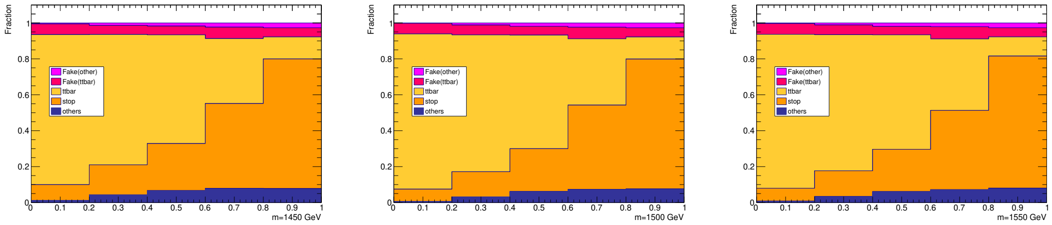

(d) m = 1450 GeV (e) m = 1500 GeV (f) m = 1550 GeV

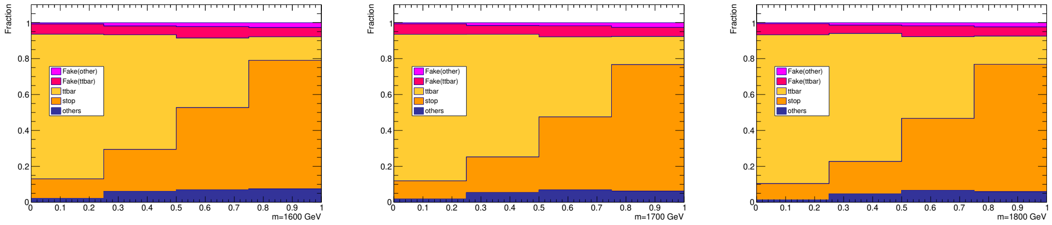

(g) m = 1600 GeV (h) m = 1700 GeV (i) m = 1800 GeV

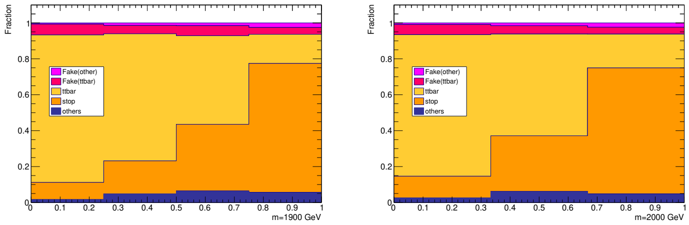

(j) m = 1900 GeV (k) m = 2000 GeV

Figure A.4: Fraction of each background components in the PNN score distributions.

Appendix B

Systematic Uncertainties

A Thoretical Uncertainties

The theoretical uncertainties are divided into two parts, normalizatoin and shape effects. The normalization uncertainties are calculated by the comparison of the nomianl caonfiguration MC samples and the alternative systematics MC samples. The shape uncertainties are calculated by the comparison of histograms between nominal and alternative samples.

A.1 Normalization Uncertainties of $t\bar{t}$ process

The normalization uncertainties of the $t\bar{t}$ process are summarized in Table B.2.

Table B.1: Normalization uncertainties for $t\bar{t}$ process.

Source	Uncertainty
ME	0.219
PS	0.135
ISR	+0.351, -0.254
FSR	+0.081, -0.065
PDF+α_s	0.116

A.2 Shape Uncertainties of $t\bar{t}$

Matrix element
Acceptance uncertainties due to the Hard Scatter Generation and matching. Fig. B.1,B.2 show comparisons of nominal and alternative samples. The alternative distributions are normalized to the nominal sample to look at the shape differences.

Parton shower
Acceptance uncertainties due to the Fragmentation/Hadronization model. Fig. B.3,B.4 show comparisons of nominal and alternative samples. The alternative distributions are normalized to the nominal sample to look at the shape differences.

ISR variation up

Acceptance uncertainties due to the additional radiation. Fig. B.5,B.6 show comparisons of nominal and alternative samples. The alternative distributions are normalized to the nominal sample to look at the shape differences.

ISR variation down

Acceprance uncertainties due to the additional radiation. Fig. B.7,B.8 show comparisons of nominal and alternative samples. The alternative distributions are normalized to the nominal sample to look at the shape differences.

FSR variation up

Acceprance uncertainties due to the additional radiation. Fig. B.9,B.10 show comparisons of nominal and alternative samples. The alternative distributions are normalized to the nominal sample to look at the shape differences.

FSR variation down

Acceprance uncertainties due to the additional radiation. Fig. B.11,B.12 show comparisons of nominal and alternative samples. The alternative distributions are normalized to the nominal sample to look at the shape differences.

PDF+α_s

Acceprance uncertainties due to the parton density function. Fig. B.13,B.14 show comparisons of nominal and alternative samples. The alternative distributions are normalized to the nominal sample to look at the shape differences.

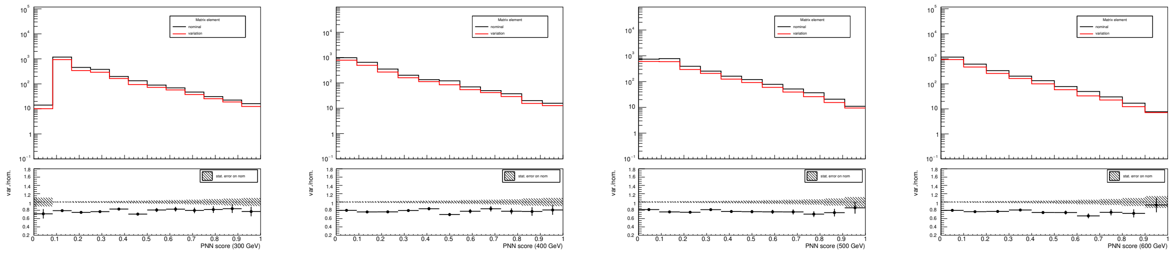

(a) m = 300 GeV (b) m = 400 GeV (c) m = 500 GeV (d) m = 600 GeV

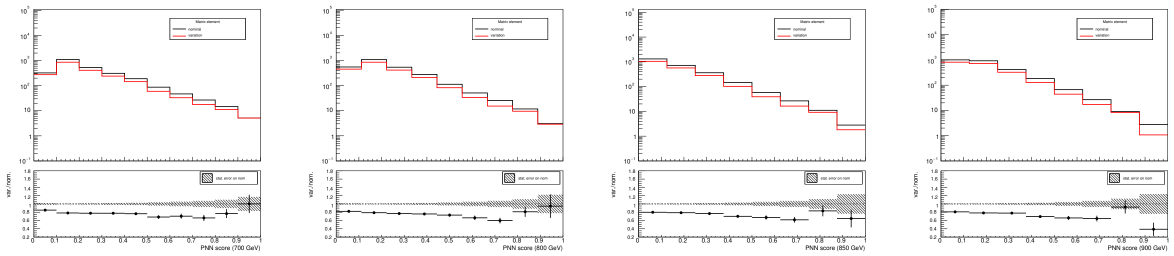

(e) m = 700 GeV (f) m = 800 GeV (g) m = 850 GeV (h) m = 900 GeV

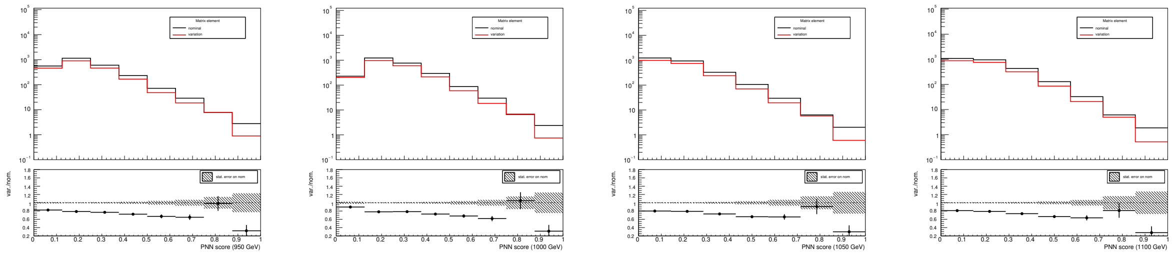

(i) m = 950 GeV (j) m = 1000 GeV (k) m = 1050 GeV (l) m = 1100 GeV

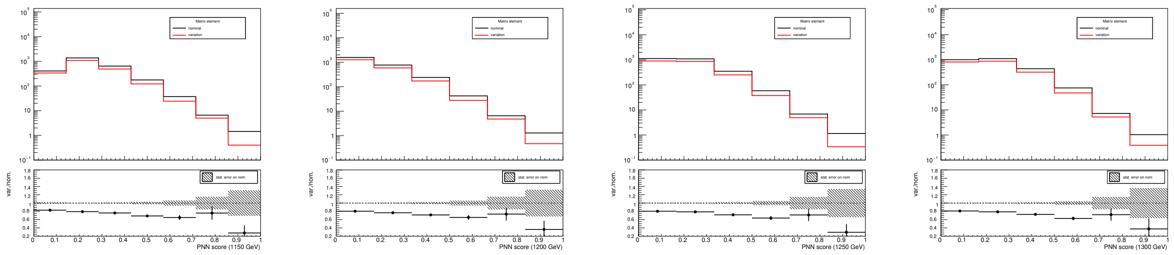

(m) m = 1150 GeV (n) m = 1200 GeV (o) m = 1250 GeV (p) m = 1300 GeV

Figure B.1: Modeling comparison of nominal and alternative PNN score distributions in the signal region for matrix element.

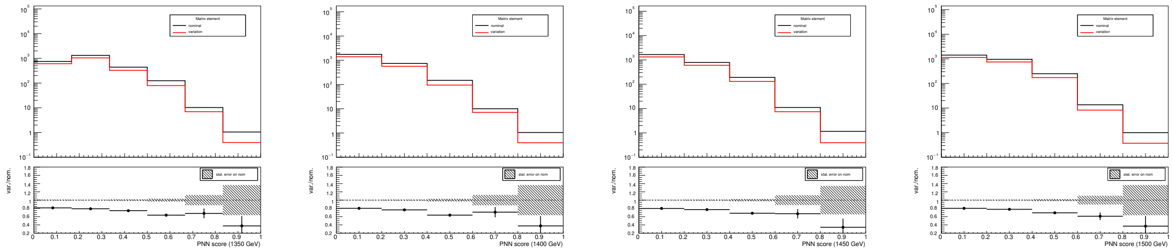

(a) m = 1350 GeV (b) m = 1400 GeV (c) m = 1450 GeV (d) m = 1500 GeV

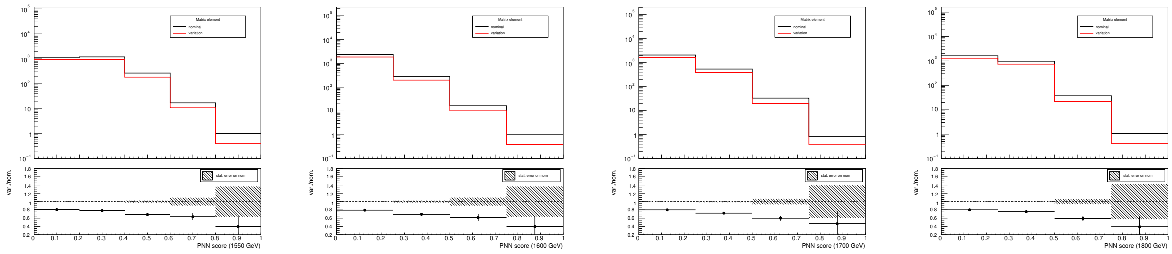

(e) m = 1550 GeV (f) m = 1600 GeV (g) m = 1700 GeV (h) m = 1800 GeV

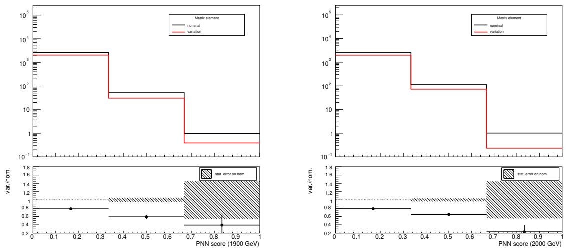

(i) m = 1900 GeV (j) m = 2000 GeV

Figure B.2: Modeling comparison of nominal and alternative PNN score distributions in the signal region for matrix element.

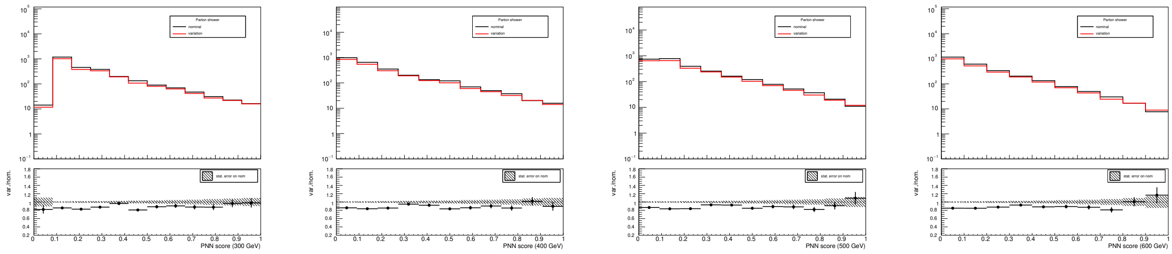

(a) m = 300 GeV (b) m = 400 GeV (c) m = 500 GeV (d) m = 600 GeV

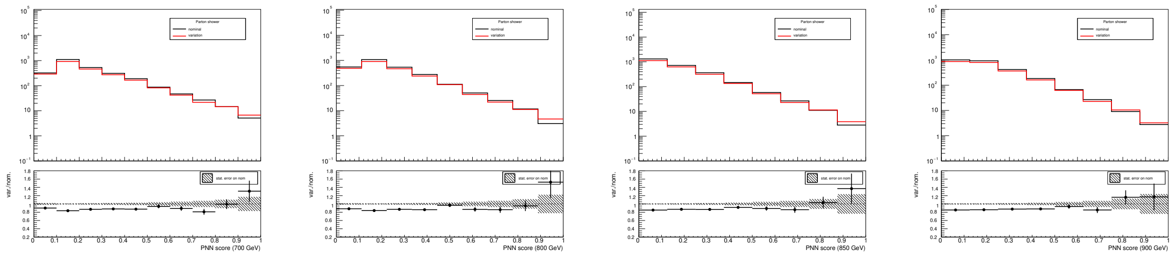

(e) m = 700 GeV (f) m = 800 GeV (g) m = 850 GeV (h) m = 900 GeV

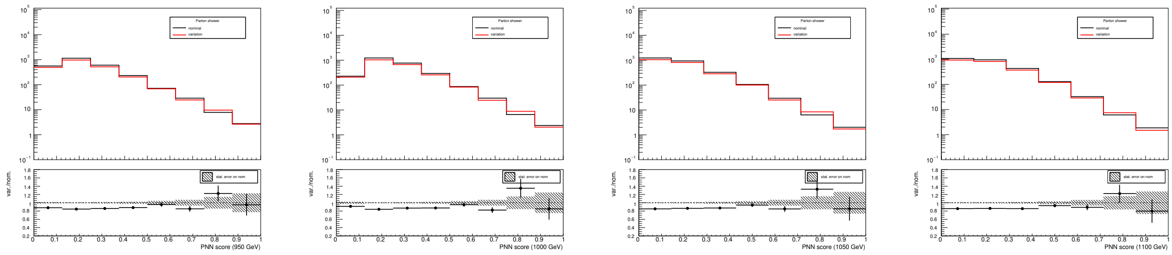

(i) m = 950 GeV (j) m = 1000 GeV (k) m = 1050 GeV (l) m = 1100 GeV

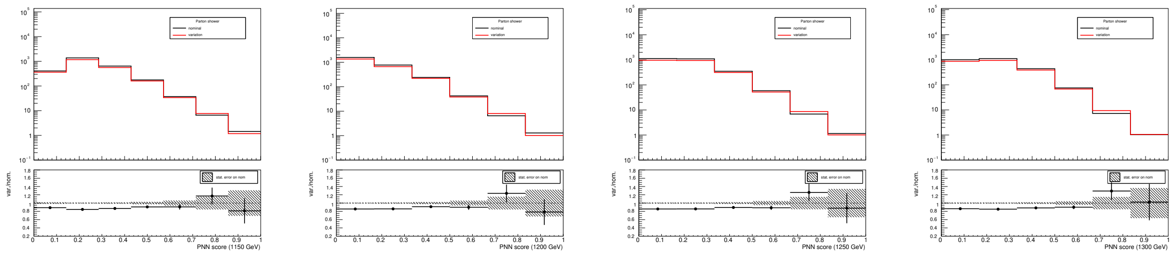

(m) m = 1150 GeV (n) m = 1200 GeV (o) m = 1250 GeV (p) m = 1300 GeV

Figure B.3: Modeling comparison of nominal and alternative PNN score distributions in the signal region for parton shower.

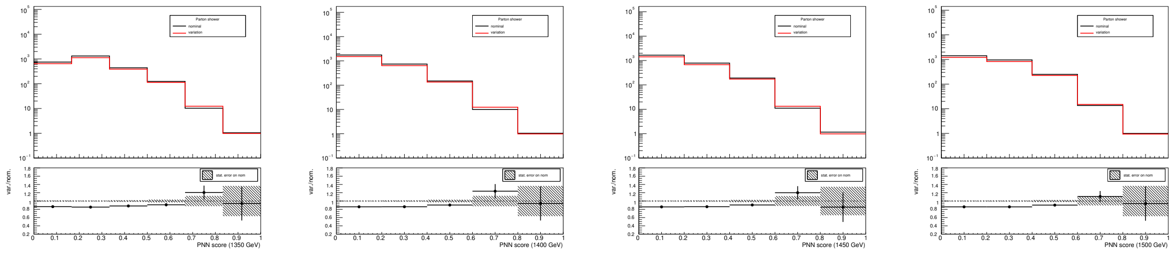

(a) m = 1350 GeV (b) m = 1400 GeV (c) m = 1450 GeV (d) m = 1500 GeV

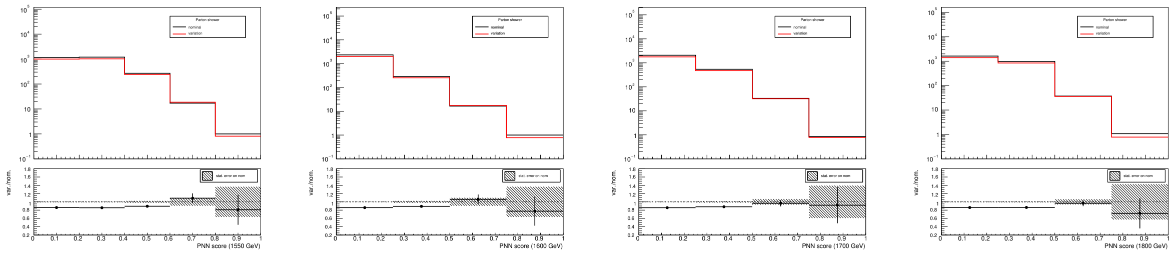

(e) m = 1550 GeV (f) m = 1600 GeV (g) m = 1700 GeV (h) m = 1800 GeV

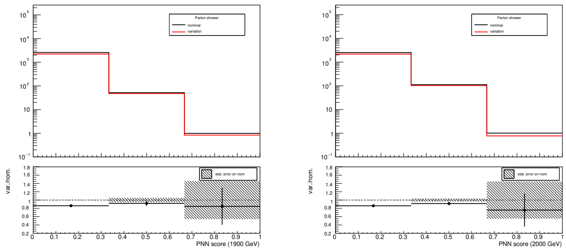

(i) m = 1900 GeV (j) m = 2000 GeV

Figure B.4: Modeling comparison of nominal and alternative PNN score distributions in the signal region for parton shower.

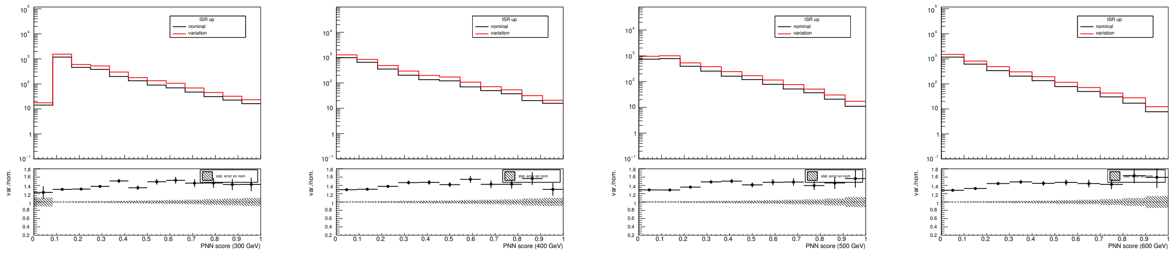

(a) m = 300 GeV (b) m = 400 GeV (c) m = 500 GeV (d) m = 600 GeV

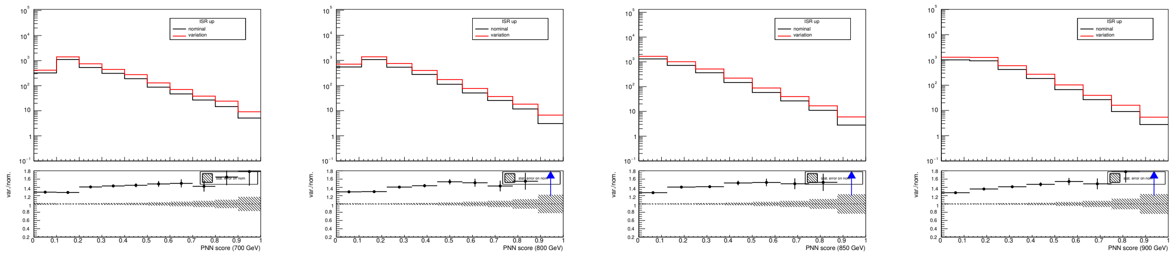

(e) m = 700 GeV (f) m = 800 GeV (g) m = 850 GeV (h) m = 900 GeV

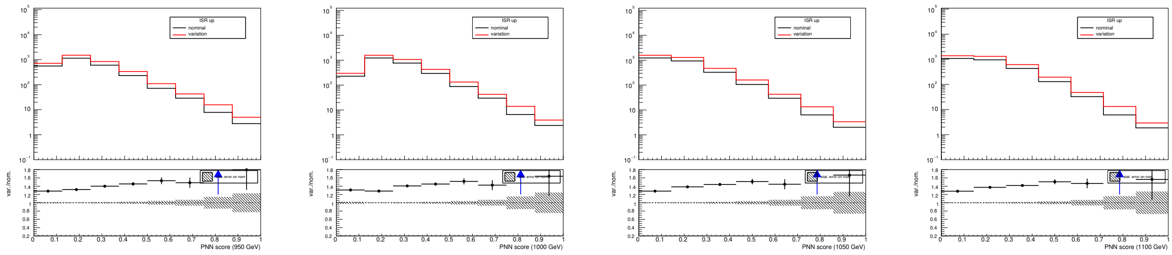

(i) m = 950 GeV (j) m = 1000 GeV (k) m = 1050 GeV (l) m = 1100 GeV

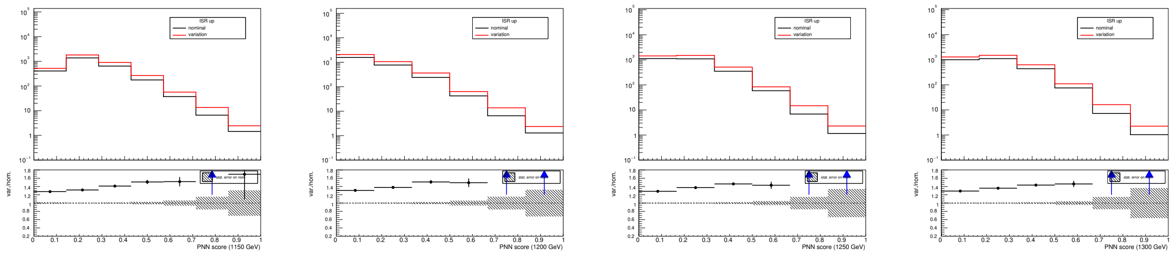

(m) m = 1150 GeV (n) m = 1200 GeV (o) m = 1250 GeV (p) m = 1300 GeV

Figure B.5: Modeling comparison of nominal and alternative PNN score distributions in the signal region for ISR up.

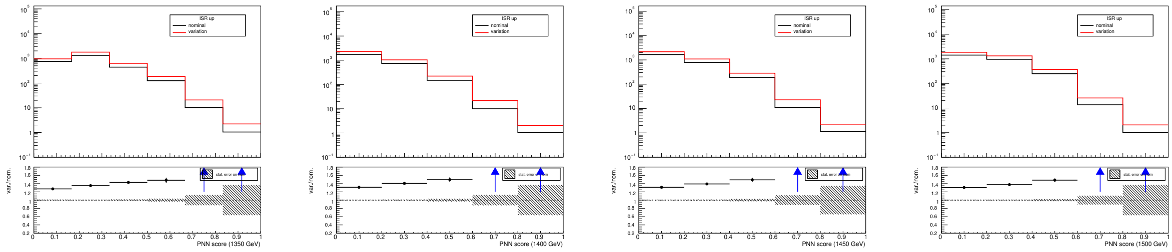

(a) m = 1350 GeV (b) m = 1400 GeV (c) m = 1450 GeV (d) m = 1500 GeV

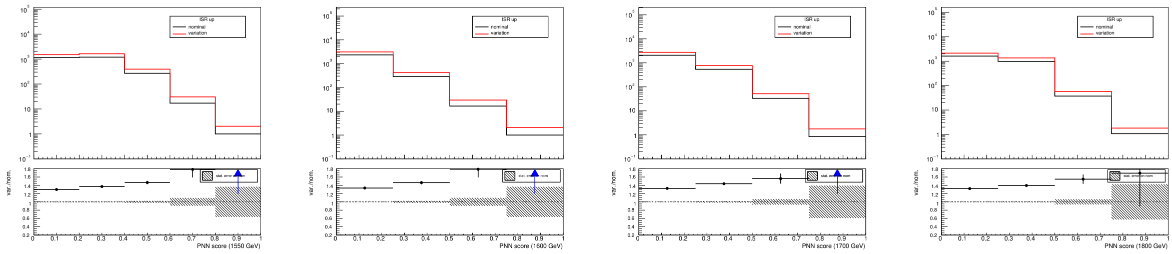

(e) m = 1550 GeV (f) m = 1600 GeV (g) m = 1700 GeV (h) m = 1800 GeV

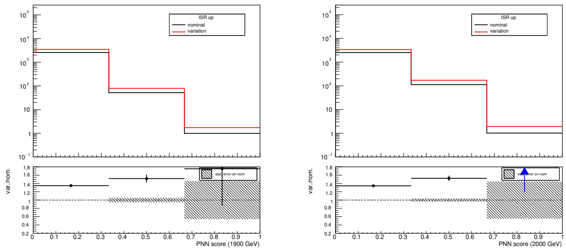

(i) m = 1900 GeV (j) m = 2000 GeV

Figure B.6: Modeling comparison of nominal and alternative PNN score distributions in the signal region for ISR up.

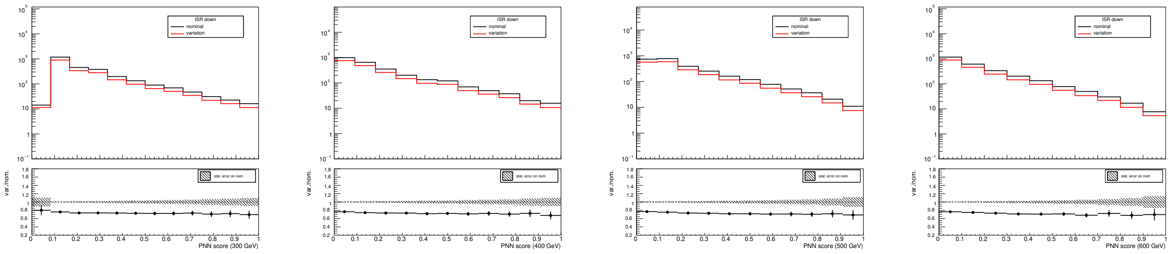

(a) m = 300 GeV (b) m = 400 GeV (c) m = 500 GeV (d) m = 600 GeV

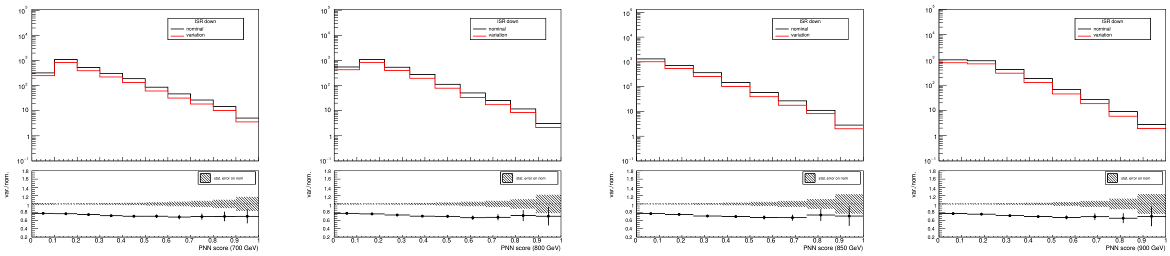

(e) m = 700 GeV (f) m = 800 GeV (g) m = 850 GeV (h) m = 900 GeV

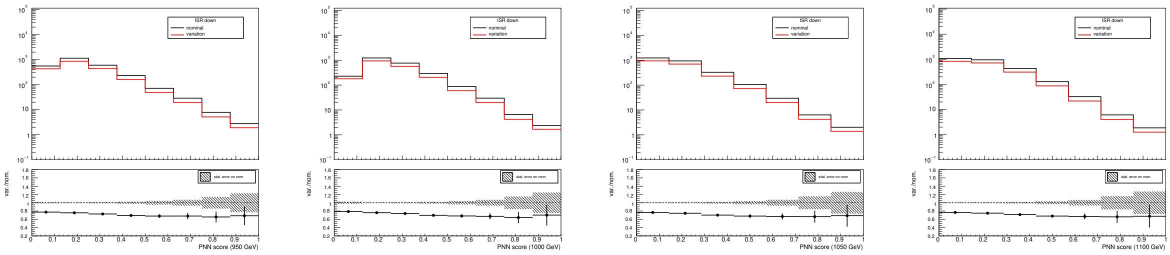

(i) m = 950 GeV (j) m = 1000 GeV (k) m = 1050 GeV (l) m = 1100 GeV

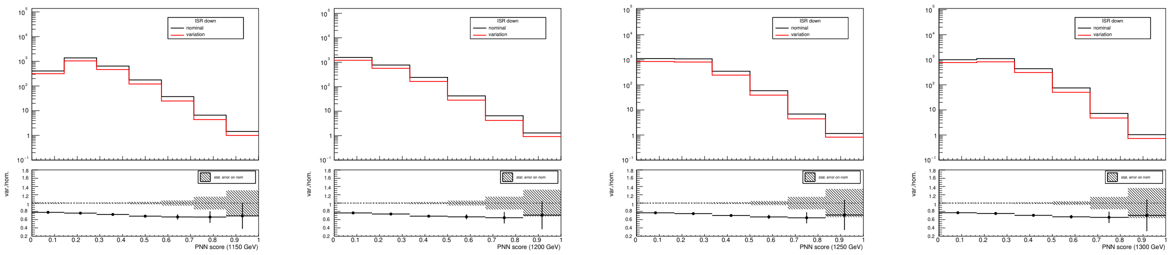

(m) m = 1150 GeV (n) m = 1200 GeV (o) m = 1250 GeV (p) m = 1300 GeV

Figure B.7: Modeling comparison of nominal and alternative PNN score distributions in the signal region for ISR down.

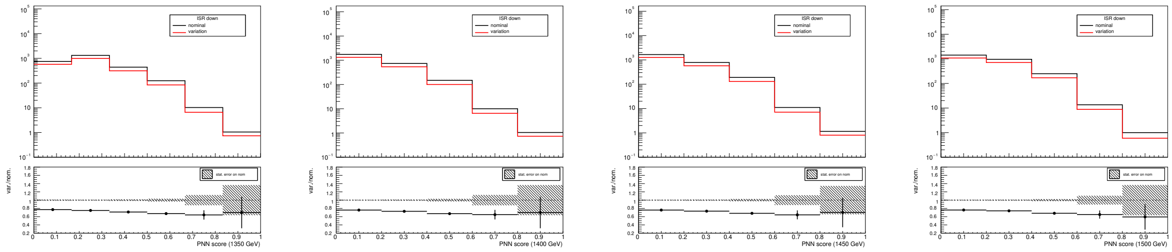

(a) m = 1350 GeV (b) m = 1400 GeV (c) m = 1450 GeV (d) m = 1500 GeV

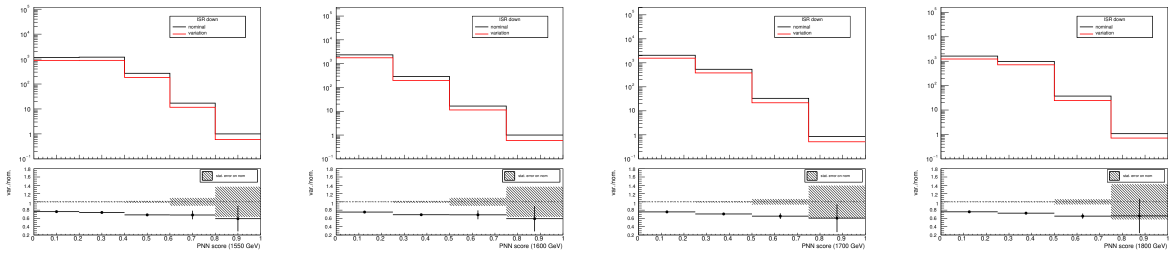

(e) m = 1550 GeV (f) m = 1600 GeV (g) m = 1700 GeV (h) m = 1800 GeV

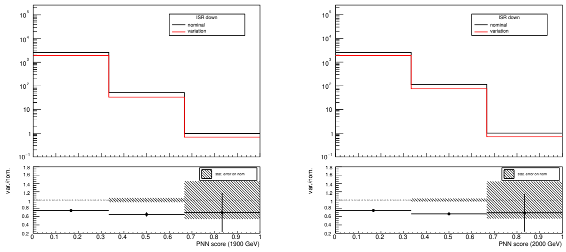

(i) m = 1900 GeV (j) m = 2000 GeV

Figure B.8: Modeling comparison of nominal and alternative PNN score distributions in the signal region for ISR down.

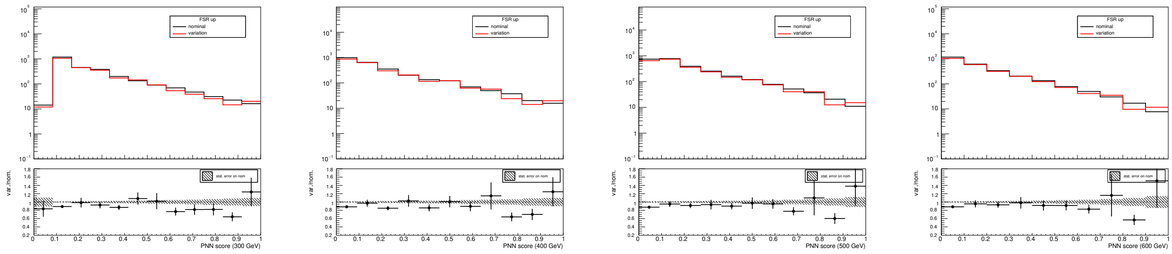

(a) m = 300 GeV (b) m = 400 GeV (c) m = 500 GeV (d) m = 600 GeV

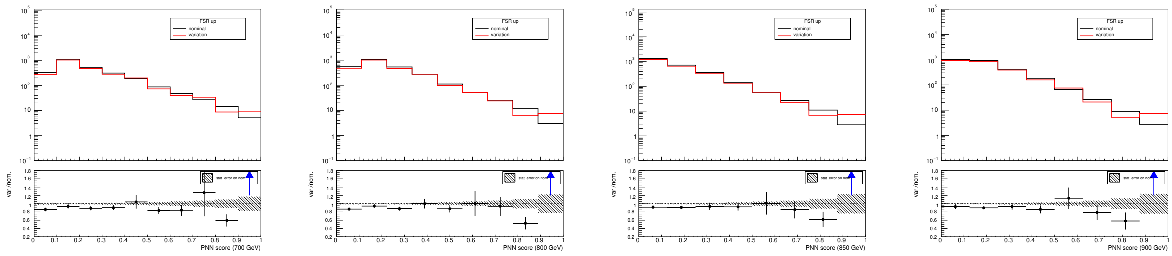

(e) m = 700 GeV (f) m = 800 GeV (g) m = 850 GeV (h) m = 900 GeV

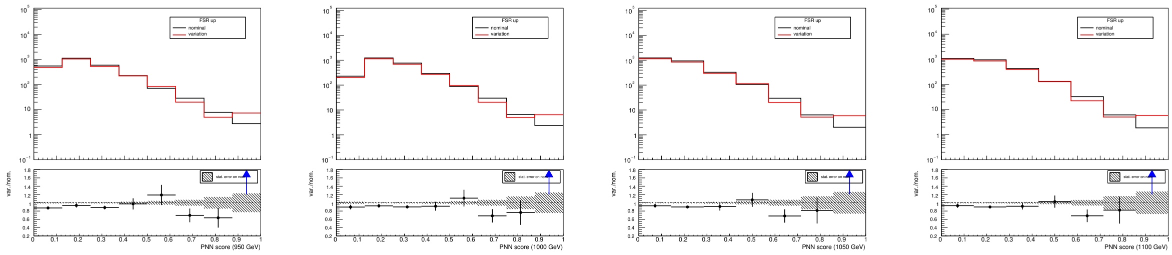

(i) m = 950 GeV (j) m = 1000 GeV (k) m = 1050 GeV (l) m = 1100 GeV

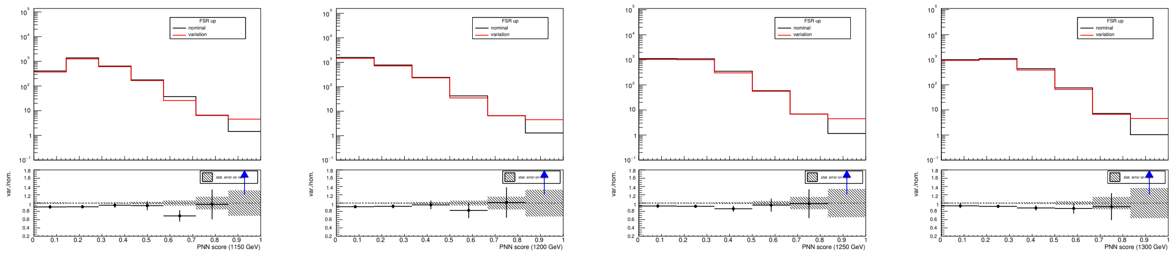

(m) m = 1150 GeV (n) m = 1200 GeV (o) m = 1250 GeV (p) m = 1300 GeV

Figure B.9: Modeling comparison of nominal and alternative PNN score distributions in the signal region for FSR up.

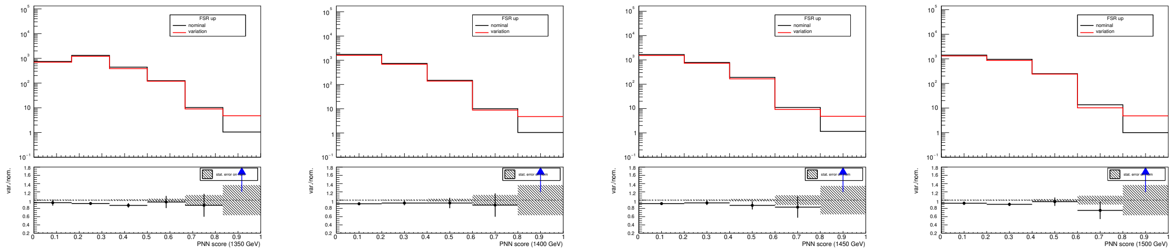

(a) m = 1350 GeV (b) m = 1400 GeV (c) m = 1450 GeV (d) m = 1500 GeV

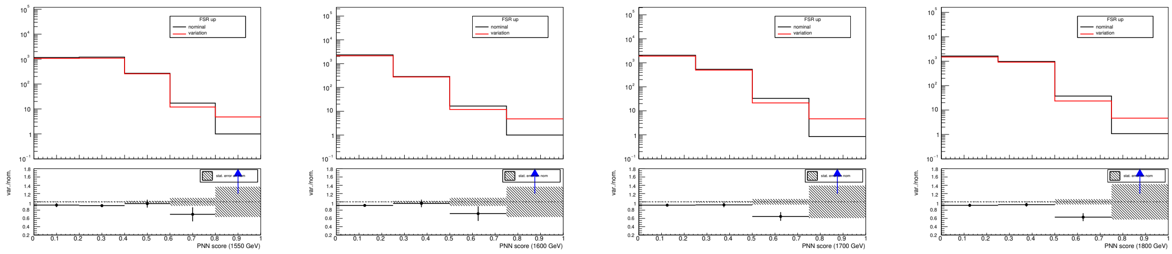

(e) m = 1550 GeV (f) m = 1600 GeV (g) m = 1700 GeV (h) m = 1800 GeV

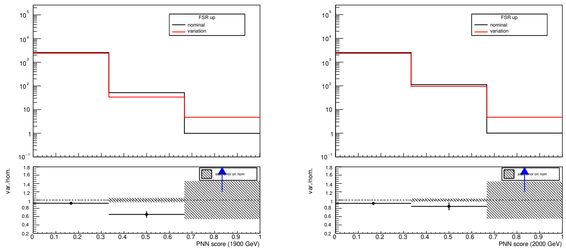

(i) m = 1900 GeV (j) m = 2000 GeV

Figure B.10: Modeling comparison of nominal and alternative PNN score distributions in the signal region for FSR up.

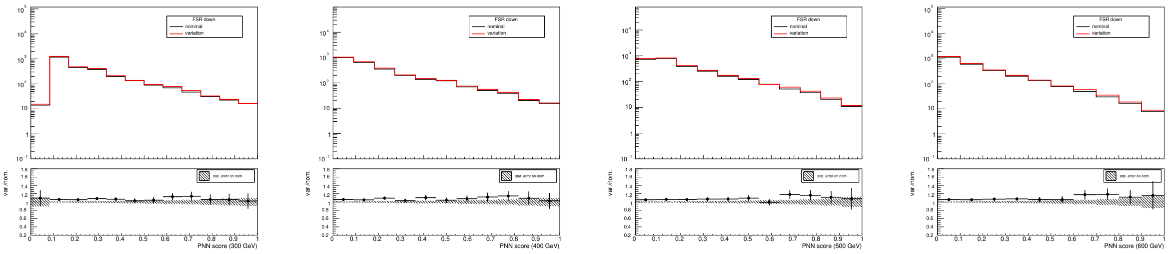

(a) m = 300 GeV (b) m = 400 GeV (c) m = 500 GeV (d) m = 600 GeV

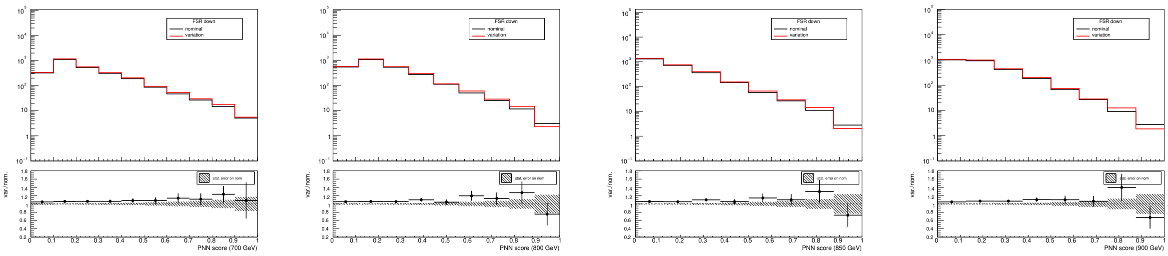

(e) m = 700 GeV (f) m = 800 GeV (g) m = 850 GeV (h) m = 900 GeV

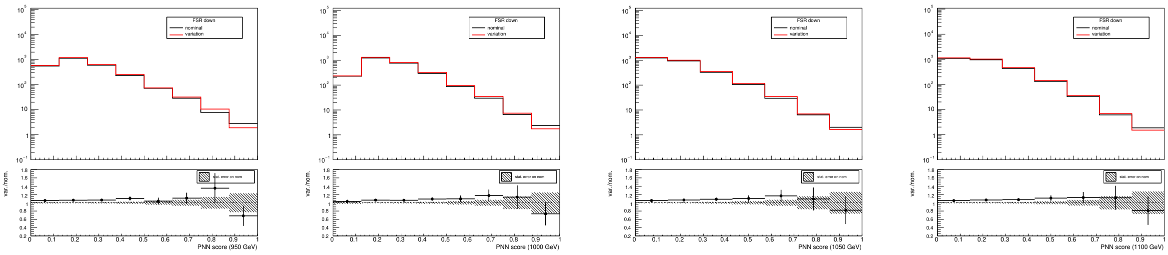

(i) m = 950 GeV (j) m = 1000 GeV (k) m = 1050 GeV (l) m = 1100 GeV

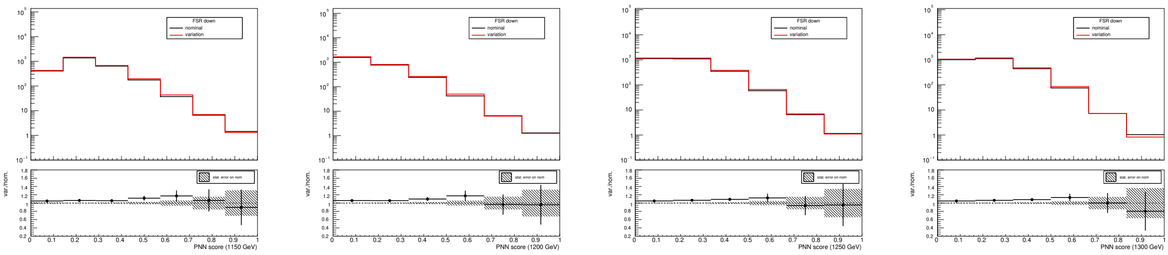

(m) m = 1150 GeV (n) m = 1200 GeV (o) m = 1250 GeV (p) m = 1300 GeV

Figure B.11: Modeling comparison of nominal and alternative PNN score distributions in the signal region for FSR down.

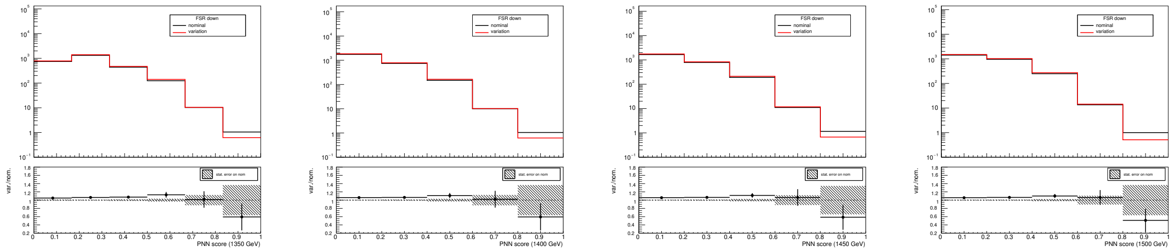

(a) m = 1350 GeV (b) m = 1400 GeV (c) m = 1450 GeV (d) m = 1500 GeV

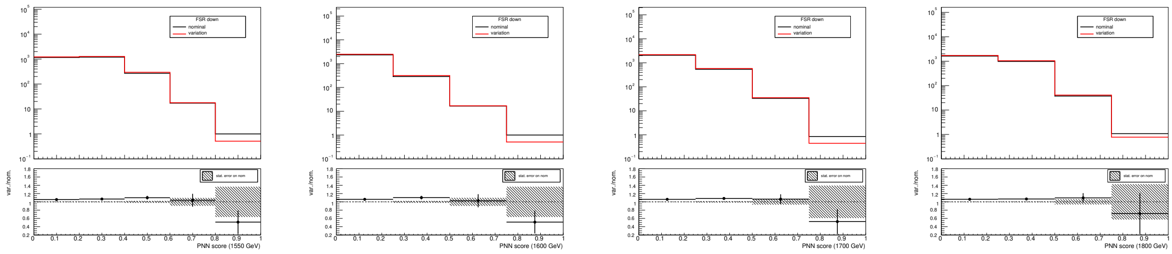

(e) m = 1550 GeV (f) m = 1600 GeV (g) m = 1700 GeV (h) m = 1800 GeV

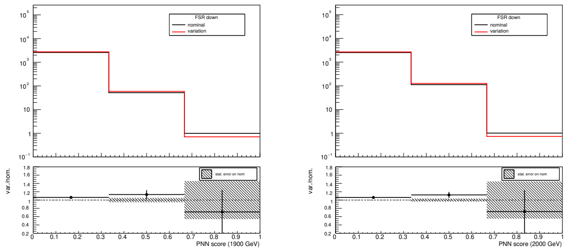

(i) m = 1900 GeV (j) m = 2000 GeV

Figure B.12: Modeling comparison of nominal and alternative PNN score distributions in the signal region for FSR down.

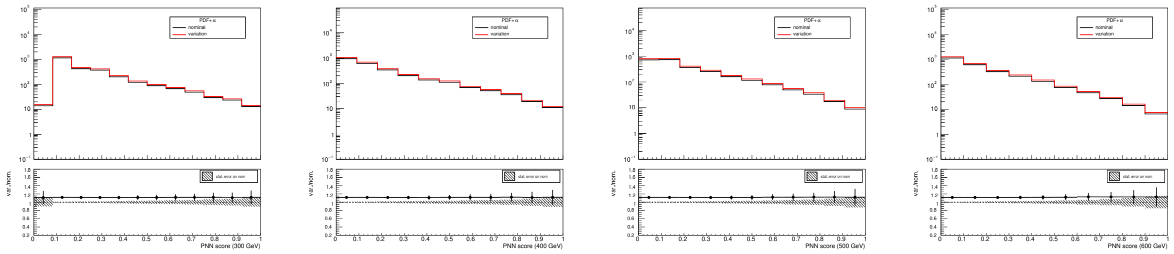

(a) m = 300 GeV (b) m = 400 GeV (c) m = 500 GeV (d) m = 600 GeV

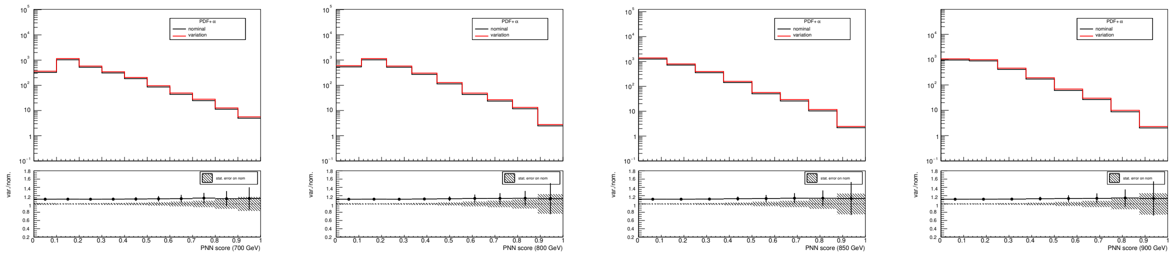

(e) m = 700 GeV (f) m = 800 GeV (g) m = 850 GeV (h) m = 900 GeV

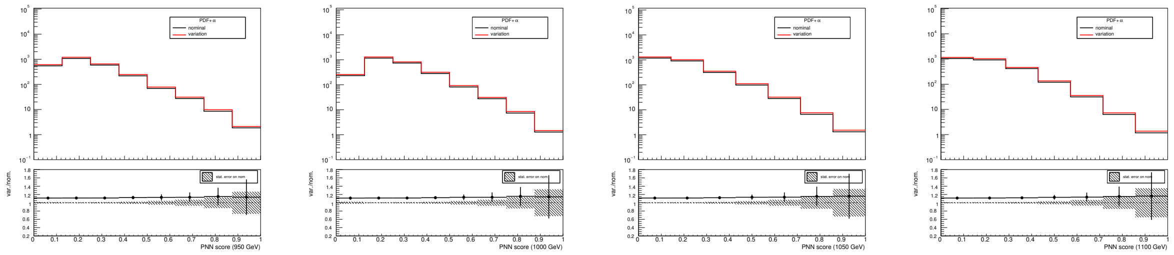

(i) m = 950 GeV (j) m = 1000 GeV (k) m = 1050 GeV (l) m = 1100 GeV

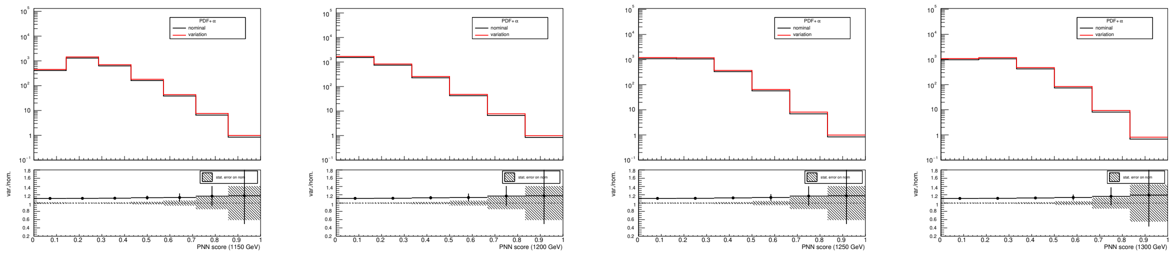

(m) m = 1150 GeV (n) m = 1200 GeV (o) m = 1250 GeV (p) m = 1300 GeV

Figure B.13: Modeling comparison of nominal and alternative PNN score distributions in the signal region for PDF+α_s.

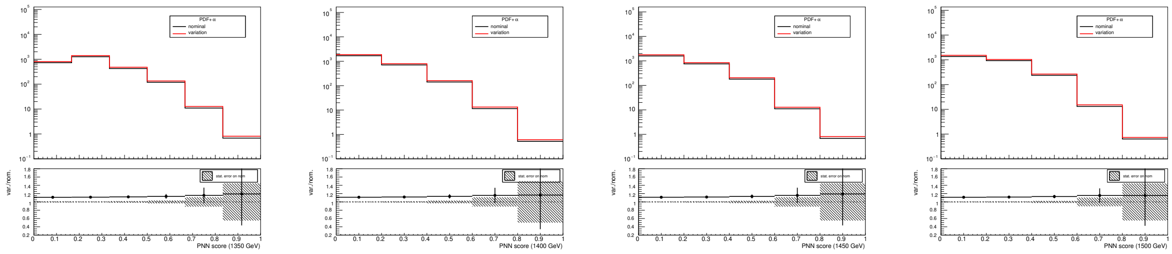

(a) m = 1350 GeV (b) m = 1400 GeV (c) m = 1450 GeV (d) m = 1500 GeV

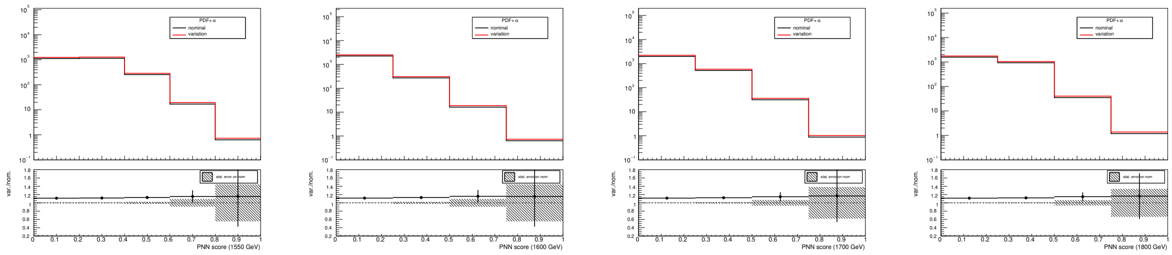

(e) m = 1550 GeV (f) m = 1600 GeV (g) m = 1700 GeV (h) m = 1800 GeV

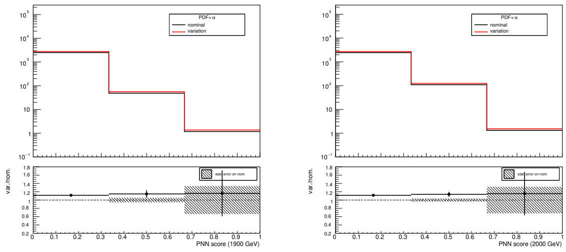

(i) m = 1900 GeV (j) m = 2000 GeV

Figure B.14: Modeling comparison of nominal and alternative PNN score distributions in the signal region for PDF+α_s.

A.3 Normalization Uncertainties of single top process

The normalization uncertainties of the $t\bar{t}$ process are summarized in Table B.2.

Table B.2: Normalization uncertainties for $t\bar{t}$ process.

Source	Uncertainty
ME	0.069
PS	0.085
ISR	+0.231, -0.146
FSR	+0.031, -0.014
PDF+α_s	0.07
Wt interference	0.576

A.4 Shape Uncertainties of single top

Matrix element

Acceptance uncertainties due to the Hard Scatter Generation and matching. Fig. B.15,B.16 show comparisons of nominal and alternative samples. The alternative distributions are normalized to the nominal sample to look at the shape differences.

Parton shower

Acceptance uncertainties due to the Fragmentation/Hadronization model. Fig. B.17,B.18 show comparisons of nominal and alternative samples. The alternative distributions are normalized to the nominal sample to look at the shape differences.

ISR variation

Acceprance uncertainties due to the additional radiation. Fig. B.19,B.20 show comparisons of nominal and alternative samples. The alternative distributions are normalized to the nominal sample to look at the shape differences.

FSR variation

Acceprance uncertainties due to the additional radiation. Fig. B.21,B.22 show comparisons of nominal and alternative samples. The alternative distributions are normalized to the nominal sample to look at the shape differences.

PDF+α_s

Acceprance uncertainties due to the parton density function. Fig. B.23,B.24 show comparisons of nominal and alternative samples. The alternative distributions are normalized to the nominal sample to look at the shape differences.

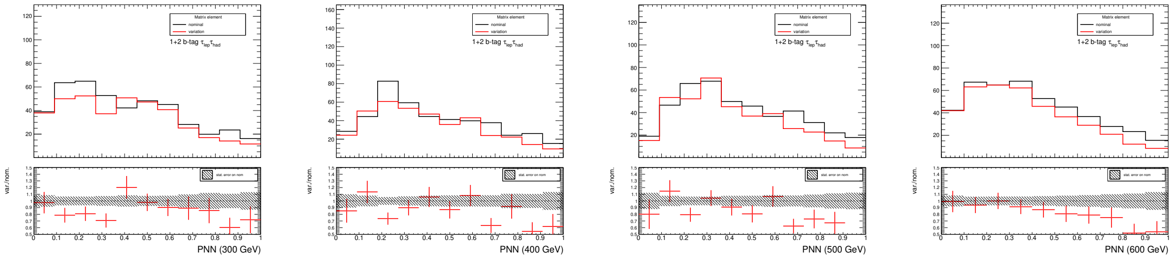

(a) m = 300 GeV (b) m = 400 GeV (c) m = 500 GeV (d) m = 600 GeV

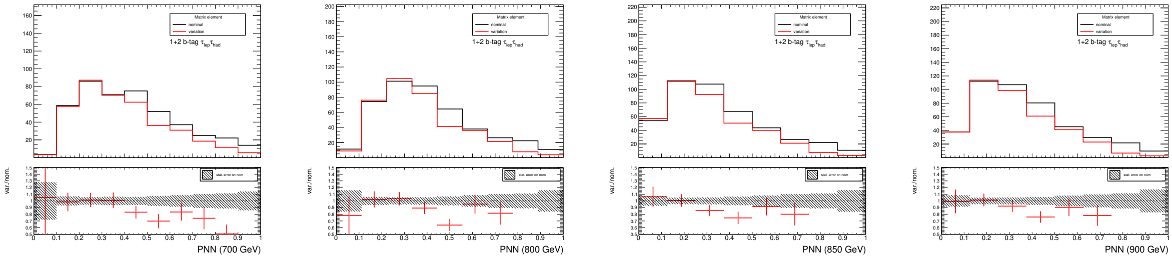

(e) m = 700 GeV (f) m = 800 GeV (g) m = 850 GeV (h) m = 900 GeV

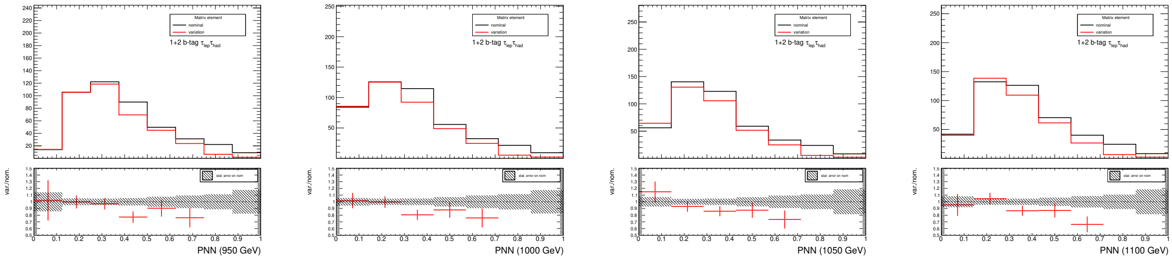

(i) m = 950 GeV (j) m = 1000 GeV (k) m = 1050 GeV (l) m = 1100 GeV

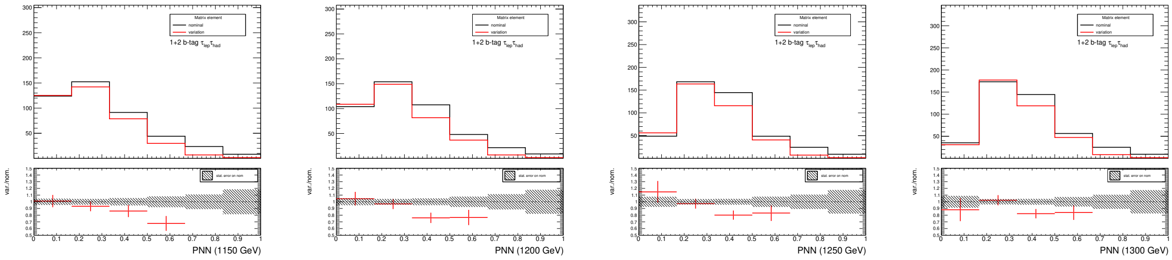

(m) m = 1150 GeV (n) m = 1200 GeV (o) m = 1250 GeV (p) m = 1300 GeV

Figure B.15: Modeling comparison of nominal and alternative PNN score distributions in the signal region for matrix element.

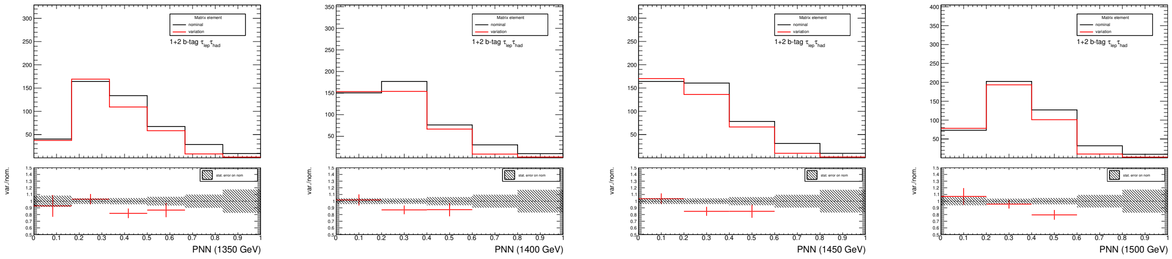

(a) m = 1350 GeV (b) m = 1400 GeV (c) m = 1450 GeV (d) m = 1500 GeV

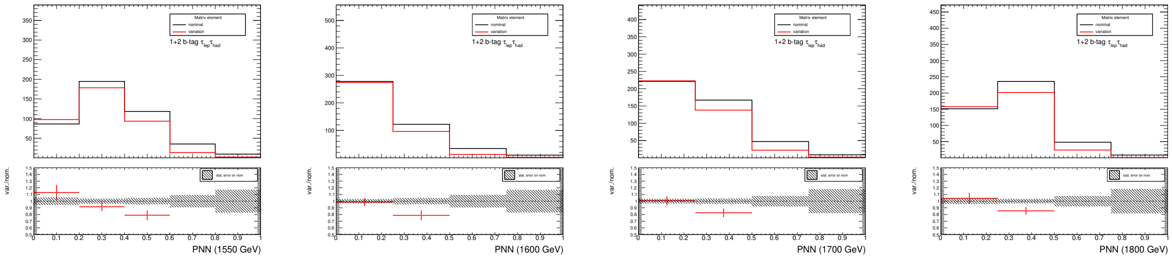

(e) m = 1550 GeV (f) m = 1600 GeV (g) m = 1700 GeV (h) m = 1800 GeV

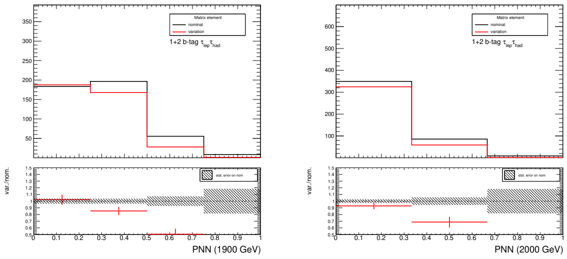

(i) m = 1900 GeV (j) m = 2000 GeV

Figure B.16: Modeling comparison of nominal and alternative PNN score distributions in the signal region for matrix element.

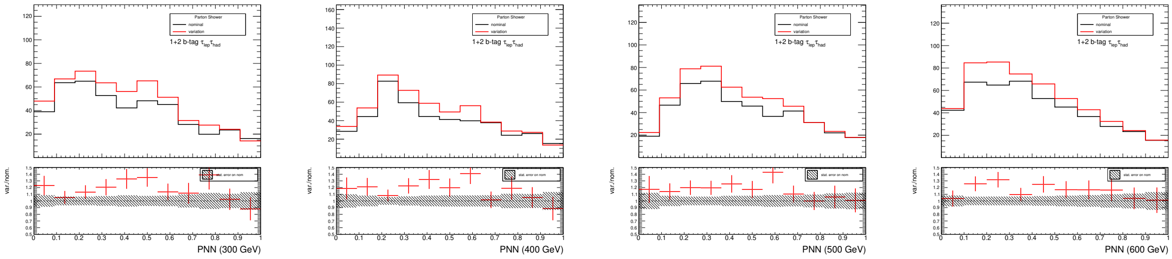

(a) m = 300 GeV (b) m = 400 GeV (c) m = 500 GeV (d) m = 600 GeV

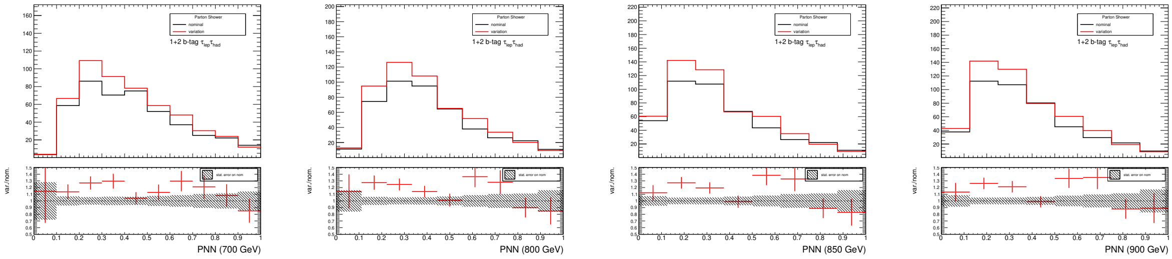

(e) m = 700 GeV (f) m = 800 GeV (g) m = 850 GeV (h) m = 900 GeV

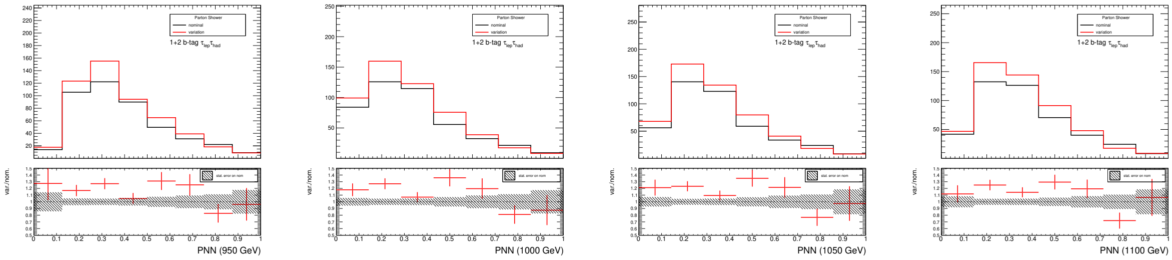

(i) m = 950 GeV (j) m = 1000 GeV (k) m = 1050 GeV (l) m = 1100 GeV

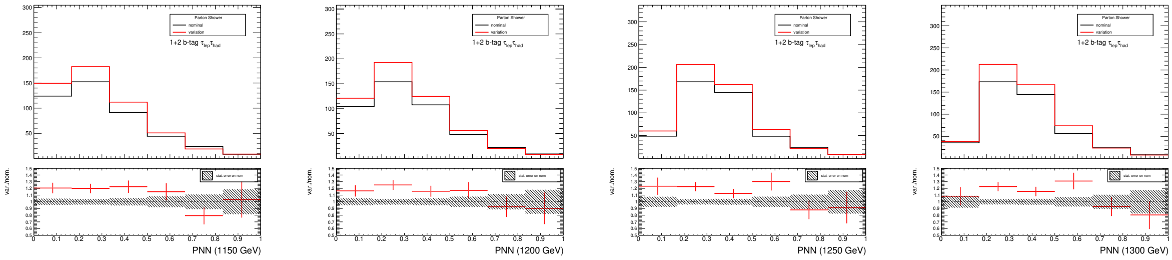

(m) m = 1150 GeV (n) m = 1200 GeV (o) m = 1250 GeV (p) m = 1300 GeV

Figure B.17: Modeling comparison of nominal and alternative PNN score distributions in the signal region for matrix element.

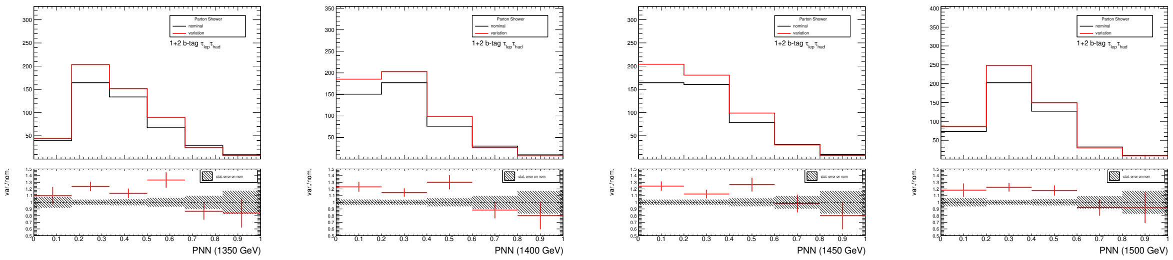

(a) m = 1350 GeV (b) m = 1400 GeV (c) m = 1450 GeV (d) m = 1500 GeV

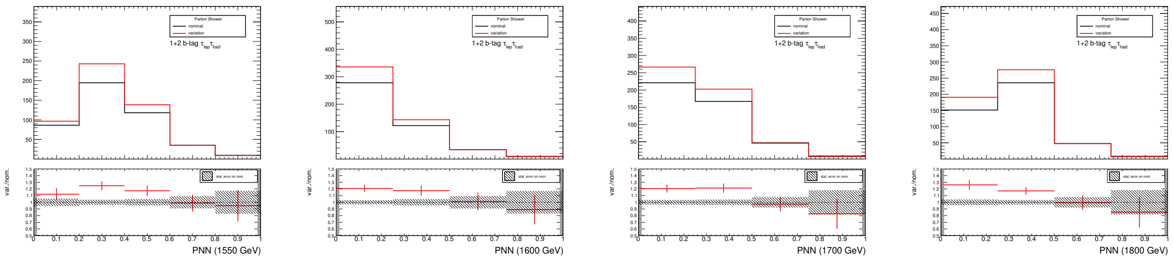

(e) m = 1550 GeV (f) m = 1600 GeV (g) m = 1700 GeV (h) m = 1800 GeV

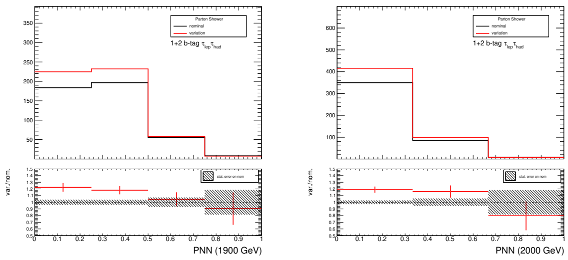

(i) m = 1900 GeV (j) m = 2000 GeV

Figure B.18: Modeling comparison of nominal and alternative PNN score distributions in the signal region for matrix element.

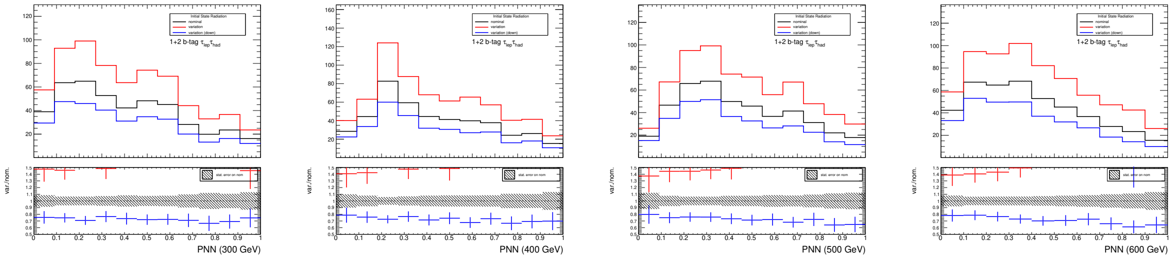

(a) m = 300 GeV (b) m = 400 GeV (c) m = 500 GeV (d) m = 600 GeV

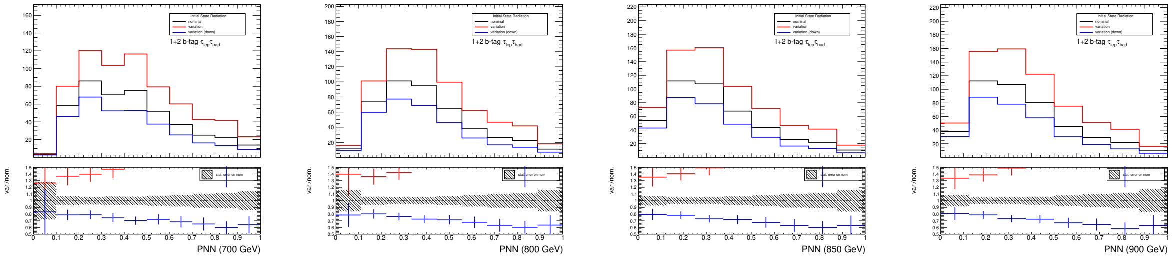

(e) m = 700 GeV (f) m = 800 GeV (g) m = 850 GeV (h) m = 900 GeV

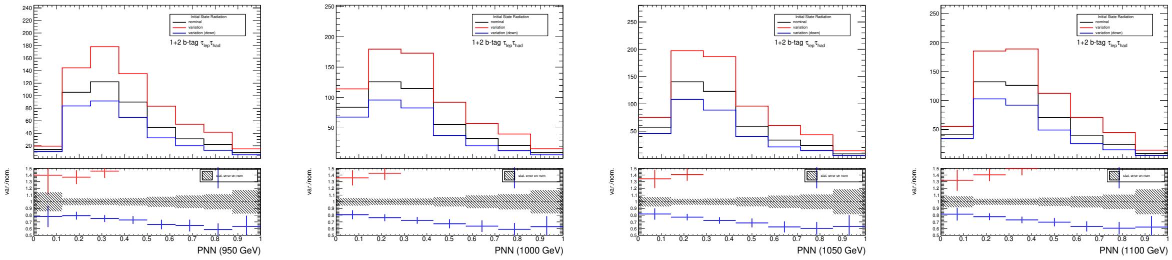

(i) m = 950 GeV (j) m = 1000 GeV (k) m = 1050 GeV (l) m = 1100 GeV

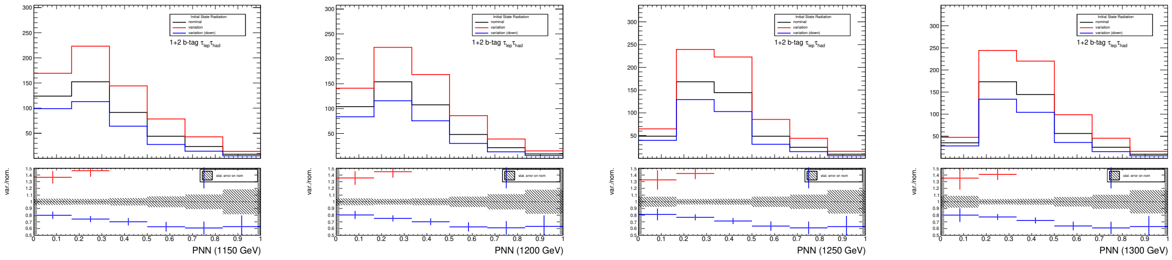

(m) m = 1150 GeV (n) m = 1200 GeV (o) m = 1250 GeV (p) m = 1300 GeV

Figure B.19: Modeling comparison of nominal and alternative PNN score distributions in the signal region for matrix element.

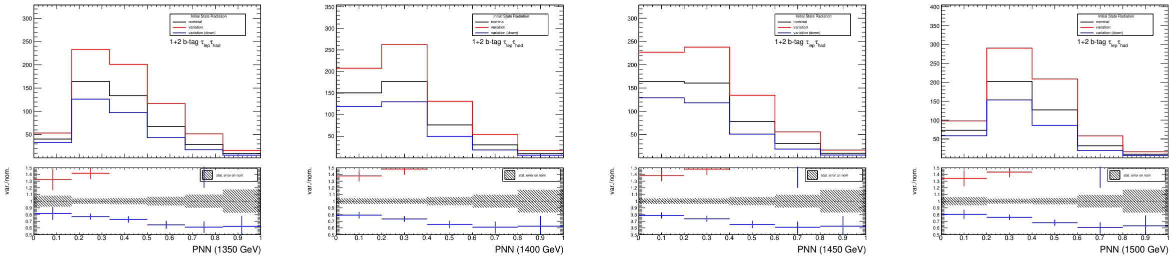

(a) m = 1350 GeV (b) m = 1400 GeV (c) m = 1450 GeV (d) m = 1500 GeV

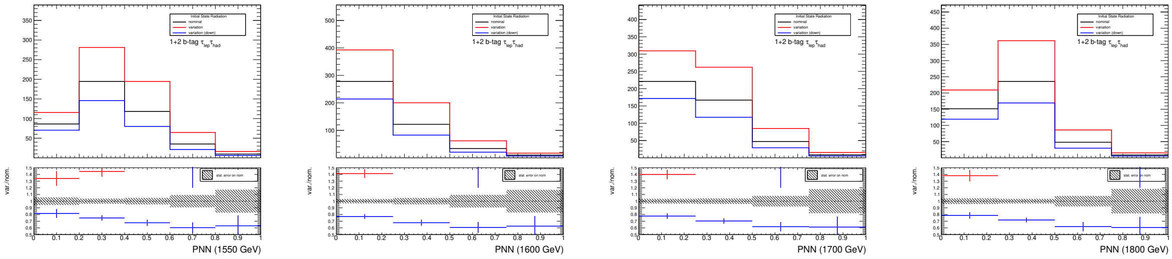

(e) m = 1550 GeV (f) m = 1600 GeV (g) m = 1700 GeV (h) m = 1800 GeV

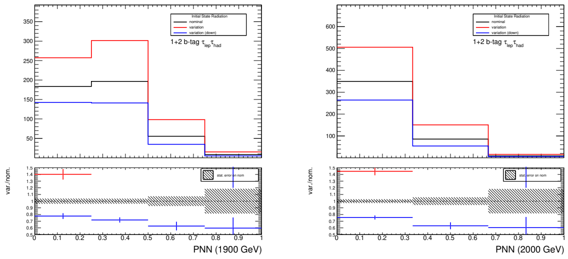

(i) m = 1900 GeV (j) m = 2000 GeV

Figure B.20: Modeling comparison of nominal and alternative PNN score distributions in the signal region for matrix element.

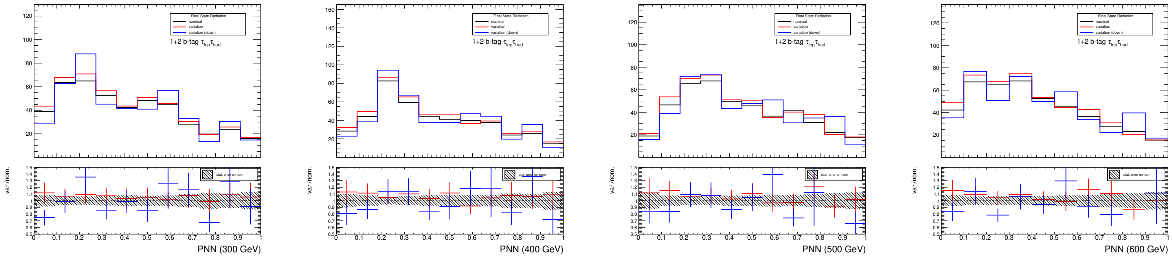

(a) m = 300 GeV (b) m = 400 GeV (c) m = 500 GeV (d) m = 600 GeV

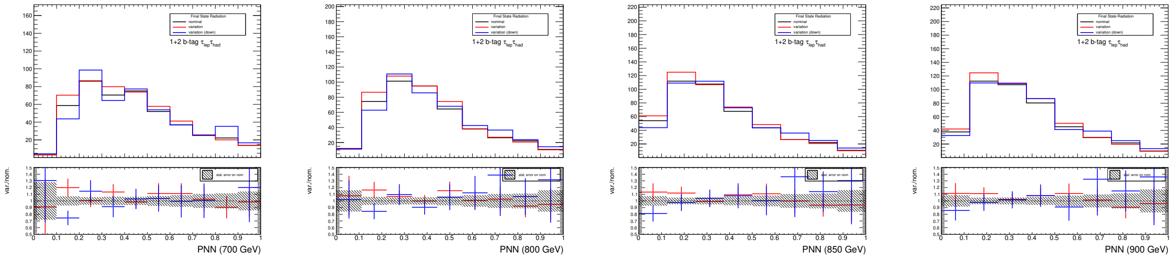

(e) m = 700 GeV (f) m = 800 GeV (g) m = 850 GeV (h) m = 900 GeV

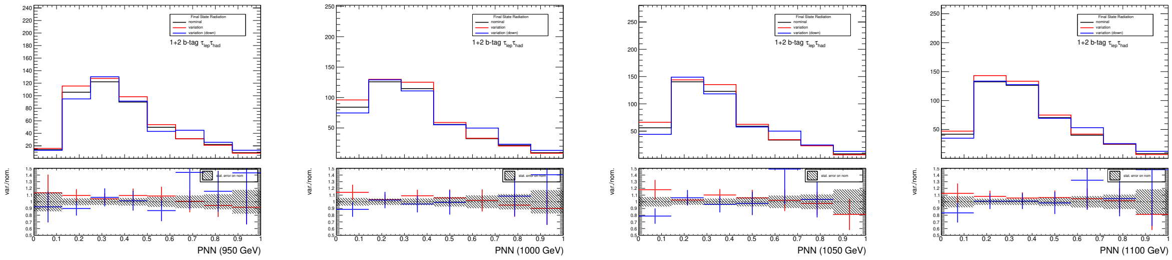

(i) m = 950 GeV (j) m = 1000 GeV (k) m = 1050 GeV (l) m = 1100 GeV

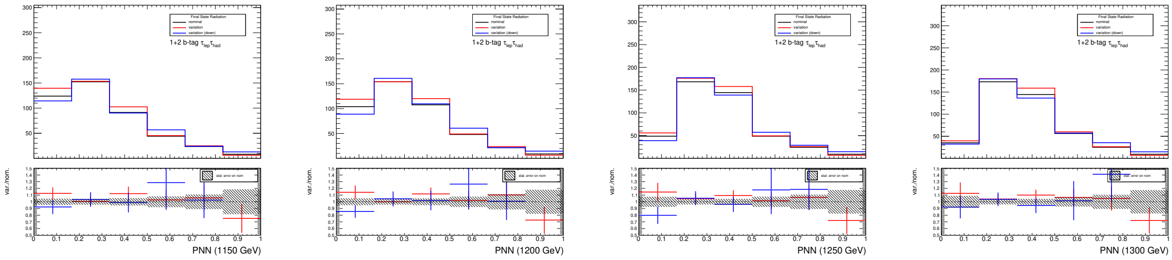

(m) m = 1150 GeV (n) m = 1200 GeV (o) m = 1250 GeV (p) m = 1300 GeV

Figure B.21: Modeling comparison of nominal and alternative PNN score distributions in the signal region for matrix element.

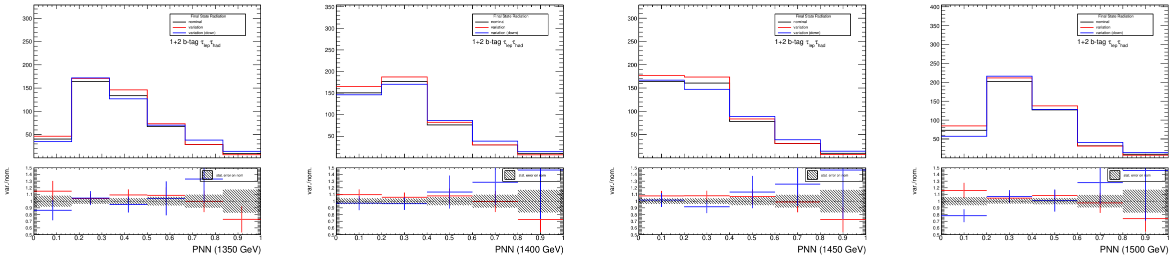

(a) m = 1350 GeV (b) m = 1400 GeV (c) m = 1450 GeV (d) m = 1500 GeV

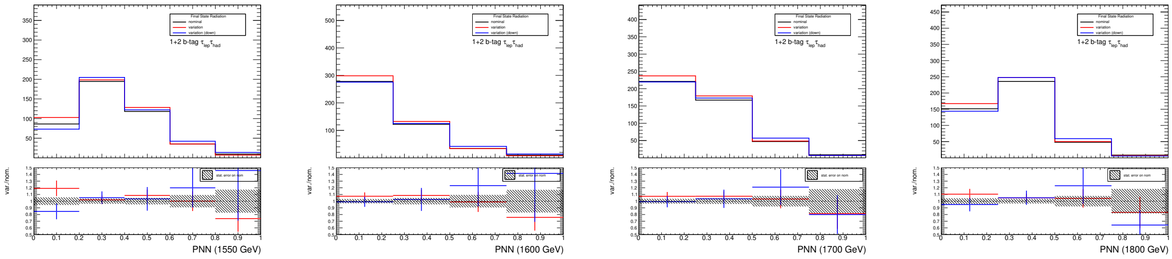

(e) m = 1550 GeV (f) m = 1600 GeV (g) m = 1700 GeV (h) m = 1800 GeV

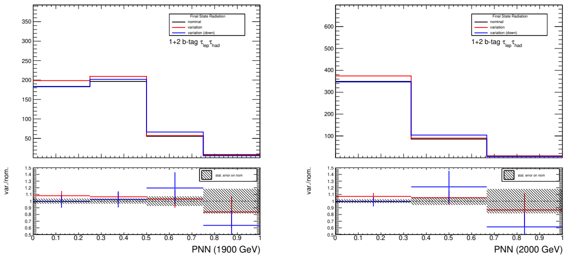

(i) m = 1900 GeV (j) m = 2000 GeV

Figure B.22: Modeling comparison of nominal and alternative PNN score distributions in the signal region for matrix element.

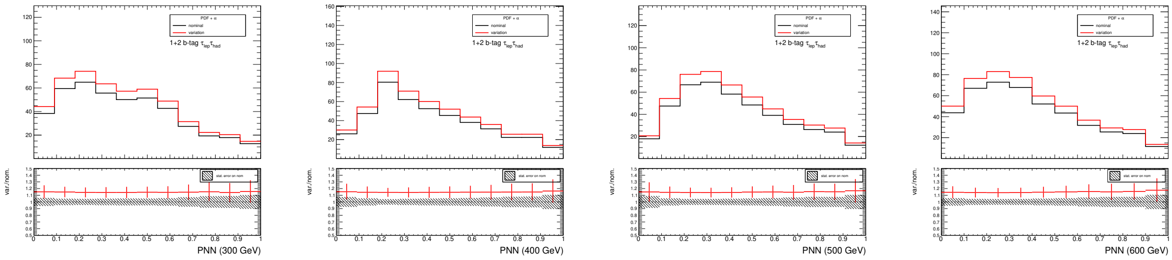

(a) m = 300 GeV (b) m = 400 GeV (c) m = 500 GeV (d) m = 600 GeV

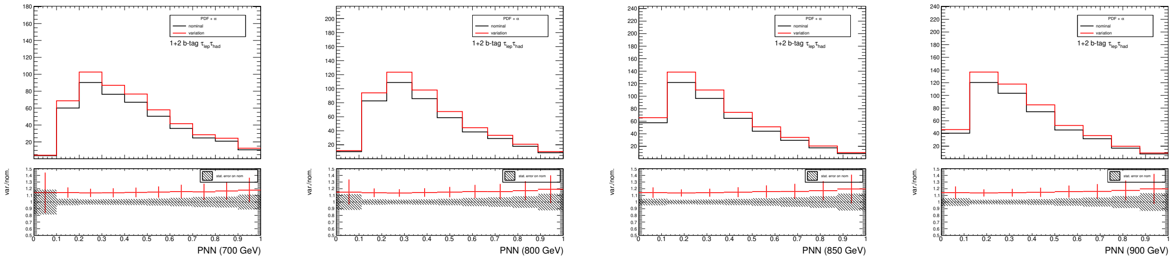

(e) m = 700 GeV (f) m = 800 GeV (g) m = 850 GeV (h) m = 900 GeV

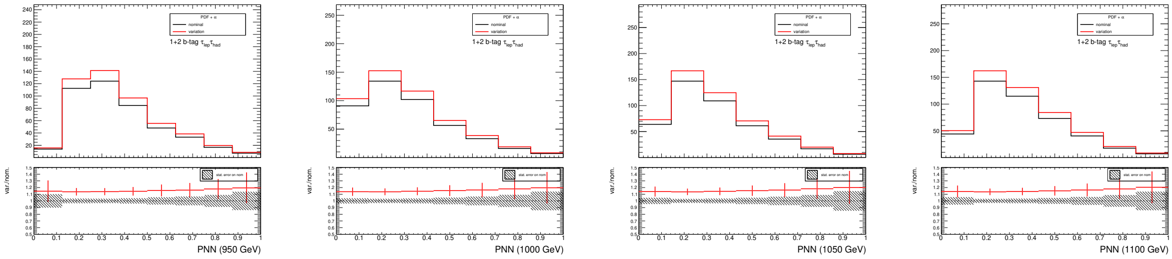

(i) m = 950 GeV (j) m = 1000 GeV (k) m = 1050 GeV (l) m = 1100 GeV

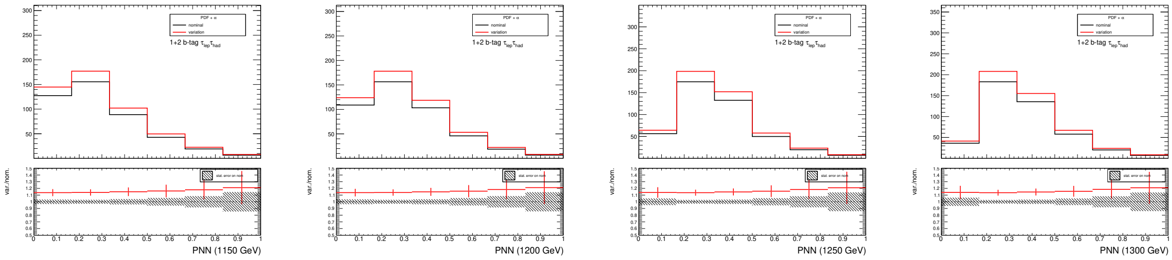

(m) m = 1150 GeV (n) m = 1200 GeV (o) m = 1250 GeV (p) m = 1300 GeV

Figure B.23: Modeling comparison of nominal and alternative PNN score distributions in the signal region for matrix element.

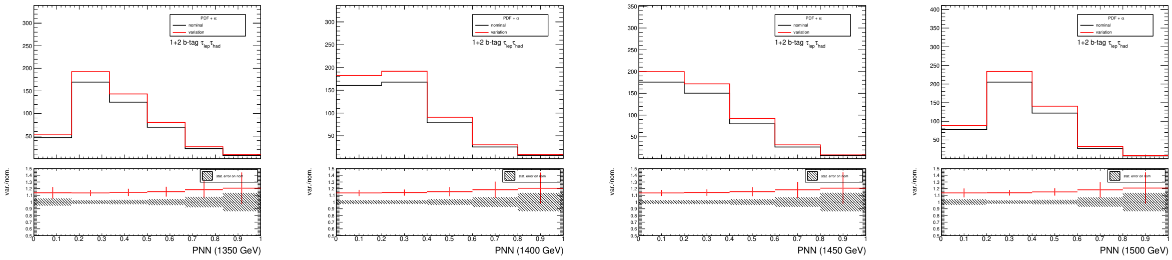

(a) m = 1350 GeV (b) m = 1400 GeV (c) m = 1450 GeV (d) m = 1500 GeV

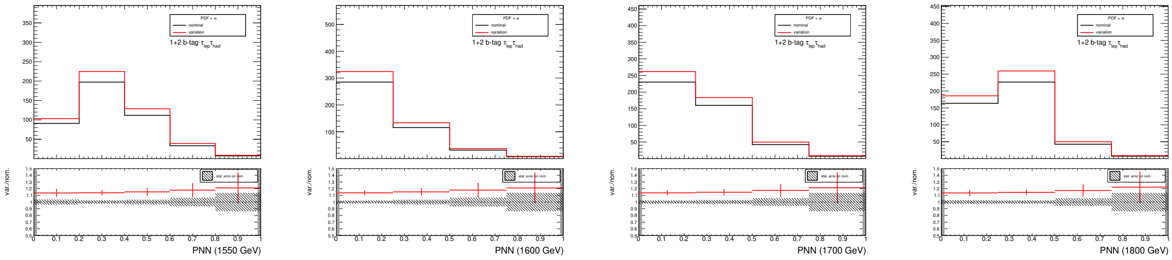

(e) m = 1550 GeV (f) m = 1600 GeV (g) m = 1700 GeV (h) m = 1800 GeV

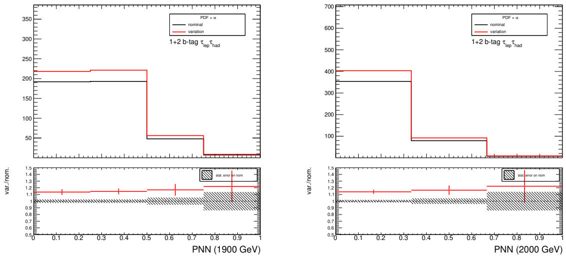

(i) m = 1900 GeV (j) m = 2000 GeV

Figure B.24: Modeling comparison of nominal and alternative PNN score distributions in the signal region for matrix element.

B Experimental Uncertainties

B.1 Definition of Experimental Uncertainties

Table B.3: Systematics uncertainties for electron objects with its technical names in the analysis code and the descriptions

Alias	Description
`EL_EFF_TRIG_TOTAL_1NPCOR_PLUS_UNCOR`	Trigger efficiency uncertainty
`EL_EFF_RECO_TOTAL_1NPCOR_PLUS_UNCOR`	Reconstruction efficiency uncertainty
`EL_EFF_ID_TOTAL_1NPCOR_PLUS_UNCOR`	Identification efficiency uncertainty
`EL_EFF_ISO_TOTAL_1NPCOR_PLUS_UNCOR`	Isolation efficiency uncertainty
`EG_RESOLUTION_ALL`	Energy resolution uncertainty
`EG_SCALE_ALL`	Energy scale uncertainty
`EG_SCALE_AF2`	

C Systematics Effect Summary

This analysis uses the PNN socres as the final discrimiant variables, then this section measures the effects of each systematics as a function of the PNN scores. The score distributions are rebinned according to the strategy Section 9.2. The bin-by-bin effects of each systematic source are summarized by using $m_{\mathrm{LQ}} = 1400$ GeV PNN classifier.

C.1 Modeling Uncertainties

The modeling uncertainties are measured as a function of the PNN score for 1400 GeV signal. The Table B.8 shows the variations from $t\bar{t}$ modelings, and the Table B.9 shows the variations from single-top modelings.

C.2 Experimental Uncertainties

In addition to the modeling uncertainties, the experimental uncertainties are also measured as a function of the PNN score for 1400 GeV signal. The Table B.10 shows the variations from e/γ objects, the Table B.11 shows the variations from muon objects, the Table B.12-Table B.13 shows the variations from tau objects, the Table B.14-Table B.16 shows the variations from jet objects, and the Table B.17 shows the variations from other objects. The `__1up` represents the $+1\sigma$ variation, and the `__1down` represents the -1σ variation.

Table B.4: Systematics uncertainties for muon objects with its technical names in the analysis code and the descriptions

Alias	Description
MUON_EFF_TrigStatUncertainty	Trigger efficiency uncertainty
MUON_EFF_TrigSystUncertainty	
MUON_EFF_RECO_STAT	Reconstruction efficiency uncertainty
MUON_EFF_RECO_SYS	
MUON_EFF_RECO_STAT_LOWPT	
MUON_EFF_RECO_SYS_LOWPT	
MUON_EFF_ISO_STAT	Isolation efficiency uncertainty
MUON_EFF_ISO_SYS	
MUON_EFF_TTVA_STAT	Track-to-vertex association uncertainty
MUON_EFF_TTVA_SYS	
MUON_ID	Momemtum resolution uncertainty from ID
MUON_MS	Momentum resolution uncertainty from MS
MUON_SAGITTA_RHO	Charge dependent momentum scale uncertainty
MUON_SAGITTA_RESBIAS	
MUON_SCALE	Momentum scale uncertainty

Table B.5: Systematics uncertainties for τ_{had} objects with its technical names in the analysis code and the descriptions

Alias	Description
TAUS_TRUEHADTAU_EFF_RECO_HIGHPT	Reconstruction efficiency uncertainty
TAUS_TRUEHADTAU_EFF_RECO_TOTAL	
TAUS_TRUEHADTAU_EFF_RNNID_(1,3)PRONGSTATSYSTPT2025	Identification efficiency uncertainty
TAUS_TRUEHADTAU_EFF_RNNID_(1,3)PRONGSTATSYSTPT2530	
TAUS_TRUEHADTAU_EFF_RNNID_(1,3)PRONGSTATSYSTPT3040	
TAUS_TRUEHADTAU_EFF_RNNID_(1,3)PRONGSTATSYSTPTGE40	
TAUS_TRUEHADTAU_EFF_RNNID_HIGHPT	
TAUS_TRUEHADTAU_EFF_RNNID_SYST	
TAUS_TRUEHADTAU_SME_TES_INSITUEXP	TES uncertainty
TAUS_TRUEHADTAU_SME_TES_INSITUFIT	
TAUS_TRUEHADTAU_SME_TES_MODEL_CLOSURE	
TAUS_TRUEHADTAU_SME_TES_PHYSICSLIST	
TAUS_TRUEELECTRON_EFF_ELEBDT_STAT	Electron veto efficiency uncertainty
TAUS_TRUEELECTRON_EFF_ELEBDT_SYST	
TAUS_TRUEHADTAU_EFF_ELEOLR_TOTAL	

Table B.6: Systematics uncertainties for E_T^{miss} objects with its technical names in the analysis code and the descriptions

Alias	Description
`MET_SoftTrk_ResoPara`	Track-based soft term related longitudinal resolution uncertainty
`MET_SoftTrk_ResoPerp`	Track-based soft term related transverse resolution uncertainty
`MET_SoftTrk_Scale(Up,Down)`	Track-based soft term related longitudinal scale uncertainty

Table B.7: Systematics uncertainties for jets objects with its technical names in the analysis code and the descriptions

Alias	Description
`JET_EtaIntercalibration_Modelling`	Energy scale uncertainty on eta-intercalibration (modeling)
`JET_EtaIntercalibration_TotalStat`	Energy scale uncertainty on eta-intercalibrations (statistics/method)
`JET_EtaIntercalibration_NonClosure_highE`	Energy scale uncertainty on eta-intercalibrations (non-closure)
`JET_EtaIntercalibration_NonClosure_negEta`	
`JET_EtaIntercalibration_NonClosure_posEta`	
`JET_Pileup_OffsetMu`	Energy scale uncertainty on pile-up (mu dependent)
`JET_Pileup_OffsetNPV`	Energy scale uncertainty on pile-up (NPV dependent)
`JET_Pileup_PtTerm`	Energy scale uncertainty on pile-up (pt term)
`JET_Pileup_RhoTopology`	Energy scale uncertainty on pile-up (density ρ)
`JET_Flavor_Composition`	Energy scale uncertainty on flavour composition
`JET_Flavor_Response`	Energy scale uncertainty on samples' flavour response
`JET_PunchThrough_MC16`	Energy scale uncertainty for punch-through jets
`JET_BJES_Response`	Energy scale uncertainty on b-jets
`JET_EffectiveNP_Detector[1,2]`	Energy scale uncertainty from the in situ analyses splits into 8 components
`JET_EffectiveNP_Mixed[1,3]`	
`JET_EffectiveNP_Modelling[1,4]`	
`JET_EffectiveNP_Statistical[1,6]`	
`JET_SingleParticle_HighPt`	Energy scale uncertainty from the behaviour of high-p_{T} jets
`JET_EtaIntercalibration_NonClosure_2018data`	
`JET_JER_DataVsMC_MC16`	Energy resolution uncertainty, each for both MC and pseudo-data
`JET_JER_EffectiveNP_[1,11]`	
`JET_JER_EffectiveNP_12restTerm`	
`JET_JVT_EFF`	JVT efficiency uncertainty
`JET_FJVT_EFF`	
`FT_EFF_Eigen_(B,C,Light)_[0,2]`	b-tagging efficiency uncertainties
`FT_EFF_extrapolation`	b-tagging efficiency uncertainty on the extrapolation to high-p_{T} jets
`FT_EFF_extrapolation_from_charm`	b-tagging efficiency uncertainty on tau jets

Table B.8: Systematics uncertainties from $t\bar{t}$ modelings as a function of the PNN scores.

Source	bin=1	bin=2	bin=3	bin=4	bin=5
ME	1.018	0.995	0.887	0.805	0.439
PS	0.989	1.005	1.058	1.149	1.314
ISR up	0.965	1.041	1.115	1.218	1.770
ISR down	1.020	0.981	0.909	0.914	0.937
FSR up	0.989	1.038	0.960	0.661	2.968
FSR down	0.999	0.994	1.029	1.036	0.938
PDF	0.949	1.039	1.249	1.409	1.414

Table B.9: Systematics uncertainties from single-top modelings as a function of the PNN scores.

Source	bin=1	bin=2	bin=3	bin=4	bin=5
ME	1.179	0.980	0.950	0.541	0.232
PS	1.030	0.993	1.075	0.782	0.694
ISR up	0.913	0.981	1.129	1.192	1.150
ISR down	1.080	1.007	0.900	0.838	0.851
FSR up	1.039	0.983	1.024	0.920	0.721
FSR down	0.933	0.943	1.120	1.261	1.386
PDF	1.039	0.977	1.029	0.920	0.794
Wt	1.512	0.967	0.482	0.143	0.019

Table B.10: Systematics uncertainties effects from e/γ as a function of the PNN scores.

Source	bin=1	bin=2	bin=3	bin=4	bin=5
SysEG_RESOLUTION_ALL__1up	1.000	0.998	1.002	1.000	1.000
SysEG_RESOLUTION_ALL__1down	0.999	1.000	1.001	1.000	0.999
SysEG_SCALE_AF2__1up	1.000	1.000	1.000	1.000	1.000
SysEG_SCALE_AF2__1down	1.000	1.000	1.000	1.000	1.000
SysEG_SCALE_ALL__1up	0.999	1.003	1.002	1.003	0.999
SysEG_SCALE_ALL__1down	1.000	0.996	0.999	1.000	1.000
SysEL_EFF_ID_TOTAL_1NPCOR_PLUS_UNCOR__1up	1.000	1.001	0.999	1.000	0.998
SysEL_EFF_ID_TOTAL_1NPCOR_PLUS_UNCOR__1down	1.000	1.001	0.999	1.000	0.998
SysEL_EFF_Iso_TOTAL_1NPCOR_PLUS_UNCOR__1up	1.000	1.001	0.999	1.000	0.998
SysEL_EFF_Iso_TOTAL_1NPCOR_PLUS_UNCOR__1down	1.000	1.001	0.999	1.000	0.998
SysEL_EFF_Reco_TOTAL_1NPCOR_PLUS_UNCOR__1up	1.000	1.001	0.999	1.000	0.998
SysEL_EFF_Reco_TOTAL_1NPCOR_PLUS_UNCOR__1down	1.000	1.001	0.999	1.000	0.998
SysEL_EFF_TriggerEff_TOTAL_1NPCOR_PLUS_UNCOR__1up	1.000	1.001	0.999	1.000	0.998
SysEL_EFF_TriggerEff_TOTAL_1NPCOR_PLUS_UNCOR__1down	1.000	1.001	0.999	1.000	0.998
SysEL_EFF_Trigger_TOTAL_1NPCOR_PLUS_UNCOR__1up	1.001	1.002	1.000	1.001	0.999
SysEL_EFF_Trigger_TOTAL_1NPCOR_PLUS_UNCOR__1down	0.999	1.000	0.998	0.999	0.997

Table B.11: Systematics uncertainties effects from muon as a function of the PNN scores.

Source	bin=1	bin=2	bin=3	bin=4	bin=5
SysMUON_EFF_ISO_STAT__1up	1.000	1.001	0.999	1.000	0.998
SysMUON_EFF_ISO_STAT__1down	1.000	1.001	0.999	1.000	0.998
SysMUON_EFF_ISO_SYS__1up	1.000	1.001	0.999	1.000	0.998
SysMUON_EFF_ISO_SYS__1down	1.000	1.001	0.999	1.000	0.998
SysMUON_EFF_RECO_STAT__1up	1.000	1.001	0.999	1.000	0.998
SysMUON_EFF_RECO_STAT__1down	1.000	1.001	0.999	1.000	0.998
SysMUON_EFF_RECO_STAT_LOWPT__1up	1.000	1.001	0.999	1.000	0.998
SysMUON_EFF_RECO_STAT_LOWPT__1down	1.000	1.001	0.999	1.000	0.998
SysMUON_EFF_RECO_SYS__1up	1.000	1.001	0.999	1.000	0.998
SysMUON_EFF_RECO_SYS__1down	1.000	1.001	0.999	1.000	0.998
SysMUON_EFF_RECO_SYS_LOWPT__1up	1.000	1.001	0.999	1.000	0.998
SysMUON_EFF_RECO_SYS_LOWPT__1down	1.000	1.001	0.999	1.000	0.998
SysMUON_EFF_TTVA_STAT__1up	1.000	1.001	0.999	1.000	0.998
SysMUON_EFF_TTVA_STAT__1down	1.000	1.001	0.999	1.000	0.998
SysMUON_EFF_TTVA_SYS__1up	1.000	1.001	0.999	1.000	0.998
SysMUON_EFF_TTVA_SYS__1down	1.000	1.001	0.999	1.000	0.998
SysMUON_ID__1up	0.999	1.002	1.000	0.998	0.997
SysMUON_ID__1down	1.001	1.000	0.997	1.002	0.996
SysMUON_MS__1up	1.000	1.001	1.000	0.998	0.998
SysMUON_MS__1down	1.000	1.001	0.997	1.000	0.998
SysMUON_SAGITTA_RESBIAS__1up	1.001	1.000	0.991	0.994	1.009
SysMUON_SAGITTA_RESBIAS__1down	1.001	0.999	0.994	1.001	0.996
SysMUON_SAGITTA_RHO__1up	1.000	1.001	0.999	1.000	0.998
SysMUON_SAGITTA_RHO__1down	1.000	1.001	0.999	1.000	0.998
SysMUON_SCALE__1up	1.000	1.001	1.000	0.997	0.996
SysMUON_SCALE__1down	1.000	1.001	0.998	1.000	0.998

Table B.12: Systematics uncertainties effects from tau as a function of the PNN scores.

Source	bin=1	bin=2	bin=3	bin=4	bin=5
SysTAUS_TRUEELECTRON_EFF_ELEBDT_STAT__1up	1.000	1.001	0.999	1.000	0.998
SysTAUS_TRUEELECTRON_EFF_ELEBDT_STAT__1down	1.000	1.001	0.999	1.000	0.998
SysTAUS_TRUEELECTRON_EFF_ELEBDT_SYST__1up	1.000	1.001	0.999	1.000	0.998
SysTAUS_TRUEELECTRON_EFF_ELEBDT_SYST__1down	1.000	1.001	0.999	1.000	0.998
SysTAUS_TRUEHADTAU_EFF_ELEOLR_TOTAL__1up	1.016	1.017	1.017	1.017	1.012
SysTAUS_TRUEHADTAU_EFF_ELEOLR_TOTAL__1down	0.984	0.985	0.981	0.983	0.984
SysTAUS_TRUEHADTAU_EFF_RECO_TOTAL__1up	1.007	1.008	1.006	1.006	1.004
SysTAUS_TRUEHADTAU_EFF_RECO_TOTAL__1down	0.993	0.994	0.992	0.993	0.991
SysTAUS_TRUEHADTAU_EFF_RNNID_1PRONGSTATSYSTPT2025__1up	1.000	1.001	0.999	1.000	0.998
SysTAUS_TRUEHADTAU_EFF_RNNID_1PRONGSTATSYSTPT2025__1down	1.000	1.001	0.999	1.000	0.998
SysTAUS_TRUEHADTAU_EFF_RNNID_1PRONGSTATSYSTPT2530__1up	1.000	1.001	0.999	1.000	0.998
SysTAUS_TRUEHADTAU_EFF_RNNID_1PRONGSTATSYSTPT2530__1down	1.000	1.001	0.999	1.000	0.998
SysTAUS_TRUEHADTAU_EFF_RNNID_1PRONGSTATSYSTPT3040__1up	1.000	1.001	0.999	1.000	0.998
SysTAUS_TRUEHADTAU_EFF_RNNID_1PRONGSTATSYSTPT3040__1down	1.000	1.001	0.999	1.000	0.998
SysTAUS_TRUEHADTAU_EFF_RNNID_1PRONGSTATSYSTPTGE40__1up	1.005	1.006	1.004	1.005	1.002
SysTAUS_TRUEHADTAU_EFF_RNNID_1PRONGSTATSYSTPTGE40__1down	0.995	0.996	0.994	0.995	0.993
SysTAUS_TRUEHADTAU_EFF_RNNID_3PRONGSTATSYSTPT2025__1up	1.000	1.001	0.999	1.000	0.998
SysTAUS_TRUEHADTAU_EFF_RNNID_3PRONGSTATSYSTPT2025__1down	1.000	1.001	0.999	1.000	0.998
SysTAUS_TRUEHADTAU_EFF_RNNID_3PRONGSTATSYSTPT2530__1up	1.000	1.001	0.999	1.000	0.998
SysTAUS_TRUEHADTAU_EFF_RNNID_3PRONGSTATSYSTPT2530__1down	1.000	1.001	0.999	1.000	0.998
SysTAUS_TRUEHADTAU_EFF_RNNID_3PRONGSTATSYSTPT3040__1up	1.000	1.001	0.999	1.000	0.998
SysTAUS_TRUEHADTAU_EFF_RNNID_3PRONGSTATSYSTPT3040__1down	1.000	1.001	0.999	1.000	0.998
SysTAUS_TRUEHADTAU_EFF_RNNID_3PRONGSTATSYSTPTGE40__1up	1.002	1.003	1.001	1.002	1.000
SysTAUS_TRUEHADTAU_EFF_RNNID_3PRONGSTATSYSTPTGE40__1down	0.998	0.999	0.997	0.998	0.995
SysTAUS_TRUEHADTAU_EFF_RNNID_HIGHPT__1up	1.003	1.005	1.006	1.010	1.014
SysTAUS_TRUEHADTAU_EFF_RNNID_HIGHPT__1down	0.997	0.997	0.992	0.989	0.982
SysTAUS_TRUEHADTAU_EFF_RNNID_SYST__1up	1.020	1.021	1.018	1.018	1.015
SysTAUS_TRUEHADTAU_EFF_RNNID_SYST__1down	0.980	0.981	0.979	0.981	0.980
SysTAUS_TRUEHADTAU_EFF_TRIGGER_STATDATA161718__1up	1.000	1.001	0.999	1.000	0.998
SysTAUS_TRUEHADTAU_EFF_TRIGGER_STATDATA161718__1down	1.000	1.001	0.999	1.000	0.998
SysTAUS_TRUEHADTAU_EFF_TRIGGER_STATDATA1718__1up	1.000	1.001	0.999	1.000	0.998
SysTAUS_TRUEHADTAU_EFF_TRIGGER_STATDATA1718__1down	1.000	1.001	0.999	1.000	0.998
SysTAUS_TRUEHADTAU_EFF_TRIGGER_STATDATA2016__1up	1.000	1.001	0.999	1.000	0.998
SysTAUS_TRUEHADTAU_EFF_TRIGGER_STATDATA2016__1down	1.000	1.001	0.999	1.000	0.998
SysTAUS_TRUEHADTAU_EFF_TRIGGER_STATDATA2018__1up	1.000	1.001	0.999	1.000	0.998
SysTAUS_TRUEHADTAU_EFF_TRIGGER_STATDATA2018__1down	1.000	1.001	0.999	1.000	0.998
SysTAUS_TRUEHADTAU_EFF_TRIGGER_STATDATA2018AFTTS1__1up	1.000	1.001	0.999	1.000	0.998
SysTAUS_TRUEHADTAU_EFF_TRIGGER_STATDATA2018AFTTS1__1down	1.000	1.001	0.999	1.000	0.998
SysTAUS_TRUEHADTAU_EFF_TRIGGER_STATMC161718__1up	1.000	1.001	0.999	1.000	0.998
SysTAUS_TRUEHADTAU_EFF_TRIGGER_STATMC161718__1down	1.000	1.001	0.999	1.000	0.998
SysTAUS_TRUEHADTAU_EFF_TRIGGER_STATMC1718__1up	1.000	1.001	0.999	1.000	0.998
SysTAUS_TRUEHADTAU_EFF_TRIGGER_STATMC1718__1down	1.000	1.001	0.999	1.000	0.998
SysTAUS_TRUEHADTAU_EFF_TRIGGER_STATMC2016__1up	1.000	1.001	0.999	1.000	0.998
SysTAUS_TRUEHADTAU_EFF_TRIGGER_STATMC2016__1down	1.000	1.001	0.999	1.000	0.998
SysTAUS_TRUEHADTAU_EFF_TRIGGER_STATMC2018__1up	1.000	1.001	0.999	1.000	0.998

Table B.13: Systematics uncertainties effects from tau as a function of the PNN scores.

Source	bin=1	bin=2	bin=3	bin=4	bin=5
SysTAUS_TRUEHADTAU_EFF_TRIGGER_STATDATA1718__1up	1.000	1.001	0.999	1.000	0.998
SysTAUS_TRUEHADTAU_EFF_TRIGGER_STATDATA1718__1down	1.000	1.001	0.999	1.000	0.998
SysTAUS_TRUEHADTAU_EFF_TRIGGER_STATDATA2016__1up	1.000	1.001	0.999	1.000	0.998
SysTAUS_TRUEHADTAU_EFF_TRIGGER_STATDATA2016__1down	1.000	1.001	0.999	1.000	0.998
SysTAUS_TRUEHADTAU_EFF_TRIGGER_STATDATA2018__1up	1.000	1.001	0.999	1.000	0.998
SysTAUS_TRUEHADTAU_EFF_TRIGGER_STATDATA2018__1down	1.000	1.001	0.999	1.000	0.998
SysTAUS_TRUEHADTAU_EFF_TRIGGER_STATDATA2018AFTTS1__1up	1.000	1.001	0.999	1.000	0.998
SysTAUS_TRUEHADTAU_EFF_TRIGGER_STATDATA2018AFTTS1__1down	1.000	1.001	0.999	1.000	0.998
SysTAUS_TRUEHADTAU_EFF_TRIGGER_STATMC161718__1up	1.000	1.001	0.999	1.000	0.998
SysTAUS_TRUEHADTAU_EFF_TRIGGER_STATMC161718__1down	1.000	1.001	0.999	1.000	0.998
SysTAUS_TRUEHADTAU_EFF_TRIGGER_STATMC1718__1up	1.000	1.001	0.999	1.000	0.998
SysTAUS_TRUEHADTAU_EFF_TRIGGER_STATMC1718__1down	1.000	1.001	0.999	1.000	0.998
SysTAUS_TRUEHADTAU_EFF_TRIGGER_STATMC2016__1up	1.000	1.001	0.999	1.000	0.998
SysTAUS_TRUEHADTAU_EFF_TRIGGER_STATMC2016__1down	1.000	1.001	0.999	1.000	0.998
SysTAUS_TRUEHADTAU_EFF_TRIGGER_STATMC2018__1up	1.000	1.001	0.999	1.000	0.998
SysTAUS_TRUEHADTAU_EFF_TRIGGER_STATMC2018__1down	1.000	1.001	0.999	1.000	0.998
SysTAUS_TRUEHADTAU_EFF_TRIGGER_STATMC2018AFTTS1__1up	1.000	1.001	0.999	1.000	0.998
SysTAUS_TRUEHADTAU_EFF_TRIGGER_STATMC2018AFTTS1__1down	1.000	1.001	0.999	1.000	0.998
SysTAUS_TRUEHADTAU_EFF_TRIGGER_SYST161718__1up	1.000	1.001	0.999	1.000	0.998
SysTAUS_TRUEHADTAU_EFF_TRIGGER_SYST161718__1down	1.000	1.001	0.999	1.000	0.998
SysTAUS_TRUEHADTAU_EFF_TRIGGER_SYST1718__1up	1.000	1.001	0.999	1.000	0.998
SysTAUS_TRUEHADTAU_EFF_TRIGGER_SYST1718__1down	1.000	1.001	0.999	1.000	0.998
SysTAUS_TRUEHADTAU_EFF_TRIGGER_SYST2016__1up	1.000	1.001	0.999	1.000	0.998
SysTAUS_TRUEHADTAU_EFF_TRIGGER_SYST2016__1down	1.000	1.001	0.999	1.000	0.998
SysTAUS_TRUEHADTAU_EFF_TRIGGER_SYST2018__1up	1.000	1.001	0.999	1.000	0.998
SysTAUS_TRUEHADTAU_EFF_TRIGGER_SYST2018__1down	1.000	1.001	0.999	1.000	0.998
SysTAUS_TRUEHADTAU_EFF_TRIGGER_SYST2018AFTTS1__1up	1.000	1.001	0.999	1.000	0.998
SysTAUS_TRUEHADTAU_EFF_TRIGGER_SYST2018AFTTS1__1down	1.000	1.001	0.999	1.000	0.998
SysTAUS_TRUEHADTAU_EFF_TRIGGER_SYSTMU161718__1up	1.000	1.001	0.999	1.000	0.998
SysTAUS_TRUEHADTAU_EFF_TRIGGER_SYSTMU161718__1down	1.000	1.001	0.999	1.000	0.998
SysTAUS_TRUEHADTAU_EFF_TRIGGER_SYSTMU1718__1up	1.000	1.001	0.999	1.000	0.998
SysTAUS_TRUEHADTAU_EFF_TRIGGER_SYSTMU1718__1down	1.000	1.001	0.999	1.000	0.998
SysTAUS_TRUEHADTAU_EFF_TRIGGER_SYSTMU2016__1up	1.000	1.001	0.999	1.000	0.998
SysTAUS_TRUEHADTAU_EFF_TRIGGER_SYSTMU2016__1down	1.000	1.001	0.999	1.000	0.998
SysTAUS_TRUEHADTAU_EFF_TRIGGER_SYSTMU2018__1up	1.000	1.001	0.999	1.000	0.998
SysTAUS_TRUEHADTAU_EFF_TRIGGER_SYSTMU2018__1down	1.000	1.001	0.999	1.000	0.998
SysTAUS_TRUEHADTAU_EFF_TRIGGER_SYSTMU2018AFTTS1__1up	1.000	1.001	0.999	1.000	0.998
SysTAUS_TRUEHADTAU_EFF_TRIGGER_SYSTMU2018AFTTS1__1down	1.000	1.001	0.999	1.000	0.998
SysTAUS_TRUEHADTAU_SME_TES_INSITUEXP__1up	1.000	1.001	0.999	1.000	0.998
SysTAUS_TRUEHADTAU_SME_TES_INSITUEXP__1down	1.000	1.001	0.999	1.000	0.998
SysTAUS_TRUEHADTAU_SME_TES_INSITUFIT__1up	1.000	1.001	0.999	1.000	0.998
SysTAUS_TRUEHADTAU_SME_TES_INSITUFIT__1down	1.000	1.001	0.999	1.000	0.998
SysTAUS_TRUEHADTAU_SME_TES_MODEL_CLOSURE__1up	1.004	1.005	1.006	1.009	0.996
SysTAUS_TRUEHADTAU_SME_TES_MODEL_CLOSURE__1down	0.993	0.995	0.992	0.989	0.998
SysTAUS_TRUEHADTAU_SME_TES_PHYSICSLIST__1up	1.013	1.011	1.018	1.009	1.024
SysTAUS_TRUEHADTAU_SME_TES_PHYSICSLIST__1down	0.985	0.986	0.983	0.982	0.988

Table B.14: Systematics uncertainties effects from tau as a function of the PNN scores.

Source	bin=1	bin=2	bin=3	bin=4	bin=5
`SysJET_BJES_Response__1up`	1.004	1.004	1.001	0.997	0.990
`SysJET_BJES_Response__1down`	0.996	0.998	1.003	0.993	0.999
`SysJET_EffectiveNP_Detector1__1up`	1.001	1.002	1.001	1.000	1.000
`SysJET_EffectiveNP_Detector1__1down`	0.999	0.999	1.000	1.000	1.000
`SysJET_EffectiveNP_Detector2__1up`	1.000	1.000	1.000	1.000	1.000
`SysJET_EffectiveNP_Detector2__1down`	1.000	1.000	1.000	1.000	1.000
`SysJET_EffectiveNP_Mixed1__1up`	1.004	1.005	1.010	1.010	1.001
`SysJET_EffectiveNP_Mixed1__1down`	0.995	0.995	0.995	0.980	0.986
`SysJET_EffectiveNP_Mixed2__1up`	0.997	0.997	0.998	1.000	0.999
`SysJET_EffectiveNP_Mixed2__1down`	1.003	1.004	1.005	1.003	0.987
`SysJET_EffectiveNP_Mixed3__1up`	1.000	1.000	1.002	1.003	1.000
`SysJET_EffectiveNP_Mixed3__1down`	1.000	1.000	1.000	1.000	1.000
`SysJET_EffectiveNP_Modelling1__1up`	1.014	1.014	1.006	1.008	0.999
`SysJET_EffectiveNP_Modelling1__1down`	0.987	0.988	0.994	0.994	0.998
`SysJET_EtaIntercalibration_Modelling__1up`	1.008	1.009	1.007	1.010	0.970
`SysJET_EtaIntercalibration_Modelling__1down`	0.992	0.989	0.992	0.993	0.988
`SysJET_JERPD_DataVsMC_MC16__1up`	1.001	1.001	1.000	1.000	0.984
`SysJET_JERPD_DataVsMC_MC16__1down`	1.000	1.000	1.000	1.000	1.000
`SysJET_EffectiveNP_Modelling2__1up`	1.001	1.002	1.003	1.003	1.001
`SysJET_EffectiveNP_Modelling2__1down`	0.999	0.998	0.997	1.002	0.984
`SysJET_EffectiveNP_Modelling3__1up`	0.999	0.998	0.999	1.003	0.987
`SysJET_EffectiveNP_Modelling3__1down`	1.001	1.003	1.001	1.000	1.000
`SysJET_EffectiveNP_Modelling4__1up`	1.000	1.001	1.002	1.000	1.000
`SysJET_EffectiveNP_Modelling4__1down`	1.000	0.999	1.000	1.000	1.000
`SysJET_EffectiveNP_Statistical1__1up`	1.000	1.001	1.003	1.003	1.001
`SysJET_EffectiveNP_Statistical1__1down`	1.000	0.999	0.998	1.000	0.999
`SysJET_EffectiveNP_Statistical2__1up`	0.999	1.000	0.999	1.000	1.000
`SysJET_EffectiveNP_Statistical2__1down`	1.001	1.000	1.001	1.002	0.987
`SysJET_EffectiveNP_Statistical3__1up`	1.000	0.999	0.998	1.000	1.000
`SysJET_EffectiveNP_Statistical3__1down`	1.000	1.002	1.003	1.000	1.000
`SysJET_EffectiveNP_Statistical4__1up`	1.001	1.002	1.001	1.000	1.000
`SysJET_EffectiveNP_Statistical4__1down`	0.999	0.999	1.001	1.000	1.000
`SysJET_EffectiveNP_Statistical5__1up`	1.000	1.001	1.000	1.000	1.000
`SysJET_EffectiveNP_Statistical5__1down`	1.000	1.000	1.000	1.000	1.000
`SysJET_EffectiveNP_Statistical6__1up`	1.000	1.001	1.001	1.000	1.000
`SysJET_EffectiveNP_Statistical6__1down`	1.000	0.999	1.000	1.000	1.000

Table B.15: Systematics uncertainties effects from tau as a function of the PNN scores.

Source	bin=1	bin=2	bin=3	bin=4	bin=5
`SysJET_EtaIntercalibration_NonClosure_2018data__1up`	1.005	1.005	1.008	1.003	0.987
`SysJET_EtaIntercalibration_NonClosure_2018data__1down`	0.995	0.996	0.994	0.996	0.988
`SysJET_EtaIntercalibration_NonClosure_highE__1up`	1.000	1.000	1.000	1.000	1.000
`SysJET_EtaIntercalibration_NonClosure_highE__1down`	1.000	1.000	1.000	1.000	1.000
`SysJET_EtaIntercalibration_NonClosure_negEta__1up`	1.000	1.000	1.000	1.000	1.000
`SysJET_EtaIntercalibration_NonClosure_negEta__1down`	1.000	0.999	1.000	1.000	1.000
`SysJET_EtaIntercalibration_NonClosure_posEta__1up`	1.000	1.000	1.000	1.000	1.000
`SysJET_EtaIntercalibration_NonClosure_posEta__1down`	1.000	1.000	1.001	1.000	1.000
`SysJET_EtaIntercalibration_TotalStat__1up`	1.002	1.002	1.000	1.002	0.987
`SysJET_EtaIntercalibration_TotalStat__1down`	0.998	0.999	0.999	1.000	1.000
`SysJET_Flavor_Composition__1up`	1.011	1.008	1.008	1.010	0.984
`SysJET_Flavor_Composition__1down`	0.989	0.990	0.994	0.998	0.996
`SysJET_Flavor_Response__1up`	0.991	0.989	0.997	0.998	1.001
`SysJET_Flavor_Response__1down`	1.008	1.009	1.009	1.007	0.997
`SysJET_JERMC_DataVsMC_MC16__1up`	1.000	1.000	1.000	1.000	1.000
`SysJET_JERMC_DataVsMC_MC16__1down`	0.997	1.004	0.996	1.015	0.985
`SysJET_JERMC_EffectiveNP_1__1up`	1.006	1.009	1.006	1.001	1.075
`SysJET_JERMC_EffectiveNP_1__1down`	1.000	1.000	1.000	1.000	1.000
`SysJET_JERMC_EffectiveNP_10__1up`	1.001	1.001	1.000	0.997	1.000
`SysJET_JERMC_EffectiveNP_10__1down`	1.002	1.003	1.002	0.997	1.032
`SysJET_JERMC_EffectiveNP_11__1up`	1.001	1.001	1.001	0.997	1.008
`SysJET_JERMC_EffectiveNP_11__1down`	1.001	1.004	1.003	1.005	1.023
`SysJET_JERMC_EffectiveNP_12restTerm__1up`	1.003	1.004	1.004	1.002	1.032
`SysJET_JERMC_EffectiveNP_12restTerm__1down`	1.000	1.000	1.000	1.000	1.000
`SysJET_JERMC_EffectiveNP_2__1up`	1.013	1.011	1.008	0.997	1.099
`SysJET_JERMC_EffectiveNP_2__1down`	0.999	1.001	1.002	1.000	1.000
`SysJET_JERMC_EffectiveNP_3__1up`	1.001	1.002	1.004	0.993	1.039
`SysJET_JERMC_EffectiveNP_3__1down`	1.001	1.007	1.001	1.010	1.005
`SysJET_JERMC_EffectiveNP_4__1up`	1.002	1.005	1.003	0.996	1.060
`SysJET_JERMC_EffectiveNP_4__1down`	1.002	1.004	1.003	1.000	1.012
`SysJET_JERMC_EffectiveNP_5__1up`	1.001	0.999	1.001	1.006	1.002
`SysJET_JERMC_EffectiveNP_5__1down`	1.000	1.008	1.000	0.990	1.046
`SysJET_JERMC_EffectiveNP_6__1up`	0.999	1.002	0.998	1.006	1.021
`SysJET_JERMC_EffectiveNP_6__1down`	1.006	1.008	1.005	0.988	1.014
`SysJET_JERMC_EffectiveNP_7__1up`	1.001	1.003	1.003	0.998	1.012
`SysJET_JERMC_EffectiveNP_7__1down`	1.001	1.002	1.001	0.998	1.047
`SysJET_JERMC_EffectiveNP_8__1up`	1.001	1.001	1.002	1.002	1.000
`SysJET_JERMC_EffectiveNP_8__1down`	1.002	1.002	1.001	1.007	1.012
`SysJET_JERMC_EffectiveNP_9__1up`	1.003	1.005	1.002	0.996	1.014
`SysJET_JERMC_EffectiveNP_9__1down`	1.000	1.001	1.002	1.001	1.020

Table B.16: Systematics uncertainties effects from tau as a function of the PNN scores.

Source	bin=1	bin=2	bin=3	bin=4	bin=5
SysJET_JERPD_EffectiveNP_1__1up	1.000	1.000	1.000	1.000	1.000
SysJET_JERPD_EffectiveNP_1__1down	1.005	1.005	1.003	0.991	1.049
SysJET_JERPD_EffectiveNP_2__1up	1.001	1.001	1.001	0.998	0.998
SysJET_JERPD_EffectiveNP_2__1down	0.999	1.004	1.008	0.983	1.058
SysJET_JERPD_EffectiveNP_3__1up	1.003	1.001	1.008	0.992	0.974
SysJET_JERPD_EffectiveNP_3__1down	1.000	1.001	1.001	0.995	1.000
SysJET_JERPD_EffectiveNP_4__1up	1.003	0.999	1.011	0.985	0.985
SysJET_JERPD_EffectiveNP_4__1down	0.998	1.004	0.999	0.998	1.016
SysJET_JERPD_EffectiveNP_5__1up	1.001	1.004	0.994	0.992	1.038
SysJET_JERPD_EffectiveNP_5__1down	1.002	0.999	1.003	1.002	0.974
SysJET_JERPD_EffectiveNP_6__1up	0.999	1.002	1.010	0.979	1.023
SysJET_JERPD_EffectiveNP_6__1down	1.001	0.999	0.999	1.009	0.978
SysJET_JERPD_EffectiveNP_7__1up	1.001	1.000	0.995	1.004	0.998
SysJET_JERPD_EffectiveNP_7__1down	1.001	1.002	1.004	1.000	0.997
SysJET_JERPD_EffectiveNP_8__1up	0.998	1.004	0.996	1.001	1.024
SysJET_JERPD_EffectiveNP_8__1down	1.002	1.001	1.003	1.001	0.972
SysJET_JERPD_EffectiveNP_9__1up	1.000	1.001	0.999	1.004	0.974
SysJET_JERPD_EffectiveNP_9__1down	1.001	1.003	1.004	0.991	1.010
SysJET_JERPD_EffectiveNP_10__1up	1.000	1.000	0.999	0.997	1.003
SysJET_JERPD_EffectiveNP_10__1down	1.002	1.001	1.001	1.004	0.986
SysJET_JERPD_EffectiveNP_11__1up	1.000	1.003	0.999	0.995	1.010
SysJET_JERPD_EffectiveNP_11__1down	1.001	1.000	1.002	1.006	0.985
SysJET_JERPD_EffectiveNP_12restTerm__1up	1.000	1.000	1.000	1.000	1.000
SysJET_JERPD_EffectiveNP_12restTerm__1down	0.999	1.003	0.997	1.000	0.998
SysJET_Pileup_OffsetMu__1up	1.003	1.006	0.997	0.994	0.996
SysJET_Pileup_OffsetMu__1down	0.997	0.999	0.997	0.996	0.994
SysJET_Pileup_OffsetNPV__1up	1.007	1.008	1.000	1.002	0.985
SysJET_Pileup_OffsetNPV__1down	0.994	0.996	0.997	0.995	0.993
SysJET_Pileup_PtTerm__1up	1.005	1.008	1.003	1.007	0.985
SysJET_Pileup_PtTerm__1down	0.997	0.995	0.995	0.991	1.007
SysJET_Pileup_RhoTopology__1up	1.016	1.014	1.001	1.005	0.983
SysJET_Pileup_RhoTopology__1down	0.985	0.990	0.999	0.991	0.994
SysJET_PunchThrough_MC16__1up	1.000	1.001	1.000	0.999	0.998
SysJET_PunchThrough_MC16__1down	1.000	1.001	0.999	0.997	0.998
SysJET_SingleParticle_HighPt__1up	1.000	1.001	0.999	1.000	0.998
SysJET_SingleParticle_HighPt__1down	1.000	1.001	0.999	1.000	0.998
SysJET_JvtEfficiency__1up	1.000	1.001	0.999	1.000	0.998
SysJET_JvtEfficiency__1down	1.000	1.001	0.999	1.000	0.998
SysJET_fJvtEfficiency__1up	1.000	1.001	0.999	1.000	0.998
SysJET_fJvtEfficiency__1down	1.000	1.001	0.999	1.000	0.998

Table B.17: Systematics uncertainties effects from others as a function of the PNN scores.

Source	bin=1	bin=2	bin=3	bin=4	bin=5
`MET_SoftTrk_ResoPara__1up`	0.997	0.997	1.001	0.993	0.997
`MET_SoftTrk_ResoPerp__1up`	0.997	0.996	0.997	1.006	1.002
`MET_SoftTrk_Scale__1down`	1.003	1.005	1.001	1.004	0.998
`MET_SoftTrk_Scale__1up`	0.995	0.995	0.998	1.001	0.998
`SysPRW_DATASF__1up`	1.000	1.002	0.996	1.005	1.000
`SysPRW_DATASF__1down`	1.000	1.000	1.001	0.995	0.996

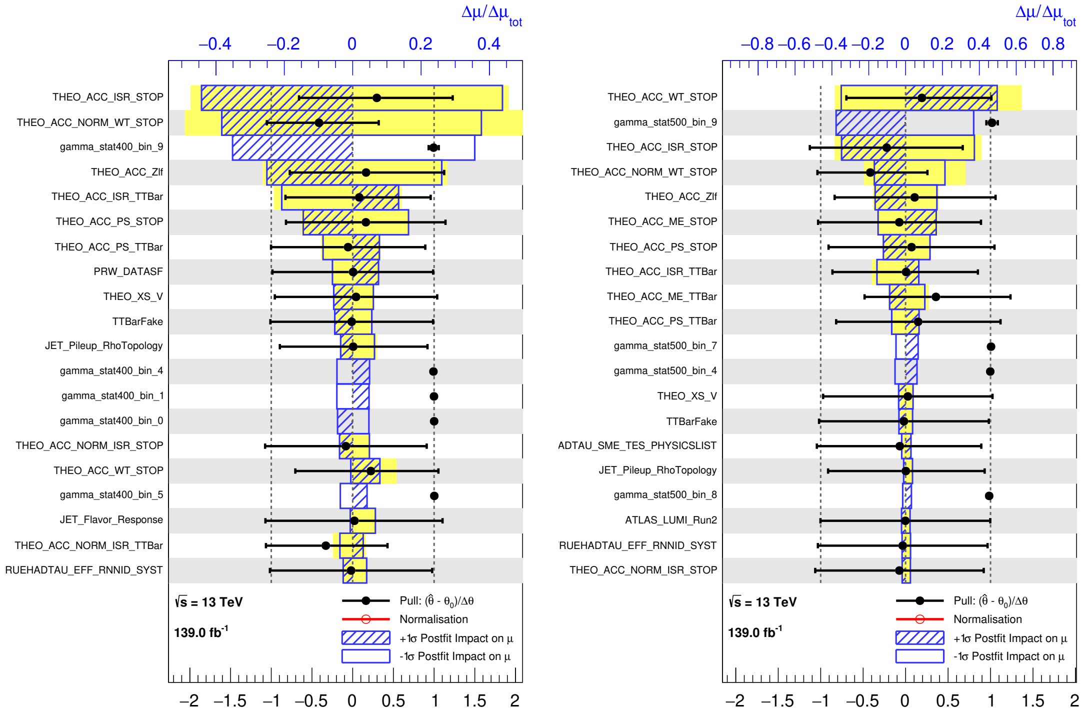

Figure B.25: Impact ranking on the analysis sensitivities and pulls of each nuisance parameter for $m_{\mathrm{LQ}} = 400$ GeV (left) and $m_{\mathrm{LQ}} = 500$ GeV (right).

D Fit Validations

This section shows how each systematics source have impact on the analysis sensitivities in Fig B.25-Fig B.30. The lower x-axis shows the pulls of each nuisance parameter and the upper x-axis shows the impact of each nuisance parameter. The yellow bands represent the pre-fit level impact and the blue hatched bands represent the post-fit level impact.

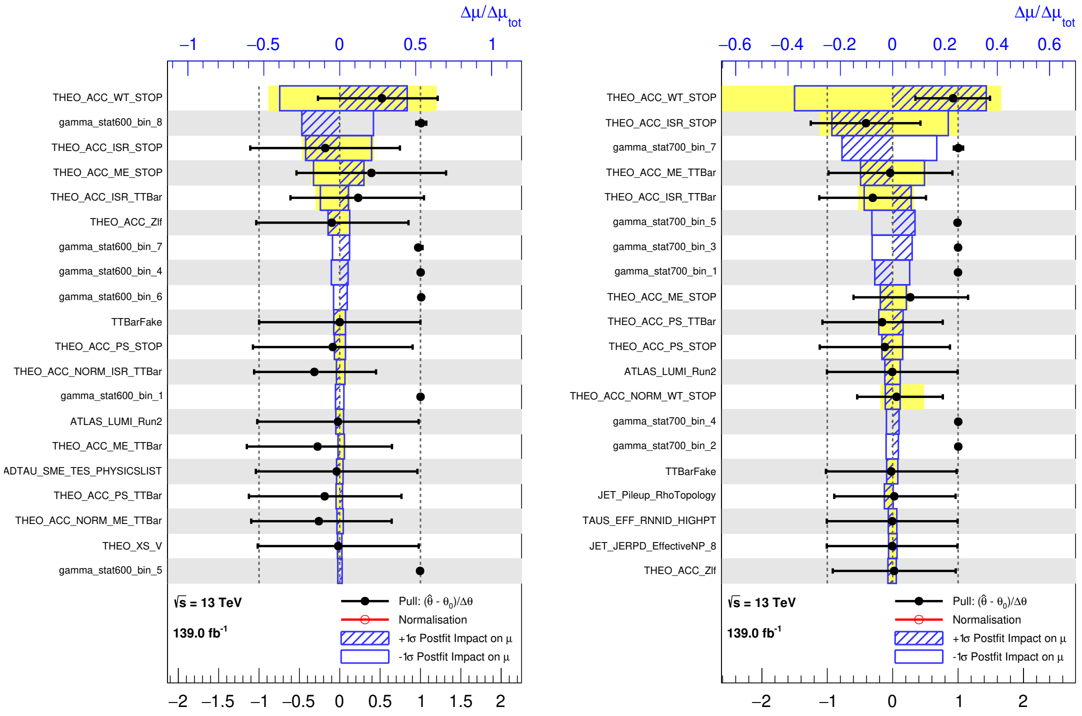

Figure B.26: Impact ranking on the analysis sensitivities and pulls of each nuisance parameter for $m_{\mathrm{LQ}} = 600$ GeV (left) and $m_{\mathrm{LQ}} = 700$ GeV (right).

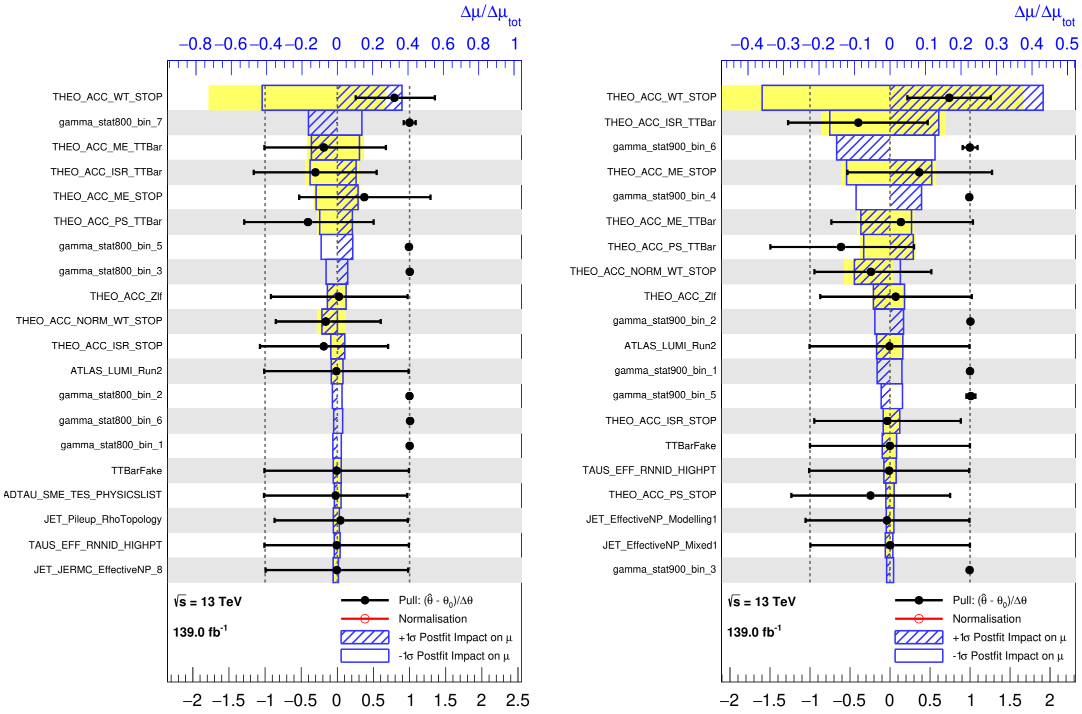

Figure B.27: Impact ranking on the analysis sensitivities and pulls of each nuisance parameter for $m_{\mathrm{LQ}} = 800$ GeV (left) and $m_{\mathrm{LQ}} = 900$ GeV (right).

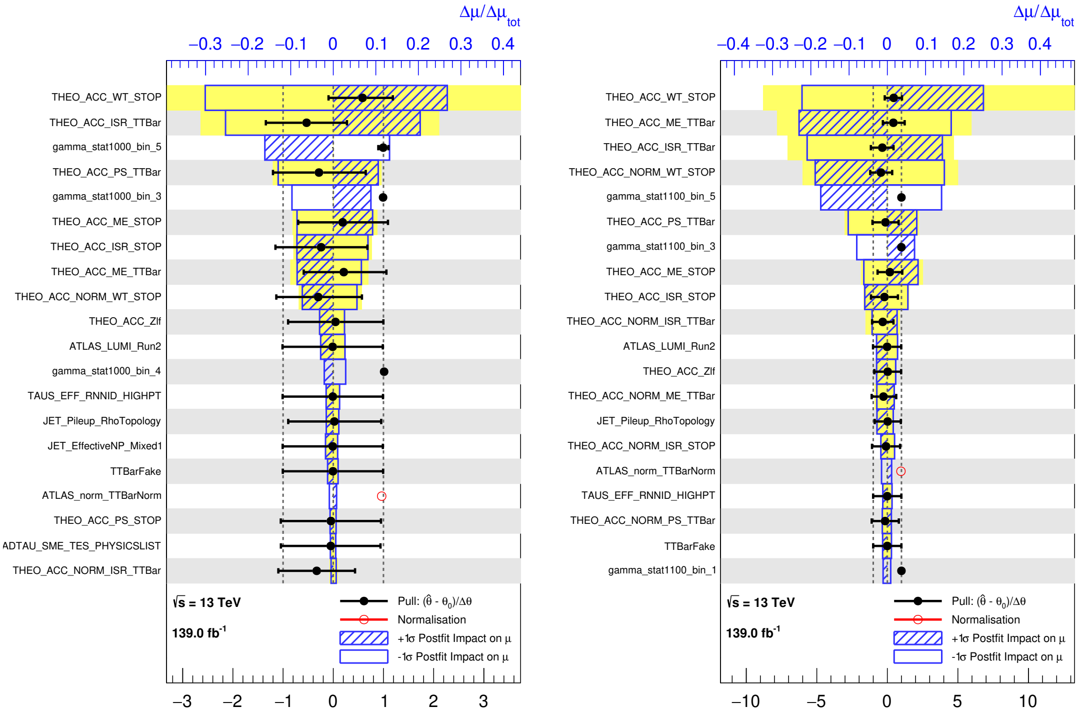

Figure B.28: Impact ranking on the analysis sensitivities and pulls of each nuisance parameter for $m_{\mathrm{LQ}} = 1000$ GeV (left) and $m_{\mathrm{LQ}} = 1100$ GeV (right).

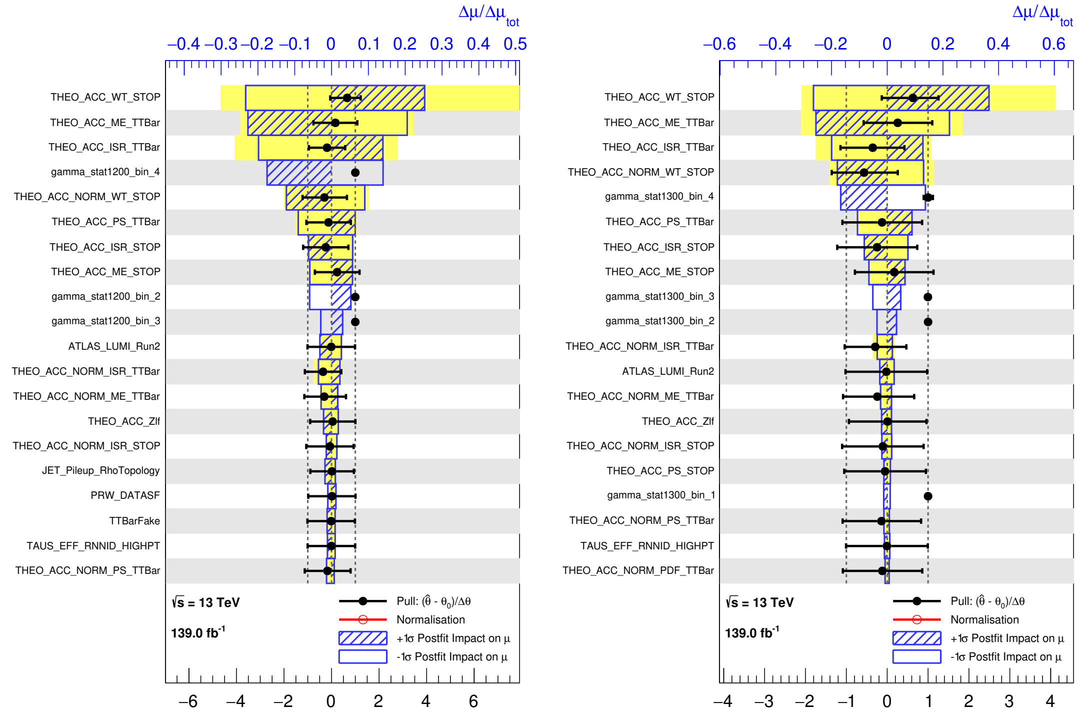

Figure B.29: Impact ranking on the analysis sensitivities and pulls of each nuisance parameter for $m_{\mathrm{LQ}} = 1200$ GeV (left) and $m_{\mathrm{LQ}} = 1300$ GeV (right).

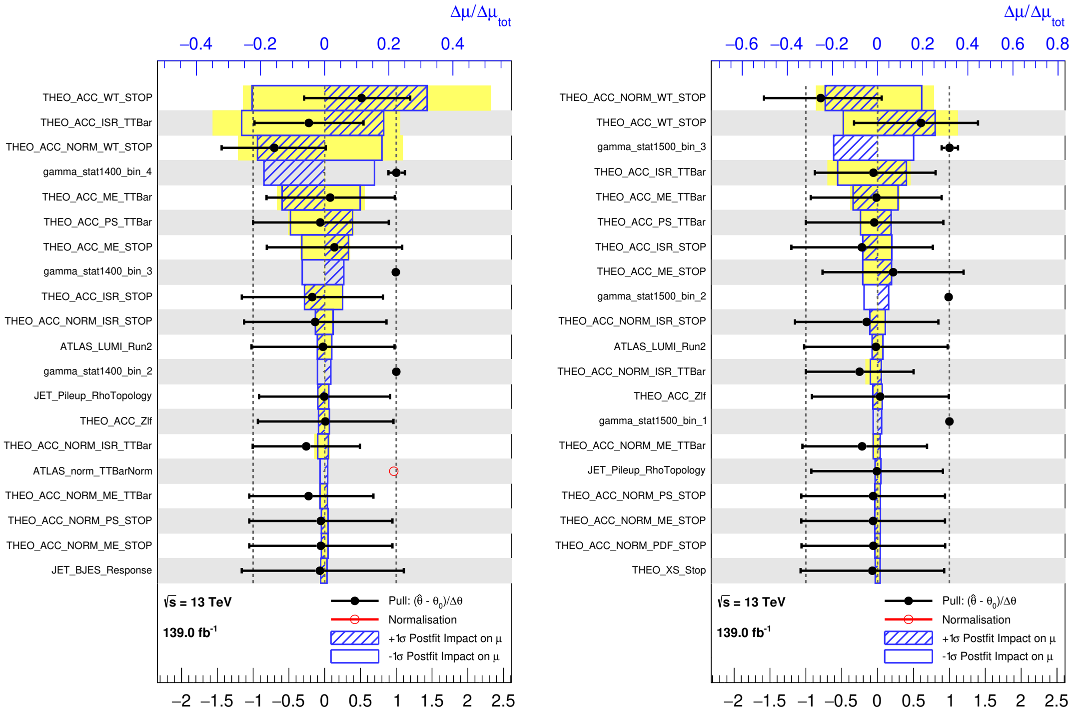

Figure B.30: Impact ranking on the analysis sensitivities and pulls of each nuisance parameter for $m_{\mathrm{LQ}} = 1400$ GeV (left) and $m_{\mathrm{LQ}} = 1500$ GeV (right).

Bibliography

[1] *The Heavy Flavor Averaging Group web page*, URL: https://hflav.web.cern.ch/content/semileptonic-b-decays.

[2] M. Aaboud et al. (The ATLAS Collaboration), *Jet reconstruction and performance using particle flow with the ATLAS Detector*, The European Physical Journal C **77** (2017), URL: http://dx.doi.org/10.1140/epjc/s10052-017-5031-2.

[3] J. C. Pati and A. Salam, *Lepton number as the fourth "color"*, Phys. Rev. D **10** (1974) 275–289, URL: https://link.aps.org/doi/10.1103/PhysRevD.10.275.

[4] B. Schrempp and F. Schrempp, *Light Leptoquarks*, Phys. Lett. B **153** (1985) 101–107.

[5] H. Georgi and S. L. Glashow, *Unity of All Elementary-Particle Forces*, Phys. Rev. Lett. **32** (1974) 438–441, URL: https://link.aps.org/doi/10.1103/PhysRevLett.32.438.

[6] H. Georgi, *The State of the Art—Gauge Theories*, AIP Conf. Proc. **23** (1975) 575–582.

[7] E. Farhi and L. Susskind, *Technicolour*, Physics Reports **74** (1981) 277 – 321, URL: http://www.sciencedirect.com/science/article/pii/0370157381901733.

[8] K. Lane and M. V. Ramana, *Walking technicolor signatures at hadron colliders*, Phys. Rev. D **44** (1991) 2678–2700, URL: https://link.aps.org/doi/10.1103/PhysRevD.44.2678.

[9] J. Wudka, *Composite leptoquarks*, Physics Letters B **167** (1986) 337 – 342, URL: http://www.sciencedirect.com/science/article/pii/0370269386903564.

[10] A. Monteux and A. Rajaraman, *B anomalies and leptoquarks at the LHC: Beyond the lepton-quark final state*, Physical Review D **98** (2018), URL: http://dx.doi.org/10.1103/PhysRevD.98.115032.

[11] W. Buchmüller, R. Rückl, and D. Wyler, *Leptoquarks in lepton-quark collisions*, Physics Letters B **191** (1987) 442 – 448, URL: http://www.sciencedirect.com/science/article/pii/037026938790637X.

[12] G. Aad et al. (The ATLAS Collaboration), *The ATLAS Experiment at the CERN Large Hadron Collider*, Journal of Instrumentation **3** (2008) S08003–S08003, URL: https://doi.org/10.1088/1748-0221/3/08/s08003.

[13] M. Aaboud et al. (The ATLAS Collaboration), *Searches for third-generation scalar leptoquarks in $\sqrt{s} = 13$ TeV pp collisions with the ATLAS detector*, Journal of High Energy Physics **2019** (2019), URL: http://dx.doi.org/10.1007/JHEP06(2019)144.

[14] P. Baldi, K. Cranmer, T. Faucett, P. Sadowski, and D. Whiteson, *Parameterized neural networks for high-energy physics*, The European Physical Journal C **76** (2016), URL: http://dx.doi.org/10.1140/epjc/s10052-016-4099-4.

[15] B. P. Roe, H.-J. Yang, J. Zhu, Y. Liu, I. Stancu, and G. McGregor, *Boosted decision trees as an alternative to artificial neural networks for particle identification*, Nuclear Instruments and Methods in Physics Research Section A: Accelerators, Spectrometers, Detectors and Associated Equipment **543** (2005) 577 – 584, URL: http://dx.doi.org/10.1016/j.nima.2004.12.018.

[16] G. Altarelli, *The Standard Model of Particle Physics*, Tech. Rep. hep-ph/0510281. CERN-PH-TH-2005-206, CERN, Geneva, Oct, 2005. URL: https://cds.cern.ch/record/899140.

[17] W. Buchmüller and C. Lüdeling, *Field Theory and Standard Model*, URL: https://cds.cern.ch/record/984122.

[18] J. Woithe, G. J. Wiener, and F. F. V. der Veken, *Let's have a coffee with the Standard Model of particle physics!*, Physics Education **52** (2017) 034001, URL: https://doi.org/10.1088/1361-6552/aa5b25.

[19] A. Bilal, *Lectures on Anomalies*, 2008.

[20] J. Blumlein and R. Ruckl, *Production of scalar and vector leptoquarks in e+ e- annihilation*, Phys. Lett. B **304** (1993) 337–346.

[21] J. Bluemlein, E. Boos, and A. Kryukov, *Leptoquark pair production in hadronic interactions*, Zeitschrift für Physik C **76** (1997) 137–153.

[22] F. Pisano and A. T. Tran, *Anomaly cancellation in a class of chiral flavor gauge models*, in *14th Brazilian Meeting on Particles and Fields*. 7, 1993.

[23] P. Langacker, *Grand unified theories and proton decay*, Physics Reports **72** (1981) 185 – 385, URL: http://www.sciencedirect.com/science/article/pii/0370157381900594.

[24] M. Hirsch, H. Klapdor-Kleingrothaus, and S. Kovalenko, *New low-energy leptoquark interactions*, Physics Letters B **378** (1996) 17 – 22, URL: http://dx.doi.org/10.1016/0370-2693(96)00419-4.

[25] S. Davidson, D. Bailey, and B. A. Campbell, *Model independent constraints on leptoquarks from rare processes*, Zeitschrift for Physik C Particles and Fields **61** (1994) 613 – 643, URL: http://dx.doi.org/10.1007/BF01552629.

[26] D. Acosta and S. K. Blessing, *Leptoquark searches at HERA and the Tevatron*, Ann. Rev. Nucl. Part. Sci. **49** (1999) 389–434.

[27] M. Schmaltz and Y.-M. Zhong, *The leptoquark Hunter' s guide: large coupling*, Journal of High Energy Physics **2019** (2019), URL: http://dx.doi.org/10.1007/JHEP01(2019)132.

[28] J. P. Lees et al. (The BABAR Collaboration), *Measurement of an excess of* $B^- \to D^{(*)}\tau \to \bar{\nu}_\tau$ *decays and implications for charged Higgs bosons*, Physical Review D **88** (2013), URL: `http://dx.doi.org/10.1103/PhysRevD.88.072012`.

[29] S. Hirose et al. (The Belle Collaboration), *Measurement of the* τ *lepton polarization and* $R(D^*)$ *in the decay* $B^- \to D^*\tau \to \bar{\nu_\tau}$ *with one-prong hadronic* τ *decays at Belle*, Physical Review D **97** (2018), URL: `http://dx.doi.org/10.1103/PhysRevD.97.012004`.

[30] R. Aaij et al. (The LHCb Collaboration), *Test of lepton flavor universality by the measurement of the* $B^0 \to D^{*-}\tau + \nu_\tau$ *branching fraction using three-prong* τ *decays*, Physical Review D **97** (2018), URL: `http://dx.doi.org/10.1103/PhysRevD.97.072013`.

[31] M. Krämer, T. Plehn, M. Spira, and P. M. Zerwas, *Pair production of scalar leptoquarks at the CERN LHC*, Phys. Rev. D **71** (2005) 057503, URL: `https://link.aps.org/doi/10.1103/PhysRevD.71.057503`.

[32] A. Belyaev, C. Leroy, R. Mehdiyev, and A. Pukhov, *Leptoquark single and pair production at LHC with CalcHEP/CompHEP in the complete model*, Journal of High Energy Physics **2005** (2005) 005 – 005, URL: `http://dx.doi.org/10.1088/1126-6708/2005/09/005`.

[33] M. Aaboud et al. (The ATLAS Collaboration), *Search for supersymmetry in events with b-tagged jets and missing transverse momentum in pp collisions at* $\sqrt{s} = 13$ *TeV with the ATLAS detector*, Journal of High Energy Physics **2017** (2017), URL: `http://dx.doi.org/10.1007/JHEP11(2017)195`.

[34] M. Aaboud et al. (The ATLAS Collaboration), *Search for top-squark pair production in final states with one lepton, jets, and missing transverse momentum using 36* fb^{-1} *of* $\sqrt{s} = 13$ *TeV pp collision data with the ATLAS detector*, Journal of High Energy Physics **2018** (2018), URL: `http://dx.doi.org/10.1007/JHEP06(2018)108`.

[35] M. Aaboud et al. (The ATLAS Collaboration), *Search for a scalar partner of the top quark in the jets plus missing transverse momentum final state at* $\sqrt{s} = 13$ *TeV with the ATLAS detector*, Journal of High Energy Physics **2017** (2017), URL: `http://dx.doi.org/10.1007/JHEP12(2017)085`.

[36] M. Aaboud et al. (The ATLAS Collaboration), *Search for top squarks decaying to tau sleptons in pp collisions at* $\sqrt{s} = 13$ *TeV with the ATLAS detector*, Physical Review D **98** (2018), URL: `http://dx.doi.org/10.1103/PhysRevD.98.032008`.

[37] M. Aaboud et al. (The ATLAS Collaboration), *The ATLAS Experiment at the CERN Large Hadron Collider*, Journal of Instrumentation **3** (2008) S08003–S08003, URL: `https://doi.org/10.1088%2F1748-0221%2F3%2F08%2Fs08003`.

[38] S. Chatrchyan et al. (The CMS Collaboration), *The CMS experiment at the CERN LHC*, Journal of Instrumentation **3** (2008) S08004–S08004, URL: `https://doi.org/10.1088%2F1748-0221%2F3%2F08%2Fs08004`.

[39] K. Adamodt et al. (The ALICE Collaboration), *The ALICE experiment at the CERN LHC*, Journal of Instrumentation **3** (2008) S08004–S08004.

[40] A. Augusto et al. (The LHCb Collaboration), *The LHCb experiment at the CERN LHC*, Journal of Instrumentation **3** (2008) S08004–S08004.

[41] C. De Melis, *The CERN accelerator complex. Complexe des accélérateurs du CERN*, URL: http://cds.cern.ch/record/2119882, General Photo.

[42] W. Herr and B. Muratori, *Concept of luminosity*, URL: https://cds.cern.ch/record/941318.

[43] R. Bruce, G. Arduini, H. Bartosik, R. De Maria, M. Giovannozzi, G. Iadarola, J. Jowett, K. S. B. Li, M. Lamont, A. Lechner, E. Metral, D. Mirarchi, T. Pieloni, S. Redaelli, G. Rumolo, B. Salvant, R. Tomas Garcia, and J. Wenninger, *LHC Run 2: Results and challenges*, URL: https://cds.cern.ch/record/2201447.

[44] M. Aaboud et al. (The ATLAS Collaboration), *The ATLAS Experiment at the CERN Large Hadron Collider*, Journal of Instrumentation **3** (2008) S08003–S08003, URL: https://doi.org/10.1088%2F1748-0221%2F3%2F08%2Fs08003.

[45] G. Aad et al. (The ATLAS Collaboration), *Studies of the performance of the ATLAS detector using cosmic-ray muons*, The European Physical Journal C **71** (2011), URL: http://dx.doi.org/10.1140/epjc/s10052-011-1593-6.

[46] The ATLAS Collaboration, *ATLAS Insertable B-Layer Technical Design Report*, Tech. Rep. CERN-LHCC-2010-013. ATLAS-TDR-19, Sep, 2010. URL: https://cds.cern.ch/record/1291633.

[47] M. Aleksa and M. Diemoz, *Discussion on the electromagnetic calorimeters of ATLAS and CMS*, Tech. Rep. ATL-LARG-PROC-2013-002, CERN, Geneva, May, 2013. URL: https://cds.cern.ch/record/1547314.

[48] M. Aaboud et al. (The ATLAS Collaboration), *ATLAS liquid-argon calorimeter: Technical Design Report*. Technical Design Report ATLAS. CERN, Geneva, 1996. URL: https://cds.cern.ch/record/331061.

[49] M. Aaboud et al. (The ATLAS Collaboration), *ATLAS tile calorimeter: Technical Design Report*. Technical Design Report ATLAS. CERN, Geneva, 1996. URL: https://cds.cern.ch/record/331062.

[50] W. Stirling. Private communication. URL: http://www.hep.ph.ic.ac.uk/~wstirlin/plots/plots.html.

[51] M. Aaboud et al. (The ATLAS Collaboration), *Performance of the ATLAS trigger system in 2015*, The European Physical Journal C **77** (2017), URL: http://dx.doi.org/10.1140/epjc/s10052-017-4852-3.

[52] M. G. Pia and G. Weidenspointner, *Monte Carlo Simulation for Particle Detectors*, Tech. Rep. arXiv:1208.0047, Aug, 2012. URL: https://cds.cern.ch/record/1471335. Comments: CERN Council Open Symposium on European Strategy for Particle Physics, 10 - 12 September 2012, Krakow, Poland.

[53] *ATLAS Computing: technical design report.* Technical Design Report ATLAS. CERN, Geneva, 2005. URL: https://cds.cern.ch/record/837738.

[54] G. Aad et al. (The ATLAS Collaboration), *ATLAS data quality operations and performance for 2015 – 2018 data-taking*, Journal of Instrumentation **15** (2020) P04003 – P04003, URL: http://dx.doi.org/10.1088/1748-0221/15/04/P04003.

[55] T. Golling, H. S. Hayward, P. U. E. Onyisi, H. J. Stelzer, and P. Waller, *The ATLAS data quality defect database system*, The European Physical Journal C **72** (2012), URL: http://dx.doi.org/10.1140/epjc/s10052-012-1960-y.

[56] *Luminosity Public Results Run2 Web Page*, URL: https://twiki.cern.ch/twiki/bin/view/AtlasPublic/LuminosityPublicResultsRun2.

[57] S. Höche, *Introduction to parton-shower event generators*, 2015.

[58] A. Buckley, J. Butterworth, S. Gieseke, D. Grellscheid, S. Höche, H. Hoeth, F. Krauss, L. Lönnblad, E. Nurse, P. Richardson, and et al., *General-purpose event generators for LHC physics*, Physics Reports **504** (2011) 145 – 233, URL: http://dx.doi.org/10.1016/j.physrep.2011.03.005.

[59] T. N. Collaboration, R. D. Ball, V. Bertone, S. Carrazza, L. D. Debbio, S. Forte, P. Groth-Merrild, A. Guffanti, N. P. Hartland, Z. Kassabov, J. I. Latorre, E. R. Nocera, J. Rojo, L. Rottoli, E. Slade, and M. Ubiali, *Parton distributions from high-precision collider data*, 2017.

[60] J. Butterworth, S. Carrazza, A. Cooper-Sarkar, A. D. Roeck, J. Feltesse, S. Forte, J. Gao, S. Glazov, J. Huston, Z. Kassabov, and et al., *PDF4LHC recommendations for LHC Run II*, Journal of Physics G: Nuclear and Particle Physics **43** (2016) 023001, URL: http://dx.doi.org/10.1088/0954-3899/43/2/023001.

[61] S. Peskin, *An introduction To Quantum Field Theory*.

[62] E. Boos, V. Bunichev, M. Dubinin, L. Dudko, V. Edneral, V. Ilyin, A. Kryukov, V. Savrin, A. Semenov, and A. Sherstnev, *CompHEP 4.4— automatic computations from Lagrangians to events*, Nuclear Instruments and Methods in Physics Research Section A: Accelerators, Spectrometers, Detectors and Associated Equipment **534** (2004) 250 – 259, URL: http://dx.doi.org/10.1016/j.nima.2004.07.096.

[63] A. Pukhov, *CalcHEP 2.3: MSSM, structure functions, event generation, batchs, and generation of matrix elements for other packages*, arXiv:hep-ph/0412191.

[64] J. Alwall, P. Demin, S. d. Visscher, R. Frederix, M. Herquet, F. Maltoni, T. Plehn, D. L. Rainwater, and T. Stelzer, *MadGraph/MadEvent v4: the new web generation*, Journal of High Energy Physics **2007** (2007) 028 – 028, URL: http://dx.doi.org/10.1088/1126-6708/2007/09/028.

[65] A. Kanaki and C. G. Papadopoulos, *HELAC: A package to compute electroweak helicity amplitudes*, Computer Physics Communications **132** (2000) 306 – 315, URL: http://dx.doi.org/10.1016/S0010-4655(00)00151-X.

[66] F. Krauss, R. Kuhn, and G. Soff, *AMEGIC++ 1.0, A Matrix Element Generator In C++*, Journal of High Energy Physics **2002** (2002) 044 – 044, `URL:` `http://dx.doi.org/10.1088/1126-6708/2002/02/044`.

[67] J. R. Mauro Moretti, Thorsten Ohl, *O'Mega: An Optimizing Matrix Element Generator*,.

[68] M. Bähr, S. Gieseke, M. A. Gigg, D. Grellscheid, K. Hamilton, O. Latunde-Dada, S. Plätzer, P. Richardson, M. H. Seymour, A. Sherstnev, and et al., *Herwig++ physics and manual*, The European Physical Journal C **58** (2008) 639 – 707, `URL:` `http://dx.doi.org/10.1140/epjc/s10052-008-0798-9`.

[69] T. Gleisberg and S. Höche, *Comix, a new matrix element generator*, Journal of High Energy Physics **2008** (2008) 039 – 039, `URL:` `http://dx.doi.org/10.1088/1126-6708/2008/12/039`.

[70] V. Gribov and L. Lipatov, *Deep inelastic e p scattering in perturbation theory*, Sov. J. Nucl. Phys. **15** (1972) 438–450.

[71] Y. L. Dokshitzer, *Calculation of the Structure Functions for Deep Inelastic Scattering and e+ e- Annihilation by Perturbation Theory in Quantum Chromodynamics.*, Sov. Phys. JETP **46** (1977) 641–653.

[72] G. Altarelli and G. Parisi, *Asymptotic Freedom in Parton Language*, Nucl. Phys. B **126** (1977) 298–318.

[73] B. Webber, *Fragmentation and hadronization*, eConf **C990809** (2000) 577–606, `arXiv:hep-ph/9912292`.

[74] D. Amati and G. Veneziano, *Preconfinement as a Property of Perturbative QCD*, Phys. Lett. B **83** (1979) 87–92.

[75] S. Agostinelli et al., *Geant4—a simulation toolkit*, Nuclear Instruments and Methods in Physics Research Section A: Accelerators, Spectrometers, Detectors and Associated Equipment **506** (2003) 250 – 303, `URL:` `http://www.sciencedirect.com/science/article/pii/S0168900203013688`.

[76] J. Allison et al., *Recent developments in Geant4*, Nuclear Instruments and Methods in Physics Research Section A: Accelerators, Spectrometers, Detectors and Associated Equipment **835** (2016) 186 – 225, `URL:` `http://www.sciencedirect.com/science/article/pii/S0168900216306957`.

[77] W. Lukas, *Fast Simulation for ATLAS: Atlfast-II and ISF*, Journal of Physics: Conference Series **396** (2012) 022031, `URL:` `https://doi.org/10.1088%2F1742-6596%2F396%2F2%2F022031`.

[78] E. Richter-Was, D. Froidevaux, and L. Poggioli, *ATLFAST 2.0 a fast simulation package for ATLAS*,.

[79] ATLAS Collaboration, *The Pythia 8 A3 tune description of ATLAS minimum bias and inelastic measurements incorporating the Donnachie-Landshoff diffractive model*, Tech.

Rep. ATL-PHYS-PUB-2016-017, CERN, Geneva, Aug, 2016. URL: https://cds.cern.ch/record/2206965.

[80] A. D. Martin, W. J. Stirling, R. S. Thorne, and G. Watt, *Parton distributions for the LHC*, The European Physical Journal C **63** (2009) 189 – 285, URL: http://dx.doi.org/10.1140/epjc/s10052-009-1072-5.

[81] P. Nason, *A New Method for Combining NLO QCD with Shower Monte Carlo Algorithms*, Journal of High Energy Physics **2004** (2004) 040–040, URL: https://doi.org/10.1088/1126-6708/2004/11/040.

[82] S. Frixione, P. Nason, and C. Oleari, *Matching NLO QCD computations with parton shower simulations: the POWHEG method*, Journal of High Energy Physics **2007** (2007) 070–070, URL: https://doi.org/10.1088/1126-6708/2007/11/070.

[83] S. Alioli, P. Nason, C. Oleari, and E. Re, *A general framework for implementing NLO calculations in shower Monte Carlo programs: the POWHEG BOX*, Journal of High Energy Physics **2010** (2010), URL: http://dx.doi.org/10.1007/JHEP06(2010)043.

[84] R. D. Ball, V. Bertone, S. Carrazza, C. S. Deans, L. Del Debbio, S. Forte, A. Guffanti, N. P. Hartland, J. I. Latorre, and et al., *Parton distributions for the LHC run II*, Journal of High Energy Physics **2015** (2015), URL: http://dx.doi.org/10.1007/JHEP04(2015)040.

[85] D. J. Lange, *The EvtGen particle decay simulation package*, Nuclear Instruments and Methods in Physics Research Section A: Accelerators, Spectrometers, Detectors and Associated Equipment **462** (2001) 152 – 155, URL: http://www.sciencedirect.com/science/article/pii/S0168900201000894, BEAUTY2000, Proceedings of the 7th Int. Conf. on B-Physics at Hadron Machines.

[86] M. Aaboud et al. (The ATLAS Collaboration), *Performance of the ATLAS track reconstruction algorithms in dense environments in LHC Run 2*, The European Physical Journal C **77** (2017), URL: http://dx.doi.org/10.1140/epjc/s10052-017-5225-7.

[87] A. Rosenfeld and J. Faltz, *Sequential Operations in Digital Picture Processing*, Journal of the ACM (1966), URL: https://doi.org/10.1145/321356.321357.

[88] R. Frühwirth, *Application of Kalman filtering to track and vertex fitting*, Nuclear Instruments and Methods in Physics Research Section A: Accelerators, Spectrometers, Detectors and Associated Equipment **262** (1987) 444 – 450, URL: http://www.sciencedirect.com/science/article/pii/0168900287908874.

[89] S. Gadomski, *ATLAS Inner Detector performance*, Nuclear Instruments and Methods in Physics Research Section A: Accelerators, Spectrometers, Detectors and Associated Equipment **462** (2001) 285 – 290, URL: http://www.sciencedirect.com/science/article/pii/S0168900201001243, BEAUTY2000, Proceedings of the 7th Int. Conf. on B-Physics at Hadron Machines.

[90] D. Wicke, *A New Algorithm for Solving Tracking Ambiguities*, URL: https://cds.cern.ch/record/2625731.

[91] T. A. collaboration, *A neural network clustering algorithm for the ATLAS silicon pixel detector*, Journal of Instrumentation **9** (2014) P09009 – P09009, URL: http://dx.doi.org/10.1088/1748-0221/9/09/P09009.

[92] T. Cornelissen, M. Elsing, I. Gavrilenko, W. Liebig, E. Moyse, and A. Salzburger, *The new ATLAS track reconstruction (NEWT)*, Journal of Physics: Conference Series **119** (2008) 032014, URL: https://doi.org/10.1088/1742-6596/119/3/032014.

[93] M. Aaboud et al. (The ATLAS Collaboration), *Reconstruction of primary vertices at the ATLAS experiment in Run 1 proton – proton collisions at the LHC*, The European Physical Journal C **77** (2017), URL: http://dx.doi.org/10.1140/epjc/s10052-017-4887-5.

[94] G. Piacquadio, K. Prokofiev, and A. Wildauer, *Primary vertex reconstruction in the ATLAS experiment at LHC*, Journal of Physics: Conference Series **119** (2008) 032033, URL: https://doi.org/10.1088/1742-6596/119/3/032033.

[95] W. Waltenberger, R. Frühwirth, and P. Vanlaer, *Adaptive vertex fitting*, Journal of Physics G: Nuclear and Particle Physics **34** (2007) N343–N356, URL: https://doi.org/10.1088/0954-3899/34/12/n01.

[96] ATLAS Collaboration, *Performance of the ATLAS Inner Detector Track and Vertex Reconstruction in the High Pile-Up LHC Environment*, Tech. Rep. ATLAS-CONF-2012-042, CERN, Geneva, Mar, 2012. URL: http://cds.cern.ch/record/1435196.

[97] G. Aad et al. (The ATLAS Collaboration), *Topological cell clustering in the ATLAS calorimeters and its performance in LHC Run 1*, The European Physical Journal C **77** (2017), URL: http://dx.doi.org/10.1140/epjc/s10052-017-5004-5.

[98] G. Pospelov and the Atlas Hadronic Calibration Group, *The overview of the ATLAS local hadronic calibration*, Journal of Physics: Conference Series **160** (2009) 012079, URL: https://doi.org/10.1088/1742-6596/160/1/012079.

[99] M. Cacciari, G. P. Salam, and G. Soyez, *The anti-k_T jet clustering algorithm*, Journal of High Energy Physics **2008** (2008) 063 – 063, URL: http://dx.doi.org/10.1088/1126-6708/2008/04/063.

[100] M. Aaboud et al. (The ATLAS Collaboration), *Jet energy scale measurements and their systematic uncertainties in proton-proton collisions at $\sqrt{s} = 13$ ⊠ TeV with the ATLAS detector*, Physical Review D **96** (2017), URL: http://dx.doi.org/10.1103/PhysRevD.96.072002.

[101] *Expected performance of the ATLAS b-tagging algorithms in Run-2*, Tech. Rep. ATL-PHYS-PUB-2015-022, CERN, Geneva, Jul, 2015. URL: http://cds.cern.ch/record/2037697.

[102] ATLAS Collaboration, *Commissioning of the ATLAS high-performance b-tagging algorithms in the 7 TeV collision data*, Tech. Rep. ATLAS-CONF-2011-102, CERN, Geneva, Jul, 2011. URL: https://cds.cern.ch/record/1369219.

[103] ATLAS Collaboration, *Identification of Jets Containing b-Hadrons with Recurrent Neural Networks at the ATLAS Experiment*, Tech. Rep. ATL-PHYS-PUB-2017-003, CERN, Geneva, Mar, 2017. URL: `https://cds.cern.ch/record/2255226`.

[104] ATLAS Collaboration, M. Paganini, *Machine Learning Algorithms for b-Jet Tagging at the ATLAS Experiment*, Tech. Rep. ATL-PHYS-PROC-2017-211. 4, CERN, Geneva, Oct, 2017. URL: `http://cds.cern.ch/record/2289214`. 7 pages, 5 figures, in proceedings of the 18th International Workshop on Advanced Computing and Analysis Techniques in Physics Research (ACAT 2017).

[105] A. Collaboration, *Electron reconstruction and identification in the ATLAS experiment using the 2015 and 2016 LHC proton-proton collision data at* $\sqrt{s} = 13$ *TeV*, Eur. Phys. J. C **79** (2019) 639. 40 p, URL: `http://cds.cern.ch/record/2657964`, 63 pages in total, author list starting page 47, 16 figures, 4 tables, final version published in EPJC. All figures including auxiliary figures are available at https://atlas.web.cern.ch/Atlas/GROUPS/PHYSICS/PAPERS/PERF-2017-01.

[106] T. G. Cornelissen, M. Elsing, I. Gavrilenko, J. F. Laporte, W. Liebig, M. Limper, K. Nikolopoulos, A. Poppleton, and A. Salzburger, *The global* χ^2 *track fitter in ATLAS*, J. Phys.: Conf. Ser. **119** (2008) 032013, URL: `https://cds.cern.ch/record/1176901`.

[107] A. Collaboration, *Electron efficiency measurements with the ATLAS detector using 2012 LHC proton-proton collision data. Electron efficiency measurements with the ATLAS detector using 2012 LHC proton-proton collision data*, Eur. Phys. J. C **77** (2016) 195. 64 p, URL: `https://cds.cern.ch/record/2237544`, 65 pages in total, author list starting page 49, 24 figures, 3 tables. Published in EPJC. All figures including auxiliary figures are available at http://atlas.web.cern.ch/Atlas/GROUPS/PHYSICS/PAPERS/PERF-2016-01.

[108] C. W. Fabjan and F. Gianotti, *Calorimetry for Particle Physics*, Rev. Mod. Phys. **75** (2003) 1243–1286. 96 p, URL: `https://cds.cern.ch/record/692252`.

[109] M. Aharrouche et al. (The ATLAS Collaboration), *Energy linearity and resolution of the ATLAS electromagnetic barrel calorimeter in an electron test-beam*, Nuclear Instruments and Methods in Physics Research Section A: Accelerators, Spectrometers, Detectors and Associated Equipment **568** (2006) 601 – 623, URL: `http://www.sciencedirect.com/science/article/pii/S0168900206013222`.

[110] *Electron and photon energy calibration with the ATLAS detector using 2015-2016 LHC proton-proton collision data*, JINST **14** (2018) P03017. 61 p, URL: `https://cds.cern.ch/record/2650720`, Submitted to JINST.

[111] G. Aad et al. (The ATLAS Collaboration), *Muon reconstruction performance of the ATLAS detector in proton− proton collision data at* $\sqrt{s} = 13$ *TeV*, The European Physical Journal C **76** (2016), URL: `http://dx.doi.org/10.1140/epjc/s10052-016-4120-y`.

[112] G. Aad et al. (The ATLAS Collaboration), *Identification and energy calibration of hadronically decaying tau leptons with the ATLAS experiment in pp collisions at* $\sqrt{s} = 8$

TeV, The European Physical Journal C **75** (2015), URL: http://dx.doi.org/10.1140/epjc/s10052-015-3500-z.

[113] ATLAS Collaboration, *Identification of hadronic tau lepton decays using neural networks in the ATLAS experiment*, Tech. Rep. ATL-PHYS-PUB-2019-033, CERN, Geneva, Aug, 2019. URL: https://cds.cern.ch/record/2688062.

[114] M. Aaboud et al. (The ATLAS Collaboration), *Performance of missing transverse momentum reconstruction with the ATLAS detector using proton – proton collisions at* $\sqrt{s} = 13$ *TeV*, The European Physical Journal C **78** (2018), URL: http://dx.doi.org/10.1140/epjc/s10052-018-6288-9.

[115] A. Elagin, P. Murat, A. Pranko, and A. Safonov, *A new mass reconstruction technique for resonances decaying to*, Nuclear Instruments and Methods in Physics Research Section A: Accelerators, Spectrometers, Detectors and Associated Equipment **654** (2011) 481 – 489, URL: http://dx.doi.org/10.1016/j.nima.2011.07.009.

[116] ATLAS Collaboration, *Trigger Menu in 2017*, Tech. Rep. ATL-DAQ-PUB-2018-002, CERN, Geneva, Jun, 2018. URL: https://cds.cern.ch/record/2625986.

[117] M. Aaboud et al. (The ATLAS Collaboration), *Monitoring and data quality assessment of the ATLAS liquid argon calorimeter*, Journal of Instrumentation **9** (2014) P07024 – P07024, URL: http://dx.doi.org/10.1088/1748-0221/9/07/P07024.

[118] R. Costa Batalha Pedro, *Operation and Performance of the ATLAS Tile Calorimeter*, URL: https://cds.cern.ch/record/2741322.

[119] G. Aad et al. (The ATLAS Collaboration), *ATLAS data quality operations and performance for 2015 – 2018 data-taking*, Journal of Instrumentation **15** (2020) P04003 – P04003, URL: http://dx.doi.org/10.1088/1748-0221/15/04/P04003.

[120] G. Cowan, K. Cranmer, E. Gross, and O. Vitells, *Asymptotic formulae for likelihood-based tests of new physics*, The European Physical Journal C **71** (2011), URL: http://dx.doi.org/10.1140/epjc/s10052-011-1554-0.

[121] K. Cranmer, *Practical Statistics for the LHC*, 2015.

[122] F. James and M. Roos, *Minuit - a system for function minimization and analysis of the parameter errors and correlations*, Computer Physics Communications **10** (1975) 343 – 367, URL: http://www.sciencedirect.com/science/article/pii/0010465575900399.

[123] ROOT Collaboration, K. Cranmer, G. Lewis, L. Moneta, A. Shibata, and W. Verkerke, *HistFactory: A tool for creating statistical models for use with RooFit and RooStats*, Tech. Rep. CERN-OPEN-2012-016, New York U., New York, Jan, 2012. URL: https://cds.cern.ch/record/1456844.

[124] Dr. Olaf Behnke, Dr. Kevin Kröninger, Dr. Grégory Schott, Dr. Thomas Schörner - Sadenius, *Data Analysis in High Energy Physics: A Practical Guide to Statistical Methods*. 2013.

[125] T. Junk, *Confidence level computation for combining searches with small statistics*, Nuclear Instruments and Methods in Physics Research Section A: Accelerators, Spectrometers, Detectors and Associated Equipment **434** (1999) 435 – 443, `URL`: `http://www.sciencedirect.com/science/article/pii/S0168900299004982`.

[126] A. Wald, *Tests of Statistical Hypotheses Concerning Several Parameters When the Number of Observations is Large*, Transactions of the American Mathematical Society **54** (1943) 426–482, `URL`: `http://www.jstor.org/stable/1990256`.

[127] ATLAS Collaboration, *Object-based missing transverse momentum significance in the ATLAS detector*, Tech. Rep. ATLAS-CONF-2018-038, CERN, Geneva, Jul, 2018. `URL`: `http://cds.cern.ch/record/2630948`.

[128] M. Aaboud et al. (The ATLAS Collaboration), *Measurements of $t\bar{t}$ differential cross-sections of highly boosted top quarks decaying to all-hadronic final states in pp collisions at $\sqrt{s} = 13$ ⊠ TeV using the ATLAS detector*, Physical Review D **98** (2018), `URL`: `http://dx.doi.org/10.1103/PhysRevD.98.012003`.

[129] D. Buscher, *Search for Higgs bosons with b-jets in the final state in proton-proton collisions with the ATLAS experiment*, Nov, 2016. `URL`: `https://cds.cern.ch/record/2232472`. Presented 26 Oct 2016.

[130] J. Pumplin, D. Stump, R. Brock, D. Casey, J. Huston, J. Kalk, H. L. Lai, and W. K. Tung, *Uncertainties of predictions from parton distribution functions. II. The Hessian method*, Physical Review D **65** (2001), `URL`: `http://dx.doi.org/10.1103/PhysRevD.65.014013`.

[131] G. Avoni et al., *The new LUCID-2 detector for luminosity measurement and monitoring in ATLAS*, Journal of Instrumentation **13** (2018) P07017–P07017, `URL`: `https://doi.org/10.1088%2F1748-0221%2F13%2F07%2Fp07017`.

[132] G. Aad et al. (The ATLAS Collaboration), *Measurement of the muon reconstruction performance of the ATLAS detector using 2011 and 2012 LHC proton - proton collision data*, The European Physical Journal C **74** (2014), `URL`: `http://dx.doi.org/10.1140/epjc/s10052-014-3130-x`.

[133] ATLAS Collaboration, *Reconstruction, Energy Calibration, and Identification of Hadronically Decaying Tau Leptons in the ATLAS Experiment for Run-2 of the LHC*, Tech. Rep. ATL-PHYS-PUB-2015-045, CERN, Geneva, Nov, 2015. `URL`: `https://cds.cern.ch/record/2064383`.

[134] M. Aaboud et al. (The ATLAS Collaboration), *Jet energy scale and resolution measured in proton-proton collisions at $\sqrt{s} = 13$ TeV with the ATLAS detector*, 2020.

[135] M. Aaboud et al. (The ATLAS Collaboration), *Measurements of b-jet tagging efficiency with the ATLAS detector using $t\bar{t}$ events at $\sqrt{s} = 13$ TeV*, Journal of High Energy Physics **2018** (2018), `URL`: `http://dx.doi.org/10.1007/JHEP08(2018)089`.

[136] A. Roodman, *Blind Analysis in Particle Physics*, tech. rep., 2003. `URL`: `https://arxiv.org/abs/physics/0312102`.